Frederik Graw
Franziska Matthäus
Jürgen Pahle *Editors*

Modeling Cellular Systems

Springer

Contributions in Mathematical and Computational Sciences

Volume 11

Series editors

Hans Georg Bock
Willi Jäger
Hans Knüpfer
Otmar Venjakob

More information about this series at http://www.springer.com/series/8861

Frederik Graw · Franziska Matthäus
Jürgen Pahle
Editors

Modeling Cellular Systems

🐴 Springer

Editors
Frederik Graw
Heidelberg University
Heidelberg
Germany

Jürgen Pahle
Heidelberg University
Heidelberg
Germany

Franziska Matthäus
Heidelberg University
Heidelberg
Germany

Preface

The life of multicellular organisms, such as humans and animals, is a complex dynamic process requiring the constant interaction of various molecules, cells, organs and other factors within the organism itself, and in exchange with the environment. In the human body, each cell has its specific task that is necessary to enable us to walk, breath, produce energy or fight infections. Only the tight regulation of multiple processes on various scales, be it on the genetic, molecular or cell population level, leads to the proper functioning of the complete system. Each cell on its own also represents a complex, multi-scale system that receives, processes and transmits information by cellular signalling, the production of enzymes and proteins, or by adapting their mechanical properties or cell cycle dynamics. While, step by step, we learn more and more about individual elements and processes of cellular dynamics and interactions, how these parts are connected within the complete system still remains an area of active research. Currently, some major topics of interest are the investigation of interacting processes across different spatio-temporal scales (i.e. the genetic or chemical regulation of complex cell behaviours like division, motility or ageing), the importance and effects of the inherent stochasticity in biological systems, and the integration of complex interactions of many cellular components to a stimulus or new environment leading to a single, well-defined cellular behaviour.

To better understand the processes regulating the functioning of single cells, or the interaction between cells, mathematical models provide help to formulate hypotheses in an abstract way and represent a means to make predictions. Mathematical models formalise physical and chemical laws underlying biological systems, for instance chemical reaction kinetics or diffusion. They allow the integration of elements and processes from various sources and scales in a systematic and quantitative framework, i.e. studying the interdependency of individual processes. Using these models, we are also able to quantify elements that are not directly observable in lab experiments and to identify key processes that shape the behaviour of the system.

The development of mathematical models as a tool to generate understanding of biological processes has always been driven by the progress of experimental

techniques. Novel experimental data and observations usually also require the development of appropriate mathematical methods in order to analyse and interpret these data in a meaningful way. The theoretical considerations on particle diffusion followed the development of microscopy. Similarly, one of the most famous mathematical models in biology—the Hodgkin–Huxley model describing the molecular basis of action potentials in nerves—was guided by observations based on voltage clamp, a new experimental technique that allowed to measure ion currents of neuronal membranes and control the membrane potential.

In recent years, biological sciences have experienced enormous advances in experimental techniques that allow the quantification of biological processes in more and more detail. In particular imaging technologies have improved substantially in terms of spatial and temporal resolution, also driven by the development of novel fluorescent dyes and techniques. Single molecule spectroscopy allows the visualisation and quantification of single molecules within individual cells. With life cell and two-photon imaging, as well as 3-D microscopy we are able to observe and track the behaviour of single cells within particular organs over time, or even across an entire organism. Further experimental techniques, such as high-throughput -omics technologies quantifying entire chemical subsystems of a cell (e.g. proteins, metabolic compounds or gene expression), cellular barcoding, which enables us to follow the fate of individual cells during differentiation and migration, or traction force microscopy, generate tremendous amounts and various types of quantitative data. We strongly expect that inspired by the data generated by these technologies novel mathematical models and methods have to be developed, in order to formalise and test newly generated hypotheses about biological processes, and to provide a systematic and quantitative understanding of the often complex structures and interactions across multiple scales. Without the help of mathematical models a proper quantification and interpretation of these novel types of data and observations is practically impossible. Mathematical models are essential to describe the underlying mechanistic processes spanning different spatio-temporal scales and the interaction of many biological components. They provide a more thorough understanding of the observed data than purely statistical approaches, as they go beyond simple quantitative and qualitative comparisons.

The process of mathematical model building is thereby challenging and often tedious, as many different requirements have to be considered:

1. Does the model correctly describe the experimental data?
2. Are the assumptions on the underlying biological processes plausible and how sensitive are our conclusions with regard to these assumptions?
3. Does the model comprise the minimum complexity necessary to explain all observed behaviours, or is a further reduction sensible?
4. Does the model allow predictions that can be tested experimentally and, thus, allow model validation?
5. Is a rigorous mathematical analysis of the model possible? If not, can the model be analysed numerically?

The chapters of this book contain examples of mathematical modelling approaches describing and analysing cellular systems on different scales. The different models and technical approaches depend on the biological system being investigated, and the particular question addressed. An important role plays the consideration of stochasticity within the modelling procedures.

The first chapter by Ádám M. Halász, Meghan McCabe Pryor, Bridget S. Wilson and Jeremy S. Edwards on "Spatiotemporal Modeling of Membrane Receptors" provides a detailed overview of mathematical modelling approaches for cellular processes with a specific focus on the processes involved in early signalling of membrane receptors. Mathematical modelling of chemical reactions and reaction networks is being discussed, as well as the necessity for stochastic approaches when the copy numbers of the involved compounds are small. The chapter introduces models of increasing complexity starting from simple approaches based on reaction–diffusion models up to models including specific spatial aspects such as agent-based modelling systems accounting for Brownian and non-Brownian motion or anomalous diffusion. This chapter describes and discusses classical modelling principles and approaches also used in the following chapters. It provides an introduction to the field of mathematical modelling in biology, also accessible to non-experts in the field. Elaborating on the topic of stochasticity of chemical reactions, Chapter "Distribution Approximations for the Chemical Master Equation: Comparison of the Method of Moments and the System Size Expansion"—contributed by Alexander Andreychenko, Luca Bortolussi, Ramon Grima, Philipp Thomas, and Verena Wolf—focuses on stochastic chemical kinetics. The chapter presents and compares two different approaches to estimate the probability distribution associated with the amounts of different chemical species: the indirect estimation via moment closure techniques and the direct approach using system size expansion. The two approximation methods analysed represent useful tools for the analysis of large-scale models.

The authors of Chapter "Sampling from T Cell Receptor Repertoires", Marco Ferrarini, Carmen Molina-París and Grant Lythe, address a related problem by trying to predict the complete repertoire of T-cell clonotypes, a specific type of immune cells, from a sample of a few hundred T-cells. The estimation of the size and the distribution of these T-cell clonotypes is challenging due to the total population size, which is distributed heterogeneously across the whole organism, and the immense natural variability of clonotype construction. Therefore, a large probability space needs to be estimated from extremely sparse experimental data. Using various assumptions on the underlying distribution of clone sizes, they investigate the possibility and challenges to infer the total population structure based on small individual samples.

Chapters "IL-2 Stimulation of Regulatory T Cells: A Stochastic and Algorithmic Approach" and "Understanding the Role of Mitochondria Distribution in Calcium Dynamics and Secretionin Bovine Chromaffin Cells" couple stochastic modelling of signalling processes determining cell–cell interactions and higher order cell functions, respectively. In Chapter "IL-2 Stimulation of Regulatory T Cells: A Stochastic and Algorithmic Approach" an algorithmic approach is presented by Luis de la Higuera, Martín López-García, Grant Lythe, and Carmen Molina-París to solve and analyse a

stochastic model of receptor-mediated cell–cell interactions. In the underlying biological scenario looking at the IL-2 dependency of regulatory T-cells, one cell type, i.e. effector T-cells, provides the chemical substance needed by the second cell type, i.e. the regulatory T-cells for survival. The authors provide an algorithmic approach to determine the rates at which receptor–ligand interactions are formed and thereby define cell fate. Chapter "Understanding the Role of Mitochondria Distribution in Calcium Dynamics and Secretion in Bovine Chromaffin Cells", contributed by Amparo Gil, Virginia González-Vélez, José Villanueva and Luis M. Gutiérrez, couples a stochastic description of intracellular calcium signalling with cell function, i.e. exocytosis. The regulatory relationship between signalling and function is hereby affected by the spatial distribution of cell organelles, in particular mitochondria, since they limit the diffusion of the involved components. The authors present a spatially explicit modelling scheme analysing the dynamics of intracellular components.

The book concludes with Chapters "Dynamical Features of the MAP Kinase Cascade" and "Numerical Treatment of the Filament-Based Lamellipodium Model (FBLM)", which comprise two different deterministic modelling approaches at two different scales. In Chapter "Dynamical Features of the MAP Kinase Cascade", Juliette Hell and Alan D. Rendall use a deterministic modelling approach to describe the dynamics of the MAPK signalling cascade, a widespread intracellular signalling pathway within eukaryotes. They perform a mathematical analysis of the system described by ordinary differential equations showing its qualitative behaviour under different conditions. Finally, Chapter "Numerical Treatment of the Filament-Based Lamellipodium Model (FBLM)", authored by Angelika Manhart, Dietmar Oelz, Christian Schmeiser and Nikolaos Sfakianakis, introduces a continuous model coupling cell mechanics with the dynamics of cytoskeleton components, discussing its mathematical analysis and showing corresponding numerical simulations based on a finite-element method.

In summary, the different chapters in this book address various types of mathematical models and methods to describe and analyse biological systems and processes on different cellular scales. They cover a variety of biological topics reaching from the analysis of intracellular signalling pathways to the level of cell mechanics and cytoskeleton structuring, up to the regulation of cell populations within immune responses. The different approaches demonstrate how challenging mathematical problems arise from the mechanistic description of cellular processes and interactions. The importance of the development of such models, as well as their rigorous mathematical and numerical analysis is steadily increasing in line with the progress of measurement techniques in quantitative biology. The combination of detailed quantitative measurements of increasing resolution in time and space with novel mathematical models will help us to get a systems level understanding of individual processes, and might finally lead us to a better understanding of the dynamics and regulation of cellular processes that shape life.

Heidelberg, Germany   Frederik Graw
                                                                                    Franziska Matthäus
                                                                                        Jürgen Pahle

Organisation

Programme Chairs

Frederik Graw (BIOMS, BioQuant/IWR, Heidelberg University)
Franziska Matthäus (BIOMS, BioQuant/IWR, Heidelberg University)
Jürgen Pahle (BIOMS, BioQuant, Heidelberg University)

Contents

Spatiotemporal Modeling of Membrane Receptors

Ádám M. Halász, Meghan McCabe Pryor, Bridget S. Wilson and Jeremy S. Edwards

Abstract We discuss our approach to the detailed computational modeling of the molecular processes involved in early signaling of membrane-bound receptors, typically exemplified by members of the receptor tyrosine kinase (RTK) family. This includes receptors whose mutations are associated with increased risk of cancers (ErbB2) or are involved in the survival of nascent tumors (Kdr). Current imaging methods can visualize individual molecules in the context of the living cell, allowing the direct observation of molecular movement and transformations. Modeling and simulation are necessary to connect these observations to the cell-level kinetics of signaling and to help reveal connections between molecular properties and cell signaling, under both normal and pathological conditions. We describe the relevant methods and provide a minimal mathematical justification for the reader interested in understanding or applying them. The chapter builds up from the simplest modeling approach to the fully spatial, agent-based simulation that is currently used by our group. This should be useful from a tutorial perspective and also to provide the proper connections between models at different levels of granularity.

Á.M. Halász (✉)
Department of Mathematics, West Virginia University,
P.O.Box 6310, Morgantown, WV 26506, USA
e-mail: halasz@math.wvu.edu

M.M. Pryor
Department of Biomedical Engineering, School of Medicine,
Johns Hopkins University, Baltimore, MD 21205, USA
e-mail: mmccabe9@jhu.edu

B.S. Wilson
Department of Pathology, University of New Mexico Health Science Center,
Albuquerque, NM 87131, USA
e-mail: BWilson@salud.unm.edu

J.S. Edwards
Department of Chemistry and Chemical Biology, University of New Mexico,
MSC03 2060, Albuquerque, NM 87131, USA
e-mail: jsedward@unm.edu

1   Introduction

The technological advances of the past few decades fueled the fast growth of a quantitative dimension to biology. The work discussed here describes computational approaches for simulating and predicting outcomes of molecular processes on the behavior and output of the overall system. The consideration of "dynamics" offers improved understanding of stochastic processes, such as diffusion-limited reactions, and is markedly distinct from approaches that infer causal connections between genes, mutations, phenotypes, and pathologies from large datasets.

We define mathematical models that, at least in part, recapitulate the behavior of living cells observable in quantitative experiments. Models that integrate the dynamics of living systems are *reductionist and mechanistic*; they result from the composition of simple, physically motivated descriptions of the various elements taken separately. In contrast with occasional misperceptions,[1] the resulting integrative dynamical models are precisely the way to understand or predict emerging system properties. Furthermore, the focus of our discussion is on processes that are *random*,[2] and therefore the predictions that such models can make are *likely versions of system behavior*.

Modeling Membrane Dynamics

Very significant advances in experimental techniques, in particular, high-resolution microscopy combined with the ability to reliably label molecules of interest, opened the door to a wealth of data on the movement and chemical state of individual molecules. This has the potential to greatly refine the already vast knowledge of the biochemistry of cell signaling, accumulated through more traditional avenues of investigation, such as in vitro identification of molecular structures and reactions, and cell-level in vivo measurements of molecular processes.

Modern microscopy has revealed that the cell membrane presents a varied landscape which modulates the movement of membrane bound proteins. The distribution of receptors and other biomolecules is typically not homogeneous, and is characterized by structures at spatial scales ranging from several hundreds to tens of nanometers. Molecules exhibit clustering and anomalous diffusion, deviating from the null-hypothesis of uniform, random movement. This complicates the interpretation of experiments aimed at ascertaining or quantifying the details of known molecular processes.

Modeling processes on the cell membrane requires taking into account both the discrete nature of molecules, and the inhomogeneous spatial context. While mature methods exist for handling both aspects, available software, and the majority of modeling effort in the field, is not well adapted to handling the relevant spatial scale,

---

[1]In a "fundamentalist" version of reductionism (motivated by nineteenth century classical Physics, but long since abandoned in the physical sciences [40]), the properties of a system must be a sum of the properties of its parts, negating the possibility of emerging system properties.

[2]There is a distinction between processes that are intrinsically random and deterministic chaotic behaviors that can be treated as random.

ranging from just above the diameter of a receptor to a fraction of a eukaryotic cell (from 10 to a few hundred nm).

The material in this chapter is naturally divided into four sections. The rest of this section discusses (1) the continuous description of well-mixed chemical reaction systems. The following sections are devoted to: (2) stochastic models for well-mixed systems; (3) modeling and simulation of Brownian motion (diffusion) of individual molecules and finally (4) stochastic, agent-based simulation of reaction–diffusion systems. We provide a brief summary and a few closing ideas in Sect. 5.

1.1 Background: Chemical Reaction Networks, ODE Simulations

The elementary building blocks of living cells are organic molecules, proteins, lipids, and sugars. Their size ranges from a few atoms to large complexes of tens of thousands of atoms that organize into molecular machines. All the functions of the cell are realized through chemical transformations, changes in shape, assembly, and movement of molecular entities.

1.1.1 Cells as Chemical Factories

The language of chemistry provides an approximate but natural framework for a quantitative description of the state and processes inside a living cell. The state of the cell is specified in terms of the number, internal state, and location of all the molecules it is comprised of. We may account for all of these by extending the notion of a chemical *species* $A, B, \ldots$ to mean a *type* of molecular aggregate, in a specific internal *state*, in a specific *location* (section) within the cell (membrane, cytoplasm, nucleus). Then, a *reaction* $A \rightarrow B + C$ may refer to an actual chemical transformation, $A^{(e)} \rightarrow A^{(i)}$ would represent the transport of a substance from the extracellular space into the cytoplasm, and $B \rightarrow B^*$ could refer to the activation of a kinase.

There is an inevitable trade-off between the scope and the level of detail of the modeling framework. Even the simplest living cells contain hundreds of different species of molecules. A practical model typically focuses on a much smaller set of biomolecular species and processes. At a minimum, one keeps track of the *amount* of each species. This is typically represented as a *concentration*, or *amount of substance* per unit of volume (or area). We will denote the concentration of substance S_i by $[S_i]$.

It is useful to specify the precise meaning of these terms. Chemical reactions described by equations such as

$$L + 2R \rightarrow RLR \tag{1}$$

refer to the way *individual* molecules interact. In particular, the reaction above refers to a process when one molecule of species L joins with two molecules of species R, and they together form a single molecule of species RLR. Even if one does not explicitly model molecules, the *stoichiometric coefficients* in (1) specify the exact proportions in which the reactants combine.

Molecules of different species typically have different sizes or molecular weights; reaction (1) does *not* mean that 1 g of L and two grams of R will combine into 1 g of RLR. The *amount of substance* is a macroscopic quantity that is proportional to the number of molecules: 1 mol of any substance corresponds to the same number of molecules, $N_{\text{Avogadro}} \approx 6 \cdot 10^{23}$ known as Avogadro's number. Going back to the reaction (1), one mol of L combined with two moles of R will indeed form 1 mol of RLR. We summarize below the connection between the concentration $[A]$, the number of molecules n_A, and the amount of substance $\nu_A = n_A / N_{\text{Avogadro}}$ in a volume V:

$$[A] \;=\; \frac{\nu_A}{V} \;=\; \frac{n_A}{V \cdot N_{\text{Avogadro}}} \quad . \tag{2}$$

The base unit for concentration is the *molar*; 1 M corresponds to 1 mol per 1 litre of solution (the concentration is often referred to as *molarity*).

1.1.2 Chemical Reaction Network Theory

In general, a *chemical reaction network* is defined by a set of species $S_1, S_2, \ldots, S_n$ that are subject to reactions $\mathscr{R}_1, \mathscr{R}_2, \ldots, \mathscr{R}_m$. Reaction $\mathscr{R}_j$ is defined by a chemical equation and a rate φ_j:

$$\sum_{i=1}^{n} \alpha_{ij} S_i \rightarrow \sum_{i=1}^{n} \beta_{ij} S_i \;\; ; \;\; \varphi_j = f_j([S_1], [S_2], \ldots, [S_n]) \,, \tag{3}$$
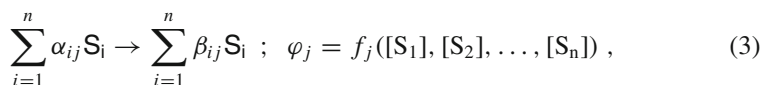
and is fully specified by the stoichiometric coefficients $\left\{\alpha_{ij}, \beta_{ij}\right\}_{i=1\ldots n}$ and the rate function $f_j(\cdot)$. The state of the system at any time t is given by the concentrations of all substances, usually arranged into a vector $\mathbf{X} = ([S_1], [S_2], \ldots, [S_n])^T$.[3] The *net* stoichiometric coefficients $\gamma_{ij} \equiv \beta_{ij} - \alpha_{ij}$ form a matrix of size $n \times m$, $\Gamma \equiv \{\gamma_{ij}\}$. If we also arrange the fluxes into a column vector $\boldsymbol{\phi} = (\varphi_1, \varphi_2, \ldots, \varphi_m)^T$, we may write out the *equations of motion* of the CRN model:

$$\frac{d\mathbf{X}}{dt} \;=\; \Gamma \cdot \boldsymbol{\phi}(\mathbf{X}) \tag{4}$$

---

[3]We implicitly assume here that the reactions take place between substances in the same solution, and therefore the stoichiometric coefficients carry over from the reactions to the concentrations.

The equations of motion are fully determined when the rate functions (or laws) $f_j(\cdot)$ in (3) are specified. The rate through a certain reaction typically depends on the concentrations of the species on the origin side; the rate is generally a nondecreasing function of these concentrations, and it must vanish if one or more of the concentrations becomes zero. Several types of functions can serve as a rate law; the exact form is ultimately determined by the system under consideration. Mass-action rates play a special role due to their close connection to simple molecular dynamics; the mass-action rate for reaction $\mathscr{R}_j$ in a generic CRN (3) is:

$$\varphi_j = k_j \prod_{i=1}^{n} [S_i]^{\alpha_{ij}} \tag{5}$$

The mass-action rate constant k_j connects the continuum description with molecular properties.

Despite the compact appearance, the equations of motion (4)–(5) define a class of complex nonlinear dynamical systems. *Chemical reaction network theory* [5, 11, 32] provided a number of results regarding the possibility and number of equilibria (steady states) of CRN systems. *Control theory* provides methods to simplify these systems and to classify their possible behaviors [36]. Such involved mathematical tools are necessary to gain insight into the complex behavior of signaling networks [4, 12, 14].

Independently of the theoretical insights, CRN models provide a basis for *numerical simulations*. There are mature methods for the simulation of sizeable ODE systems, implemented in widely available software tools. Simulations can be used to predict the behavior of cells under a variety of conditions, and are a valuable tool in biological, pharmaceutical, and medical research.

1.1.3 Need for a Stochastic Approach

The molecular nature of matter is always reflected in the exact proportions in which different substances combine. In a macroscopic context, the number of molecules involved is very large, comparable to Avogadro's number $N_{Avogadro} \approx 6 \cdot 10^{23}$ copies/mol; the discrete nature of matter is irrelevant when it comes to measuring the amount of substance. This is emphatically not the case with living cells. The diameter of a human cell is a few microns; consider a cell of $10\,\mu m^3$ that contains $100\,nM$ of a certain molecular species. That works out to

$$N = (10 \cdot 10^{-18}\,m^3) \times \left(100 \cdot 10^{-9} \cdot 10^3\,\frac{mol}{m^3}\right) \times \left(6 \cdot 10^{23}\,\frac{copies}{mol}\right) = 60\,copies \quad.$$

With larger cells and concentrations of several μM, the copy number becomes large, albeit not astronomical. The number of membrane bound receptors of one type ranges from a few thousand to 10^5 per cell, certainly not a small number. However, adding

spatial structure, for instance signaling islands that contain a few tens or hundreds of receptors, further reduces the number of copies of a molecule that can be reasonably thought of as "uniformly distributed" in a specific region of space.

Thus, the notion of describing the amount of substance of a certain type as a continuous quantity is not necessarily correct, raising questions about the validity of a modeling approach along the lines of (1)–(5). For instance, it is not very meaningful to talk about the "concentration" of a certain gene/promoter combination, when referring to a single, specific cell. The gene is either present or not; it may have more than one copy, but there cannot be exactly 1.376 copies of it.

On the other hand, it is perfectly meaningful to talk about an average copy number of 1.376, referring to cells within a population. Even when dealing with relatively small numbers of molecules within a given cell, the amount of substance or its various proxies[4] may be understood as averages over a large population.

The connection between continuous dynamics as described by (1)–(5) and the physical processes includes averaging the stochastic dynamics of a large number of cells. Individual cell behaviors may factor in the ensemble average in ways that cannot be accounted for in the ODE picture; the continuum equations of motion provide a necessary framework for large-scale modeling, but they may not capture the primordial physical reality.

Thus, kinetic constants that reasonably recapitulate the observed behavior of cell populations may be very different from the physical constants that control the underlying molecular processes. One goal of the more detailed (and necessarily, more resource intensive) modeling approaches discussed here is to investigate and uncover quantitative relations between the average and the relevant microscopic properties.

2   Reactions (Stochastic)

The discrete and stochastic nature of biomolecular processes limits the validity of continuous, ordinary differential equation based (ODE) models (4), but does not eliminate our ability to predict the future states of the system. While we cannot predict the exact states of the system, we can estimate the probabilities of the possible outcomes, either individually, or defined by certain quantifiable features (observables). Such a calculation comes as close as possible to a deterministic model, in that it provides the likelihood of all possible versions of the future behavior of the system.

Accounting for all possible states is practical only for relatively simple systems. As the number of random elements in the system increases, the number of *possible* outcomes grows exponentially; typically, the set of *likely* outcomes does not increase as fast and represents an increasingly small fraction. Consideration of all individual outcomes becomes both exceedingly expensive and unnecessary.

---

[4]Such as concentration, mass, etc.

Fig. 1 The probability that the difference between number of heads and tails exceeds 10% of the number of flips of a fair coin decreases dramatically with the number of trials. For 1,000 flips the probability is $8.6 \cdot 10^{-4}$, and for 10,000 it becomes astronomically small, $7.75 \cdot 10^{-24}$. A significant bias observed in a large number of trials would strongly indicate that the coin is not fair
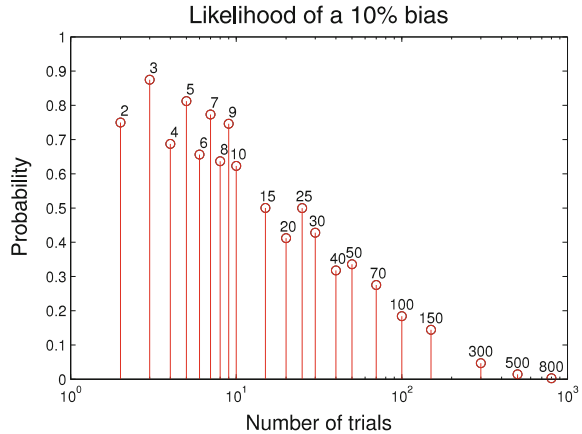
Instead, enough insight can be gained by generating a sample of possible outcomes by emulating the random variables in the system. Stochastic *simulations* are the main approach used in the biomolecular context. It is important to keep in mind that, unlike ODE simulations which predict the future behavior of the system, a stochastic simulation produces one possible future behavior of the system.

Example: Sets of Coin Flips

A much-invoked analogy with games of chance may be illuminating for some readers. One cannot predict the outcome of a single coin flip, but (assuming the coin is fair) we expect that on average, the two possible outcomes (head and tail) are equally likely. Given the probability of the elementary outcomes, we can *calculate* the likelihood of a specific number of outcomes of one type from a given number of repeated trials. We may only be interested in the excess number of heads or tails; the probability that the difference $|N_{\text{heads}} - N_{\text{tails}}|$ exceeds 10% of the number of trials $N_{\text{flips}} = N_{\text{heads}} + N_{\text{tails}}$ is shown in Fig. 1.[5] The number of excess heads or tails is an example of an *observable*, a measurable quantity that can be derived from an ordered set of coin flips.

The set of possible values an observable could take is much smaller than the set of possible outcomes (or *sample space*). The length of the largest sequence of consecutive heads or tails in a set of 1,000 flips is an observable which also depends on the order of individual coin flips; the number of distinct outcomes is enormous, $2^{100} \approx 10^{30}$, while the length of the longest streak can only take 1,000 values.

---

[5]Note that for an odd number of trials the number of heads and tails cannot be equal, increasing the likelihood of a given relative difference.

2.1 Dealing with the Molecular Nature of Chemical Reactions

In a molecular framework, we keep track of the copy number of molecules of each species. This defines the state of the system, which can be changed through reactions. Reactions occur at random times; the physical flux (or rate) through each reaction (3) is replaced by a probability per time for the occurrence of an instance of the reaction.

2.1.1 Intrinsic Transformation of a Single Molecule

To illustrate the principle of representing reactions by random processes, consider a system with two types of molecules A, B and a single reaction type, A $\rightarrow$ B. The state of the system at any time t is defined by the number of molecules of the two types, $(n_A(t), n_B(t))$. The idealized model for this type of transformation is an abstraction of molecular dynamics acting on finer time and spatial scales; we assume that each molecule of type A has an intrinsic tendency to spontaneously convert into a molecule of type B.

For each A molecule that exists at time t, the probability that it will convert to B over the subsequent *short* time interval $(t, t + \Delta t)$, is proportional to the length Δt[6]:

$$\lim_{\Delta t \to 0} \frac{\Delta p_{A \to B}(t, t + \Delta t)}{\Delta t} = k_{A \to B} \quad \Rightarrow \quad \Delta p_{A \to B}(t, t + \Delta t) \approx k_{A \to B} \Delta t \ . \quad (6)$$

The proportionality constant $k_{A \to B}$ is an inverse time, and is characteristic to the transformation. The transition is triggered independently of the rest of the system and of the past history of the transitioning molecule.

This defines a *Poisson process* with rate $k_{A \to B}$ that triggers the transition; the process 'fires' at some time, $\tau \in (t, t + \Delta t)$, with probability as described above. It can be conceptualized as a random experiment whose outcome is the firing time τ; alternatively we think of it as a time dependent random system whose state changes from A to B.

The meaning of the probability (6) is clarified if we think of multiple copies of the system. Assume we started with N_A molecules of A and we have $n_A(t)$ of them at time t. The change in n_A over $(t, t + \Delta t)$ is the same as the number of A $\rightarrow$ B transformations that take place in this time, which can be approximated by (6):

$$n_A(t) - n_A(t + \Delta t) \approx \Delta p_{A \to B}(t, t + \Delta t) \cdot n_A(t) \approx n_A(t) \cdot k_{A \to B} \cdot \Delta t + \mathcal{O}(\Delta t^2). \quad (7)$$

The approximate equalities in (7) neglect relative differences on the order of $1/\sqrt{\Delta n_A}$. For molecule counts $n_A(t)$ comparable to $N_{\text{Avogadro}} \approx 6 \times 10^{23}$, this is

---

[6]Strictly speaking, only the limit version of Eq. (6) is exact; the second form is for $\Delta p \ll 1$.

perfectly satisfactory, with room for infinitesimally small time steps $\Delta t \ll 1/k$. In this interpretation, we may treat n_A as continuous (replacing it with $v_A = n_A/N_{\text{Avogadro}}$), and write (7) as a proper limit similarly to (6):

$$\lim_{\Delta t \to 0} \frac{n_A(t + \Delta t) - n_A(t)}{\Delta t} = \frac{dn_A}{dt} = -k_{A \to B} \cdot n_A(t). \tag{8}$$

With the initial condition $n_A(0) = N_A$, the differential equation implies

$$n_A(t) = N_A \cdot e^{-k_{A \to B}t} \ . \tag{9}$$

Not surprisingly, Eqs. (8) and (9) are formally identical to those one would obtain for the concentration in the continuum picture (4)–(5). If N_A is large, the relative fluctuations around this average are small (on the order of $1/\sqrt{N_A}$).

But what about small copy numbers, where $\Delta n_A = n_A \, k_{A \to B} \, \Delta t \ll 1$, making the limit in Eq. (8) meaningless? The interpretation that also works in this case is that since we are describing a *stochastic* system of initially N_A copies of A molecules, $n_A(t)$ represents the *average* $\langle n_A(t) \rangle$, of the number of A molecules at time t. The average can be thought of taken over a large number of copies of the system.

Importantly for our purposes, we can also think of N_A in terms of a similar thought experiment, as the number of copies of the random system represented by a single A molecule that exists at time 0. Then, the ratio $n_A(t)/N_A$ approaches the probability that, at time t, the molecule under consideration has not yet converted to B;

$$p_A(t) = \lim_{N_A \to \infty} \frac{n_A(t)}{N_A} = e^{-k_{A \to B} \, t} \ . \tag{10}$$

This line of reasoning also provides the PDF (probability density function) $f(\tau)$ of the time τ when a specific A particle converts into B. Assuming that the particle belongs to species A at time $\tau = 0$, the probability that it is still an A at time $\tau = t$ is the integral of $f(\tau)$ over the interval $[0, t]$:

$$\int_0^t f(\tau)d\tau \ = \ e^{-k_{A \to B} \, t} \ \Leftrightarrow \ f(\tau) \ = \ k_{A \to B} \cdot e^{-k_{A \to B} \, \tau} \ . \tag{11}$$

2.1.2 Combining Poisson Processes

We know how to describe or simulate the behavior of a single molecule of A. We did estimate the average number $n_A(t)$ of A molecules left after time t (9). A complete analysis should provide either the probability of having exactly $0, 1, 2, \ldots, N_A$ molecules at an arbitrary time t, or a prescription to simulate the evolution of the system, consistently with the underlying stochastic properties.

The key mathematical element is the composition property of Poisson processes [34]. Suppose that at $t = 0$ we start two independent Poisson processes, with rates k_1 and k_2, and that we are only interested in the *first time either of them fires*. It turns out that the time the first one fires follows the same law as the firing time of a Poisson process that starts at $t = 0$ and has rate $k_T = k_1 + k_2$. This can be shown rigorously, using the PDF of the two firing times (11). Furthermore, the probability that process 1 fires first is $p_1 = k_1/k_T$.

Based on this property, we can easily show that the probability that any one of the $n_A(t)$ molecules of species A that exist at time t converts over $t, t + \Delta t$ is $n_A \cdot k_{A \to B} \cdot \Delta t$. In other words, the conversion of any one of the n_A molecules is triggered by a Poisson process with rate $g_{A \to B} = n_A \cdot k_{A \to B}$. Finally, the time of this next instance of the reaction $A \to B$ is distributed according to the PDF

$$f(\tau) \;=\; g_{A \to B} \cdot e^{-g_{A \to B}\,\tau} \;\; ; \;\; g_{A \to B} = n_A \cdot k_{A \to B} \tag{12}$$

The *propensity* $g_{A \to B}$ refers to all possible instances of the reaction $A \to B$.

The principle of combining Poisson processes also helps when we have several types of reactions. Suppose that A can also convert into C, with a molecular rate $k_{A \to C}$. The "dilemma" facing each A molecule is easily quantified: the rate of a given A molecule converting to either B or C is $k_{A \to X} = k_{A \to B} + k_{A \to C}$; the probability that it becomes a B as a result, is $p_B = k_{A \to B}/k_{A \to X}$. Finally, in a system with n_A copies of A, the propensity of $A \to C$ is $g_{A \to C} = n_A \cdot k_{A \to C}$, the joint propensity of the two reactions is $n_A \cdot k_{A \to X}$, and the probability that the next reaction is $A \to B$ is still $p_B = k_{A \to B}/k_{A \to X}$.

2.1.3 Simulations

A simulation provides the evolution of the state of a system over time, based on the knowledge of its dynamics. An ODE model along the lines of (3)–(5) is deterministic in the sense that the initial conditions fully determine the state of the system at any future time. By contrast, a stochastic model allows for several possible future states; the initial state determines the probabilities of the different possible outcomes. As both the ODE and the stochastic models we discuss are *surrogates* of the system being modeled, the future states we obtain are those of the respective *model systems*.

A simulation of an ODE model provides *the* future behavior of the (model) system,[7] while a single simulation run of a stochastic model provides *one possible version* of the future (a single *realization* of a probabilistic experiment). A complete account of the future behavior of a stochastic system should specify the probabilities of all possible states over time. A possible starting point for this approach is the so

---

[7]Which, in light of the discussion at Eqs. (7)–(9), approximates the average behavior of a more detailed, stochastic model of the same biomolecular system, and by extension, the average behavior of the system being modeled.

called Master Equation [34], which can be readily set up for the type of stochastic models discussed in this section.

A major drawback of "brute force" approaches along these lines is that the likely states typically represent a very small fraction of the set of possible states. Going back to the example of coin tosses, the likelihood of observing a streak of $l \geq 25$ consecutive heads or tails in a single set of 1000 flips is $\approx 2.25 \cdot 10^{-7}$, or one in 4.4 million. Even though the longest streak can be anywhere between 1 and 1,000, only $\approx 2.5\%$ of these possible outcomes are ever observed.

We will focus exclusively on *stochastic simulations* that provide individual histories of the system, by emulating the random processes involved using random numbers generated from the appropriate distributions. A sizeable number of simulation runs provides an incomplete but informative account of the future states of the system, by necessarily sampling the likely states and avoiding the unlikely states. As we proceed to discuss various simulation methods, we ask the reader to keep in mind that the proper use of all stochastic simulations implies the estimation of the variability of the predicted values, typically by generating a sample of several simulation runs.

2.2 Stochastic Simulation Algorithm

The exact stochastic simulation algorithm (SSA) for a generic system of chemical reactions is often referred to as Gillespie simulation [8, 9] due to the pioneering work of Gillespie, who defined the terminology and proposed the use of the approach for mesoscopic, well-mixed chemical systems.

Consider a system of several species and reactions among them, similar to (3). We will denote the species by $A, B, C, \ldots$ The states of the system are defined by the number of molecules (copies) of each molecular species, $(n_A, n_B, \ldots)$. Reactions occur as instantaneous, random events. In the context of the SSA we do not identify individual molecules of the same species; similarly, an instance of a reaction corresponds to a discrete state transition that converts one set of molecules of the appropriate species, according to the chemical equation. For example, one instance of the reaction $A \rightarrow B + C$ means $(n_A, n_B, n_C) \rightarrow (n_A - 1, n_B + 1, n_C + 1)$. The set of all possible states of a given system is therefore discrete and may be finite or infinite.

Reactions are triggered by Poisson processes, similarly to what we discussed for the reaction $A \rightarrow B$. In the context of the SSA, we associate a single Poisson process to all the instances of a given reaction. The rate of the corresponding Poisson process is called the *propensity* of the reaction (denoted g), and it typically depends on the copy number of the species that are involved. The exact functional dependence reflects modeling and empirical considerations.

2.2.1 Mass-Action Propensities

In the discussion leading up to (12) we assumed that the possible instances of the reaction $\mathsf{A} \to \mathsf{B}$ were driven by identical random processes, and were therefore equally likely. If we can generally assume that *each possible instance of a reaction is equally likely*, irrespective of past history and the configuration of the system, we obtain the stochastic equivalent of mass-action kinetics.

In this model, each reaction is triggered by a Poisson process, whose rate is called the *propensity* of the reaction. The propensity of a given reaction $\mathscr{R}$, starting from a given state of the system $(n_A, n_B, \ldots)$ is the number of possible instances $Z_{\mathscr{R}}$ multiplied by an *elementary propensity* $k_{\mathscr{R}}^{(\mathrm{molec})}$ that characterizes the reaction,

$$g_{\mathscr{R}}(n_A, n_B, \ldots) = Z_{\mathscr{R}}(n_A, n_B, \ldots) \cdot k_{\mathscr{R}}^{(\mathrm{molec})} \quad . \tag{13}$$

The role of elementary propensities is similar to that of the macroscopic rate constants $k_{\mathscr{R}}^{(\mathrm{macro})}$. They can be related to molecular considerations or to macroscopic rates.

For first-order reactions (involving a single molecule: $\mathsf{A} \to \cdots$), the number of possible instances is $Z_{\mathsf{A} \to \cdots} = n_{\mathsf{A}}$, same as that of available A particles. We have stated (12) that the elementary propensity coincides with the mass-action rate constant and reflects the intrinsic (quantum mechanical) transition rate of the molecule, $k_{\mathsf{A} \to \cdots}^{(\mathrm{molec})} = k_{\mathsf{A} \to \cdots}^{(\mathrm{macro})}$.

Let us spell out the reasoning behind this. We obtained a differential equation (8) for the number of particles: $n'_A(t) = -k_{\mathsf{A} \to \mathsf{B}}^{(\mathrm{molec})} n_A(t)$. We noticed it had the same form as the mass-action equation of motion (4)–(5) for the concentration $[A]$, namely $[A]'(t) = -k_{\mathsf{A} \to \mathsf{B}}^{(\mathrm{macro})}[A](t)$. Since the concentration and number of molecules are proportional (2), we identified the ratio $[A]'/[A] \approx n'_A/n_A$ and the propensity per A particle:

$$\frac{[A]'(t)}{[A](t)} = \lim_{V \to \infty} \frac{g_{\mathsf{A} \to \mathsf{B}}}{n_A} = -k_{\mathsf{A} \to \mathsf{B}} \quad . \tag{14}$$

For second-order reactions such as $\mathsf{A} + \mathsf{B} \to \mathsf{D}$, the number of possible instances is $Z_{\mathsf{A} + \mathsf{B} \to \mathsf{D}} = n_A \cdot n_B$, the number of A, B pairs that can be formed from available molecules.[8] The propensity also depends on the collision rate between the two molecules involved, and we therefore expect it to be inversely proportional to the volume or space in which the molecules can move. It also reflects the interplay of different collision geometries with the dynamics of the reaction; its estimation from first principles is possible, but would have to include detailed molecular dynamics considerations.

Alternatively, we may estimate the propensity by relating it to the physical kinetic constant for the reaction. From the perspective of one participating A molecule, the situation is similar to the first-order case: the propensity per *molecule* is the probability per unit time of being involved in a reaction. In the macroscopic picture,

---

[8]If the reacting particles are identical, we have a combinatorial factor: $Z_{\mathsf{A} + \mathsf{A} \to \mathsf{C}} = \frac{1}{2} n_A \cdot (n_A - 1)$.

this should be comparable to the logarithmic derivative $[A]'/[A]$:

$$[A]' = -k_{A+B\to D}^{(macro)} \cdot [A] \cdot [B] \; ; \; g_{A+B\to D} = n_A \cdot n_B \cdot k_{A+B\to D}^{(molec)}$$

$$\frac{[A]'}{[A]} = \lim_{V\to\infty} \frac{g_{A+B\to D}}{n_A} \; \Rightarrow \; k_{A+B\to D}^{(molec)} = \frac{k_{A+B\to D}^{(macro)}}{V \cdot N_{Avogadro}} \qquad (15)$$

The connection between elementary propensities and rate constants can be generalized to higher order reactions, by including the appropriate number of $V \cdot N_{Avogadro}$ concentration to particle number conversion factors.

2.2.2 Competing Reactions: The Gillespie SSA and the First Reaction Method

In a generic CRN system (3) with several species and reactions, we associate a Poisson process to each reaction. The mass-action reaction propensities are calculated as described,

$$g_j(n_1, n_2, \ldots) = k_j^{(molec)} \cdot \prod_{i=1}^{n} (n_i)^{\alpha_{ij}} = k_j^{(macro)} V \cdot N_{Avogadro} \cdot \prod_{i=1}^{n} \left(\frac{n_i}{V \cdot N_{Avogadro}} \right)^{\alpha_{ij}} \quad (16)$$

The Poisson processes for each possible reaction compete, in the sense that they run concurrently and independently of each other, until one of them fires. At that moment, one instance of the "winning" reaction - let it be $\mathscr{R}_k$ - occurs, changing the state of the system by the vector $\boldsymbol{\gamma}_k = (\gamma_{1k}, \gamma_{2k}, \ldots)$:

$$\mathbf{x} = (n_1, n_2, \ldots) \to \mathbf{x}^* = (n_1^*, n_2^*, \ldots) \equiv (n_1 + \gamma_{1k}, n_2 + \gamma_{2k}, \ldots) \; . \quad (17)$$

All Poisson processes restart, with propensities reflecting the new state vector $\mathbf{x}^* = (n_1^*, n_2^*, \ldots)$.

The above defines a Markov chain, an idealized stochastic, well-mixed model of the chemical reaction network. It has been shown [15] that, in the limit of infinite volume, the expectation of concentrations predicted by this model coincides with the traditional ODE description with mass-action rate laws (4)–(5). While this model is still a mathematical construct, it emulates the random behavior of the number of molecules of a real system and its average behavior matches the ODE model, it therefore represents a more detailed description of reality.

The Gillespie stochastic simulation algorithm [9] (exact SSA, or *first reaction method*), is a first principles simulation of the Markov chain model. The state of the system is given by the vector $\mathbf{x} = (n_1, n_2, \ldots)$. The update step is as follows. The propensities g_j of all possible reactions $\mathscr{R}_j$ are calculated according to (16). For each reaction $\mathscr{R}_j$, a tentative firing time τ_j is generated from a random distribution (11) with PDF $f_j(\tau) = g_j \exp(-g_j\tau)$. The smallest of the set $\{\tau_1, \tau_2, \ldots\}$ defines the *first*

reaction, $\mathcal{R}_k$. The firing time τ_k is added to the simulation time $t \to t^* = t + \tau_k$, and one instance of $\mathcal{R}_k$ is implemented by adding the vector $\boldsymbol{\gamma}_{\cdot k} = (\gamma_{1k}, \gamma_{2k}, \ldots)$ to the state vector: $\mathbf{x} \to \mathbf{x}^* = \mathbf{x} + \boldsymbol{\gamma}_{\cdot k}$.

Many alternative algorithms have been developed to simulate the Markov chain model of CRN more efficiently [3, 7, 10]. Gillespie's original *direct method* [8, 9] is important in that it uses the addition property of Poisson processes to avoid the generation of a full set of reaction times at each update. When the set of propensities is updated to reflect the new state of the system, a total propensity is calculated, $g_T = g_1 + g_2 + \cdots$. The next reaction time is generated from the PDF $f(\tau) = g_T \exp(-g_T \tau)$. The identity of the reaction is chosen by comparing a uniform random number $r \in [0, 1]$ to the cumulative sums of the reaction probabilities, $0 \le s_1 \le \cdots s_n = 1$, where $s_k \equiv \sum_{l=1}^{k} p_l$, $p_l \equiv g_l / g_T$.

The hypotheses behind the Markov chain model can be relaxed to some extent, as long as the system can be satisfactorily described by keeping track of only the number of molecules of each species. In principle, any macroscopic rate law can be implemented by defining an 'effective' rate constant that depends on the concentrations (or particle numbers); for a generic rate law (3), the propensity would be the macroscopic reaction rate (flux) converted to "instances per time per particle":

$$g_j(n_1, n_2, \ldots) = \varphi_j([S_1^*], [S_2^*], \ldots) \cdot V \cdot N_{\text{Avogadro}} \text{ where } [S_i^*] \equiv \frac{n_i}{V \cdot N_{\text{Avogadro}}} \quad (18)$$

3 Diffusion

An important fraction (if not most) of molecular transformations relevant to the biological functions of living cells involve the *interaction* of two or more molecules that can move independently. Such processes require the physical proximity of the participants, and therefore depend on the position and movement of biomolecules.

The preceding discussion took into account the spatial aspect of molecular processes only to the extent required to distinguish densities and concentrations from mass and number of molecules. The dynamical picture ignored the spatial positions of the interacting particles, consistent with an assumption of spatial homogeneity. This is called the *well-mixed* hypothesis. A system where molecules are not distributed homogeneously is not well mixed, and its dynamics is influenced by the location of individual molecules.

Someone approaching this subject with a background in a mature quantitative field may find the complexity of the reaction networks "challenging enough" by itself. The need to take into account the stochastic nature of the processes and the spatial aspect that we are about to discuss add additional layers of complexity. However, the study of spatial organization is necessary if we are to understand the chains of causation that lead from mutations to pathology.

This is especially true for systems involving membrane proteins, whose dimerization and dissociation reactions are important. Signal initiation by a host of membrane bound receptor-ligand families relies on ligand-induced dimerization or the formation of larger cross-linked aggregates [14, 19]. Spatial inhomogeneity, or rather, the emergence of multiple levels of spatial organization, are a constant feature of the cell membrane. This nontrivial landscape modulates the movement of proteins along the membrane [18, 21, 41].

This section focuses on the movement (diffusion) of molecules along the membrane; we will discuss methods for combining diffusion with reactions in the next section.

3.1 Diffusion Basics

Historically, the term Brownian motion referred to a specific type of random motion characteristic of particles in a colloidal suspension. Here we follow the more current usage, to mean the idealized random motion that is consistent with classical (Fickian) diffusion. A particle moving in two dimensions with position vector $\mathbf{r}(t) = (x(t), y(t))$ is said to be *Brownian* if the components $\Delta x, \Delta y$ of the displacement vector $\Delta \mathbf{r} = \mathbf{r}(t + \Delta t) - \mathbf{r}(t)$ over any interval $(t, t + \Delta t)$ are random variables distributed according to the PDF

$$f(\Delta x, \Delta y; \Delta t) = \frac{1}{4\pi D \Delta t} \exp\left(-\frac{\Delta x^2 + \Delta y^2}{4D \Delta t}\right) . \tag{19}$$

The above simply states that the x- and y-displacements are distributed independently, each following a normal distribution with variance $\sigma^2 = 2D \cdot \Delta t$. The parameter D is a measure of the mobility of the particle.

Brownian motion is random; even if we know the exact position of the particle, its position x, y at a later time can be predicted only in terms of a distribution. If we place a single Brownian particle at (x_0, y_0) at time $t = 0$, the *localization probability density* coincides with (19), with $\Delta x = x - x_0$, $\Delta y = y - y_0$, and $\Delta t = t$.

$$p(x, y; t) = \frac{1}{4\pi Dt} \exp\left(-\frac{(x - x_0)^2 + (y - y_0)^2}{4Dt}\right) . \tag{20}$$

Properties of the normal distribution ensure that the function (20) is normalized at all $t > 0$: $\iint p(x, y; t)\, dx\, dy = 1$. Its time evolution is consistent with (19), in that the localization density at any time $t = t_0 + s > t_0$ can be obtained as a convolution of the localization density at time t_0 and the displacement PDF over $\Delta t = s$[9]:

---

[9]Note that (20) approaches a Dirac delta at $t = 0$: $\lim_{t \to 0} p(x, y; t) = \delta(x)\delta(y)$.

$$p(x, y;\ t_0 + s) = \iint p(x', y';\ t_0)\, f(x - x', y - y';\ s)\, \mathrm{d}x'\mathrm{d}y'\ . \qquad (21)$$

This behavior on the level of individual particles is closely related to the 'bulk' physical process of diffusion. Setting the matter of overlaps between particles aside for now,[10] we can describe a set of n Brownian particles by the *sum* of the individual localization probability density functions $p^{(j)}(x, y;\ t)$. This joint localization density function is normalized to the number of particles:

$$\rho(x, y;\ t) \equiv \sum_{j=1}^{n} p^{(j)}(x, y;\ t)\ ;\ \iint \rho(x, y;\ t)\, \mathrm{d}x\mathrm{d}y = n\ . \qquad (22)$$

The integral of $\rho(x, y)$ over any finite area corresponds to the *average number* of particles in that area. The joint density function inherits the convolution property (21). It can be shown that for $t \geq t_0$, the localization probability $p(x, y; t)$ defined by (19)–(21), as well as $\rho(x, y;\ t)$ defined in (22) verify a diffusion equation:

$$\frac{\partial p}{\partial t} = D \left(\frac{\partial^2 p}{\partial x^2} + \frac{\partial^2 p}{\partial y^2} \right)\ . \qquad (23)$$

In other words, the particles of a substance that undergoes standard (Fickian) diffusion with diffusion coefficient D, perform Brownian motion as defined by the PDF (19). The mathematical equivalence between (23) and (19) is crucial in connecting the behavior of individual particles to bulk properties such as diffusion coefficients and (as we shall see in the next section) reaction rates.

We end this discussion with two applications of (19) used in single particle tracking (SPT). SPT trajectories [24] are derived from microscopic images (frames) recorded at equal time intervals τ. Particles are identified based on the spatial pattern of the fluorescent light they emit. The process results in a sequence of positions $\{(x_0, y_0), (x_1, y_1), \dots (x_k, y_k), \dots\}$, corresponding to recording times $t_0 + k\tau$. One way to characterize the observed movement is by comparing the *displacements* $\Delta x_{jk} = x_k - x_j$, $\Delta y_{jk} = y_k - y_j$ over time intervals of length $t_k - t_j = (k - j)\tau$. Statistics of displacements can be obtained from one or more trajectories, over one or more time intervals of a chosen length.[11]

A quantity often analyzed is the *square displacement* over time θ:

$$s^2(\theta) \equiv (\Delta \mathbf{r})^2 = \Delta x^2 + \Delta y^2\ ;\ \Delta \mathbf{r} = \mathbf{r}(t + \theta) - \mathbf{r}(t) \qquad (24)$$

If the particles follow (19) with the same parameter D, the x- and y-displacements are independent with expectation zero and variance $\sigma^2 = 2D\theta$. The *mean square*

---

[10]This is justified at low overall densities, and also when the density of the particle species *that are explicitly modeled* is sufficiently low.

[11]When the same trajectory is sampled for intervals corresponding to multiple frames, the intervals must not overlap in order to avoid oversampling.

displacement (MSD) over time θ is the sum of $\langle \Delta x^2 \rangle$ and $\langle \Delta y^2 \rangle$, and therefore

$$\langle \Delta x^2 \rangle = \langle \Delta y^2 \rangle = 2D\theta \ ; \ \langle s^2(\theta) \rangle = \langle \Delta x^2 \rangle + \langle \Delta y^2 \rangle = 4D\theta \ . \tag{25}$$

The distribution of *square* displacements corresponding to time intervals of length θ can be derived[12] from (19):

$$g(s^2; \theta) = \frac{1}{\langle s^2(\theta) \rangle} \exp\left(-\frac{s^2}{\langle s^2(\theta) \rangle} \right) \ . \tag{26}$$

The above should not be confused with the distribution function for the *absolute value* of the displacement $s = \sqrt{\Delta x^2 + \Delta y^2}$, which is proportional to $s \cdot \exp(-s^2/\langle s^2 \rangle)$.

3.2 Brownian or Not Brownian?

The motion of a particle in two dimensions is in general described by a position vector that varies with time, $\mathbf{r}(t) = (x(t), y(t))$. The motion is random if the future values $\mathbf{r}(t + \Delta t); \Delta t > 0$ are set by a process that has (any) random elements. One may define such random walks by providing the distribution (or PDF) $f(\Delta x, \Delta y; \Delta t)$ of the two components of the displacement vector $\Delta \mathbf{r} = \mathbf{r}(t + \Delta t) - \mathbf{r}(t)$.

In Brownian motion as described in the previous section, displacements over intervals of length Δt are distributed according to (19); the components of the displacement vector $\Delta \mathbf{r}$ along any direction follow a normal distribution with the same standard deviation, which is proportional to the length of time: $\sigma = 2D\Delta t$. Consequently, the mean squared displacement (MSD) over a time interval should increase proportionally with the length of the interval.

Deviations from standard Brownian motion result in *anomalous diffusion* [24, 30]; the term is somewhat misleading in that such deviations are typical, rather than unusual. Brownian motion is an idealized mathematical model; it describes a *limiting behavior* which is approximated by many real systems, but not truly followed by any of them. Such caveats apply to any mathematical model, but in the case of Brownian motion there are two aspects that merit a brief mathematical discussion.

First, by the Central Limit Theorem (CLT), [34] *any isotropic random walk approaches ideal Brownian motion* in the limit of large time (or spatial) scales. Consider a set of N independent and identically distributed random variables $\{X_k\}_{k=1,...,N}$ with mean zero ($\langle X_k \rangle = 0$) and finite variance $\langle X_k^2 \rangle = \sigma^2$. Define a new random variable Y_N as the sum of the X_k's, divided by $\sqrt{N}$. The theorem states that in the limit of $N \to \infty$, the PDF of Y_N converges to a *normal distribution* centered on 0 and with the same variance σ^2 as the individual X_k's.

---

[12]To obtain (26) we need to first change variables from (x, y) to $(r, \alpha) \to \mathrm{d}x\mathrm{d}y = r\mathrm{d}r\mathrm{d}\alpha$; integrate out the angle α, then change variable to $w = r^2 \to \mathrm{d}w = 2r\mathrm{d}r$.

Consider now a random walk where the x-displacements ΔX over some characteristic time τ are distributed randomly with mean zero and standard deviation σ_0 (so that $\langle \Delta X \rangle = 0$; $\langle \Delta X^2 \rangle = \sigma_0^2$). The displacement over a multiple $T = N\tau$ of the characteristic time τ, is the sum of N independent, identically distributed displacements $Z(T) = \Delta X_1 + \cdots \Delta X_N$ (where ΔX_k is the displacement over the k-th interval). The CLT applies to $Y(T) = Z(T)/\sqrt{N}$. In the limit when T becomes much larger than the characteristic time (i.e., $T/\tau = N \to \infty$), the distribution of $Y(T)$ must approach a normal centered on zero, with variance σ_0^2. It follows that, in the same limit, $Z(T) = \sqrt{N} \cdot Y(T)$ approaches a normal distribution centered on zero, with variance $\langle Z(T)^2 \rangle = N\sigma_0^2 = T\sigma_0^2/\tau$. This is identical to the distribution of the x-displacement of a Brownian particle (19) with diffusion coefficient

$$D_{\text{eff}} = \frac{\sigma_0^2}{2\tau} \ . \tag{27}$$

In summary, for a random walk whose displacement along one direction, over a characteristic time τ, has mean zero and standard deviation σ_0, the distribution of displacements over time T approaches a normal with standard deviation $\sigma(T) = \sqrt{2T \cdot D_{\text{eff}}}$ as $T \gg \tau$ where D_{eff} is given by (27). Finally, if the movement is in two dimensions and the displacements along both x and y verify the assumptions (zero mean and standard deviation σ_0 over τ), then, in the limit $T/\tau \to \infty$, the system approaches ideal Brownian motion with diffusion coefficient (27).

The second issue is that perfect Brownian motion is a mathematical idealization that is, in fact, *physically impossible*. There are various physical limitations to how far a membrane-bound particle could possibly travel over a given time, even in the absence of any barriers. Yet, the PDF (19) implies that given *any* finite time Δt, no matter how large a distance B is, there is a nonzero probability that the displacement ΔX over Δt will be larger than B. This would imply that our particle could exceed any such limit (including the speed of light).

Brownian trajectories have counterintuitive features: the function $x(t)$ describing a specific trajectory (in one dimension) has an infinite number of zero-crossings over any finite time interval, and it is continuous but not differentiable. One of the most consequential properties is also quite obvious. Consider a Brownian trajectory that we sample at time intervals of length τ. The standard deviation corresponding to each time step, $\sigma(\tau) = \sqrt{\langle (x(t + \tau) - x(t))^2 \rangle} = \sqrt{2D\tau}$, is proportional to $\tau^{1/2}$. The standard deviation is a measure of the typical displacement over the time step; this implies that the "typical velocity" $\sigma(\tau)/\tau$ varies like $\tau^{-1/2}$, that is, it *increases* and grows indefinitely as the sampling time step is decreased. The closer one looks at a Brownian trajectory, the less smooth it gets.

Potential artifacts of the Brownian motion model can be resolved by falling back to a more realistic model of molecular motion. Randomness in physical motion typically results from a process with a characteristic time; for instance, particles travel along straight lines and change direction because of collisions. The *rate* of direction changes defines the characteristic time; movement on shorter time scales is actually deterministic, and is interspersed with random events.

In summary, we could say that all physical random motion looks Brownian if examined on a long enough time scale; on the other hand examination over a short enough time scale of will reveal that any apparently Brownian motion is in fact, "anomalous". This and similar issues have to be kept in mind when performing Brownian motion simulations.

3.3   Brownian Motion Based Simulations

We now develop the elements of simulations of particle motion on the cell membrane, and then discuss how motion simulators are combined with reaction simulation algorithms.

Simulations that take into account the location of individual particles generally require significantly more organization and memory than nonspatial algorithms.[13] In a nonspatial algorithm (16)–(17) with N_S species, the state of the system is fully determined by N_s integers, $(n_1, n_2, \ldots, n_{N_s})$ that represent the number of molecules of each type. In a spatial algorithm we need to keep track, at a minimum, of the location of each particle of each species: $\left\{(x_j, y_j, s_j)\right\}_{j=1...N_P}$; where $N_P = \sum n_k$ is the total number of particles.

With the availability of computer memory, the bookkeeping aspect is much less of a limitation than it was 10–15 years ago. In the scheme we outlined, one would need 2 floating point numbers and an integer for each particle. For a million particles, this works out to $3 \cdot 10^6 \approx 3$ Mb, which is not at all a logistical challenge. However, the implementation of the updates may make a big difference, and fully spatial simulations continue to be significantly more work and resource intensive.

The simplest spatial simulation applies the definition of Brownian motion to a set of particles. Given N_p coordinate pairs $\{\mathbf{r}_k = (x_k, y_k)\}_{k=1...N_p}$ at time t, the positions at time $t + \Delta t$ are obtained as $\mathbf{r}_k(t + \Delta t) = \mathbf{r}_k(t) + \Delta \mathbf{r}_k$, with the components of $\Delta \mathbf{r}_k = (\Delta x_k, \Delta y_k)$ chosen randomly, according to the Brownian PDF (19). Assume we store the coordinates in an $N_P \times 2$ array. Then, for each update step, we simply need to generate an array of the same size, filled with normally distributed random numbers and add it to the coordinates.

The largest computational cost is in generating the random numbers. Algorithms for the generation of normally distributed random numbers (based on a uniform random number generator) are well known and easy to implement. The Brownian update step is a typical candidate for *vectorization*, the ability to perform operations with arrays without relying on a loop. Array operations as well as functions that provide sets of normally distributed random numbers are readily available in environments such as MATLAB, where the entire update step can be implemented in a single line of code.

---

[13]With the one possible exception of nonspatial, but "rule based" simulations that keep track of individual molecule parts [12].

In the absence of limitations to the allowed values of the positions, the procedure described here can be employed for any time increment Δt, which can be chosen as long or as short as the other elements of the model dictate. A typical implementation would be as a fixed time step algorithm. Most of the effort in setting up this type of simulation goes into dealing with limitations to unimpeded movement, which may stem from the simulation landscape and the size of the diffusing molecules.

Depending on the context of the simulation, physical details of the molecular motion become relevant. A more realistic description of the movement of membrane proteins is a sequence of short, straight line displacements, interrupted by collisions with small molecules. In principle, when there is any doubt about the proper approach to a specific situation, one should go back to this picture as the true, physical reality.

A general feature of microscopic simulation methods is that one does not necessarily aim at reproducing the physical reality over a short time or spatial scale; rather, simulations are validated by approaching the proper Brownian behavior (or macroscopic reaction kinetics) in the limit of large time and spatial scales.

3.4 Anomalous Diffusion/Barriers to Movement

Elements that limit the free diffusion of membrane bound receptors (and other proteins) are a central feature of membrane dynamics and signaling. Far from being homogeneous, the membrane presents a varied landscape of linear boundaries and two-dimensional domains [1, 16, 33, 37, 39].

Virtually any experimental observation of these molecular aggregates has striking features that point to inhomogeneity and limited movement, indicating a pattern of spatial organization. Indeed, a significant fraction of our data analysis and modeling effort is aimed at characterizing these features and understanding their possible role in signaling.

3.4.1 Emulating Open Space with a Limited Simulation Area

Currently, a detailed simulation of the entire cell membrane is not practical. For a single signaling pathway [14], this would involve on the order of 10^6 molecules. The limitation is not so much in terms of memory capacity than in terms of execution time. The high computational cost is a result of the need to update all diffusing particles at each time step, combined with the necessarily short steps required by numerous other considerations.

Suppose we focus on a rectangular patch of dimensions B_x, B_y, which represents a fraction of $B_x B_Y / A_T$ of a membrane of total area A_T. The number of molecules of each species of interest can be set proportionally, using the copy number per cell

or an area-based concentration.[14] If diffusion is unimpeded, the molecules initially in the simulation area would leak out. On a real cell, the molecules that leave would be replaced by others entering the area. To emulate this in a simulation, we usually impose *reflecting* or *periodic* boundary conditions.

The boundary conditions are mathematically equivalent to those for differential equations. In simulations, they are implemented by modifying the position update rules for instances that would result in a boundary crossing. Suppose our simulation area is the rectangle $\mathscr{S} = [0, B_x] \times [0, B_y]$ defined by $0 \leq x \leq B_x, 0 \leq y \leq B_y$. The boundary rule is applied to all particles whose "raw" updated position $\mathbf{r}_k(t + \Delta t) = (x^*, y^*)$, resulting from the procedure discussed in Sect. 3.3 falls outside $\mathscr{S}$.

With *periodic* boundary conditions, the updated coordinate(s) that would fall outside the $[0, B]$ interval are shifted up or down by the interval length. In the case of the x coordinate, we replace $x^* \rightarrow (x^* - B_x)$ if $x^* > B_x$, and $x^* \rightarrow (x^* + B_x)$ if $x^* < 0$, with an analogous prescription for y. This is equivalent to imagining that the plane is tiled with an infinite number of identical copies of $\mathscr{S}$; when a particle leaves one copy of $\mathscr{S}$, it enters the next one, without changing its direction. The corresponding condition for Eq. (23) is: $\rho(0, y) = \rho(B_x, y)$, $\partial_x \rho(0, y) = \partial_x \rho(B_x, y)$.

With *reflecting* boundary conditions, each "overshooting" coordinate is reflected by the boundary position; the additional update rule is $x^* \rightarrow (-x^*)$ if $x^* < 0$ and $x^* \rightarrow (B_x - x^*)$ if $x^* > B_x$. Geometrically, this rule corresponds to a reflection of the displacement vector by the boundary. The differential equation equivalent is the *zero flux* boundary condition: $\partial_x \rho(0, y) = 0$, $\partial_x \rho(B_x, y) = 0$.

The price of not simulating the entire membrane is that both of these procedures come with artifacts, unintended features that have no correspondent in reality. With periodic boundary conditions, the geometry (topology) of the simulation box is that of a *torus*, rather than a sphere. When particle interactions are taken into account, reflecting boundary conditions potentially change the local distribution pattern by inducing a "pile-up" of molecules at the boundary, a phenomenon that does occur in the presence of physical barriers; this approach is used to emulate various obstacles. For this reason, periodic boundary conditions are preferable for the purpose of emulating open space without "leakage" of particles.

3.4.2 Physical Obstacles

Aside from collision with other molecules,[15] physical obstacles encountered by membrane bound molecules typically [17, 23] act as linear, *semipermeable* barriers. These can be modeled by expanding the approach for reflecting boundaries.

Suppose there is a barrier along the line $x = B$, faced by particles diffusing in the xy plane. For a strict boundary that enforces $x \leq B$, a proposed updated value

---

[14]A potentially confusing practice is to characterize the amount of a membrane bound species in terms of a (volume) concentration that reflects the copy number per cell multiplied by the concentration of cells in a suspension.

[15]We will discuss intermolecular collisions in the context of reaction–diffusion models.

for $x(t + \Delta t) = x^*$ such that $x^* > B$ would be replaced by $(B - x^*)$. For a partially permeable barrier we relax the rule and *allow* the boundary-crossing update x^* with a probability p_{cross}, and we replace $x^* \to (B - x^*)$ with probability $(1 - p_{\text{cross}})$.

A linear barrier can be approached from two sides. The barrier rule applies to any particle whose current $x(t) \equiv x_{\text{old}}$ and "raw" updated $x(t + \Delta t) \equiv x^*$ coordinates are on opposite sides of $x = B$, in other words, $(x^* - B) \cdot (x_{\text{old}} - B) < 0$. The crossing probability reflects the way the diffusing particle interacts with the boundary and the surrounding membrane. It may have different values for each species, reflecting molecular mobility; it may have different values for crossing in one or the other direction, reflecting an affinity of a type of molecule for one or the other side of the barrier.

The implementation of these barriers in simulations should be informed by the nature of the obstacle, and, ideally, by some insight into the molecular mechanism that interferes with the diffusing particles. One type of linear obstacle is represented by large, linear protein structures—actin filaments or elements of the cytoskeleton. Diffusing membrane proteins are generally blocked from crossing these structures. Crossings are possible through small, transient gaps that open and close due to the relative movement of the membrane and the barrier [17, 20].

Another source of linear obstacles may be the boundaries between different phases of the mix of lipids that form the membrane. In addition to an overall barrier potential, electrostatic interaction between the tails of the lipids and the transmembrane domains of diffusing proteins may result in a net force or potential difference that favors the movement of the protein in one direction over the other [6, 28, 31].

4 Reaction–Diffusion Systems

The main goal of this contribution is to discuss stochastic modeling of reaction–diffusion systems. This level of detail is necessary in the modeling of biomolecular processes in living cells, when the number of molecules involved does not justify a continuum (ODE or PDE) description, and when the hypothesis of spatial homogeneity does not hold. Modeling and simulation of reaction–diffusion systems are required to connect experimental results from the study of membrane dynamics on the molecular scale to cell-level behavior. The remaining task is to combine the simulation methods we discussed previously for well-mixed reaction systems with those for diffusion.

The core aspect of molecular reaction–diffusion simulations is the coupling between the location of the molecules and the triggering of individual reaction events. To avoid ambiguity, we will assume that the *chemical equations reflect the actual participants* in the molecular event corresponding to an instance of a reaction. For instance, an enzymatic reaction where an enzyme E converts S into P is sometimes described as $\mathsf{S} \xrightarrow{\mathsf{E}} \mathsf{P}$, while the correct equation should be $\mathsf{S} + \mathsf{E} \to \mathsf{P} + \mathsf{E}$,

irrespective of the reaction mechanism or the rate law.[16] Consistent with a level of detail that accounts for the location of individual molecules, we disallow reaction events that involve "magical" action at a distance; if the conversion of S into P is facilitated by a third species E, then each reaction event must require the close proximity of both participants, one copy of S and one copy of E.

Possible exceptions would emerge in a hybrid modeling framework, when only certain species of interest (larger, more scarce molecules) are modeled in spatial detail. For the purposes of this discussion, we assume that all species are accounted for and that a reaction event requires the physical proximity of no less and no more than the set of molecules implied by the incoming side of the chemical equation.
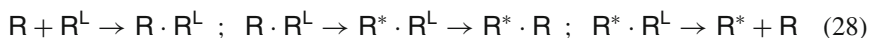
4.1 First-Order Reactions and Diffusion

If all the reactions in the system are first order (such as $A \rightarrow B$ or $A \rightarrow B + C$), then individual instances of reactions are triggered independently of the position of the molecules. In a sense, the dynamics of reactions and of diffusion take place in parallel, without influencing each other. This is a good opportunity to develop a unified framework that simulates the two phenomena without having to deal with some of the more complex issues.

The *state of the system* is defined by the position and chemical species of all particles. The spatial aspect requires that we track the position of each particle. The fact that particles have an identity requires a major change in the way chemical dynamics is accounted for. All the methods we discussed previously tracked only the copy number of particles of each species. In the course of these well-mixed simulations one would estimate the time when an instance of a reaction type would occur, and then implement it by changing the particle numbers accordingly.

With identifiable particles we need to deal with two additional tasks: choosing the actual particles involved in each reaction event, and managing the relation between particle identities and chemical species. The choice of the reacting particle is straightforward. For first-order reactions, once the reaction type is set, it comes down to choosing one of otherwise identical possibilities.

The concept of *particle identity* helps limit the size and changes to the lists of particles we maintain. It is most useful when a relatively small set of *moieties* can combine in different ways. Consider a system with a single receptor type R, which may be liganded (R^L) and/or phosphorylated (R^*), and may form dimers ($R \cdot R$). The following sequence of reaction events:

$$R + R^L \rightarrow R \cdot R^L \;\; ; \;\; R \cdot R^L \rightarrow R^* \cdot R^L \rightarrow R^* \cdot R \;\; ; \;\; R^* \cdot R^L \rightarrow R^* + R \quad (28)$$

---

[16]For a proper rendering of the Michaelis–Menten mechanism, one should include an intermediate, reversible step.

allows straightforward identification of the specific receptors that participate.[17] The identity-species relationship is not always this simple, with species transforming in ways that do not allow consistent identification of individual molecules (moieties) beyond one reaction step.

4.1.1 One-to-One Reactions: Chemical Species as an Attribute

If reactions are strictly one to one ($A \rightarrow B$, $A \rightarrow C$, $C \rightarrow A$, ...), particles change their type but in a sense keep their identity, so the total number of particles never changes. In this case we may treat the chemical species as a discrete valued variable assigned to each particle. The state of the system at time t is then characterized by an array of size $N \times 3$, $\{(x_k, y_k, s_k)\}_{k=1...N}$ where $(x_k, y_k) = \mathbf{r}_k(t)$ define the position and $s_k(t)$ is the chemical species of particle k at time t.

First-order chemical reactions are triggered within each particle, by Poisson processes that are independent of the position or of the presence of others. If the system follows mass-action, reaction $A \rightarrow B$ is characterized by an intrinsic rate constant $k_{A \rightarrow B}$, and the joint propensity for all instances of the reaction is $g_{A \rightarrow B} = k_{A \rightarrow B} n_A(t)$, independently of the spatial configuration. If such considerations apply to all the reactions in the system, we may simulate the reaction dynamics following the direct method [9]. We calculate a total propensity g_T as the sum of all reaction propensities at a given time t. The time to the next reaction (of any type) is obtained by generating a random value τ_{react} using the PDF $f(\tau) = g_T \exp(-g_T \tau)$. The probability that the next reaction is $A \rightarrow B$, is given by $g_{A \rightarrow B}/g_T$; the type of the next reaction can be chosen using a second random number.

To fully determine the next chemical transformation, we need to identify the actual molecule that undergoes the predicted transformation. The total propensity $g_{A \rightarrow B} = n_A k_{A \rightarrow B}$ corresponds to the joint Poisson process that triggers the next one of the n_A possible instances of the reaction $A \rightarrow B$. Each A particle has the same intrinsic propensity $k_{A \rightarrow B}$, and is equally likely to be the one reacting. The choice can be made similarly to that of the reaction type, by comparing a uniform random number $r \in [0, 1]$ with the partition of the interval $[0, 1]$ induced by the set $\left\{ \frac{1}{n_A}, \frac{2}{n_A}, \dots, \frac{n_A-1}{n_A} \right\}$. The probability that r falls into the subinterval $\left[\frac{j-1}{n_A}, \frac{j}{n_A} \right]$ is the same for all integers j from 1 to n_A, and the resulting j^* is a proper way to identify the transitioning particle.

Once we obtained the value for τ_{react}, selected the type of the next reaction ($A \rightarrow B$), and the identity of the particle involved (the j^*-th particle of type A), the reaction event is to be implemented by simply changing the species value s_{k^*} from A to B at the time of the reaction, $t + \tau_{\text{react}}$.

Having established that there would be no chemical transformations between t and $t + \tau_{\text{react}}$, we may evolve the spatial dynamics over this interval without concern for

---

[17]All four reaction instances can be encoded as changes to the states of two receptor molecules: *Receptor 1* forms a dimer with *Receptor 2* which is initially liganded; then *Receptor 1* is phosphorylated; after that, *Receptor 2* loses its ligand; finally, the dimer breaks up.

chemical transformations. If particle–particle collisions are not an issue, Brownian motion can be estimated over any time interval Δt by obtaining a single set of displacement values from the Brownian PDF (19). We can either perform a Brownian motion update using the time to the next reaction, or, if we have a fixed time step τ_{step}, perform the diffusion update up to whichever time comes first, $t_{next} = \min(t + \tau_{step}, t + \tau_{react})$. If $\tau_{step} < \tau_{react}$, we can perform successive Brownian updates until the time of the reaction.

4.1.2 First-Order Reactions with Particle Number Change: Bookkeeping Versus Rules

If all reactions are first order, each instance takes place independently of all the molecules in the system, other than the one undergoing the molecular transformation. Thus, the choice of the upcoming reaction type and of the reacting molecule, as well as the diffusion update between reaction events, can be performed as described above, whether or not the reactions are one to one ($A \rightarrow B$) or not ($A \rightarrow A^* + B$, $A \rightarrow \emptyset, \ldots$). The difference is in how the reaction event is implemented and the machinery required to keep track of the chemical composition of the system.

When reactions change the number of molecules, we have to deal with the creation and disappearance of particles. A particle is represented by at least two real numbers (the spatial coordinates); depending on the algorithm, it can become a fairly complex entity—similar to a record in a table or list.

One strategy is to maintain separate lists of particles of each type (species). In this approach, each reaction event involves at a minimum, moving a record between lists ($A \rightarrow B$), but may also require the deletion ($A \rightarrow \emptyset$) or creation of new ones ($A \rightarrow B + C$). Care is required to properly handle memory issues stemming from the continuously changing size of the respective arrays. High-level programming environments such as MATLAB allow dynamic resizing of arrays; if no other precautions are taken, this can result in dramatic loss of execution speed. A safer strategy is to preallocate arrays with the expected largest number of particles of each species and manage the lists in a way that the blank records are always at the end.

Given that particles must be created and deleted, the idea of keeping a single list with the chemical species as an attribute is not easily applicable. Somewhat similar ideas are used in the rule-based approach to biochemical reaction network modeling [12], where the entities of interest are parts of molecules that connect to each other following a set of rules. For the reader who is not at all acquainted with the idea, the best analogy is Lego blocks with several types of connectors. This approach is useful in dealing with the complexity of biomolecules, dramatically reducing the number of chemical species. Implementation requires keeping track of each building block copy and of its connections to others. The resulting structures can easily be expanded to include position information [25].

4.2   Second-Order Reactions

Things get more complicated with binary reactions, such as $A + B \rightarrow \cdots$. For this to happen, the interacting A and B molecules have to be in close proximity, or collide. The way we represent the position of our particles, using a two-component position vector $\mathbf{r}_k = (x_k, y_k)$, only specifies a geometric point, with no size or shape. When thinking about molecular collisions, we have to account for these, as well.

Molecular dynamics [29] studies the geometry of biomolecules and can in principle provide detailed information about the size and shape of receptors and other membrane proteins. For now (2015), this is yet another example of a level of detail that may provide useful information, but cannot be *directly* integrated into a simulation of tens of thousands of molecules. Here we will assume that, given two molecules of a given types with position vectors $\mathbf{r}_A$, $\mathbf{r}_B$, we can tell that they are in collision (either overlapping or close enough to interact) based only on their distance:

$$|\mathbf{r}_A - \mathbf{r}_B| \leq d_{AB}^{\text{coll}} \tag{29}$$

We will use conditions similar to (29) to determine if a pair of molecules are eligible to interact, or if their positions are physically overlapping and thus inconsistent with free Brownian motion.

In the preceding section, the time horizon of the motion simulator was only limited by the time τ_{react} to the next reaction event; this time was obtained from an exponential PDF $f(\tau) = g_T \exp(-g_T \tau)$ using the joint reaction propensity $g_T = \sum_j g_j$. In particular, in a Brownian motion simulation algorithm, we could use (19) with $\Delta t = \tau_{\text{react}}$ to obtain the next set of particle positions. Collisions (that may or may not lead to a reaction event) complicate the simulation of molecular motion.

4.2.1   Elastic Collisions

If the molecules of interest take up a significant fraction of the space available, their movement will be limited by the presence of other molecules. A tentative configuration where two or more molecules overlap (their distance is less than the sum of their physical radii) corresponds to a *collision*.

We call a collision *elastic* if it does not lead to a chemical transformation. A motion simulator that takes into account molecular sizes must resolve all colliding configurations, replacing them with a physically possible version. Elastic collisions are generally more common than reactive ones; they may be ignored at low particle densities, but may require a significant computational effort at high particle densities, due to the combinatorial explosion of the number of possible overlaps.

One approach to resolving prospective overlapping configurations is similar to the way we dealt with reflective boundaries: construct a corrected updated position that is not overlapping (similarly to reflection off the boundary), or simply leave one or both colliding particles in their original position.

As the density of particles increases, random position updates are *increasingly likely to result in overlaps*. The computational effort in rejecting these updates reflects the physical reality of crowding, where the movement of individual particles is limited, and in extreme cases made practically impossible by surrounding particles. Crowding and traffic jams are believed to be a significant factor in membrane dynamics [16].

A further complication at high densities is the possibility of multiple concurrent interactions. Let us say for example that in the proposed update, particle 1 overlaps with particle 2. Changing the position of particle 2 will make it overlap with particle 3. Whether we now reject the second prospective position of particle 2, or keep that and generate a new position for particle 3, is a matter of choice of strategy/algorithm. Here, we only wanted to emphasize that as the density of particles increases, the number of collisions that may occur grows in a combinatorial fashion.

This aspect is exacerbated by large time steps, which result in increased travel distance $|\Delta \mathbf{r}|$ per update; the number of possible collision partners is set by the volume of a sphere of radius $\Delta \mathbf{r} + \rho_1 + \rho_2$, where ρ_1, ρ_2 are the physical radii of the particles. Conversely, reducing the simulation time step results in fewer concurrent collisions and reduces the chances of complex interactions.

Another issue that arises with large time steps is that of *missed collisions*, situations where the previous and the updated positions of two molecules do not overlap, but a collision is likely to have occurred between the two time points. At low densities one may take the position that intermediate collisions are accounted for by the Brownian PDF, which reflects a complex trajectory that results from multiple collisions. However, at high densities, particles may end up tunneling through each other, in the sense that a Brownian update may put a particle past another one blocking its way.

Neither of the issues listed here is intractable, but hopefully the reader can appreciate that properly accounting for elastic intermolecular collisions at high density can be an exceedingly complex task, both in terms of algorithm development, and computation time. The right approach is very much determined by the purpose of the simulation and the physical situation of interest. Possible strategies include: (i) reducing the simulation time step to keep the number of collisions per update manageable; (ii) use physical insight into the details of molecular movement to replace Brownian motion with realistic trajectories that can be used to predict collisions; (iii) ignore elastic collisions altogether and adjust the parameters of the simulated Brownian motion based on effective diffusion parameters.

In the discussion that follows, we will assume that a kinetic simulation module takes care of elastic collisions (close encounters of particles that cannot enter into a chemical reaction), in a way that does not directly limit the choice of the time step employed in the rest of the calculation. One possibility is (iii) above that elastic collisions can be ignored; another one ((ii) above) is that we have a readily available motion simulator that generates updated, nonoverlapping positions over an arbitrary time horizon.

4.2.2   Reactive Collisions

We will focus on simulating binary reactions triggered by the physical proximity of the two participants. In particular, assume that our system has a reversible dimerization/dissociation reaction

$$A + B \rightarrow C \;\; ; \;\; C \rightarrow A + B \tag{30}$$
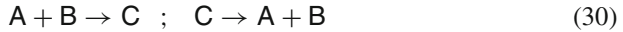
We briefly addressed dissociation reactions when they occurred isolated from dimerization. Here we are interested in the interplay of the two reaction types. In the well-mixed picture, the total propensity $G_{A+B\rightarrow C}$ of the forward reaction (30) is proportional to the number of eligible A, B pairs of molecules, and an elementary propensity $g_{A+B\rightarrow C}$ that relates to the mass-action rate constant $k_{A+B\rightarrow C}$, the volume,[18] and Avogadro's number.

$$G_{A+B\rightarrow C} \;=\; n_A \cdot n_B \cdot g_{A+B\rightarrow C} \;\; ; \;\; g_{A+B\rightarrow C} = \frac{k_{A+B\rightarrow C}}{V_0 \cdot N_{\text{Avogadro}}} \tag{31}$$

When designing a simulation, often the mass-action rate constant is all that is known about the kinetics of a given reaction. If no further physical information is available, the only requirement for the implementation of this particular reaction is the principle that in the limit of large volumes, the simulation must reproduce the rate predicted by (31).

Recall that the elementary propensity of a first-order reaction is a rate (probability per time) that reflects the internal dynamics of one molecule. It can be readily used in *simulations* as the rate of a Poisson process; this rate can be directly measured in *experiments*, because it coincides with the macroscopic rate constant. For second-order reactions, the relation between propensities, the simulation of individual events, and experimentally accessible quantities is more complicated.

A reaction such as $A + B \rightarrow C$ is typically one of several possible outcomes[19] of a molecular collision event. The identity and location of the resulting particles is the stochastic outcome of a quantum mechanical process, which is susceptible to the incoming spatial configuration (impact parameter, relative orientation). The elementary propensity $g_{A+B\rightarrow C}$ is the (average) probability rate for the occurrence of one a specific $A + B$ collision in the system under consideration, and that the collision will result in the creation of a dimer $A + B \rightarrow C$. The value of $g_{A+B\rightarrow C}$ in a given system is the average over all possible A, B pairs, and all their future trajectories over the simulation time step Δt. The formula (31) relates $g_{A+B\rightarrow C}$ to an

---

[18]In the case of membrane-bound species, the volume is replaced by area, and the conversion between the per-pair propensity and the physical (effective) rate constant has to account for the units used for concentration. As we pointed out, sometimes molar concentrations are used for receptors, representing a molar concentration based on a density in suspension of a specific type of cell, and the average number of receptors per cell.

[19]If nothing else, the collision may be elastic.

experimentally accessible number. But how do we implement binary reaction events in a spatial simulation?

First Principles

In principle, quantum mechanical calculations [25] can provide the distribution (PDF) for the future state of each pair of molecules; from here, we could derive the PDF for the time and location where each specific pair reacts, and use a joint distribution to generate the time of the next reaction event of type $A + B \rightarrow C$.

With a prescription that identifies the next reaction event, we may proceed the same way as described for first-order reactions—identify the next reaction event using an approach along the lines of the next reaction method. This would be very efficient, since we could evolve our simulation clock from one reaction event to the next, implement the reaction event, and simply generate new Brownian motion positions for all the other particles.

For this we would have to analyze all $n_A \cdot n_B$ pairs of molecules and predict (generate) the time of their next inelastic collision. We must do this in a way that we can be confident that other molecules have not precluded the pair under consideration from interacting. Even if the two-body analysis could be performed, the three, four-body problems get complicated quickly, but can be tackled with appropriate computational resources. One approach in this direction is the GFRD algorithm [38].

Using an Effective Reaction Distance

The number of A, B pairs that may possibly react over the next time step is drastically reduced if we impose a maximal reaction distance (29), and neglect the possibility of reaction if the distance between molecules exceeds this maximum. This choice neglects a small probability of reaction for pairs that are further apart.

For pairs within the reaction distance, one could perform a detailed analysis as outlined above; in most cases, this first principles approach is still impractical, due to the large number of different reactions, the complexity of the necessary calculations, and the lack of detailed knowledge of reaction mechanisms and molecular structures.

A practical alternative is to assign an average reaction probability $p_{A+B \rightarrow C}^{(\text{reaction})}$, conditioned on the two molecules being within the reaction distance. In a given system, the total reaction propensity is then the product of the collision rate (probability per time that an A, B pair comes within reaction distance) and the conditional reaction probability:

$$G_{A+B \rightarrow C} = G_{A+B}^{(\text{coll})} \cdot p_{A+B \rightarrow C}^{(\text{reaction})} \tag{32}$$

A comparison of (31) and (32) highlights the difficulty in relating spatial simulations of binary reactions to mass-action rate constants. The well-mixed rate constant is an average rate that applies to all $A + B$ pairs; it reflects not only the ability of the two molecules to react once they are close, it also depends on the characteristics of molecular movement: the diffusion rate, as well as any features of the space, which in our case is the membrane with its varied landscape.

As opposed to this, in (32) mobility is accounted for by the collision rate $G_{A+B}^{(coll)}$, and the conditional reaction probability is an intrinsic parameter. In a simulation (once the reaction distance is specified) the spatial movement algorithm (such as the BM simulator) automatically provides $G_{A+B}^{(coll)}$. The actual reaction rate is therefore set separately from the motion simulator, by specifying the collision radius and the conditional reaction probability. This approach is especially useful when building a simulation required to match observed diffusion rates and reaction rates. The reaction distance and conditional probability are not unique; decreases in one can be compensated, to some extent, increasing the other.

4.2.3   Implementation Aspects

We will describe our algorithm in detail in the next subsection. The general idea is that second-order reactions are triggered by the proximity of the participating molecules. Within the type of simulation we have outlined in the preceding sections second-order reactions can be implemented together with the spatial position updates.

At each update, after the tentative new positions are generated and any first-order reactions have been implemented, we identify the A, B pairs that verify the reaction condition $d(A, B) \leq R_{A+B\rightarrow C}$. Not all of these reactions can be carried out, because some of them might be mutually exclusive. For instance, the same A molecule may be within reaction distance of two different B molecules. Such situations are similar to the multiple collisions discussed in Sect. 4.2.1. Their likelihood increases with particle density and the reaction radius. Reducing the time step can reduce but not avoid the occurrence of contradictory reactions.

Ultimately, one has to eliminate some of the proposed reactions and identify a noncontradictory subset. Each pair in this set is then allowed to react with probability $p_{A+B\rightarrow C}^{(reaction)}$. The choice of the reactions to be implemented must be performed in a way that is not biased with respect to the specific molecules that are involved. Because the elimination of some reacting pairs, the reaction radius and/or the probability must be adjusted to match the required overall reaction rates.

Finally, when dissociation reactions are also present, the placement of the reaction products needs to be done in a way the does not result in new collisions (reactive or elastic).

4.3   Smoluchowski Model—Binding Radius Approach to Bimolecular Reactions

Bimolecular reactions are the product of two reactive molecules colliding. In our current simulation, we use an approach similar to that of *Smoldyn* [2].
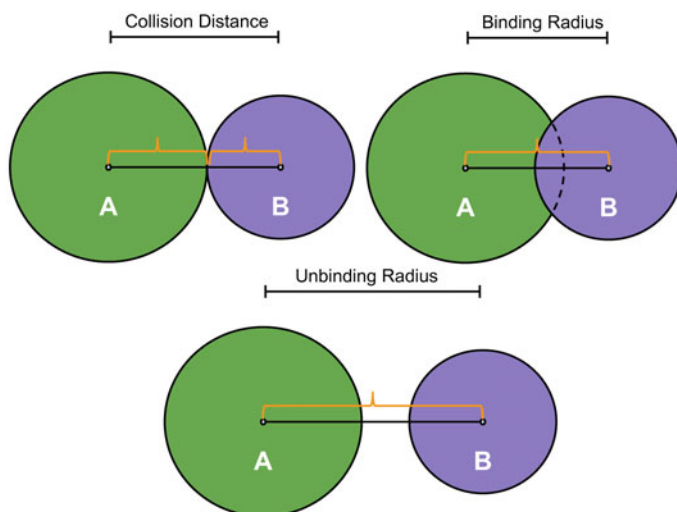
Fig. 2 Collision distance, binding radius, unbinding radius. The binding radius is the distance (between points representing a pair of particles) below which a reaction event is triggered

4.3.1   Irreversible Bimolecular Reactions

Marian V. Smoluchowski sought to develop a model for diffusion-influenced systems, including irreversible bimolecular reactions, using diffusion coefficients and molecular radii [35]. The model describes interacting particles within a solution as point particles that do not interact except for instances of irreversible chemical reactions that are instantaneous, and triggered by proximity. Assuming Brownian motion for diffusing particles, the issue with bimolecular reactions ($A + B \rightarrow \cdots$) is quantifying the moment when the two species involved in the reaction will actually react with one another to form the product/complex. Smoluchowski tackled this issue by using the molecular radii to determine when two particles would collide, and therefore react. This collision distance was the sum of the molecular radii of the two particles, and provided an analytical calculation of the corresponding (macroscopic) binding rate.

However, using the sum of the molecular radii as the reaction threshold is equivalent to a purely diffusion-limited model, which does not take into consideration the activation energy of the reaction. This results in an overestimation of reaction occurrences. One way to correct this [2] is to replace the molecular radii with a *binding radius*, a length shorter than the collision distance, to account for the slower rate of reaction.[20] At the highest level overview, the binding radius is the distance required in simulation to achieve the same rate of reaction observed in wet lab experiments.

---

[20]Alternatives include using a reaction probability that controls whether a reaction occurs upon collision, as well as manipulating the unbinding radius discussed in the next paragraph.

To achieve this rate in the context of a specific computation, the binding radius must take into account not only the bimolecular reaction rate, but also both molecules' diffusion coefficients, as well as the simulation time step (Fig. 2).

The term "binding radius" is somewhat counterintuitive. In our simulation approach, following the Smoluchowski model and [2], particles are represented by points that diffuse freely, irrespective of the presence of other particles. The binding radius is the maximum distance between two points indicating the two corresponding particles will react with one another. The important distinction here is between an idealized geometric point and a particle/molecule. A point can be interpreted as the center of a molecule and as having no volume, while a particle/molecule has a certain physical size (that can be represented by an average radius) and corresponding volume. It follows that the binding radius can be, and typically is, smaller than the actual collision radius between two molecules. See [2] for a more in-depth discussion of the binding radius.

4.3.2   Reversible Bimolecular Reactions

The reverse of a bimolecular reaction, $A + B \rightarrow C$, is a first-order reaction, $C \rightarrow A + B$, that results in the consumption of one molecule and generation of two molecules. The first-order reaction is modeled as discussed above, however, the placement of the product molecules requires additional considerations. In the approach of [2], the Smoluchowski model was expanded to include reversible bimolecular reactions by including an unbinding radius term. The unbinding radius is the initial distance between two product molecules when they are generated in a reaction. This distance is an important factor in controlling geminate recombination of product molecules.

Geminate recombination is the re-reaction of two product molecules to reform the original reactant molecule. An example reaction would be: $C \rightarrow A + B \rightarrow C$. This is a real phenomenon whose occurrence may be artificially increased in a simulation. To address the issue, Andrews and Bray [2] use a probability of geminate recombination to calculate the unbinding radius: $P_{GR} = R_{binding}/R_{unbinding}$. The default probability used in [2] is 0.2, meaning there is a 20% chance of rebinding/re-reaction upon the formation of the initial product molecules.

The use of an unbinding radius to limit recombination is one of several possible choices.[21] It introduces an additional unphysical feature in that it violates the principle of detailed balance; when dimerization and dissociation are at equilibrium, the spatial distribution of A and B particles entering the bound state (C) is different from that of the same particles exiting the bound state. However, this is one of several artifacts of the model that emerge at short length scales, and has the advantage of reducing the computational burden due to repeated rebinding.

---

[21] An alternative would be to use a larger binding radius and trigger reactions with probability <1.

4.3.3   Implementation Details

Our simulation area corresponds to a membrane patch of approximately 400×400 nm, typically featuring a landscape of attractive domains derived from microscopy data. The current version of our simulation code uses a fixed time step, Δt. To resolve spatial and reaction conflicts, the logic is equivalent to updating particles one at a time, in random order. A one-particle update corresponds to a small time step of $\delta t = \Delta t / N$, where N is the number of individual particles in the initial simulation space.

   The one-particle update proceeds as follows. After choosing the particle, a new position of the particle is chosen following the Brownian motion PDF (19) for displacements over the full time step Δt. Depending on the purpose of the calculation, the diffusion coefficient is set by species, based either on a macroscopic value, or directly, based on SPT data. The proposed position update is adjusted (accepted or rejected and re-sampled) to satisfy boundary conditions, both for the simulation area (periodic) and the attractive domains (semipermeable). Due to the relatively low particle density, we do not currently check for elastic collisions, but the algorithm allows it.

   Once the new position is set, depending on the particle species, we check for potential reaction partners, molecules that may participate in a binary reaction with the current particle, and whose distance to it is less than the corresponding reaction radius. If more than one such particle is found, one of them is chosen randomly. Once a single partner has been chosen, the corresponding reaction is carried out.[22]

   If the particle does not participate in a binary reaction, depending on the species, (assume it is an A), a first-order reaction is implemented with probability

$$1 - e^{-\Delta t\, g_{A \to \cdots}} \;\approx\; \Delta t \cdot g_{A \to \cdots} \tag{33}$$

where $g_{A \to \cdots}$ is the joint propensity for all first-order reactions involving the species A. If a reaction occurs, the specific reaction type ($A \to C$, $A \to B + D$, ...) is selected using the corresponding relative probabilities $g_{A \to C}/g_{A \to \cdots}$, $g_{A \to B+D}/g_{A \to \cdots}$, $\cdots$. For dissociation reactions (other than one-to-one), the position of the reaction product(s) is set randomly in a circle of the corresponding unbinding radius.

5   Conclusion

In this chapter we discussed methods for spatial stochastic simulation of reaction–diffusion systems. This framework is necessary to accommodate features of molecular processes involving membrane-bound receptors, ligands, and other species involved in signal initiation. While some of the methods presented here are widely

---

[22]In our current EGF related work [17], all membrane bound species are either monomer or dimer receptors; which may only participate in dimerization or dissociation reactions, respectively.

used in the field of biomolecular modeling, the particular combination of spatial scales and experimental features is not commonly addressed by general purpose software or in methods papers.

A careful reader will find many instances where the spatial simulation as described in the preceding section is "unphysical"—from infinitely detailed Brownian motion to a schematic representation of binary reactions. We should point out that the goal is to account for the movement of molecules in a way that is consistent with experimentally available information, *from macroscopic down to just above the molecular scale*. Similarly to the relation between well-mixed stochastic and ODE models, these spatial simulation methods allow the inclusion of more detail than nonspatial models can, but they are still just an approximation of reality.

In analyzing nano-microscopy data on membrane dynamics, major challenges arise from the fact that the existing information on reaction kinetics is based either on cell-level measurements or is derived from *in vitro* conditions. A similar situation exists regarding the mobility of membrane proteins. Ongoing single particle tracking and other high spatial resolution methods provide direct observation of molecular motion and transformations.

One important function of our modeling effort is to reconcile the observed behavior with established, macroscopically derived kinetics. Other special aspects emerge from the role of the membrane landscape. Modeling is needed both for identifying landscape features, and for predicting their effect on signaling. This aspect will likely require further refinement of spatial models. The current modeling paradigm [2] is to calibrate microscopic parameters by matching known macroscopic (cell-level) kinetics. This may need to be revisited as direct information on *microscopic* molecular behavior becomes the main point of validation.

Summary of the Chapter

In the first section, we introduced the notation and basic elements of the traditional approach to the dynamics chemical reaction systems. This approach is well mixed and continuous, in that the amount of each substance is represented by a single quantity that can take any nonnegative value. The state vector of the system evolves according to a set of chemical rate laws that amount to a dynamical system obeying a set of ordinary differential equations (ODE). Even though this approach serves as a baseline, the dynamical systems emerging from ODE models of chemical reaction networks (CRN) are complex dynamical systems that are studied in their own right [32] and in the context of control theory [36]. In particular, a lot of the literature on signaling network dynamics [14, 22] provide such ODE models.

The second section is devoted to the stochastic description of well-mixed CRN systems. A stochastic model is necessary when the copy number of molecules of one or more chemical species becomes too small to be described as a continuum. At this level, the fundamentally probabilistic nature of molecular processes becomes important. This approach can be seen as a refinement of well-mixed ODEs, or conversely, well-mixed ODEs can be seen as a simplified approximation of the more general stochastic description. The random movement of molecules is discussed in the third section. Here we introduce Brownian motion and briefly discuss its role as a

limiting behavior of any random walk. We describe algorithms that directly simulate Brownian motion in two dimensions, in the presence of physical obstacles; we focus on Brownian motion based simulators and do not discuss lattice-based models.

Section 4 brings together the stochastic treatment of chemical processes with random spatial movement. We explain how the two can be combined in a single simulation algorithm and describe the main approach we currently use for such simulations. One salient point here is the notion of the binding/unbinding radius, which is a simulation model parameter used to tune the on- and off-rates of dimerization/diffusion reactions.

Emerging Roles of Modeling

Dynamical models can predict the behavior of a system based on the characteristics of its components, far exceeding the ability of verbal reasoning in doing so.

In the context of ongoing research in membrane biology, dynamical modeling in our group has two fairly distinct roles, integration and data interpretation. The first refers to the traditional function of bringing together detailed information on the components of a system to predict emerging behavior. [13, 27] Ongoing work focuses on the impact of the membrane landscape and of emerging biochemistry and molecular dynamics on ErbB2/ErbB3 signaling.

The second aspect emerged in response to increasing amounts of nano-microscopy data that provide completely novel insights but raise previously unexpected challenges. This modality is the primary source of information on the membrane landscape, as well as on the movement and molecular dynamics of membrane proteins within this landscape. We are developing methods aimed at identifying landscape features and to characterize the motion of receptors. The output of this approach consists of diffusion coefficients, identification of the binding state of the molecules (moieties) under observations, as well as the location and characteristics of membrane features that modulate molecular movement.

References

1. Andrews, N.L., Lidke, K.A., Pfeiffer, J.R., Burns, A.R., Wilson, B.S., Oliver, J.M., Lidke, D.S.: Actin restricts FcεRI diffusion and facilitates antigen-induced receptors immobilization. Nature Cell Biol. **10**(8), 955–963 (2008). doi:10.1038/ncb1755
2. Andrews, S.S., Bray, D.: Stochastic simulation of chemical reactions with spatial resolution and single molecule detail. Physical Biology **1**, 137–151 (2004)
3. Cao, Y., Li, H., Petzold, L.: Efficient formulation of the stochastic simulation algorithm for chemically reacting systems. J Chem Phys **121**(9), 4059–4067 (2004)
4. Chen, K.C., Csikasz-Nagy, A., Gyorffy, B., Val, J., Novák, B., Tyson, J.J.: Kinetic analysis of a molecular model of the budding yeast cell cycle. Molecular Biology of the Cell **11**(1), 369–391 (2000)

5. Craciun, G., Tang, Y., Feinberg, M.: Understanding bistability in complex enzyme-driven reaction networks. Proc. Nat. Acad. Sci. USA **103**, 8697–8702 (2006)

6. Edidin, M.: Lipid microdomains in cell surface membranes. Current opinion in structural biology **7**(4), 528–532 (2001)

7. Gibson, M.A., Bruck, J.: Efficient exact stochastic simulation of chemical systems with many species and many channels. J Phys. Chem. **A 104**, 1876–1889 (2000)

8. Gillespie, D.T.: A general method for numerically simulating the stochastic time evolution of coupled chemical reactions. J Comput Phys **22**, 403–434 (1976)

9. Gillespie, D.T.: Exact stochastic simulation of coupled chemical reactions. J Phys Chem **81**, 2340–2361 (1977)

10. Gillespie, D.T.: Approximate accelerated stochastic simulation of chemically reacting systems. J Chem Phys **115**(4), 1716–1733 (2001)

11. Gunawardena, J.: A linear framework for time-scale separation in nonlinear biochemical systems. PLoS One **7**(5), e36,321 (2012). doi:10.1371/journal.pone.0036321

12. Hlavacek, W.S., Faeder, J.R., Blinov, M.L., Posner, R.G., Hucka, M., Fontana, W.: Rules for modeling signal-transduction systems. Science Signaling **2006**(344), re6 (2006). doi:10.1126/stke.3442006re6

13. Kerketta, R, Halász, Á.M., Steinkamp, M.P., Wilson, B.S., Edwards, J.S.: Effect of Spatial Inhomogeneties on the Membrane Surface on Receptor Dimerization and Signal Initiation. Frontiers in Cell and Developmental Biology 4:81 (2016)

14. Kholodenko, B.N., Demin, O.V., Moehren, G., Hoek, J.B.: Quantification of short term signaling by the epidermal growth factor receptor. The Journal of Biological Chemistry **274**(42), 30169–30181 (1999)

15. Kurtz, T.G.: The relationship between stochastic and deterministic models for chemical reactions. J Chem Phys **57**(7), 2976–2978 (1972)

16. Kusumi, A., Nakada, K., Ritchie, K., Murase, K., Suzuki, K., Murakoshi, H., Kasai, R.S., Kondo, J., Fujiwara, T.: Paradigm shift of the plasma membrane concept from the two dimensional continuum fluid to the partitioned fluid: high-speed single-molecule tracking of membrane molecules. Annu. Rev. Biophys. Biomol. Struct. **34**, 351–378 (2005)

17. Kusumi, A., Sako, Y.: Cell surface organization by the membrane skeleton. Current opinion in cell biology **8**(4), 566–574 (1996)

18. Lavi, Y., Edidin, M., Gheber, L.A.: Lifetime of major histocompatibiliy complex class-i membrane clusters is controlled by the actin cytoskeleton. Biophys. J. **102**, 1543–1550 (2012)

19. Lemmon, M.A., Schlessinger, J.: Cell signaling by receptor tyrosine kinases. Cell **141**, 1117–1134 (2010)

20. Lillemeier, B., Pfeiffer, J.R., Surviladze, Z., Wilson, B.S., Davis, M.: Plasma membrane-associated proteins are clustered into islands attached to the cytoskeleton. Proc. Natl. Acad. Sci. U.S.A. **103**(50), 18,992 (2006)

21. Low-Nam, S.T., Lidke, K.A., Cutler, P.J., Roovers, R.C., van Bergen en Henegouwen, P.M., Wilson, B.S., Lidke, D.S.: ErbB1 dimerization is promoted by domain co-confinement and stabilized by ligand binding. Nature Structural and Molecular Biology **18** (2011)

22. MacGabhann, F., Popel, A.S.: Systems Biology of Vascular Endothelial Growth Factors. Microcirculation **15**(8), 715–738 (2008)

23. Niehaus, A.M.S., Edwards, J.S., Plechac, P., Tribe, R.: Microscopic Simulation of Membrane Molecule Diffusion on Corralled Membrane Surfaces. Biophys. J. **94**(5), 1551–1564 (2008)

24. Pezzarossa, A., Fenz, S., Schmidt, T.: Probing structure and dynamics of the cell membrane with single fluorescent proteins. In: Fluorescent Proteins II, pp. 185–212. Springer, Berlin, Heidelberg (2011)

25. Popov, A.V., Agmon, N.: Three-dimensional simulations of reversible bimolecular reactions: the simple target problem. J Chem Phys **115**(19), 8921–8932 (2001)

26. Pryor, M.M., Low-Nam, S.T., Halász, Á.M., Lidke, D.S., Wilson, B.S., Edwards, J.S.:Dynamic transition states of ErbB1 phosphorylation predicted by spatial-stochastic modeling. Biophys. J. **105**(6), 1533–1543 (2013)

27. Pryor, M.M., Steinkamp, M.P., Halász, Á.M., Chen, Y., Yang, S., Smith, M.S., Zahoransky-Kohalmi, G., Swift, M., Xu, X-P., Hanien, D., Volkmann, N., Lidke, D., Edwards, J.S., Wilson, B.S.: Orchestration of ErbB3 signaling through heterointeractions and homointeractions. Mol. Biol. Cell 26:4109–4123 (2015)
28. Saikh, S.R., Edidin, M.A.: Membranes are not just rafts. Chem. Phys. Lipids **144**(1), 1–3 (2006)
29. Schlessinger, J.: Ligand-induced, receptor-mediated dimerization and activation of egf receptor. Cell **110**, 669–672 (2002)
30. Schmidt, T., Schütz, G.J.: Single-Molecule Analysis of Biomembranes. In: Handbook of Single-Molecule Biophysics, pp. 19–42. Springer US, New York, NY (2009)
31. Schmidt, T., Schütz, G.J., Baumgartner, W., Gruber, H.J., Schindler, H.: Photophysics and motion of single fluorescent molecules in phospholipid membranes. J. Phys. Chem **99**, 17662–17668 (1995)
32. Shinar, G., Alon, U., Feinberg, M.: Sensitivity and robustness in chemical reaction networks. SIAM Journal of Applied Mathematics **69**(4), 977–998 (2009).
33. Simson, R., Yang, B., Moore, S.E., Doherty, P., Walsh, F.S., Jacobson, K.A.: Structural mosaicism on the submicron scale in the plasma membrane. Biophys. J. **74**, 297–308 (1998)
34. van Kampen, N.G.: Stochastic Processes in Physics and Chemistry. North-Holland, Amsterdam (1992)
35. von Smoluchowski, M.V.: Z. Phys. Chem. **92**, 129 (1917)
36. Sontag, E.: Monotone and near-monotone biochemical networks. Systems and Synthetic Biology **1**, 59–87 (2007)
37. Spira, F., Mueller, N.S., Beck, G., von Olshausen, P., Beig, J., Wedlich-Söldner, R.: Patchwork organization of the yeast plasma membrane into numerous coexisting domains. Nature Cell Biol. **14**(6), 640–648 (2012)
38. Takahashi, K., Tanase-Nicola, S., ten Wolde, P.R.: Spatio-temporal correlations can drastically change the response of a mapk pathway. Proc Natl Acad Sci USA **107**(6), 2473–2478 (2010)
39. S. Wieser, M. Moertelmaier, E. Fuertenbauer, H. Stockinger, Shutz, G.: (un)confined diffusion of cd59 in the plasma membrane determined by high-resolution single molecule microscopy. Biophys. J. **92**(10), 3719–3728 (2007). doi:10.1529/biophysj.106.095398
40. Woese, C.R.: A new biology for a new century. Microbiology and Molecular Biology Reviews **68**(2), 173–186 (2004)
41. Yang, S., Raymond-Stintz, M.A., Ying, W., Zhang, J., Lidke, D.S., Steinberg, S., Williams, L., Oliver, J.M., Wilson, B.S.: Mapping ErbB receptors on breast cancer cell membranes during signal transduction. Journal of Cell Science **120**(16), 2763–2773 (2007). doi:10.1242/jcs.007658

Distribution Approximations for the Chemical Master Equation: Comparison of the Method of Moments and the System Size Expansion

Alexander Andreychenko, Luca Bortolussi, Ramon Grima, Philipp Thomas and Verena Wolf

Abstract   The stochastic nature of chemical reactions has resulted in an increasing research interest in discrete-state stochastic models and their analysis. A widely used approach is the description of the temporal evolution of such systems in terms of a chemical master equation (CME). In this paper we study two approaches for approximating the underlying probability distributions of the CME. The first approach is based on an integration of the statistical moments and the reconstruction of the distribution based on the maximum entropy principle. The second approach relies on an analytical approximation of the probability distribution of the CME using the system size expansion, considering higher order terms than the linear noise approximation. We consider gene expression networks with unimodal and multimodal protein distributions to compare the accuracy of the two approaches. We find that both methods provide accurate approximations to the distributions of the CME while having different benefits and limitations in applications.

A. Andreychenko · L. Bortolussi · V. Wolf (✉)
Modelling and Simulation Group, Saarland University, Saarbrücken, Germany
e-mail: wolf@cs.uni-saarland.de

A. Andreychenko
e-mail: makedon@cs.uni-saarland.de

L. Bortolussi
Department of Mathematics and Geosciences, University of Trieste, Trieste, Italy
e-mail: luca@dmi.units.it

R. Grima
School of Biological Sciences, University of Edinburgh, Edinburgh, UK
e-mail: ramon.grima@ed.ac.uk

P. Thomas
Department of Mathematics, Imperial College London, London, UK
e-mail: p.thomas@imperial.ac.uk

1 Introduction

It is widely recognized that noise plays a crucial role in shaping the behavior of biological systems [1–4]. Part of such noise can be explained by intrinsic fluctuations of molecular concentrations inside a living cell, caused by the randomness of biochemical reactions, and fostered by the low numbers of certain molecular species [2]. As a consequence of this insight, stochastic modeling has rapidly become very popular [5], dominated by Markov models based on the chemical master equation (CME) [5, 6].

The CME represents a system of differential equations that specifies the time evolution of a discrete-state stochastic model that explicitly accounts for the discreteness and randomness of molecular interactions. It has therefore been widely used to model gene regulatory networks, signaling cascades and other intracellular processes which are significantly affected by the stochasticity inherent in reactions involving low number of molecules [7].

A solution of the CME yields the probability distribution over population vectors that count the number of molecules of each chemical species. While a numerical solution of the CME is rather straightforward, i.e. via a truncation of the state space [8, 9], for most networks the combinatorial complexity of the underlying state space renders efficient numerical integration infeasible. Therefore, the stochastic simulation algorithm (SSA), a Monte Carlo technique, is commonly used to derive statistical estimates of the corresponding state probabilities [10].

An alternative to stochastic simulation is to rely on approximation methods that can provide fast and accurate estimates of some aspects of stochastic models. Typically, most approximation methods focus on the estimation of moments of the distributions [11–16]. However, two promising approaches for the approximate computation of the distribution underlying the CME have recently been developed, whose complexity is independent of the molecular population sizes.

The first method discussed here is based on the inverse problem, i.e., reconstructing the probability distribution from its moments. To this end, a closure on the moment equations is employed which yields an approximation of the evolution of all moments up to order K of the joint distribution [14–16]. Thus, instead of solving one equation per population vector we solve $\sum_{k=1}^{K} \binom{N_S+k-1}{k}$ equations if N_S is the number of different chemical species. Given the (approximate) moments at the final time instant, it is possible to reconstruct the corresponding marginal probability distributions using the maximum entropy principle [17, 18]. The reconstruction requires the solution of a nonlinear constrained optimization problem. Nevertheless, the integration of the moment equations and the reconstruction of the underlying distribution can for most systems be carried out very efficiently and thus allows a fast approximation of the CME.

The second method, which is based on van Kampen's system size expansion [19], does not resort to moments but instead represents a direct analytical approximation of the probability distribution of the CME. Unlike the method of moments, the technique assumes that the distribution can be expanded about its deterministic limit

rate equations using a small parameter called the system size. For biochemical systems, the system size coincides with the volume to which the reactants are confined. The leading order term of this expansion is given by the linear noise approximation which predicts that the fluctuations about the rate equation solution are approximately Gaussian distributed [19] in agreement with the central limit theorem that is valid for large number of molecules. For low molecule numbers, the non-Gaussian corrections to this law can be investigated systematically using the higher order terms in the system size expansion. A solution to this expansion has recently been given in closed form as a series of the probability distributions in the inverse system size [20]. Although in general the positivity of this distribution approximation cannot be guaranteed, it often provides simple and accurate analytical approximations to the non-Gaussian distributions underlying the CME.

Since many reaction networks involve very small molecular populations, it is often questionable whether the system size expansion and moment based approaches can appropriately capture their underlying discreteness. For example, the state of a gene that can either be 'on' or 'off' while the number of mRNA molecules is of the order of only a few tens on average. In these situations, hybrid approaches are more appropriate, and supported by convergence results in a hybrid sense in the thermodynamic limit [21]. A hybrid moment approach for the solution of the CME integrates a small master equation for the small populations while a system of conditional moment equations is integrated for the large populations which is coupled with the equation for the small populations. Equations of unlikely states of the small populations can be truncated and then, with a similar computational effort, a more accurate approximation of the CME is obtained compared to the standard method of moments. Similarly, a conditional system size expansion can be constructed that tracks the probabilities of the small populations and applies the system size expansion to the large populations conditionally. Presently, such an approach has employed the linear noise approximation for gene regulatory networks with slow promoters invoking timescale separation [22]. The validity of a conditional system size expansion including higher than linear noise approximation terms is, however, still under question.

Given these recent developments, it remains to be clarified how these two competing approximation methods perform in practice. Here, we carry out a comparative study between numerical results obtained using the method of moments and analytical results obtained from the system size expansion for two common gene expression networks. The outline of the manuscript is the following: In Sect. 2 we will briefly review the CME formulation. Section 3 outlines the methods of (conditional) moments and the reconstruction of the probability distributions using the maximum entropy principle. In Sect. 4 the approximate solution of the CME using the SSE is reviewed. We then carry out two detailed case studies in Sect. 5. In the first case study, we investigate a model of a constitutively expressed gene leading to a unimodal protein distribution. In a second example we study the efficacy of the described hybrid approximations using the method of conditional moments and the conditional system size expansion for the prediction of multimodal protein distributions from the expression of a self-activating gene. These two examples are typical

scenarios encountered in more complex models, and as such provide ideal benchmarks for a qualitative and quantitative comparison of the two methods. We conclude with a discussion in Sect. 6.

2 Stochastic Chemical Kinetics

A biochemical reaction network is specified by a set of N_S different chemical species $S_1, \ldots, S_{N_S}$ and by a set of R reactions of the form

$$\ell_{r,1}^- S_1 + \cdots + \ell_{r,N_S}^- S_{N_S} \xrightarrow{k_r} \ell_{r,1}^+ S_1 + \cdots + \ell_{r,N_S}^+ S_{N_S}, \quad 1 \leq r \leq R.$$
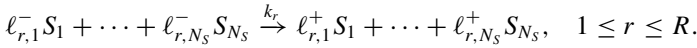
Given a reaction network, we define a continuous-time Markov chain $\{\mathbf{X}(t), t \geq 0\}$, where $\mathbf{X}(t) = (X_1(t), \ldots, X_{N_S}(t))$ is a random vector whose i-th entry $X_i(t)$ is the number of molecules of type S_i. If $\mathbf{X}(t) = \mathbf{x} = (x_1, \ldots, x_{N_S}) \in \mathbb{N}_0^{N_S}$ is the state of the process at time t and $x_i \geq \ell_{r,i}^-$ for all i, then the r-th reaction corresponds to a possible transition from state $\mathbf{x}$ to state $\mathbf{x} + \mathbf{v}_r$ where $\mathbf{v}_r$ is the change vector with entries $v_{r,i} = \ell_{r,i}^+ - \ell_{r,i}^- \in \mathbb{Z}^{N_S}$. The rate of the reaction is given by the propensity function $\gamma_r(\mathbf{x})$, with $\gamma_r(\mathbf{x})\mathrm{d}t$ being the probability of a reaction of index r occurring in a time instant $\mathrm{d}t$, assuming that the reaction volume is well-stirred. The most common form of propensity function follows from the principle of mass action and depends on the volume Ω to which the reactants are confined, $\gamma_r(\mathbf{x}) := \Omega k_r \prod_{i=1}^{N_S} \Omega^{-\ell_{r,i}^-} \binom{x_i}{\ell_{r,i}^-}$, as it can be derived on the basis of physical kinetics [6, 23].

We now fix the initial condition $\mathbf{x}_0$ of the Markov process to be deterministic and let $\Pi(\mathbf{x}, t) = \mathrm{Prob}(\mathbf{X}(t) = \mathbf{x} \mid \mathbf{X}(0) = \mathbf{x}_0)$ for $t \geq 0$. The time evolution of $\Pi(\mathbf{x}, t)$ is governed by the Chemical Master Equation (CME) as

$$\frac{\mathrm{d}\Pi(\mathbf{x}, t)}{\mathrm{d}t} = \sum_{r=1}^{R} \left(\gamma_r(\mathbf{x} - \mathbf{v}_r)\Pi(\mathbf{x} - \mathbf{v}_r, t) - \gamma_r(\mathbf{x})\Pi(\mathbf{x}, t) \right). \tag{1}$$

We remark that the probabilities $\Pi(\mathbf{x}, t)$ are uniquely determined when we consider the equations of all states that are reachable from the initial conditions.

Example 1 In the sequel we will use the following system as a running example. It describes the expression of a gene with enzymatic degradation [24].

$$\varnothing \xrightarrow{k_0} M \xrightarrow{k_1} \varnothing, \quad M \xrightarrow{k_2} M + P, \quad P \xrightarrow{f(x_P)} \varnothing,$$
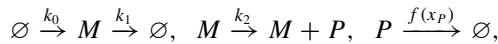
where $f(x_P)$ is a propensity function that depends on the number of molecules of type P (see also Sect. 5.1 for more details). A state of the associated Markov process is a vector $\mathbf{x} = (x_M, x_P)$ where $x_M, x_P \in \mathbb{N}_0$ are the number of mRNA (M) and protein (P) molecules in the system.

3 Method of Moments

For most realistic examples the number of reachable states is extremely large or even infinite, which renders an efficient numerical integration of Eq. (1) impossible. An approximation of the moments of the distribution over time can be obtained by considering the corresponding moment equations that describe the dynamics of the moments up to order $K < \infty$. We refer to this approach as the method of moments (MM). In this section we will briefly discuss the derivation of the corresponding moment equations following the lines of Ale et al. [16].

Let $\mathbf{f} : \mathbb{N}_0^{N_S} \rightarrow \mathbb{R}^n$ be a function that is independent of t where $n \in \mathbb{N}$. In the sequel we will exploit the following relationship,

$$
\begin{aligned}
\frac{d}{dt} E(\mathbf{f}(\mathbf{X}(t))) &= \sum_{\mathbf{x}} \mathbf{f}(\mathbf{x}) \cdot \frac{d}{dt} \Pi(\mathbf{X}(t) = \mathbf{x}) \\
&= \sum_{r=1}^{R} E\big[\gamma_r(\mathbf{X}(t)) \cdot (\mathbf{f}(\mathbf{X}(t) + \mathbf{v}_r) - \mathbf{f}(\mathbf{X}(t)))\big].
\end{aligned}
\tag{2}
$$

For $\mathbf{f}(\mathbf{x}) = \mathbf{x}$ this yields a system of equations for the population means

$$
\frac{d}{dt} E(\mathbf{X}(t)) = \sum_{r=1}^{R} \mathbf{v}_r E(\gamma_r(\mathbf{X}(t))).
\tag{3}
$$

Note that the system of ODEs in Eq. (3) is only closed if at most monomolecular mass action reactions ($\sum_{i=1}^{N_S} \ell_{r,i}^- \leq 1$) are involved. For most networks the latter condition is not true and higher order moments appear on the right side.

Let us write $\mu_i(t)$ for $E(X_i(t))$ and $\boldsymbol{\mu}(t)$ for the vector with entries $\mu_i(t)$, $1 \leq i \leq N_S$. Then a Taylor expansion of the function $\gamma_r(\mathbf{X}(t))$ about the mean $E(\mathbf{X}(t))$ yields

$$
\begin{aligned}
E(\gamma_r(\mathbf{X})) &= \gamma_r(\boldsymbol{\mu}) + \frac{1}{1!} \sum_{i=1}^{N_S} E(X_i - \mu_i) \frac{\partial}{\partial \mu_i} \gamma_r(\boldsymbol{\mu}) \\
&\quad + \frac{1}{2!} \sum_{i=1}^{N_S} \sum_{k=1}^{N_S} E((X_i - \mu_i)(X_k - \mu_k)) \frac{\partial^2}{\partial \mu_i \partial \mu_k} \gamma_r(\boldsymbol{\mu}) + \ldots,
\end{aligned}
\tag{4}
$$

where we omitted t to improve the readability. Note that $E(X_i(t) - \mu_i) = 0$ and assuming that all propensities follow the law of mass action and all reactions are at most bimolecular, the terms of order three and more disappear. By letting C_{ik} be the covariance $E[(X_i(t) - \mu_i)(X_k(t) - \mu_k)]$ we get

$$
E(\gamma_r(\mathbf{X})) = \gamma_r(\boldsymbol{\mu}) + \frac{1}{2} \sum_{i=1}^{N_S} \sum_{k=1}^{N_S} C_{ik} \frac{\partial^2}{\partial \mu_i \partial \mu_k} \gamma_r(\boldsymbol{\mu}).
\tag{5}
$$

Next, we derive an equation for the covariances by first exploiting the relationship

$$
\frac{d}{dt} C_{ik} = \frac{d}{dt} E(X_i X_k) - \frac{d}{dt}(\mu_i \mu_k) = \frac{d}{dt} E(X_i X_k) - \left(\frac{d}{dt}\mu_i\right)\mu_k - \mu_i\left(\frac{d}{dt}\mu_k\right),
\tag{6}
$$

and if we couple this equation with the equations for the means, the only unknown term that remains is the derivative $\frac{d}{dt}E(X_i X_k)$ of the second moment. For this, we can apply the same strategy as before by using Eq. (2) for the test function $f(\mathbf{x}) := x_i x_k$. This equation will contain the expectations $E(\gamma_r(\mathbf{X}))$ and $E(\gamma_r(\mathbf{X})X_i)$ for which we again consider the Taylor expansion about the mean. For the expansion of $E(\gamma_r(\mathbf{X})X_i)$ moments of order three come into play since derivatives of order three of $\gamma_r(\mathbf{x})x_i$ may be nonzero. It is possible to take these terms into account by deriving additional equations for moments of order three and higher. These equations will then include moments of even higher order such that theoretically we end up with an infinite system of equations. Different strategies to close the equations have been proposed in the literature [25–29]. Here we consider a low dispersion closure and assume that all moments of order $> K$ that are centered around the mean are equal to zero. E.g., if we choose $K = 2$, then we can obtain a closed system of equations that does not include higher order terms. Then we can integrate the time evolution of the means and that of the covariances and variances.

Example 2 To illustrate the method we consider Example 1. Assuming that all central moments of order three and higher are equal to zero, we get the following equations for the means of the species.

$$
\begin{aligned}
\frac{d}{dt}\mu_M &= \Omega k_0 - k_1 \mu_M \\
\frac{d}{dt}\mu_P &= k_1 \mu_M - f(\mu_P) - \frac{1}{2}\frac{\partial^2 f(\mu_P)}{\partial \mu_P{}^2}C_{P,P}
\end{aligned}
\tag{7}
$$

where the expectations of the species are given by μ_M and μ_P and the variance of P is given by $C_{P,P}$. Equations for covariances are omitted.

In many situations, the approximation provided by the MM approach is very accurate even if only the means and covariances are considered. In general, however, numerical results show that the approximation tends to become worse if systems exhibit complex behavior such as multistability or oscillations and the resulting equations may become very stiff [14, 30]. For some systems increasing the number of moments improves the accuracy [16]. Generally, however such a convergence is not seen [31], except in the limit of large volumes [32].

3.1 Equations for Conditional Moments

For many reactions networks a hybrid moment approach, called method of conditional moments (MCM), can be more advantageous, in which we decompose $\mathbf{X}(t)$ into small and large populations. The reason is that small populations (often describing the activation state of a gene) have distributions that assign a significant mass of probability only to a comparatively small number of states. In this case we can

integrate the probabilities directly to get a more accurate approximation of the CME compared to an integration of the moments.

Formally, we consider $\mathbf{X}(t) = (\mathbf{Y}(t), \mathbf{Z}(t))$, where $\mathbf{Y}(t)$ corresponds to the small, and $\mathbf{Z}(t)$ to the large populations. Similarly, we write $\mathbf{x} = (\mathbf{y}, \mathbf{z})$ for the states of the process and $\mathbf{v}_r = (\hat{\mathbf{v}}_r, \tilde{\mathbf{v}}_r)$ for the change vectors, $r \in \{1, \ldots, R\}$. Then, we condition on the state of the small populations and apply the MM to the conditional moments but not to the distribution of $\mathbf{Y}(t)$. The probabilities for $\mathbf{Y}(t) = \mathbf{y}$ are called mode probabilities. Now, Eq. (1) becomes

$$\frac{d\Pi(\mathbf{y}, \mathbf{z})}{dt} = \sum_{r=1}^{R} [\gamma_r(\mathbf{y} - \hat{\mathbf{v}}_r, \mathbf{z} - \tilde{\mathbf{v}}_r)\Pi(\mathbf{y} - \hat{\mathbf{v}}_r, \mathbf{z} - \tilde{\mathbf{v}}_r) - \gamma_r(\mathbf{y}, \mathbf{z})\Pi(\mathbf{y}, \mathbf{z})]. \quad (8)$$

Next, we sum over all possible $\mathbf{z}$ to get the time evolution of the mode probabilities $\Pi(\mathbf{y}) = \sum_{\mathbf{z}} \Pi(\mathbf{y}, \mathbf{z})$.

$$\frac{d}{dt}\Pi(\mathbf{y}) = \sum_{\mathbf{z}} \sum_{r=1}^{R} \gamma_r(\mathbf{y} - \hat{\mathbf{v}}_r, \mathbf{z} - \tilde{\mathbf{v}}_r)\Pi(\mathbf{y} - \hat{\mathbf{v}}_r, \mathbf{z} - \tilde{\mathbf{v}}_r) - \sum_{\mathbf{z}} \sum_{r=1}^{R} \gamma_r(\mathbf{y}, \mathbf{z})\Pi(\mathbf{y}, \mathbf{z})$$

$$= \sum_{r=1}^{R} \Pi(\mathbf{y} - \hat{\mathbf{v}}_r)E[\gamma_r(\mathbf{y} - \hat{\mathbf{v}}_r, \mathbf{Z}) \mid \mathbf{Y} = \mathbf{y} - \hat{\mathbf{v}}_r] - \sum_{r=1}^{R} \Pi(\mathbf{y})E[\gamma_r(\mathbf{y}, \mathbf{Z}) \mid \mathbf{Y} = \mathbf{y}]. \quad (9)$$

Note that in this small master equation that describes the change of the mode probabilities over time, the sum runs only over those reactions that modify $\mathbf{y}$, since for all other reactions the terms cancel out. Moreover, on the right side we have only mode probabilities of neighboring modes and conditional expectations of the $\mathbf{z}$-part of the reaction rate. For the latter, we can use a Taylor expansion about the conditional population means. Similar to Eq. (5), this yields an equation that involves the conditional means and centered conditional moments of second order (variances and covariances). Thus, in order to close the system of equations, we need to derive equations for the time evolution of the conditional means and centered conditional moments of higher order. Since the mode probabilities may become zero, we first derive an equation for the evolution of the partial means (conditional means multiplied by the probability of the condition)

$$\frac{d}{dt}(E[\mathbf{Z} \mid \mathbf{y}]\Pi(\mathbf{y})) = \sum_{\mathbf{z}} \mathbf{z} \frac{d}{dt}\Pi(\mathbf{y}, \mathbf{z})$$

$$= \sum_{r=1}^{R} E[(\mathbf{Z} + \tilde{\mathbf{v}}_r)\gamma_r(\mathbf{y} - \hat{\mathbf{v}}_r, \mathbf{Z}) \mid \mathbf{y} - \hat{\mathbf{v}}_r]\Pi(\mathbf{y} - \tilde{\mathbf{v}}_r) \quad (10)$$

$$- \sum_{r=1}^{R} E[\mathbf{Z}\gamma_r(\mathbf{y}, \mathbf{Z}) \mid \mathbf{y}]\Pi(\mathbf{y}),$$

where in the second line we applied Eq. (8) and simplified the result. The conditional expectations $E[(\mathbf{Z} + \tilde{\mathbf{v}}_r)\gamma_r(\mathbf{y} - \hat{\mathbf{v}}_r, \mathbf{Z}) \mid \mathbf{y} - \hat{\mathbf{v}}_r]$ and $E[\mathbf{Z}\gamma_r(\mathbf{y}, \mathbf{Z}) \mid \mathbf{y}]$ are then replaced by their Taylor expansion about the conditional means such that the

equation involves only conditional means and higher centered conditional moments [33]. For higher centered conditional moments, similar equations can be derived. If all centered conditional moments of order higher than K are assumed to be zero, the result is a (closed) system of differential algebraic equations (algebraic equations are obtained whenever a mode probability $\Pi(\mathbf{y})$ is equal to zero). However, it is possible to transform the system of differential algebraic equations into a system of (ordinary) differential equations after truncating modes with insignificant probabilities. Then we can get an accurate approximation of the solution after applying standard numerical integration methods. For the case study in Sect. 5 we derived the system of ODEs using the tool SHAVE [34] which implements a truncation based approach and solves the ODEs using an explicit Runge–Kutta method.

Example 3 We apply the MCM approach to Example 1. The modes of the system correspond to the number of molecules of type M. Here we provide equations only for the first two modes, $M = 0$ and $M = 1$. The equations for the corresponding mode probabilities (p_0, p_1) and the expected number of proteins ($\mu_{P,0}$, $\mu_{P,1}$) conditioned on the modes are given below. This equation system has to be closed not only by setting to zero all the central moments of order higher than 2, but also by truncating the infinite population of M. This can be done by assuming that $p_n = 0$ from a certain number n on.

$$
\begin{aligned}
\frac{d}{dt} p_0 &= -\Omega k_0 p_0 + k_1 p_1 \\
\frac{d}{dt} p_1 &= \Omega k_0 p_0 - k_1 p_1 - \Omega k_0 p_1 \\
\frac{d}{dt} \left(\mu_{P,0}\, p_0 \right) &= -\Omega k_0 \mu_{P,0} p_0 + k_1 \mu_{P,1} p_1 - f(\mu_{P,0}) p_0 - \frac{1}{2} \frac{\partial^2 f(\mu_{P,0})}{\partial \mu_{P,0}{}^2} C_{P,P,0} p_0 \\
\frac{d}{dt} \left(\mu_{P,1}\, p_1 \right) &= \Omega k_0 \mu_{P,0} p_0 - \Omega k_0 \mu_{P,1} p_1 - k_1 \mu_{P,1} p_1 - f(\mu_{P,1}) p_1 \\
&\qquad - \frac{1}{2} \frac{\partial^2 f(\mu_{P,1})}{\partial \mu_{P,1}{}^2} C_{P,P,1} p_1 + k_2 p_1
\end{aligned}
\tag{11}
$$

3.2 Maximum Entropy Distribution Reconstruction

Given the (approximated) moments of a distribution up to order K it is possible to reconstruct the corresponding probability distribution. Since a finite number of moments defines a set of distributions, we apply the *maximum entropy principle* where we choose among the distributions, that fulfill the moment equations, the one that maximizes the entropy. For instance, the normal distribution is chosen among all continuous distributions with equal mean and variance.

In the sequel we describe how to obtain the one-dimensional marginal probability distributions of a reaction network when we use the moments up to order K. We mostly follow Andreychenko et al. [17] and simply write X for the corresponding molecular count at some fixed time instant t. Given a sequence of $K + 1$ noncentral

moments[1] $E(X^k) = \mu^{(k)}, k = 0, 1, \ldots, K$, the set $\mathcal{G}$ of allowed (discrete) probability distributions consists of all non-negative functions g for which the following conditions hold:

$$\sum_x x^k g(x) = \mu^{(k)}, k = 0, 1, \ldots, K. \tag{12}$$

Here x ranges over possible arguments (usually $x \in \mathbb{N}_0$) with positive probability. Note that we have included the constraint $\mu_0 = 1$ in order to guarantee that g is a probability distribution. According to the maximum entropy principle, we choose the distribution $q \in \mathcal{G}$ that maximizes the entropy $H(g)$, i.e.,

$$q = \arg\max_{q \in \mathcal{G}} H(g) = \arg\max_{g \in \mathcal{G}} \left(-\sum_x g(x) \ln g(x) \right). \tag{13}$$

The problem of finding the maximum entropy distribution is a nonlinear constrained optimization problem that can be addressed by considering the Lagrangian functional

$$\mathcal{L}(g, \lambda) = H(g) - \sum_{k=0}^{K} \lambda_k \left(\sum_x x^k g(x) - \mu^{(k)} \right),$$

where $\lambda = (\lambda_0, \ldots, \lambda_K)$ are the corresponding Lagrangian multipliers. The maximum of the unconstrained Lagrangian $\mathcal{L}$ corresponds to the solution of the constrained maximum entropy problem (13). Note that setting the derivatives of $\mathcal{L}(g, \lambda)$ w.r.t. λ_k, to zero results in the moment constraints. The general form of the maximum is obtained by setting $\frac{\partial \mathcal{L}}{\partial g(x)}$ to zero which yields

$$q(x) = \exp\left(-1 - \sum_{k=0}^{K} \lambda_k x^k \right) = \tfrac{1}{Z} \exp\left(-\sum_{k=1}^{K} \lambda_k x^k \right),$$

where

$$Z = e^{1+\lambda_0} = \sum_x \exp\left(-\sum_{k=1}^{M} \lambda_k x^k \right) \tag{14}$$

is a normalization constant. The last equality in Eq. (14) follows from the fact that q is a distribution and thus λ_0 is uniquely determined by $\lambda_1, \ldots, \lambda_K$. Next we insert the above general form into the Lagrangian, thus transforming the problem into an unconstrained convex minimization problem of the dual function w.r.t. the variables λ_k. This yields the dual function

---

[1]Noncentral moments can be easily obtained from central ones. For instance, the second noncentral moment $\mu^{(2)}$ is obtained from the variance σ^2 and the mean μ as $\mu^{(2)} = \sigma^2 + \mu^2$.

$$\Psi(\lambda) = \ln Z + \sum_{k=1}^{K} \lambda_k \mu^{(k)}. \tag{15}$$

According to the Kuhn–Tucker theorem, the solution $\lambda^* = \arg \min \Psi(\lambda)$ of the minimization problem determines the solution q of the original constrained optimization problem in Eq. (13) (see [35]). We solve this unconstrained optimization problem using the Newton method from the MATLAB's numerical minimization package `minFunc`, where we choose $\lambda^{(0)} = (0, \ldots, 0)$ as an initial starting point and use the approximated gradient and Hessian matrix. Since for the systems that we consider, the dual function is convex [36–38], there exists a unique minimum $\lambda^* = (\lambda_1^*, \ldots, \lambda_K^*)$ where all first derivatives are zero and where the Hessian is positive definite. The final results λ^* of the iteration yields the distribution

$$\tilde{q}(x) = \exp\left(-1 - \sum_{k=0}^{K} \lambda_k^* x^k\right),$$

which is an approximation of the marginal distribution of the process at time t.

The sequence of moments $\mu^{(k)}, k = 0, \ldots, K$ obtained using MM or MCM serves as an input to the maximum entropy reconstruction procedure. Due to the high sensitivity with respect to the accuracy of the highest order moment $E\left(X_P^K\right)$, we compute all moments up to $E\left(X_P^{K+1}\right)$ to get a better estimation but use moments only up to $E\left(X_P^K\right)$ in the entropy maximization.

The maximum entropy approach provides a useful extension of moment-based integration methods of the CME. In order to reconstruct a probability distribution, we require that moments of the reconstructed distribution match with those obtained by the method of moments. We apply the maximum entropy principle to the infinitely many distributions satisfying these constraints, i.e., we pick the distribution that maximizes the uncertainty. The advantage of this choice are that we can efficiently learn the maximum entropy distribution in one or two dimensions. Furthermore, it seems to produce reasonably accurate results, as validated a posteriori [17, 18].

The reconstruction of the distributions of higher dimension is more involved due to numerical instabilities arising when using the ill-conditioned Hessian matrix [36, 39] in the optimization procedure. As mentioned in the numerical results that we present in the sequel, problems may arise if the support of the distribution (which serves as an input argument to the optimization procedure) is not chosen adequately. The true support of the distribution is often infinite and a reasonable truncation has to be used [40]. A possible solution is addressed in [18] where we introduce an iterative heuristic-based procedure of the support approximation. However, generally this approach gives very accurate results relative to the information about the distribution given by the moment constrains.

4   System Size Expansion of the Probability Distribution

We here describe the use of the system size expansion [19] to obtain approximate but simple expressions for the probability distributions of the CME. For simplicity, we will focus on the case of a single species and follow the approach developed by *Thomas and Grima* [20]. The system size expansion makes use of the macroscopic limit of the CME which is attained for large reaction volumes. When concentrations are held constant, large volumes imply large number of molecules, and hence the macroscopic concentration $[X]$ follows the deterministic rate equation

$$\frac{\mathrm{d}[X]}{\mathrm{d}t} = \sum_{r=1}^{R} \nu_r f_r^{(0)}([X]). \tag{16}$$

Note that here $\nu_r = \nu_{r,1}$ because we only consider a single species. A prerequisite for Eq. (16) to be the deterministic limit of the CME is that the rate functions satisfy the scaling

$$\gamma_j(\Omega[X], \Omega) = \Omega\big[f_r^{(0)}([X]) + \Omega^{-1} f_r^{(1)}([X]) + \ldots\big], \tag{17}$$

which holds for instance in the case of mass action kinetics [20]. The first term in this series, $f_r^{(0)}([X]) = \lim_{\Omega \to \infty} \frac{\gamma_r(\Omega[X])}{\Omega}$, is the macroscopic rate function. Note that for an unimolecular reaction only the first term in Eq. (17) is present while for a bimolecular one the first two terms are nonzero.

The expansion allows to characterize the deviations from this deterministic behavior by successively taking into account higher order terms. Specifically, van Kampen proposed separating the dynamics of the molecular concentration into the deterministic part $[X]$ and a fluctuating component ε that reads

$$\frac{x}{\Omega} = [X] + \Omega^{-1/2}\varepsilon. \tag{18}$$

This ansatz can be used to expand the CME in powers of the inverse square root of the volume by changing variables from x to ε. Assuming that this transformation is continuous, i.e., $\Pi(\varepsilon, t) = \Pi(\Omega[X] + \Omega^{1/2}\varepsilon, t)\Omega^{1/2}$, the CME becomes

$$\frac{\partial}{\partial t}\Pi(\varepsilon, t) = \mathcal{L}_0\Pi(\varepsilon, t) + \sum_{k=1}^{N} \Omega^{-k/2}\mathcal{L}_k\Pi(\varepsilon, t) + O(\Omega^{-(N+1)/2}). \tag{19}$$

When the above equation is truncated after the Nth term, it approximates the CME by a partial differential equation. It is shown in Ref. [20] that the differential operators $\mathcal{L}_k$ can be written down explicitly and are given by

$$\mathcal{L}_k = \sum_{s=0}^{\lceil k/2 \rceil} \sum_{p=1}^{k-2(s-1)} \frac{\mathcal{D}_{p,s}^{k-p-2(s-1)}}{p!(k-p-2(s-1))!} (-\partial_\varepsilon)^p \varepsilon^{k-p-2(s-1)}, \tag{20}$$

where the coefficients

$$\mathcal{D}_{p,s}^q = \sum_{r=1}^{R} (\nu_r)^p \frac{\partial^q f_r^{(s)}([X])}{\partial[X]^q}, \tag{21}$$

depend only on the solution of the rate equation. We will solve Eq. (19) perturbatively by expanding the probability density as

$$\Pi(\varepsilon, t) = \sum_{j=0}^{N} \Omega^{-j/2} \pi_j(\varepsilon, t) + O(\Omega^{-(N+1)/2}). \tag{22}$$

Using the above series in Eq. (19) and equating order Ω^0 terms, one finds

$$\left(\frac{\partial}{\partial t} - \mathcal{L}_0 \right) \pi_0 = 0, \tag{23a}$$

while equating terms to order $\Omega^{-j/2}$, one finds

$$\left(\frac{\partial}{\partial t} - \mathcal{L}_0 \right) \pi_j(\varepsilon) = \mathcal{L}_1 \pi_{j-1} + \cdots + \mathcal{L}_j \pi_0, \tag{23b}$$

for $j > 0$. The first equation, Eq. (23a), is called the linear noise approximation [19] and its solution is a Gaussian distribution

$$\pi_0(\varepsilon, t) = \frac{1}{\sqrt{2\pi \sigma^2(t)}} \exp \left(-\frac{\varepsilon^2}{2\sigma^2(t)} \right), \tag{24}$$

with zero mean meaning that the rate equation are valid on average. Its variance $\sigma^2(t)$ follows the equation

$$\frac{\partial \sigma^2}{\partial t} = 2\mathcal{J}(t)\sigma^2 + \mathcal{D}_2^0(t), \tag{25}$$

where we have denoted by $\mathcal{J}(t) = \mathcal{D}_1^1(t)$ the Jacobian of the rate Eq. (16).

The solution of the partial differential equations (23b) can then be obtained using the eigenfunctions of $\mathcal{L}_0$. In particular, we can write

$$\pi_j(\varepsilon, t) = \sum_{m=1}^{3j} a_m^{(j)}(t) \psi_m(\varepsilon, t) \pi_0(\varepsilon, t)$$

where $\psi_m(\varepsilon, t) = \pi_0^{-1}(-\partial_\varepsilon)^m \pi_0 = \frac{1}{\sigma^m(t)} H_m\left(\frac{\varepsilon}{\sigma(t)}\right)$ and H_m are the Hermite polynomials. The solution of the system size expansion is therefore

$$\Pi(\varepsilon, t) = \pi_0(\varepsilon, t)\left(1 + \sum_{j=1}^{N} \Omega^{-j/2} \sum_{m=1}^{3j} a_m^{(j)}(t)\psi_m(\varepsilon, t)\right) + O(\Omega^{-(N+1)/2}). \quad (26a)$$

Mathematically speaking the above equation represents an asymptotic series solution to the CME. Equations for the coefficients can be obtained using the orthogonality of the Hermite polynomials, and are given the ordinary differential equations

$$\left(\frac{\partial}{\partial t} - n\mathcal{J}\right) a_n^{(j)} = \sum_{k=1}^{j} \sum_{m=0}^{3(j-k)} a_m^{(j-k)} \sum_{s=0}^{\lceil k/2 \rceil} \sum_{p=1}^{k-2(s-1)} \mathcal{D}_{p,s}^{k-p-2(s-1)} \mathcal{I}_{mn}^{p,k-p-2(s-1)},$$

$$(26b)$$

with

$$\mathcal{I}_{mn}^{\alpha\beta} = \frac{\sigma^{\beta-\alpha+n-m}}{\alpha!} \sum_{s=0}^{\min(n-\alpha,m)} \binom{m}{s} \frac{(\beta+\alpha+2s-(m+n)-1)!!}{(\beta+\alpha+2s-(m+n))!(n-\alpha-s)!}, \quad (26c)$$

and zero for odd $(\alpha + \beta) - (m + n)$. Note that $a_n^{(j)} = 0$ when $n + j$ is odd. Explicit expressions for the probability density can now be evaluated to any desired order. Relatively simple and explicit solutions are obtained in steady state conditions by letting the time derivative on the left-hand side of Eq. (26b) go to zero. It follows that the first term in Eq. (26a), the linear noise approximation π_0, describes the distribution in the infinite volume limit. For finite volumes, implying finite number of molecules, higher order terms given by Eq. (26) have to be taken into account.

It is, however, the case that this approximation can become inaccurate for processes whose mean behavior differs significantly from the rate equation. This is because in van Kampen's ansatz, Eq. (18), the average concentration is approximated by the solution of the rate equation $[X]$. For biochemical networks involving bimolecular reactions, the rate equation provides only an approximation to the true average predicted by the CME because its propensities depend nonlinearly on the concentrations [41]. In applications it is important to account for these deviations from the rate equation solution and the linear noise approximation. We therefore calculate the true concentration mean and variance using the system size expansion a priori and then perform the expansion about the true mean. A posteriori, this leads to an expansion about the mean

$$\frac{x}{\Omega} = \underbrace{\left\langle\frac{x}{\Omega}\right\rangle}_{\text{mean}} + \underbrace{\Omega^{-1/2}\bar{\varepsilon}}_{\text{fluctuations}}, \quad (27)$$

which is different than the one proposed by van Kampen, Eq. (18), who expands the CME about the solution of the rate equation. Here, the averages are calculated from $\left\langle \frac{x}{\Omega} \right\rangle = [X] + \Omega^{-1/2}\langle \varepsilon \rangle$ such that $\bar{\varepsilon} = \varepsilon - \langle \varepsilon \rangle$ is a centered random variable quantifying the fluctuations about the true average. The result is the following expansion

$$\bar{\pi}(\bar{\varepsilon}, t) = \bar{\pi}_0(\bar{\varepsilon}, t) + \sum_{j=1}^{N} \Omega^{-j/2} \sum_{m=1}^{3j} \bar{a}_m^{(j)} \psi(\bar{\varepsilon}, t) \bar{\pi}_0(\bar{\varepsilon}, t) + O(\Omega^{-(N+1)/2}), \quad (28a)$$

where $\bar{\pi}_0(\bar{\varepsilon})$ is a Gaussian different from the linear noise approximation because it is centered about the true mean (instead of the rate equation). The coefficients in the above equation can be calculated from

$$\bar{a}_m^{(j)} = \sum_{k=0}^{j} \sum_{n=0}^{3k} a_n^{(k)} \kappa_{m-n}^{(j-k)}, \qquad (28b)$$

and

$$\kappa_j^{(n)} = \frac{1}{n!} \sum_{m=0}^{\lfloor j/2 \rfloor} (-1)^{(j+m)} \sum_{k=j-2m}^{n-m} \binom{n}{k} B_{k,j-2m}\left(\left\{\zeta! a_1^{(\zeta)}\right\}\right) B_{n-k,m}\left(\left\{\frac{\zeta!}{2}\bar{\sigma}_{(\zeta)}^2\right\}\right). \tag{28c}$$

Here $a_1^{(j)}$ and $\bar{\sigma}_{(j)}^2 = 2\big[a_2^{(j)} - B_{j,2}(\{\zeta! a_1^{(\zeta)}\})/j!\big]$ denote the coefficients in the expansions of mean and variance

$$\langle \varepsilon \rangle = \sum_{j=1}^{N} \Omega^{-j/2} a_1^{(j)} + O(\Omega^{-(N+1)/2}), \qquad (29a)$$

$$\bar{\sigma}^2 = \sigma^2 + \sum_{j=1}^{N} \Omega^{-j/2} \sigma_{(j)}^2 + O(\Omega^{-(N+1)/2}), \qquad (29b)$$

respectively, and $B_{k,n}(\{y_\zeta\})$ denotes the partial Bell polynomials [42] defined as

$$B_{n,k}(\{y_\zeta\}_{\zeta=1}^{n-k+1}) = \sum{}' \frac{n!}{j_1! \dots j_{n-k+1}!} \left(\frac{y_1}{1!}\right)^{j_1} \dots \left(\frac{y_{n-k+1}}{(n-k+1)!}\right)^{j_{n-k+1}}. \tag{30}$$

Note that $\sum'$ denotes the summation over all sequences $j_1, \dots, j_{n-k+1}$ of non-negative integers such that $j_1 + \dots + j_{n-k+1} = k$ and $j_1 + 2j_2 + \dots + (n-k+1) j_{n-k+1} = n$. Note that the expansion about the mean has generally less nonzero coefficients because $\bar{a}_1^{(j)} = \bar{a}_2^{(j)} = 0$ for all j. Note also that for systems whose propensities depend at most linearly on the concentrations, mean and variance are exact to order Ω^0 (linear noise approximation), and hence for this case expansion (26a) coincides

with Eq. (28a). In Sect. 5 we show that typically a few terms in this expansion (28a) are sufficient to capture the underlying distributions of the CME.

A particularly relevant case, namely the stationary solution of the CME, turns out to be obtained quite straightforwardly. For example, truncating after Ω^{-1}-terms, from Eq. (29) it follows that $\langle \varepsilon \rangle = \Omega^{-1/2} a_1^{(1)} + O(\Omega^{-3/2})$ and $\bar{\sigma}^2 = \sigma^2 + \Omega^{-1}(2a_2^{(2)} - (a_1^{(1)})^2) + O(\Omega^{-3/2})$. Letting now the left hand side of Eq. (26b) go to zero, solving for the coefficients $a_n^{(j)}$ and using the solution in Eq. (28b) one finds that to order $\Omega^{-1/2}$ the only nonzero coefficient is

$$\bar{a}_3^{(1)} = -\frac{\sigma^4 \mathcal{D}_1^2}{6\mathcal{J}} + \frac{\sigma^2 \mathcal{D}_2^1}{6\mathcal{J}} + \frac{\mathcal{D}_3^0}{18\mathcal{J}}, \tag{31a}$$

while to order Ω^{-1}, one finds

$$\bar{a}_4^{(2)} = -\frac{\mathcal{D}_4^0}{96\mathcal{J}} - \frac{\sigma^2 \mathcal{D}_3^1}{24\mathcal{J}} - \frac{\sigma^4 \mathcal{D}_2^2}{16\mathcal{J}} - \frac{\sigma^6 \mathcal{D}_1^3}{24\mathcal{J}} - \bar{a}_3^{(1)} \left(\frac{3\mathcal{D}_2^1}{8\mathcal{J}} + \frac{3\sigma^2 \mathcal{D}_1^2}{4\mathcal{J}} \right),$$
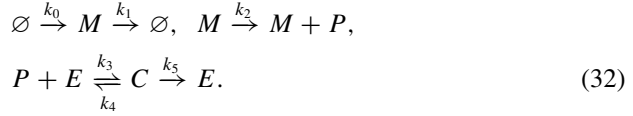$$\bar{a}_6^{(2)} = \frac{1}{2}(\bar{a}_3^{(1)})^2. \tag{31b}$$

The above equations determine the series solution of the CME, Eq. (28a), in stationary conditions to order Ω^{-1}.

5 Results

In this section we will compare the (hybrid) method of moments (MM and MCM approach) and the (conditional) system size expansion (SSE approach) by considering the quality of the resulting distribution approximations. In the former case we use the maximum entropy approach outlined in Sect. 3.2 and the approximate solution obtained from the SSE in the latter case. We base our comparison on two simple but challenging examples. The first one describes the bursty expression of a protein which degrades via an enzyme-catalyzed reaction. The second example describes the expression of a protein activating its own expression resulting in a multimodal protein distribution.

5.1 Example 1: Bursty Protein Production

In order to compare the performance of the two methods, we will employ a simple model of gene expression with enzymatic degradation described in Ref. [24]. The system is described by the following set of biochemical reactions:

$$\varnothing \xrightarrow{k_0} M \xrightarrow{k_1} \varnothing, \quad M \xrightarrow{k_2} M + P,$$

$$P + E \underset{k_4}{\overset{k_3}{\rightleftharpoons}} C \xrightarrow{k_5} E. \tag{32}$$

Recently, such active protein degradation has been recognized to be an important factor in skewing nuclear protein distributions in mammalian cells toward high molecule numbers [43]. In our model we explicitly account for mRNA which is important even when the mRNA half-life is shorter than the one of the corresponding protein [44]. Assuming binding and unbinding of P and E are fast compared to protein degradation, the degradation kinetics can be simplified as in Refs. [43, 45], resulting in a Michaelis–Menten like kinetic rate:

$$P \xrightarrow{f(x_P)} \varnothing, \tag{33}$$

with $f(x_P) = \frac{\Omega v_M x_P}{\Omega K_M + x_P}$, where x_P is the number of proteins and $K_M = \frac{k_4 + k_5}{k_3}$ is the Michaelis–Menten constant. Less obviously for this reduction to hold in the stochastic case, one also requires $k_4 \gg k_5$ as shown in Refs. [45, 46]. Here rates are set to $k_0 = 8, k_1 = 10, k_2 = 100, v_M = 100, K_M = 20, \Omega = 1$. In particular, the reaction rates involving mRNA are chosen such that proteins are produced in bursts of size $b = k_2/k_1$, i.e., on average 10 protein molecules are synthesized from a single transcript.

5.1.1 Method of Moments and Maximum Entropy Reconstruction

We compute an approximation of the moments of species M and P up to order 4 ($K + 1 = 4$) and 6 ($K + 1 = 6$) using the MM as explained in Sect. 3. The moments of P are then used to reconstruct the marginal probability distribution of P. For instance, given the moments $E\left(X_P^0\right), E\left(X_P^1\right), E\left(X_P^2\right), E\left(X_P^3\right), E\left(X_P^4\right)$ we approximate the distribution of P with $\tilde{q}(x) \approx \Pi(X_P = x)$ (see Sect. 3.2). Due to the high sensitivity of the maximum entropy method even to small approximation errors of the moments of highest order considered (in this case the approximation of $E\left(X_P^4\right)$ and $E\left(X_P^6\right)$, respectively), we use moments only up to $E\left(X_P^3\right)$ for the reconstruction. The same holds for all results presented below. In Fig. 1 we plot the two reconstructed distributions.

While for most parts of the support (including the tail) the distribution is accurately reconstructed even with $K = 3$, the method is less precise when considering the probability of small copy numbers of P. To improve the reconstruction, we may use more moments, for instance $K = 7$. However, in this case the moment equations become so stiff that the numerical integration fails completely. This happens due to a combination of highly nonlinear derivatives of the rate function $f(x_P)$ with large values of the higher order moments.
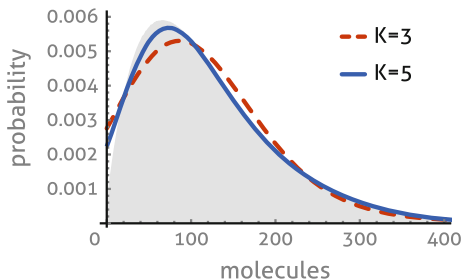
Fig. 1 Bursty protein production: reconstruction based on MM. The reconstructed distribution (cf. Eq. (3.2)) is compared to the distribution estimated with stochastic simulations (*shaded gray area*), where we use $K = 3$ (*dashed red*) and $K = 5$ (*solid blue line*) for the moments in the maximum entropy method. We find that taking into account moments of higher order increases the accuracy significantly, in particular in the region of 0–200 proteins

5.1.2 Solution Using the System Size Expansion

The approximate solution to the distribution functions using the system size expansion as outlined in Sect. 4 is available for networks of a single species only. We therefore concentrate on the case where the mRNA dynamics is much faster than the one of the protein, called the burst approximation [44]. It can be shown that the reaction scheme (32) follows the reduced CME

$$\frac{\mathrm{d}}{\mathrm{d}t} \Pi(x) = \Omega h_0 \sum_{z=0}^{\infty} (E_x^{-z} - 1)\varphi(z)\Pi(x) + \Omega(E_x^{+1} - 1)\frac{v_M x}{\Omega K_M + x}\Pi(x), \quad (34)$$

where E_x^{-z} is the step operator defined by $E_x^{-z} f(x) = f(x - z)$ for any function f. Note that protein synthesis occurs in random bursts z following a geometric distribution $\varphi(z) = \frac{1}{1+b}\left(\frac{b}{1+b}\right)^z$ with average b. The relation between the parameters in scheme (32) and Eq. (34) are $h_0 = k_0 k_2 / k_1$ and $b = k_2 / k_1$. Within this description protein synthesis involves many reactions: one for each value of z with probability $\varphi(z)$. The coefficients in the expansion of the CME follow from Eq. (21), and are given by

$$\mathcal{D}_n^m = \delta_{m,0} h_0 \langle z^n \rangle_\varphi + (-1)^n v_M \frac{\partial^m}{\partial [P]^m} \frac{[P]}{K_M + [P]}, \quad (35)$$

and $\mathcal{D}_{n,s}^m = 0$ for $s > 0$, where $[P]$ denotes the protein concentration according to the rate equation solution and $\langle z^n \rangle_\varphi = \sum_{z=0}^{\infty} z^n \varphi(z) = \frac{1}{1+b} \mathrm{Li}_{-n}(\frac{b}{1+b})$ denotes the average over the geometric distribution in terms of the polylogarithm function $\mathrm{Li}_{-n}(x) = \sum_{k=1}^{\infty} k^n x^k$. The rate Eq. (16) can be solved together with the linear noise approximation, Eq. (25), in steady state conditions. For $v_M < b h_0$ the solution is

$$[P] = K_M \left(1 - \frac{v_M}{bh_0}\right)^{-1}, \quad \sigma^2 = K_M(b+1)\varsigma(\varsigma+1), \tag{36a}$$

where we have defined by $\varsigma = \frac{[P]}{K_M}$ the reduced substrate concentration. In Fig. 2a we show that the expansion performed about the rate equation solution leads to large undulations, we therefore focus on the expansion about the mean. To this end, we have to take into account higher order corrections to the first two moments, we find $\langle \varepsilon \rangle = \Omega^{-1/2}(1+b)\varsigma$ and $\bar{\sigma}^2 = \sigma^2 + \Omega^{-1}(b+1)\varsigma(b(\varsigma+2)+\varsigma+1)$. The nonzero coefficients to order Ω^{-1} given by Eq. (31) then evaluate to

$$\bar{a}_3^{(1)} = \frac{\sigma^2}{6}(2b(\varsigma+1)+2\varsigma+1),$$

$$\bar{a}_4^{(2)} = \frac{\sigma^2}{4}\left[(b+1)^2\varsigma^2 + (b+1)(2b+1)\varsigma + \frac{1}{6}(6b(b+1)+1)\right],$$

$$\bar{a}_6^{(2)} = \frac{1}{2}[\bar{a}_3^{(1)}]^2. \tag{36b}$$

The coefficients to order $\Omega^{-3/2}$ can be obtained from Eq. (28) and read

$$\bar{a}_3^{(3)} = \frac{1}{6}(b+1)\varsigma \left[2(b+1)^2\varsigma^2 + 3b(2b+3)\varsigma + 6b(b+1) + 3\varsigma + 1\right],$$

$$\bar{a}_5^{(3)} = \frac{\bar{a}_3^{(1)}}{20}\left[1 + 12b(b+1) + 12(b+1)^2\varsigma^2 + 12(b+1)(2b+1)\varsigma\right],$$

$$\bar{a}_7^{(3)} = \bar{a}_3^{(1)}\bar{a}_4^{(2)}, \quad \bar{a}_9^{(3)} = \frac{1}{6}[\bar{a}_3^{(1)}]^3. \tag{36c}$$

The analytical form of these coefficients represents a particularly simple way of solving the CME. The approximation resulting from using these in Eq. (28a) is shown in Fig. 2b (dot-dashed blue line). This approximation captures much better the true distribution obtained from exact stochastic simulation using the SSA (shaded gray area) than the linear noise approximation (dashed red line). We found that including higher order terms in Eq. (28) helped to improve the agreement. However, the resulting expressions turn out to be more elaborate and are hence omitted. A quantitative assessment of this agreement will be given in Sect. 5.3.

5.2 Example 2: Cooperative Self-Activation of Gene Expression

As a second application of our methods we consider the regulatory dynamics of a single gene inducing its own, leaky expression. We therefore consider the case where gene activation occurs by binding of its own protein P to two independent sites
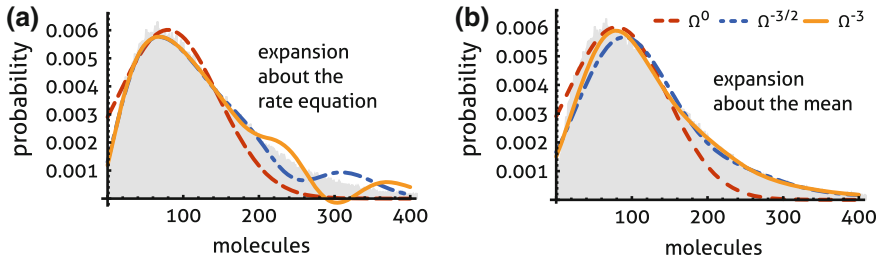
Fig. 2 Bursty protein production: system size expansion solution. **a** We compare the solution obtained using the system size expansion about the rate equation solution, Eq. (26a), that is truncated after Ω^0 (*dashed red*), $\Omega^{-3/2}$ (*dot-dashed blue*) and Ω^{-3}-terms (*solid yellow line*) to stochastic simulations (*shaded gray area*). We observe that the series yields large undulations and negative probabilities. **b** The system size expansion about the mean is shown when the series in Eq. (28a) truncated after Ω^0 (*dashed red*), $\Omega^{-3/2}$ (*dot-dashed blue*) and Ω^{-3}-terms (*solid yellow line*). We find that these approximations avoid undulations and converge rapidly with increasing truncation order to the distributions obtained from simulations using the SSA

$$G + P \underset{k_{-1}}{\overset{k_1}{\rightleftharpoons}} G^*,$$

$$G^* + P \underset{k_{-2}}{\overset{k_2}{\rightleftharpoons}} G^{**}, \tag{37}$$

which is modeled explicitly using mass action kinetics. In effect, there are three gene states with increasing transcriptional activity, G, G^* and G^{**}, corresponding to zero, one or two activators bound and leading to a cooperative form of activation. Translation of a transcript denoted by M therefore must occur via one of the following reactions

$$G \xrightarrow{k_G} G + M,$$

$$G^* \xrightarrow{k_{G^*}} G^* + M,$$

$$G^{**} \xrightarrow{k_{G^{**}}} G^{**} + M, \tag{38}$$
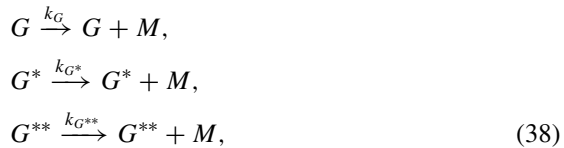
where k_G denotes the basal transcription rate, k_{G^*} the transcription rate of the semi-induced state G^*, and $k_{G^{**}}$ the rate of the fully induced gene. Finally, by the standard model of translation and neglecting active degradation we have

$$M \xrightarrow{k_3} M + P,$$

$$M \xrightarrow{k_4} \varnothing, \quad P \xrightarrow{k_5} \varnothing, \tag{39}$$

In the following two parameter sets listed in Table 1 leading to moderate and low protein numbers are considered. As we shall see the protein distributions are multi-modal in both cases representing ideal test cases for the distribution reconstruction using conditional moment closures and the conditional system size expansion.

Table 1 The two parameter sets used to study the multimodal expression of a self-activating gene described by the reactions (37)–(39). Set (A) leads moderate protein levels while set (B) yields low protein levels. Note that we have set $\Omega = 1$

Parameter	k_1	k_{-1}	k_2	k_{-2}	k_G	k_{G^*}	$k_{G^{**}}$	k_3	k_4	k_5
Set (A)	5×10^{-4}	3×10^{-3}	5×10^{-4}	2.5×10^{-2}	4	12	24	1200	300	1
Set (B)	5×10^{-4}	2×10^{-4}	5×10^{-4}	2×10^{-3}	4	60	160	30	300	1

5.2.1 Method of Conditional Moments and Maximum Entropy Reconstruction

We compare the distribution reconstruction using an approximation of the first 3, 5, and 7 moments of all the species obtained by the MCM (see Sect. 3). As for the previous case study, the values of the moments of P are used to reconstruct the corresponding marginal distribution. However, here we use the conditional moments $E\left(X^k|G = 1\right)$, $E\left(X^k|G^* = 1\right)$, $E\left(X^k|G^{**} = 1\right)$ instead. We construct the function $\tilde{q}(x)$ that approximates the distribution of P by applying the law of total probability

$$\tilde{q}(x) = \sum_{S \in \{G, G^*, G^{**}\}} P\left(S = 1\right) \tilde{q}(x|S = 1). \tag{40}$$

The results of the approximation are plotted in Fig. 3. As we can see, the multimodality of the distribution is captured pretty well, and the quality of the reconstructed distribution is quite good in particular when using 7 moments.
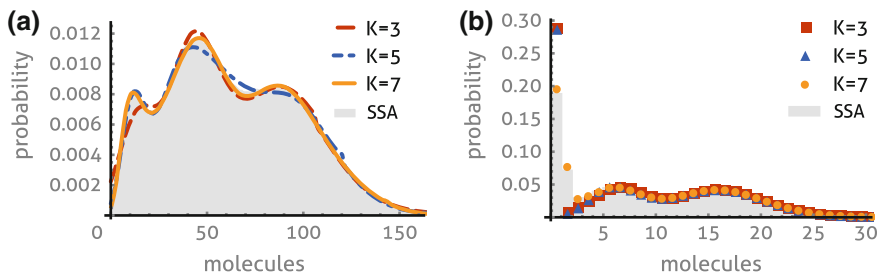

Fig. 3 Self-activating gene: reconstruction based on MCM. The reconstructed distribution (cf. Eq. (40)) for the case of moderate (**a**) and slow (**b**) protein production is compared to the distribution estimated with stochastic simulations (*shaded gray area*), where we use $K = 3$, $K = 5$, and $K = 7$ for the conditional moments in the maximum entropy method. Again we find a significant improvement if moments of higher order are taken into account, in particular in those regions where the shape of the distribution is complex such as the region for 0–5 proteins in case of (**b**)

5.2.2 Conditional System Size Expansion

An alternative technique to approximate distributions for gene regulatory networks with multiple gene states has been given by Thomas et al. [22]. The method makes use of timescale separation by grouping reactions into reactions that change the gene state and reactions that affect only the protein distributions. Based on a conditional variant of the linear noise approximation it was shown that when the gene transitions are slow, protein distributions are well approximated by Gaussian mixture distributions. Implicit in this approach was, of course, that the protein numbers are sufficiently large to justify an application of an linear noise approximation. We will here extend this framework considering higher order terms in the system size expansion to account for low number of protein molecules.

To this end, we describe by the vector $\mathbf{G}$ one of the three gene states $G = (1, 0, 0)$, $G^* = (0, 1, 0)$, and $G^{**} = (0, 0, 1)$ and by x the number of proteins. We will assume that gene transitions between these states evolve slowly on a timescale $1/\mu$. Rescaling time via $\tau = t/\mu$, the CME on the slow timescale reads

$$\frac{d\Pi(\mathbf{G}, x, \tau)}{d\tau} = \mu \mathcal{W}_0(\mathbf{G})\Pi(\mathbf{G}, x, \tau) + \mathcal{W}_1 \Pi(\mathbf{G}, x, \tau), \tag{41}$$

where $\mathcal{W}_0(\mathbf{G})$ describes the reactions (38) and (39) in the burst approximation

$$\mathcal{W}_0(\mathbf{G}) = \sum_{z=0}^{\infty} (E_x^{-z} - 1) \mathbf{k} \cdot \mathbf{G}\, \varphi(z) + (E_x^{+1} - 1)k_4 x, \tag{42}$$

where $\mathbf{k} = (k_G, k_{G^*}, k_{G^{**}})$ and $\mathcal{W}_1$ denotes the transition matrix of the slow gene binding kinetics given by the reactions (37). Note that as before $\varphi(z)$ is the geometric distribution with mean $b = k_3/k_4$. Using the definition of conditional probability, we can write $\Pi(\mathbf{G}, x, \tau) = \Pi(x | \mathbf{G}, \tau)\Pi(\mathbf{G}, \tau)$ which transforms Eq. (41) into

$$\frac{d\Pi(x|\mathbf{G}, \tau)}{d\tau}\Pi(\mathbf{G}, \tau) + \Pi(x|\mathbf{G}, \tau)\frac{d\Pi(\mathbf{G}, \tau)}{d\tau}$$
$$= \mu\,\Pi(\mathbf{G}, \tau)\,\mathcal{W}_0(\mathbf{G})\Pi(x|\mathbf{G}, \tau) + \mathcal{W}_1\Pi(x|\mathbf{G}, \tau)\Pi(\mathbf{G}, \tau). \tag{43}$$

Marginalizing the above equation we find

$$\frac{d\Pi(\mathbf{G}, \tau)}{d\tau} = \left(\sum_{x=0}^{\infty} \mathcal{W}_1\,\Pi(x|\mathbf{G})\right)\Pi(\mathbf{G}, \tau), \tag{44}$$

where the term in brackets is a conditional average of the slow dynamics over the protein concentrations. In steady state conditions the above is equal to the equations $0 = \Pi(G)[P|G] - \Pi(G^*)K_1$, $0 = \Pi(G^*)[P|G^*] - K_2\Pi(G^{**})$ and $\Pi(G^{**}) = 1 - \Pi(G) - \Pi(G^*)$ by conservation of probability. Here $[P|G]$ denotes the conditional protein concentration that remains to be obtained from $\Pi(x|\mathbf{G})$. The steady

state solution can be found analytically

$$\Pi(G) = \frac{K_1 K_2}{K_1 K_2 + K_2 [P|G] + [P|G][P|G^*]},$$

$$\Pi(G^*) = \frac{K_2 [P|G]}{K_1 K_2 + K_2 [P|G] + [P|G][P|G^*]},$$

$$\Pi(G^{**}) = \frac{[P|G][P|G^*]}{K_1 K_2 + K_2 [P|G] + [P|G][P|G^*]}, \qquad (45)$$

where $K_1 = \frac{k_{-1}}{k_1}$ and $K_2 = \frac{k_{-2}}{k_2}$ are the respective association constants of the DNA-protein binding. The protein distribution is then given by a weighted sum of the probability that a product is found given a particular gene state, times the probability of the gene being in that state:

$$\Pi(x) = \sum_{\mathbf{G}} \Pi(x|\mathbf{G})\Pi(\mathbf{G}). \qquad (46)$$

It is however difficult to obtain $\Pi(x|\mathbf{G})$ analytically, we will therefore employ the limit of slow gene transitions ($\mu \to \infty$) in Eq. (43) to obtain

$$\mathcal{W}_0(\mathbf{G})\,\Pi_\infty(x|\mathbf{G}) = 0, \qquad (47)$$

where $\Pi_\infty(x|\mathbf{G}) = \lim_{\mu \to \infty} \Pi(x|\mathbf{G}, \tau)$. We can now perform the system size expansion for the conditional distribution $\Pi_\infty(x|\mathbf{G})$ that is determined by Eq. (47) using the ansatz

$$\frac{x}{\Omega}\Big|\mathbf{G} = [P|\mathbf{G}] + \Omega^{-1/2}\varepsilon|\mathbf{G}, \qquad (48)$$

for the conditional random variables describing the protein fluctuations. The coefficients in the expansion of the CME (47) are

$$\mathcal{D}_n^m = \delta_{m,0}\left(\mathbf{k}' \cdot \mathbf{G}\,\langle z^n \rangle_\varphi + (-1)^n k_1 [P|\mathbf{G}]\right) + \delta_{m,1}(-1)^n k_1, \qquad (49)$$

with $\mathbf{k}' = \mathbf{k}/\Omega$ and $\mathcal{D}_{n,s}^m = 0$ for $s > 0$. The solution of the rate equation and the conditional linear noise approximation are given by

$$[P|\mathbf{G}] = \mathbf{k}' \cdot \mathbf{G}\,\frac{b}{k_5}, \quad \sigma_{P|\mathbf{G}}^2 = [P|\mathbf{G}](1 + b), \qquad (50)$$

respectively. Note that there are no further corrections in Ω to this conditional linear noise approximation because the conditional CME (47) depends only linearly on the protein variables. The conditional distribution can now be obtained using the result (26a). Associating with $\pi_0(\varepsilon|\mathbf{G})$ a centered Gaussian of variance as given in Eq. (50), we find to order Ω^{-1},

$$\Pi_\infty(\varepsilon|\mathbf{G}) = \pi_0(\varepsilon|\mathbf{G})\Big[1 + \Omega^{-1/2}a_3^{(1)}(\mathbf{G})\psi_{3,\mathbf{G}}(\varepsilon)$$

$$+ \Omega^{-1}a_4^{(2)}(\mathbf{G})\psi_{4,\mathbf{G}}(\varepsilon) + \Omega^{-1}a_6^{(2)}(\mathbf{G})\psi_{6,\mathbf{G}}(\varepsilon)\Big] + O(\Omega^{-3/2}).$$

(51a)

By the definition given before Eq. (26a) the polynomials $\psi_{m,\mathbf{G}}(\varepsilon)$ depend on the gene state via the conditional variance Eq. (50). The coefficients obtained from Eq. (31) take the particularly simple form

$$a_3^{(1)}(\mathbf{G}) = \frac{1}{6}\left(2b^2 + 3b + 1\right)[P|\mathbf{G}], \tag{51b}$$

$$a_4^{(2)}(\mathbf{G}) = \frac{1}{24}(b+1)\left(6b^2 + 6b + 1\right)[P|\mathbf{G}], \qquad a_6^{(2)}(\mathbf{G}) = \frac{1}{2}\left[a_3^{(1)}(\mathbf{G})\right]^2. \tag{51c}$$

Finally, we remark that $\Pi(x|\mathbf{G})$ and $\Pi(\varepsilon|\mathbf{G})$ are related by $\Pi(x|\mathbf{G}) = \Omega^{-1/2}\Pi(\varepsilon = \Omega^{-1/2}x - \Omega^{1/2}[P|\mathbf{G}]|\mathbf{G})$.

In Fig. 4a, this conditional system size expansion is compared to stochastic simulations using the SSA. We find that the conditional linear noise approximation, Eq. (51), truncated after Ω^0 captures well the multimodal character of the distributions but misses to predict the precise location of its modes. In contrast, the conditional approximation of Eq. (51) taking into account up to Ω^{-1} terms accurately describes the location of these distribution maxima. We note however that a continuous approximation such as Eq. (51a) may fail in situations when the effective support of the conditional distributions represents the range of a few molecules. Such case is depicted in Fig. 4b. In this case the distributions are captured better by an approximation with discrete support as has been given in Ref. [20], Eqs. (35) and (36) therein. The resulting approximation, (blue filled circles) using the analytical form of the coefficients (51) is in excellent agreement with stochastic simulations performed using the SSA (shaded gray area). These findings highlight clearly the need to go beyond the conditional Gaussian approximation for the two cases studied here.

5.3 Comparison of Numerical Results

In order to compare both methods quantitatively, we calculated absolute $|\Pi(x) - \Pi^*(x)|$ and relative errors $|\Pi(x) - \Pi^*(x)|/\Pi(x)$ between the exact distribution $\Pi(x)$, which was estimated from simulations via the SSA, and the distribution approximation obtained either via the MM or via the SSE denoted by $\Pi^*(x)$. The results for the first case study are shown in Fig. 5. We observe that the maximum absolute and relative errors occur close to the boundary of zero molecules for both approximation methods. However, the SSE is more accurate than MM here. In this
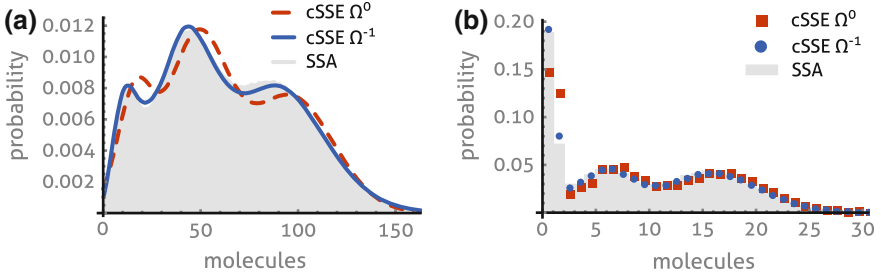
Fig. 4 Self-activating gene: conditional system size expansion. The conditional system size expansion (cSSE), Eqs. (45), (46) and (51), for the moderate (**a**) and slow (**b**) protein production is compared to stochastic simulations (SSA). While the conditional linear noise approximation (Ω^0) captures the multimodal character of the distribution, it misses the precise location of its modes. We find that the Ω^{-1}-estimate of the cSSE given by Eq. (51) agrees much better with the SSA. **b** The discrete approximation of Ref. [20], see main text for details, is shown when truncated after Ω^0 and Ω^{-1} terms. The analytical form of the coefficients in Eq. (51) has been used with parameter set B in Table 1
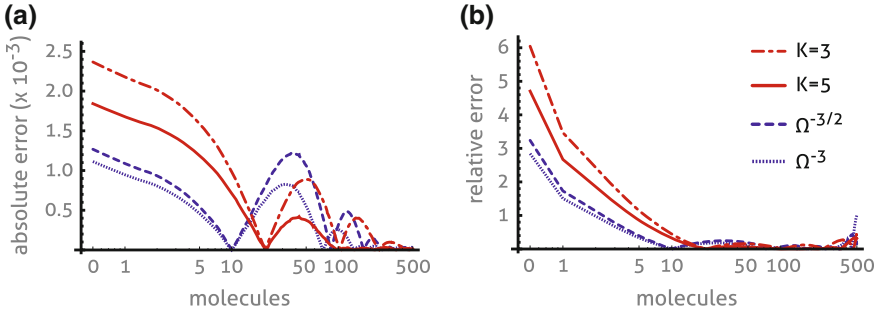
Fig. 5 Bursty protein production: absolute and relative error. We plot the absolute (**a**) and relative (**b**) errors of the MM (for moments up to order $K = 3$ and $K = 5$, Fig. 1) and the SSE (truncated after $\Omega^{-3/2}$ and Ω^{-3} terms, Fig. 2). The SSE for this example yields the percentage error $||\varepsilon||_V$ to be 5.1% ($\Omega^{-3/2}$) and 2.8% (Ω^{-3}) while the moment based approach yields 5.6% ($K = 3$) and 2.0% ($K = 5$). Both approaches become more accurate as more moments or higher order terms in the SSE are taken into account. For both methods, the maximum errors occurs at zero molecules

region a direct representation of the probabilities (as in the hybrid approaches) may be more appropriate. For measuring the overall agreement of the distributions we computed the percentage statistical distance

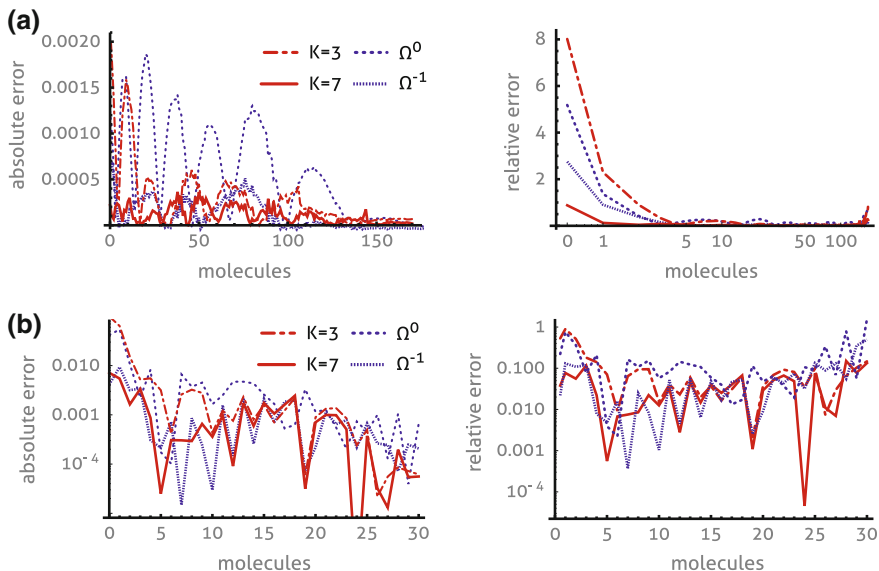$$||\varepsilon||_V = \frac{100\%}{2} \sum_{x=0}^{\infty} |\Pi(x) - \Pi^*(x)|. \tag{52}$$

Fig. 6 Self-activating gene: absolute and relative error. We plot the absolute (*left*) and relative (*right*) errors of the MCM (for moments up to order $K = 3$ and $K = 7$) and the cSSE (truncated after Ω^0 and Ω^{-1} terms). For moderate protein production (**a**), corresponding to the distributions shown in Figs. 3a and 4a, the MCM yields a percentage error $||\varepsilon||_V$ of 2.4% ($K = 3$) and 1.0% ($K = 7$) while the cSSE yields 5.4% (Ω^0) and 1.4% (Ω^{-1}), respectively. For slow protein production (**b**), corresponding to the distributions shown in Figs. 3b and 4b, we find $||\varepsilon||_V = 10.9\%$ ($K = 3$) and 1.7% ($K = 7$) for the MCM as well as $||\varepsilon||_V = 8.3\%$ (Ω^0) and 1.9% (Ω^{-1}) for the cSSE, respectively

This distance can also be interpreted as the maximum percentage difference between the probabilities of all possible events assigned by the two distributions [47, 48] and achieves its maximum (100% error) when the distributions do not overlap. The numerical values given in the caption of Fig. 5 reveal that the estimation errors of the MM and the SSE decrease as more moments or higher order terms in the SSE are taken into account. The respective error estimates are of the same order of magnitude. However, the analytical solution obtained using the SSE, given in Sect. 5.1.2 including only low order terms is slightly more accurate than the MM with only few moments, while the MM with a larger number of moments becomes more accurate than the SSE including up to Ω^{-3}-terms.

For the second case study, we find that the absolute and relative estimation errors of the method of moments and the SSE are of the same order of magnitude, compare Fig. 6. However, we found that the method of moments including three conditional moments ($K = 3$) is overall more accurate than the conditional linear noise approximation (Ω^0). The approximations become comparable as higher order conditional moments and higher orders in conditional SSE are employed. However, the method

of moments including 7 conditional moments turned out to be slightly more accurate than the analytical SSE solution to order Ω^{-1} given in Sect. 5.2.2.

6 Discussion

We have here studied the accuracy of two recently proposed approximations for the probability distribution of the CME. The method of moments utilizes moment closure to approximate the first few moments of the CME from which the distribution is reconstructed via the maximum entropy principle. In contrast, the SSE method does not rely on a moment approximation but instead the probability distribution is obtained analytically as a series in a large parameter that corresponds roughly to the number of molecules involved in the reactions. Interestingly, our comparative study revealed that both methods yield comparable results. While generally both methods provide highly accurate approximations for the distribution tails and capture well the overall shape of the distributions, we found that for both methods the largest errors occur close to the boundary of zero molecules. We observed a similar behavior when conditional moments or the conditional SSE were used. These discrepancies could be resolved by taking into account higher order moment closure schemes or, equivalently, by taking into account higher order terms in the expansion of the probability distribution.

From a computational point of view, the method based on moment closure is limited by the number of moments that can be numerically integrated due to the stiffness of the resulting high-dimensional ODE system. Our investigation showed that such difficulties are encountered when one closes the moment equations beyond the 8th moment. In contrast, the analytical solution provided by the SSE technique does not suffer from these issues because it is provided in closed form. We note however that the SSE solution given here is limited to a single species while the method of moments has no such limitation. Moreover, the conditional SSE solution relies on timescale separation which the method of conditional moments does not assume.

The computational cost of the analytical approximation provided by the SSE is generally less than that of the moment based approach because it avoids numerical integration and optimization. This fact may be particularly advantageous when wide ranges of parameters are to be studied, as for instance in parameter estimation from experimental data. We note, however, that the moment-based approach is still much faster than the one of the SSA because it avoids large amounts of ensemble averaging. Therefore the moment based approach may be preferable in situations where the SSE cannot be applied as we have mentioned above. We hence conclude that both approximation schemes provide complementary strategies for the analysis of stochastic behavior of biological systems. Most importantly, they both provide computationally more efficient strategies compared with simulation and numerical integration of the CME while preserving an high degree of accuracy. The methods thus have an high potential for the analysis of large-scale models.

References

1. H. H. McAdams and A. Arkin.: "Stochastic mechanisms in gene expression". Proc Natl Acad Sci 94.3 (1997), pp. 814–819.
2. P. S. Swain, M. B. Elowitz, and E. D. Siggia.: "Intrinsic and extrinsic contributions to stochasticity in gene expression". Proc Natl Acad Sci 99.20 (2002), pp. 12795–12800.
3. T. J. Perkins and P. S. Swain.: "Strategies for cellular decision-making". Mol Syst Biol 5 (2009).
4. M. B. Elowitz et al.: "Stochastic gene expression in a single cell". Sci Signal 297.5584 (2002), p. 1183.
5. D. Wilkinson.: Stochastic Modelling for Systems Biology. Chapman & Hall, 2006.
6. D. T. Gillespie.: "Exact stochastic simulation of coupled chemical reactions". J Phys Chem 81.25 (1977), pp. 2340–2361.
7. N. Maheshri and E. K. O'Shea.: "Living with noisy genes: how cells function reliably with inherent variability in gene expression". Annu Rev Biophys Biomol Struct 36 (2007), pp. 413–434.
8. B. Munsky and M. Khammash.: "The finite state projection algorithm for the solution of the chemical master equation". J Chem Phys 124.4 (2006), p. 044104.
9. M. Mateescu et al.: "Fast Adaptive Uniformisation of the Chemical Master Equation". IET Syst Biol 4.6 (2010), pp. 441–452.
10. D. T. Gillespie.: "Stochastic simulation of chemical kinetics". Annu Rev Phys Chem 58 (2007), pp. 35–55.
11. J. Elf and M. Ehrenberg.: "Fast evaluation of fluctuations in biochemical networks with the linear noise approximation". Genome Res 13.11 (2003), pp. 2475–2484.
12. R Grima. "An effective rate equation approach to reaction kinetics in small volumes: Theory and application to biochemical reactions in nonequilibrium steady-state conditions". J Chem Phys 133.3 (2010), p. 035101.
13. P. Thomas, H. Matuschek, and R. Grima.: "How reliable is the linear noise approximation of gene regulatory networks?" BMC Genomics 14. Suppl 4 (2013), S5.
14. S. Engblom.: "Computing the moments of high dimensional solutions of the master equation". Appl Math Comput 180 (2 2006), pp. 498 -515.
15. C. Gillespie. "Moment-closure approximations for mass-action models". IET Syst Biol 3.1 (2009), pp. 52–58.
16. A. Ale, P. Kirk, and M. P. H. Stumpf.: "A general moment expansion method for stochastic kinetic models". J Chem Phys 138.17 (2013), p. 174101.
17. A. Andreychenko, L. Mikeev, and V.Wolf.: "Model Reconstruction for Moment-Based Stochastic Chemical Kinetics". ACM Trans Model Comput Simul 25.2 (2015), 12:1–12:19.
18. A. Andreychenko, L. Mikeev, and V. Wolf.: "Reconstruction of Multimodal Distributions for Hybrid Moment-based Chemical Kinetics". To appear in Journal of Coupled Systems and Multiscale Dynamics (2015).
19. N. G. Van Kampen.: Stochastic Processes in Physics and Chemistry. Third. Amsterdam: Elsevier, Amsterdam, 1997.
20. P. Thomas and R. Grima. : "Approximate probability distributions of the master equation". Phys Rev E 92.1 (2015), p. 012120.
21. L. Bortolussi.: "Hybrid Behaviour of Markov Population Models". Information and Computation (2015 (accepted)).
22. P. Thomas, N. Popović, and R. Grima.: "Phenotypic switching in gene regulatory networks". Proc Natl Acad Sci 111.19 (2014), pp. 6994–6999.

23. D. T. Gillespie: "A diffusional bimolecular propensity function". J Chem Phys 131.16 (2009), p. 164109.

24. P. Thomas, H. Matuschek, and R. Grima.: "Computation of biochemical pathway fluctuations beyond the linear noise approximation using iNA". Bioinformatics and Biomedicine (BIBM), 2012 IEEE International Conference on. IEEE. 2012, pp. 1–5.

25. P. Whittle.: "On the Use of the Normal Approximation in the Treatment of Stochastic Processes". J R Stat Soc Series B Stat Methodol 19.2 (1957), pp. 268–281.

26. J. H. Matis and T. R. Kiffe.: "On interacting bee/mite populations: a stochastic model with analysis using cumulant truncation". Environ Ecol Stat 9.3 (2002), pp. 237–258.

27. I. Krishnarajah et al.: "Novel moment closure approximations in stochastic epidemics". Bull Math Biol 67.4 (2005), pp. 855–873.

28. A. Singh and J. P. Hespanha.: "Lognormal moment closures for biochemical reactions". Decision and Control, 2006 45th IEEE Conference on. IEEE. 2006, pp. 2063–2068.

29. A. Singh and J. P. Hespanha.: "Approximate moment dynamics for chemically reacting systems". Automatic Control, IEEE Transactions on 56.2 (2011), pp. 414–418.

30. D. Schnoerr, G. Sanguinetti, and R. Grima.: "Comparison of different momentclosure approximations for stochastic chemical kinetics". J Chem Phys 143.18 (2015), p. 185101.

31. D. Schnoerr, G. Sanguinetti, and R. Grima.: "Validity conditions for moment closure approximations in stochastic chemical kinetics". J Chem Phys 141.8 (2014), p. 084103.

32. R. Grima.: "A study of the accuracy of moment-closure approximations for stochastic chemical kinetics". J Chem Phys 136.15 (2012), p. 154105.

33. J. Hasenauer et al.: "Method of conditional moments for the Chemical Master Equation". J Math Biol (2013), pp. 1–49.

34. M. Lapin, L. Mikeev, and V. Wolf.: "SHAVE - Stochastic Hybrid Analysis of Markov Population Models". Proceedings of the 14th International Conference on Hybrid Systems: Computation and Control (HSCC'11). ACM International Conference Proceeding Series. 2011.

35. A.L. Berger, V.J.D. Pietra, S.A.D. Pietra, A Maximum Entropy Approach to Natural Language Processing. Comput Ling **22**(1), 39–71 (1996)

36. R. Abramov.: "The multidimensional maximum entropy moment problem: a review of numerical methods". Commun Math Sci 8.2 (2010), pp. 377–392.

37. Z. Wu et al.: "A fast Newton algorithm for entropy maximization in phase determination". SIAM Rev 43.4 (2001), pp. 623–642.

38. L. R. Mead and N. Papanicolaou: "Maximum entropy in the problem of moments". J Math Phys 25 (1984), p. 2404.

39. G. W. Alldredge et al.: "Adaptive change of basis in entropy-based moment closures for linear kinetic equations". J Comput Phys 258 (2014), pp. 489–508.

40. Á . Tari, M. Telek, and P. Buchholz.: "A unified approach to the moments based distribution estimation-unbounded support". Formal Techniques for Computer Systems and Business Processes. Springer, 2005, pp. 79–93.

41. J. Elf et al.: "Mesoscopic kinetics and its applications in protein synthesis". Systems Biology. Springer, 2005, pp. 95–18.

42. L. Comtet.: Advanced Combinatorics: The art of finite and infinite expansions. Springer Science & Business Media, 1974.

43. E. Giampieri et al.: "Active Degradation Explains the Distribution of Nuclear Proteins during Cellular Senescence". PloS one 10.6 (2015), e0118442.

44. V. Shahrezaei and P. S. Swain.: "Analytical distributions for stochastic gene expression". Proc Natl Acad Sci 105.45 (2008), pp. 17256–17261.

45. P. Thomas, A. V. Straube, and R. Grima.: "Communication: Limitations of the stochastic quasi-steady-state approximation in open biochemical reaction networks". J Chem Phys **135**(18), 181103 (2011)

46. K. R. Sanft, D. T. Gillespie, and L. R. Petzold.: "Legitimacy of the stochastic Michaelis-Menten approximation". Syst Biol, IET 5.1 (2011), pp. 58–69.

47. D. A. Levin, Y. Peres, and E. L. Wilmer.: Markov chains and mixing times. American Mathematical Soc., 2009.

48. T. M. Cover and J. A. Thomas.: Elements of information theory. John Wiley & Sons, 2012.

Sampling from T Cell Receptor Repertoires

Marco Ferrarini, Carmen Molina-París and Grant Lythe

Abstract   Modern single-cell sequencing techniques allow the unique T cell receptor (TCR) signature of each of a sample of hundreds of T cells to be read. The mathematical challenge is to extrapolate from the properties of a sample to those of the whole repertoire of an individual, made up of many millions of T cells. We consider the distribution of the number of repeats of any TCR in a sample, the mean number of cells needed to find a repeat with probability one half, and the relationship between the true distribution of clonal sizes and that experimentally observed in a sample. In the simplest hypothesis for the structure of the repertoire, the same number of cells make up each clonotype. We also consider the case where the distribution of clonal sizes is geometric, and examples where a small fraction of clones in the repertoire are expanded.

1   Introduction

Approximately 4×10^{11} T cells circulate in the adult human body [1]. About 30,000 T cell receptors (TCRs) are on the surface of each T cell, usually of only one specificity [2]. T cells are selected in the thymus by binding to self-peptides expressed in association with major histocompatibility complex molecules (self-pMHC) [1, 3–5]. The set of cells with the same TCR defines a T cell clonotype, and the set of T cells in the body can be thought of as a repertoire of clonotypes. CD8$^+$ T cells recognise peptide bound to MHC class I molecules and CD4$^+$ T cells recognise peptide bound to MHC class II molecules [2]. How many TCR clonotypes are there in humans, mice and other mammals? [6–10]. Direct measurement is not possible even with the latest

M. Ferrarini (✉) · C. Molina-París (✉) · G. Lythe (✉)
Department of Applied Mathematics, School of Mathematics, University of Leeds,
Leeds LS2 9JT, UK
e-mail: mmmf@leeds.ac.uk

C. Molina-París
e-mail: carmen@maths.leeds.ac.uk

G. Lythe
e-mail: grant@maths.leeds.ac.uk

developments in sequencing techniques. Estimates of the number of different TCRs that could, in principle, be produced by VDJ gene rearrangement in the thymus, are about 10^{15} [11–14]. However, the human body cannot contain even one T cell of 10^{15} possible types: 10^{15} T cells would weigh about 500 kg [15].

The number of distinct TCR clonotypes, N, is equal to the total number of T cells divided by the mean number of cells per clonotype. Equivalently, N is equal to the product of the rate of release of new clonotypes from the thymus to the periphery and the mean lifetime of a clonotype in the periphery [16]. Lower limits on the number of distinct TCR β chains in the repertoire are about 4×10^6 [17–20]. If each TCR β chain combines with 25 α chains, then the number of distinct clonotypes in one human is at least 10^8 [21].

Direct estimates of β chain diversity have been made by PCR amplification of mRNA from pools of cells, but the technique is less suitable for measuring distributions of clonal sizes because numbers of mRNA vary from cell to cell and PCR amplification may depend on the TCR. Single-cell measurements, where PCR and sequencing are performed on one cell at a time, avoid biases. However, their expense means that only hundreds of cells are usually sequenced from a single mammal, and estimates of diversity must therefore rely on mathematical extrapolation from small samples [19, 22–24].

In our analysis, we use the geometric distribution as a basic model for the distribution of clonal sizes in the repertoire. The mean number of cells per clonotype, in the repertoire, is the total number of cells in the repertoire divided by the number of clonotypes. We find, using probability generating functions, the distribution of number of copies of cells of each clone that are found in a sample of cells taken at random from the repertoire. When the sample is small, most clonotypes are not present at all in the sample, and the majority of clonotypes that are in the sample are only present as one copy. We show that the observed distribution of clonal sizes, which is the distribution of sequences seen once, twice, three times, . . . in the sample, also has a geometric distribution, and calculate the corresponding mean value.

1.1   Sampling from a Repertoire

What can be deduced from a sample of m cells taken from a repertoire of T cells if the total number of cells in the repertoire, S, is very large? Let us begin by describing the structure of the repertoire, which is divided into N subsets, called TCR clonotypes. Denote by n_i the number of cells of a clonotype labelled i. The index i runs from 1 to N, and $\sum_i n_i = S$ (see Fig. 1). Typically S is known, but N and n_i with $1 \leq i \leq N$, are not.

When the number of cells in the sample, m, is much smaller than the number of cells in the repertoire, S, and much smaller even than the number of TCR clonotypes, N, it is not obvious how to draw direct conclusions. On the other hand, some mathematical simplifications can be made. Let us consider one TCR clonotype, with
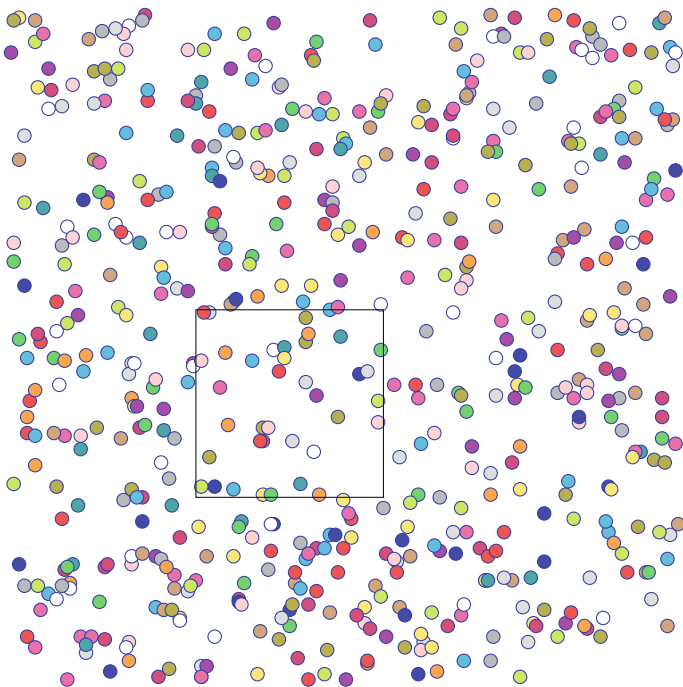
Fig. 1 The repertoire contains S cells, divided up into N TCR clonotypes. Here, cells are represented by *circles*, a TCR clonotype is the set of cells of one shade, and a random sample of cells is represented by those inside the *black square*

label i and $1 \le i \le N$. If $m\, n_i \ll S$ then, instead of the full expressions involving multinomial distributions, we can use the following approximations:

1. the probability that none of the m cells in the sample are of clonotype i is $\left(1 - \frac{n_i}{S}\right)^m$,
2. the probability that exactly one of the m cells in the sample is of clonotype i is $m\, \frac{n_i}{S} \left(1 - \frac{n_i}{S}\right)^{m-1}$, and
3. the probability that exactly two of the m cells in the sample are of clonotype i is $\frac{1}{2}\, m\, (m-1)\, \frac{n_i}{S}\, \frac{n_i - 1}{S} \left(1 - \frac{n_i}{S}\right)^{m-2}$.

Denote the number of cells of clonotype i in the sample by Y_i. If $m \gg 1$ but $m\, n_i \ll S$, then $\mathscr{P}\,(Y_i = 2) \simeq r_i$, where

$$r_i = \frac{1}{2} \left(\frac{m}{S}\right)^2 n_i\, (n_i - 1)\ . \tag{1}$$

We say there is a repeat in the sample if two (or more) of the m cells are of the same clonotype. Let us consider a group of M identified clonotypes in the repertoire, with numbers of cells $n_1, n_2, \ldots, n_M$, respectively. How many repeats, of clonotypes in this group, will we see in our sample? If $r_i \ll 1$, $\forall i = 1, \ldots, M$, so that the

occurrences of repeats in distinct clonotypes can be taken as independent events, then

$$\mathbb{E} \text{ (number of repeats of identified clonotypes)} = \sum_{i=1}^{M} r_i = \frac{1}{2} \left(\frac{m}{S} \right)^2 \sum_{i=1}^{M} n_i (n_i - 1) \ .$$

That is,

$$\mathbb{E} \text{ (number of repeats of identified clonotypes)} = \frac{1}{2} \frac{m^2}{S^2} M \, \mathbb{E} \, (n_i(n_i - 1)) \ , \qquad (2)$$

where the expectation is taken over the M clonotypes

$$\mathbb{E} \, (n_i(n_i - 1)) = M^{-1} \sum_{i=1}^{M} n_i \, (n_i - 1) \ .$$

Repertoires can be constructed and sampled inside a simple computer programme, where each clonotype is assigned a label i and values of n_i are assigned according to a probability distribution. We have constructed repertoires with uniform, geometric and double-geometric distributions of clonal sizes to verify the conclusions presented here.

2 Results

2.1 The Mean Number of Repeats

To find the mean number of repeats of *any clonotype* in the sample, we put $M = N$ in (2) and write $S = N \, \mathbb{E} \, (n_i)$, to obtain

$$\mathbb{E} \text{ (number of repeats)} = \sum_{i=1}^{N} r_i = \frac{m^2}{2N} \frac{\mathbb{E} \, (n_i(n_i - 1))}{\mathbb{E} \, (n_i)^2} \ . \qquad (3)$$

The expression (3) is the product of the factor $\frac{m^2}{2N}$, that does not depend on the distribution of clonal sizes, and the factor $\frac{\mathbb{E} \, (n_i(n_i-1))}{\mathbb{E} \, (n_i)^2}$, that does. The latter can be written

$$\frac{\mathbb{E} \, (n_i(n_i - 1))}{\mathbb{E} \, (n_i)^2} = \frac{\mathbb{E} \, (n_i^2)}{\mathbb{E} \, (n_i)^2} - \frac{1}{\mathbb{E} \, (n_i)} \ .$$

- If $n_i = \bar{n}$ for every i then

$$\frac{\mathbb{E} \, (n_i^2)}{\mathbb{E} \, (n_i)^2} = 1 \qquad \text{and} \qquad \frac{\mathbb{E} \, (n_i(n_i - 1))}{\mathbb{E} \, (n_i)^2} = 1 - \frac{1}{\bar{n}} \ .$$

Fig. 2 Mean number of repeats as a function of the number of cells in the sample, from a repertoire of $N = 10^5$ clonotypes and a geometric distribution of clonal sizes, with $\bar{n} = 10$
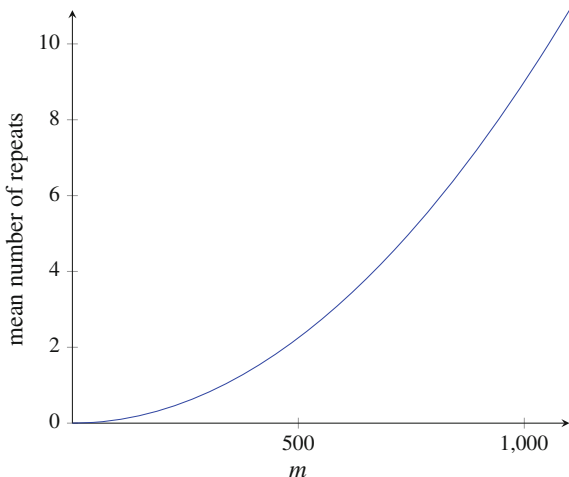
- If n_i has a geometric distribution with mean $\bar{n}$ (that is, $\mathscr{P}(n_i \geq k) = \left(1 - \frac{1}{\bar{n}}\right)^{k-1}$, $k = 1, 2, \ldots$) then

$$\frac{\mathbb{E}(n_i^2)}{\mathbb{E}(n_i)^2} = 2 - \frac{1}{\bar{n}} \qquad \text{and} \qquad \frac{\mathbb{E}(n_i(n_i - 1))}{\mathbb{E}(n_i)^2} = 2\left(1 - \frac{1}{\bar{n}}\right).$$

See Fig. 2.

2.2 Number of Draws to Find the First Repeat

Let us consider the probability of finding no repeats in a sample of m cells. With r_i defined in (1), we approximate by $1 - r_i$ the probability that fewer than two cells of clonotype i are found in the sample, so that

$$\mathscr{P}(\text{no repeat in sample of } m \text{ cells}) = \prod_{i=1}^{N} (1 - r_i).$$

We can then write

$$\log\left(\mathscr{P}(\text{no repeat in a sample of } m \text{ cells})\right) = \sum_{i=1}^{N} \log(1 - r_i)$$

$$\simeq -\sum_{i=1}^{N} r_i$$

assuming $r_i \ll 1$ for every i. Thus, we have

$$\mathscr{P} \text{ (no repeat in sample of } m \text{ cells)} = \exp(-\lambda)$$

where

$$\lambda = \frac{m^2}{2N} \frac{\mathbb{E}\,(n_i(n_i - 1))}{\mathbb{E}\,(n_i)^2} \tag{4}$$

is the mean number of repeats in a sample of m cells.

How many cells do we need to sample in order to have a 50 percent chance of finding a repeat? Let this number be $m_{0.5}$. Then

$$m_{0.5}^2 = \frac{\mathbb{E}\,(n_i)^2}{\mathbb{E}\,(n_i(n_i - 1))}\, 2\,N\,\log 2 \ . \tag{5}$$

In the simplest case, when all clonotypes have the same number of cells, $\bar{n}$, we find $\mathscr{P} \text{ (no repeat in sample of } m \text{ cells)} = \exp\left(-\frac{m^2}{2N}\left(1 - \frac{1}{n}\right)\right)$ and

$$m_{0.5} = \left(\frac{2\,N\,\log 2}{1 - \frac{1}{n}}\right)^{\frac{1}{2}} \ .$$

When the distribution of the number of cells per clonotype is geometric with mean $\bar{n}$, the desired number is

$$m_{0.5} = \left(\frac{N\,\log 2}{1 - \frac{1}{\bar{n}}}\right)^{\frac{1}{2}} \ .$$

See Fig. 3.

2.3 Poisson Distribution of Number of Repeats in a Sample

Let k be the total number of repeats in a sample of m cells. For example, if 96 sequences are found once and 2 sequences are found twice, then $m = 100$ and $k = 2$. We have already seen the case $k = 0$ and analysed $\mathscr{P}\,(k = 0)$. Let us consider the case $k = 1$

$$\mathscr{P}\,(k = 1) = \sum_{i=1}^{N} r_i \prod_{\substack{j=1 \\ j \neq i}}^{N} (1 - r_j) \ .$$

Fig. 3 Mean number of
cells that need to be sampled
in order to have a 50 percent
chance of one repeat, from a
repertoire of N clonotypes
and a geometric distribution
of clonal sizes, with $\bar{n} = 10$
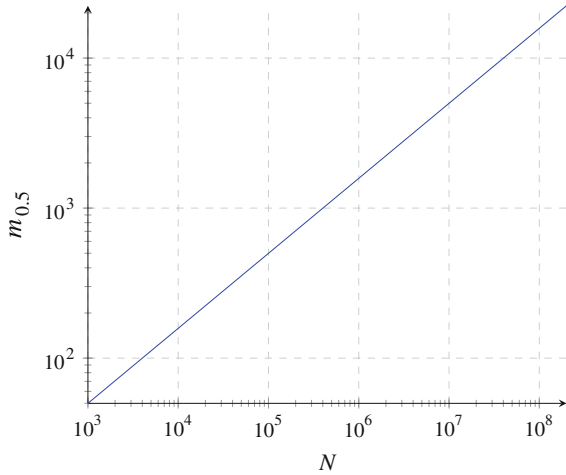
If $r_i \ll 1$ for every i, then $\displaystyle\prod_{\substack{j=1 \\ j \neq i}}^{N}(1 - r_j) \simeq \prod_{i=1}^{N}(1 - r_i)$ and

$$\mathscr{P}(k = 1) = \lambda\, e^{-\lambda}\,.$$

The same argument works for all $k \ll m$, so that the number of repeats in a sample
has a Poisson distribution

$$\mathscr{P}(\text{number of repeats in sample of } m \text{ cells is } k) = \frac{\lambda^k}{k!}\, e^{-\lambda}\,.$$

2.4 Estimating the Size of the Repertoire from One Repeat

Suppose there is one repeat in a sample of m_1 cells. We then use (4) to estimate N.
Putting $\lambda = 1$ and, assuming a geometric distribution of clonal sizes, we conclude
that

$$N = m_1^2 \left(1 - \frac{1}{\bar{n}}\right)\,.$$

If we find one repeat per 100 cells, we estimate the size of the repertoire is 10^4. If we
find one repeat per 1,000 cells, we estimate that the size of the repertoire is 10^6. In
practice, the estimate m_1^2 is likely to be conservative, because any clonal expansion
will increase the number of observed repeats.

2.5   The Observed Distribution of Clonal Sizes

In this section, our goal is to find the probability distribution of the number of instances of k copies of a TCR in a random sample of m cells. First, consider the point of view of one cell in the total of S cells in the repertoire. The probability, which we denote q, that this cell is one of the m cells in the sample is equal to m/S. Next, let us define the Bernoulli random variable B

$$\mathcal{P}\,(B = 0) = 1 - q \ \text{and} \ \mathcal{P}\,(B = 1) = q \,, \qquad \text{where} \quad q = \frac{m}{S} \,. \qquad (6)$$

The probability generating function of B is

$$\phi_B(z) = \sum_{k=0}^{\infty} \mathcal{P}\,(B = k)\, z^k = 1 - q + q\,z \,. \qquad (7)$$

If n_i is the number of cells of a clonotype labelled i, then the number of cells of type i in the sample is the random variable Y_i, which can be written

$$Y_i = B_1 + \cdots + B_{n_i} \,, \qquad (8)$$

where $B_j, j = 1, \ldots, n_i$ are random variables with the same distribution as B. With the approximation that the B_j are **independent** random variables, the probability generating function of Y_i is

$$\phi_{Y_i}(z) = \phi_B(z)^{n_i} = (1 - q + qz)^{n_i} \,. \qquad (9)$$

Let Y be the number of copies of a *randomly chosen clonotype* found in the sample of m cells, which can take the value 0 or any integer greater than 0. That is,

$$\mathcal{P}\,(Y = k) = \sum_{n} \mathcal{P}\,(n_i = n)\mathcal{P}\,(Y_i = k|n_i = n) \,.$$

Suppose that the probability generating function of the random variable n_i is $\phi_n(z)$. Then

$$\phi_Y(z) = \sum_{n} \mathcal{P}\,(n_i = n)(1 - q + qz)^n$$

$$= \phi_n(1 - q + qz) \,.$$

For example, if n_i has a geometric distribution with mean $\bar{n}$, then $\phi_n(z) = \dfrac{z}{\bar{n} - (\bar{n} - 1)z}$, so that

$$\phi_Y(z) = \frac{1 - q + qz}{\bar{n} - (\bar{n} - 1)(1 - q + qz)} = \frac{1 - q + qz}{1 + (\bar{n} - 1)q(1 - z)} . \tag{10}$$

Let us consider the distribution of observed clonal sizes (the histogram that is obtained by plotting the number of TCRs as a function of the number of cells in the sample). Observed clonal sizes can take integer values greater than, but not including, 0. We define $s_1, s_2, \ldots$ by

$$s_k = \frac{\mathscr{P}(Y = k)}{1 - \mathscr{P}(Y = 0)} .$$

That is, the distribution is that of Y, conditioned on not being 0. Then

$$s_k = \frac{\gamma^{k-1}}{1 + (\bar{n} - 1)q} \qquad k \geq 1 , \tag{11}$$

and

$$\gamma = \frac{(\bar{n} - 1)q}{1 + (\bar{n} - 1)q} . \tag{12}$$

Note that $\frac{s_{k+1}}{s_k} = \gamma$. That is, if the distribution of clonal sizes in the repertoire is geometric, with mean $\bar{n}$, then the observed distribution of clonal sizes is also geometric, with mean $1 + (\bar{n} - 1)q$ (see Fig. 4).

2.6 Expansion of a Fraction of the Repertoire

In this Section, we assume that a fraction $f \ll 1$ of clonotypes are "expanded". Even if expanded clonotypes are rare, they will be over-represented in the repeats found in a sample. Let us define a simple repertoire with expanded clonotypes. Let us suppose that the fraction $1 - f$ of clonotypes consist of n cells each, while the remaining fraction f consist of αn cells each, where $\alpha \gg 1$. Then, the probability generating function of the random variable n_i is

$$\phi_{n_i}(z) = (1 - f)\, z^n + f\, z^{\alpha n} . \tag{13}$$

In this case, the probability generating function of the random variable Y, the number of copies of a randomly chosen clonotype found in the sample of m cells, is

$$\phi_Y(z) = \phi_{n_i}(1 - q + qz) = (1 - f)\, (1 - q + qz)^n + f\, (1 - q + qz)^{\alpha n} . \tag{14}$$

If $\alpha \gg 1$, $f \ll 1$ and $\alpha n q \ll 1$, then $\mathscr{P}(Y = 1) \simeq n q + f \alpha n q$ and $\mathscr{P}(Y = 2) = \frac{1}{2} f (\alpha n q)^2$. To give a concrete example, suppose that $n = 2$, $q = 10^{-5}$, $f = 10^{-4}$ and $\alpha = 4 \times 10^3$. Then $(\mathscr{P}(Y = 1) - \mathscr{P}(Y = 2))/\mathscr{P}(Y = 1) =$
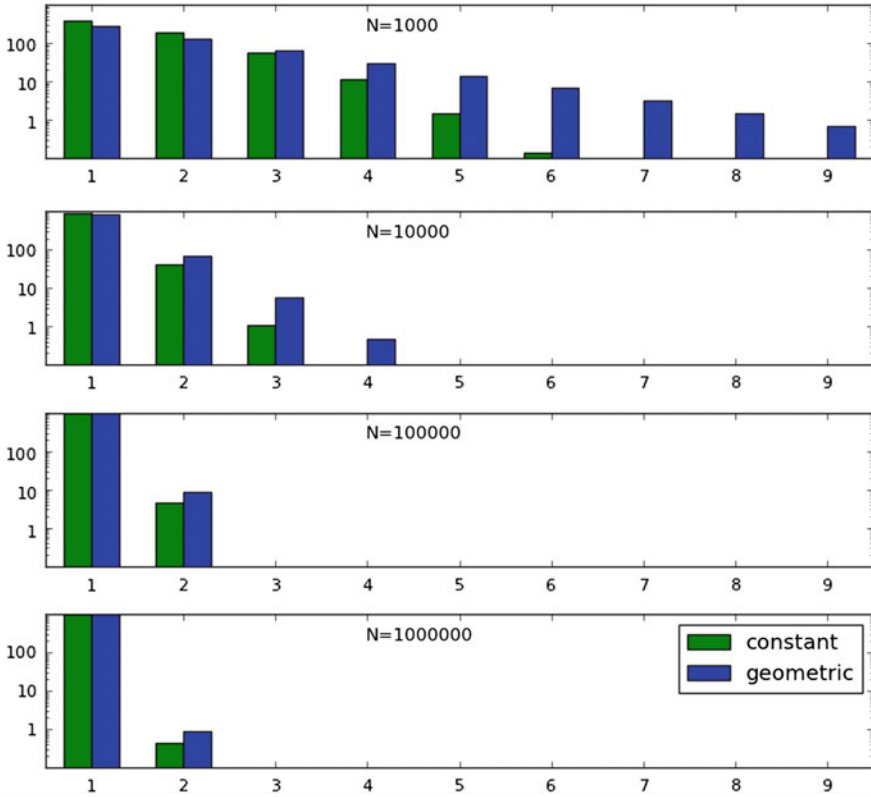
Fig. 4 Observed clonal size distribution in a sample of 1,000 cells, from repertoires containing different numbers of clones, N. A "constant" repertoire means that there are $\bar{n} = 10$ cells of each clonotype. In a "geometric" repertoire, the number of cells in each clonotype is drawn from a geometric distribution with mean $\bar{n} = 10$

0.99, which means that 99% of sequences in a sample of m sequences will be found as a single copy.

Finally, we consider a more realistic case in which the distribution of the number of cells per clonotype is "double geometric". That is, both the unexpanded and expanded clonotypes have clonal sizes that follow a geometric distribution. The mean of n_i for unexpanded clonotypes is $\bar{n}$ and the mean of n_i for expanded clonotypes is $\alpha\bar{n}$. Then, the probability generating function of the random variable Y is

$$\phi_Y(z) = (1-f)\,\psi(1-q+qz,\bar{n}) + f\,\psi(1-q+qz,\alpha\bar{n})\,, \tag{15}$$

where

$$\psi(z,n) = \frac{z}{n-(n-1)\,z}\,. \tag{16}$$

That is,

$$
\mathscr{P}(Y = k) =
\begin{cases}
f \dfrac{1-q}{1+q(\alpha\bar{n}-1)} + (1-f)\dfrac{1-q}{1+q(\bar{n}-1)}, & k = 0 \\[3ex]
f \dfrac{(\alpha\bar{n}-1)^{k-1}\alpha\bar{n}\,q^k}{(1+q(\alpha\bar{n}-1))^{k+1}} + (1-f)\dfrac{(\bar{n}-1)^{k-1}\bar{n}\,q^k}{(1+q(\bar{n}-1))^{k+1}}, & k \geq 1.
\end{cases}
$$

To give a concrete example, similar to that above, suppose that $\bar{n} = 2$, $q = 10^{-5}$, $f = 10^{-4}$ and $\alpha = 4 \times 10^3$. Then 98% of sequences in a sample of m sequences will be found as a single copy.

3 Discussion

Small samples from a large repertoire are obtained in single-cell sequencing experiments of T cell receptors. Estimates of the diversity of the TCR repertoire, that can be deduced, depend on the distribution of clonal sizes, which is also unknown. However, small sample sizes allow the simplifying approximation that random variables describing quantities of interest, such as the numbers of cells of different types in the sample, are independent. Then, the probability generating function of the distribution of clonal sizes in the sample is the composition of that of a Bernoulli random variable (that takes values 0 or 1) and that of the true distribution of clonal sizes in the repertoire that is being sampled from. Our work is motivated by studies of the repertoire of T cells in humans and mice. Bulk sequencing has been used to set a lower limit, in the millions, of the number of distinct TCRs in an individual. In this type of experiment, where mRNA is extracted from a pool of cells, it is difficult to obtain statistics of the number of cells of each clonotype (abundance data) that is free from biases. Single-cell TCR sequencing can eliminate biases but can, at present, only be carried out on a few hundred cells from one individual.

References

1. M.K. Jenkins, H.H. Chu, J.B. McLachlan, and J.J. Moon. On the composition of the preimmune repertoire of T cells specific for peptide-major histocompatibility complex ligands. *Annual Review of Immunology*, 28:275–294, 2009.

2. R. Varma. TCR triggering by the pMHC complex: valency, affinity, and dynamics. *Science Signaling*, 1(19):pe21, 2008.

3. Benedita Rocha and Harald von Boehmer. Peripheral selection of the T cell repertoire. *Science*, 251(4998):1225–1228, 1991.

4. I. Bains, R. Antia, R. Callard, and A.J. Yates. Quantifying the development of the peripheral naive CD4$^+$ T-cell pool in humans. *Blood*, 113(22):5480, 2009.

5. François Van Laethem, Anastasia N Tikhonova, and Alfred Singer. MHC restriction is imposed on a diverse T cell receptor repertoire by CD4 and CD8 co-receptors during thymic selection. *Trends in Immunology*, 33(9):437–441, 2012.

6. RE Langman and M Cohn. The ET (elephant-tadpole) paradox necessitates the concept of a unit of B-cell function: the protecton. *Molecular Immunology*, 24(7):675–697, 1987.

7. Joseph N Blattman, Rustom Antia, David JD Sourdive, Xiaochi Wang, Susan M Kaech, Kaja Murali-Krishna, John D Altman, and Rafi Ahmed. Estimating the precursor frequency of naive antigen-specific CD8 T cells. *Journal of Experimental Medicine*, 195(5):657–664, 2002.

8. Stanca M Ciupe, Blythe H Devlin, Mary Louise Markert, and Thomas B Kepler. Quantification of total T-cell receptor diversity by flow cytometry and spectratyping. *BMC Immunology*, 14(1):1–12, 2013.

9. Niclas Thomas, Katharine Best, Mattia Cinelli, Shlomit Reich-Zeliger, Hilah Gal, Eric Shifrut, Asaf Madi, Nir Friedman, John Shawe-Taylor, and Benny Chain. Tracking global changes induced in the CD4 T cell receptor repertoire by immunization with a complex antigen using short stretches of CDR3 protein sequence. *Bioinformatics*, page btu523, 2014.

10. Tania Cukalac, Wan-Ting Kan, Pradyot Dash, Jing Guan, Kylie M Quinn, Stephanie Gras, Paul G Thomas, and Nicole L La Gruta. Paired TCR$\alpha\beta$ analysis of virus-specific CD8$^+$ T cells exposes diversity in a previously defined "narrow" repertoire. *Immunology and Cell Biology*, 2015.

11. Andrew K Sewell. Why must T cells be cross-reactive? Nature Reviews *Immunology*, 12(9):669–677, 2012.

12. Janko Nikolich-Žugich, Mark K. Slifka, and Ilhem Messaoudi. The many important facets of T-cell repertoire diversity. *Nature Reviews Immunology*, 4(2):123–132, 2004.

13. Veronika Zarnitsyna, Brian Evavold, Louie Schoettle, Joseph Blattman, and Rustom Antia. Estimating the diversity, completeness, and cross-reactivity of the T cell repertoire. *Frontiers in Immunology*, 4:485, 2013.

14. Anand Murugan, Thierry Mora, Aleksandra M Walczak, and Curtis G Callan. Statistical inference of the generation probability of T-cell receptors from sequence repertoires. *Proceedings of the National Academy of Sciences*, 109(40):16161–16166, 2012.

15. D. Mason. A very high level of crossreactivity is an essential feature of the T-cell receptor. *Immunology Today*, 19(9):395–404, 1998.

16. Grant Lythe, Robin E Callard, Rollo L Hoare, and Carmen Molina-París. How many TCR clonotypes does a body maintain? *Journal of Theoretical Biology*, 389:214–224, 2016.

17. T.P. Arstila, A. Casrouge, V. Baron, J. Even, J. Kanellopoulos, and P. Kourilsky. A direct estimate of the human $\alpha\beta$ T cell receptor diversity. *Science*, 286(5441):958, 1999.

18. Can Keşmir, José AM Borghans, and Rob J de Boer. Diversity of human $\alpha\beta$ T cell receptors. *Science*, 288(5469):1135–1135, 2000.

19. Harlan S Robins, Paulo V Campregher, Santosh K Srivastava, Abigail Wacher, Cameron J Turtle, Orsalem Kahsai, Stanley R Riddell, Edus H Warren, and Christopher S Carlson. Comprehensive assessment of T-cell receptor β-chain diversity in $\alpha\beta$ T cells. *Blood*, 114(19):4099–4107, 2009.

20. René L Warren, J Douglas Freeman, Thomas Zeng, Gina Choe, Sarah Munro, Richard Moore, John R Webb, and Robert A Holt. Exhaustive T-cell repertoire sequencing of human peripheral blood samples reveals signatures of antigen selection and a directly measured repertoire size of at least 1 million clonotypes. *Genome Research*, 21(5):790–797, 2011.

21. Qian Qi, Yi Liu, Yong Cheng, Jacob Glanville, David Zhang, Ji-Yeun Lee, Richard A Olshen, Cornelia M Weyand, Scott D Boyd, and Jörg J Goronzy. Diversity and clonal selection in the human T-cell repertoire. *Proceedings of the National Academy of Sciences*, 111(36):13139–13144, 2014.

22. Vanessa Venturi, Katherine Kedzierska, Stephen J Turner, Peter C Doherty, and Miles P Davenport. Methods for comparing the diversity of samples of the T cell receptor repertoire. *Journal of Immunological Methods*, 321(1):182–195, 2007.
23. N. Sepúlveda, C.D. Paulino, and J. Carneiro. Estimation of T-cell repertoire diversity and clonal size distribution by poisson abundance models. *Journal of Immunological Methods*, 353(1):124–137, 2010.
24. D.J. Laydon, C.R.M. Bangham, B. Asquith, Estimating T-cell repertoire diversity: limitations of classical estimators and a new approach. *Philosphical Transactions of the Royal Society B* 370, (2015).

IL-2 Stimulation of Regulatory T Cells: A Stochastic and Algorithmic Approach

Luis de la Higuera, Martín López-García, Grant Lythe and Carmen Molina-París

Abstract Regulatory T cells express IL-2 receptor (IL-2R) complexes on their surface, but do not produce IL-2 molecules. Survival of a population of regulatory T cells depends on the production of IL-2 by other cells, such as effector T cells. We formulate a stochastic version of the model of Busse (Dynamics of the IL-2 cytokine network and T-cell proliferation, Logos, Berlin, 2010, [1]), for the synthesis of IL-2R by a regulatory T cell in constitutive (ligand-independent) and in ligand-induced conditions, with the assumption that synthesis is a function of the number of IL-2/IL-2R bound complexes present on the cell surface. Exact analysis of the stochastic Markov process, by considering its master equation, is usually not possible. Here, we develop an algorithmic approach, which leads to the analysis of suitable random variables. In particular, we focus on the time to reach a threshold number of IL-2/IL-2R bound complexes on the cell surface, and the number of receptors synthesised in this time. These descriptors provide a way to quantify the rates at which IL-2/IL-2R bound complexes and IL-2R free receptors are formed in the cell, and how these rates relate to each other. By following first-step arguments, the different order moments of these random variables are obtained. We illustrate our approach with numerical realisations. The contributions of the constitutive and the ligand-induced synthesis pathways are quantified under different signalling hypotheses.

L. de la Higuera and M. López-García have contributed equally to this work.

L. de la Higuera (✉) · M. López-García (✉) · G. Lythe · C. Molina-París
Department of Applied Mathematics, School of Mathematics, University of Leeds,
Leeds LS2 9JT, UK
e-mail: mmldlh@leeds.ac.uk

M. López-García
e-mail: m.lopezgarcia@leeds.ac.uk

G. Lythe
e-mail: grant@maths.leeds.ac.uk

C. Molina-París
e-mail: carmen@maths.leeds.ac.uk

1   Introduction

T lymphocytes (T cells) are a fundamental part of the adaptive immune system.
T cell precursors originate in the bone marrow and mature in the thymus, undergoing
positive and negative selection [2, 3]. Only around 3% of immature T cells entering
the thymus complete the maturation process and are released into the periphery [4].
Maturation in the thymus ensures that thymocytes display functional T cell receptors
(TCRs) on their surface, and at the same time, will not mount a potential autoimmune
response in the periphery [5]. T cells in the periphery recognise pathogens during
an infection by means of a specific molecule that they express on their surface, the
T cell receptor. Peripheral T cells have different functions depending on the class
they belong to. *Helper* T cells (CD4$^+$ T cells) assist other cells of the immune system
during an immune response, such as B cells or *cytotoxic* T cells. Cytotoxic T cells
(CD8$^+$ T cells) are directly capable of killing virus-infected cells by recognition
of particular molecules expressed on their surface. These molecules, called pMHC
complexes, are formed by peptides presented by *antigen presenting cells* (APCs),
by means of *major histocompatibility complexes* (MHCs). T cell receptors on the
surface of T cells can bind pMHC complexes. Those T cells which have been released
from the thymus into the periphery and have not participated in an immune response
are called *naive* T cells. Upon primary infection, the subset of naive T cells which are
able to recognise pathogen-derived pMHC complexes on the surface of APCs, such
as dendritic cells, undergo proliferation and clonal expansion. Once the infection
is cleared, a clonal contraction follows [6]. After clonal contraction, a small pool
of those T cells that participated in the immune response is selected to remain in
the periphery, becoming *memory* T cells. These cells will be able then to mount
a faster immune response, following a potential secondary exposure to the same
pathogen [7]. Regulatory T cells are responsible for restraining the immune response
within *safe* levels (tolerance mechanisms), as well as for avoiding the occurrence of
potential autoimmune responses, caused by T lymphocytes which may have escaped
negative selection in the thymus [7]. We refer the reader to Ref. [8] for an interesting
introduction to these immune processes and other basic mechanisms of the immune
system.

   The proper functioning of the different T cell classes introduced above, as well
as the interaction between them, not only depends on the TCR and the pMHC com-
plexes, but also depends on a group of cytokines called the *interleukin* family. Our
interest here is in the molecule interleukin-2 (IL-2), a cytokine involved in a number of
immunological processes (T cell thymic development [9, 10], immune responses [7]
and regulation of homeostatic levels of regulatory T cells [11–13]). Regulatory T cell
survival in the periphery depends on IL-2, as regulatory T cells are characterised
by the constitutive expression of IL-2 receptor (IL-2R) molecules on their surface
[11–13]. Since regulatory T cells do not produce IL-2, they depend on the production
of IL-2 by other cells in the periphery, such as effector T cells. We refer the reader
to Ref. [14] for a review on the role of IL-2 in the immune system.

In this chapter, we aim to introduce, develop and analyse a stochastic version of the deterministic model presented in Ref. [1] for the interaction between a helper T cell and a regulatory T cell by means of the IL-2 molecule. When analysing a biological system like this one from a mathematical and computational perspective, deterministic or stochastic approaches can be followed. The advantage of a deterministic approach is that it allows one to elucidate the dynamics of the process in an analytical manner, as the mathematical analysis of the system is usually more tractable than in a stochastic approach. However, a stochastic approach reveals the intrinsic randomness that naturally arises in these processes, being specially desirable when small numbers of molecules are involved (e.g. T cell responses have been reported to be mediated only by around 10 IL-2/IL-2R molecules [15]). When analysing a stochastic model, the usual approach is to study the *master equation* of the process (a system of differential equations involving the probabilities of the process being at each possible state at any particular time). This system, which is usually referred to as the Kolmogorov equations [16], does not often have closed-form analytical solutions. Under these circumstances, different approaches are implemented in the literature to analyse the dynamics of these processes. For example, standard Gillespie stochastic simulations [17] allow one to produce realisations of the process under study. A trajectory corresponding to a single Gillespie simulation represents an exact sample from the probability mass function that is the solution of the master equation. On the other hand, moment-based approximations [18] focus on analysing the dynamics of average quantities (e.g. average number of molecules).

Our aim in this Chapter is to introduce and develop an alternative algorithmic method: the *matrix-analytic* approach. This method makes use of a matrix formalism and was originally developed by Marcel F. Neuts in the area of queueing theory [19]. It has recently been applied in different areas of mathematical biology, such as population dynamics [20], epidemiology [21, 22], or cellular and molecular biology [23]. The analysis developed here relies on the introduction of *stochastic descriptors*, which are conveniently defined random variables that provide detailed information about the dynamics of the process, yet do not require the analysis of the time-dependent dynamics in the master equation.

The Chapter is structured as follows. In Sect. 2, the stochastic process based on the deterministic model of Ref. [1] is introduced and described. The stochastic descriptors are defined in Sect. 3. They enable us to study the rate at which IL-2/IL-2R complexes are formed on the regulatory T cell surface, as well as the rate at which IL-2R molecules are synthesised. An algorithmic approach, discussed in the Appendix, allows us to analyse these descriptors in an efficient manner. Finally, numerical results are obtained and discussed in Sect. 4. A summary and the main conclusions are given in Sect. 5.

2 Stochastic Model

Our aim is to develop a stochastic version of the deterministic model proposed in Ref. [1] for the interaction between a helper T cell and a regulatory T lymphocyte, mediated by the interleukin-2 cytokine (IL-2) and its receptor (IL-2R). We restrict our study to the dynamics of regulatory T cells: the synthesis of IL-2R by regulatory T cells is induced by IL-2 that is secreted by helper T cells, but sensed by regulatory T cells in a paracrine fashion.

   We consider here the stochastic counterpart of the mathematical model introduced in Ref. [1], which considers the following molecules: IL-2 cytokine or free ligand molecules (L), IL-2R (R) on the regulatory T cell surface, bound IL-2/IL-2R complexes on the cell surface (C), and bound complexes in the endosome of regulatory T cells (E). The model under study is represented in Fig. 1 and involves the analysis of the following random variables:

$$R(t) = \text{``Number of free IL-2R receptors on the cell surface at time } t\text{''},$$
$$C(t) = \text{``Number of IL-2/IL-2R complexes on the cell surface at time } t\text{''},$$
$$E(t) = \text{``Number of IL-2/IL-2R complexes in the endosome at time } t\text{''},$$
$$L(t) = \text{``Number of free extra} - \text{cellular IL-2 molecules at time } t\text{''},$$

for any $t \geq 0$, where we assume an initial number $L(0) = n_L$ of IL-2 molecules (ligand), and an initial number $R(0) = n_R$ of free IL-2Rs, with $C(0) = E(0) = 0$. In what follows, and as we are not explicitly modelling the dynamics of helper T cells, their IL-2 secretion, or the spatial diffusion of IL-2 from helper T cells to regulatory T cells, we assume a constant background of ligand, so that $L(t) = n_L \ \forall t \geq 0$, in the spirit of Ref. [24]. Finally, we consider that the total number of receptors per cell is bounded by a *carrying capacity* of the regulatory T cells. Thus, we assume that
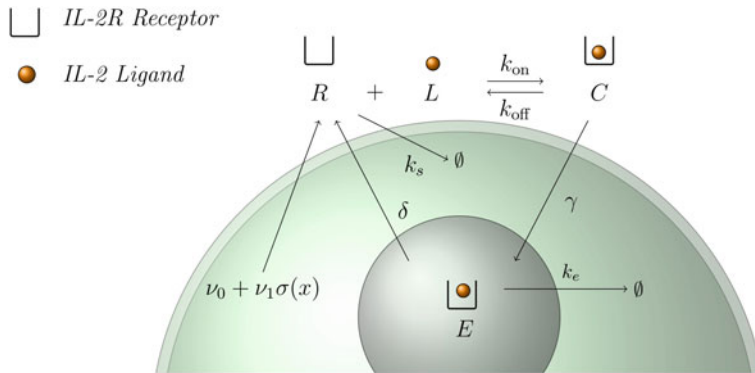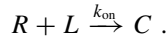

Fig. 1 Model of IL-2 stimulation of a regulatory T cell

$$R(t) + C(t) + E(t) \leq n_R^{max} \ ,$$

for all $t \geq 0$, so that $n_R \leq n_R^{max}$.

Once the variables of the model have been described, we introduce the set of reactions considered (see Fig. 1):
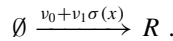
($\mathbb{R}_1$) **Binding of ligand to receptor**: Extra-cellular IL-2 molecules can bind to IL-2R on the surface of regulatory T cells, forming IL-2/IL-2R complexes, with rate k_{on},

$$R + L \xrightarrow{k_{on}} C \ .$$

($\mathbb{R}_2$) **Dissociation of ligand and receptor**: Bound complexes C can dissociate with rate k_{off},

$$C \xrightarrow{k_{off}} R + L \ .$$
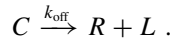
($\mathbb{R}_3$) **Synthesis of IL-2R**: We assume both constitutive and IL-2 induced synthesis of new IL-2R molecules,

$$\emptyset \xrightarrow{v_0 + v_1 \sigma(x)} R \ .$$

The synthesis of new receptors occurs at a rate

$$v_0 + v_1 \sigma(x) = v_0 + v_1 \frac{x^3}{x^3 + K_c^3} \ ,$$

where x is the number of bound IL-2/IL-2R complexes on the cell surface at a given time,[1] v_0 is the constitutive synthesis rate and v_1 is the ligand-induced synthesis rate. The positive feedback of bound complexes on IL-2R synthesis is represented by a Hill function with half-saturation constant $K_c = 1,000$ and Hill coefficient $m = 3$, as discussed and considered in Ref. [1].

($\mathbb{R}_4$) **Internalisation of bound complexes**: IL-2/IL-2R complexes are internalised from the membrane of the cell into the endosome with rate γ,

$$C \xrightarrow{\gamma} E \ .$$
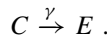
($\mathbb{R}_5$) **Endosomal degradation**: Internalised IL-2/IL-2R complexes are degraded in the endosome with rate k_e,

$$E \xrightarrow{k_e} \emptyset \ .$$

---

[1] Other hypotheses for x are discussed and considered in Sect. 4. In particular, $x = C(t)$ in the original model of Ref. [1], while alternative possibilities $x = E(t)$ and $x = C(t) + E(t)$ are introduced and analysed here in Sect. 4.

($\mathbb{R}_6$) **Receptor recycling**: IL-2R recycling takes place from internalised IL-2/IL-2R complexes with rate δ,

$$E \xrightarrow{\delta} R .$$
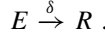
($\mathbb{R}_7$) **Surface receptor degradation**: Free IL-2R receptors on the cell surface are degraded with rate k_s,

$$R \xrightarrow{k_s} \emptyset .$$

Under Markovian assumptions, we can introduce a continuous-time Markov process $\mathscr{X}(t) = \{(R(t), C(t), E(t)) : t \geq 0\}$ defined over the space of states $\mathscr{S} = \{(n_1, n_2, n_3) \in (\mathbb{N} \cup \{0\})^3 : n_1 + n_2 + n_3 \leq n_R^{max}\}$, with non-null infinitesimal transition rates, according to mass-action kinetics, given by

$$q_{(n_1,n_2,n_3),(n_1',n_2',n_3')} = \begin{cases} k_{\text{on}} \, n_1 \, n_L , & \text{if } (n_1', n_2', n_3') = (n_1 - 1, n_2 + 1, n_3) , \\ k_{\text{off}} \, n_2 , & \text{if } (n_1', n_2', n_3') = (n_1 + 1, n_2 - 1, n_3) , \\ k_s \, n_1 , & \text{if } (n_1', n_2', n_3') = (n_1 - 1, n_2, n_3) , \\ \gamma \, n_2 , & \text{if } (n_1', n_2', n_3') = (n_1, n_2 - 1, n_3 + 1) \\ \delta \, n_3 , & \text{if } (n_1', n_2', n_3') = (n_1 + 1, n_2, n_3 - 1) , \\ k_e \, n_3 , & \text{if } (n_1', n_2', n_3') = (n_1, n_2, n_3 - 1) , \\ \nu_0 + \nu_1 \, \sigma(n_2) , & \text{if } (n_1', n_2', n_3') = (n_1 + 1, n_2, n_3) . \end{cases} \tag{1}$$

In Sect. 4 we discuss the values for all the rates.

The dynamics of this process can be analysed in terms of the probabilities $\{\mathbb{P}_{\mathbf{n}}(t) : t \geq 0, \ \mathbf{n} \in \mathscr{S}\}$, where $\mathbb{P}_{\mathbf{n}}(t) = \mathbb{P}((R(t), C(t), E(t)) = \mathbf{n})$ is the probability of the process being in state $\mathbf{n}$ at time t, for a given initial state $\mathbf{n}_0 = (n_R, 0, 0)$. These probabilities verify the master equation, which is the name commonly used in quantitative biology to refer to the Kolmogorov differential equations corresponding to the Markov process under consideration [16]:

$$\frac{d\mathbb{P}_{\mathbf{n}}(t)}{dt} = \sum_{\mathbf{n}' \in \mathscr{S}, \mathbf{n}' \neq \mathbf{n}} q_{(\mathbf{n}',\mathbf{n})} \, \mathbb{P}_{\mathbf{n}'}(t) - \sum_{\mathbf{n}' \in \mathscr{S}, \mathbf{n}' \neq \mathbf{n}} q_{(\mathbf{n},\mathbf{n}')} \, \mathbb{P}_{\mathbf{n}}(t) , \quad \forall \mathbf{n} \in \mathscr{S} .$$

This system of differential equations cannot, in general, be solved analytically. Different methods have been proposed and used in the literature to study the Kolmogorov equations of a given Markov process, such as carrying out Gillespie simulations [17], or making use of moment-based approaches by means of the analysis of the average number of individuals (cells, molecules, etc.) within each *species* [18].

Our objective here is to propose, in Sect. 3, an alternative approach: the introduction of new stochastic descriptors, which are random variables of interest to the process under consideration. This approach, based on a matrix formalism, requires

arranging the space of states $\mathscr{S}$ in groups of states, and the use of several algorithmic techniques, known as the matrix-analytic approach [25].

3 Stochastic Descriptors

Our aim in this section is to introduce and analyse two stochastic descriptors: a continuous and a discrete one. The descriptors will allow us to study the role of the rate at which IL-2/IL-2R bound complexes are formed and the rate at which IL-2R molecules are synthesised in the dynamics of the process. We introduce:

- the time to reach a threshold number, B, of bound IL-2/IL-2R complexes simultaneously present on the cell surface, and
- the number of newly synthesised receptors during that time.

The first descriptor gives us an absolute measure of the rate at which bound complexes are formed and stay on the cell surface to reach a threshold number, while the second descriptor allows us to relate this threshold number with its direct output, the synthesis of new receptors.

Our choice for the first descriptor is guided by experimental observations that support the hypothesis that cellular responses to receptor-mediated signals only take place "once a threshold number of bound receptor-ligand complexes have been formed on the cell surface" [26–29]. The second descriptor has been considered to quantify the effect of receptor-ligand signalling in protein synthesis. In the case of IL-2R, and for T cells, there is experimental evidence for the fact that signalling through the IL-2R (mediated by IL-2) leads to transcription and translation (or de novo synthesis) of IL-2R. Given the differences between regulatory T cells, naive and activated T cells (regarding production of IL-2 and expression of the high affinity chain of IL-2R, CD25 or IL-2Rα), it is of interest to compute the number of synthesis events during the IL-2R signalling process [11, 12].

In order to analyse the stochastic descriptors we need to arrange the space of states $\mathscr{S}$ by *levels* as follows:

$$\mathscr{S} = \bigcup_{k=0}^{n_R^{max}} \mathscr{S}(k) \, ,$$

where each level, $\mathscr{S}(k) = \{(n_1, n_2, n_3) \in \mathscr{S} \, : \, n_2 = k\}$, is organised in sub-levels

$$\mathscr{S}(k) = \bigcup_{r=0}^{n_R^{max}-k} \mathscr{S}(k; r) \, , \quad 0 \leq k \leq n_R^{max} \, ,$$

with $\mathscr{S}(k; r) = \{(n_1, n_2, n_3) \in \mathscr{S} : n_1 = r, \ n_2 = k\} \subset \mathscr{S}(k)$. That is, level $\mathscr{S}(k)$ is the group of states within $\mathscr{S}$ representing a total number of bound complexes on the cell surface equal to k, while each sub-level $\mathscr{S}(k; r)$ is formed by those states within $\mathscr{S}(k)$, representing a total number of free receptors equal to r, for $0 \leq r \leq n_R^{max} - k$, $0 \leq k \leq n_R^{max}$. Finally, it is easy to show that

$$J(k) = \#\mathscr{S}(k) = \frac{(n_R^{max} - k + 1)(n_R^{max} - k + 2)}{2} ,$$
$$J(k; r) = \#\mathscr{S}(k; r) = n_R^{max} - k - r + 1 ,$$

for $0 \leq k \leq n_R^{max}, 0 \leq r \leq n_R^{max} - k$. This organisation of $\mathscr{S}$ allows us to follow an algorithmic approach when analysing the descriptors under study. This analysis is based on the use of first-step arguments, Laplace–Stieltjes transforms and probability generating functions, and is developed in the following sections. In Sect. 3.1 the time to reach a total threshold number, B, of bound complexes simultaneously present on the cell surface is studied as a random variable. We then obtain its Laplace–Stieltjes transform and its order moments are computed. In Sect. 3.2, we analyse the probability generating function of the random variable representing the number of receptors synthesised during the time it takes to reach a threshold number, B, of bound complexes simultaneously present on the cell surface. We obtain not only the different order moments of this random variable, but also an algorithmic approach for computing its probability mass function.

3.1   Time to Reach a Threshold Number of Bound Complexes on the Cell Surface

The time to reach a threshold number of bound complexes simultaneously present on the cell surface can be analysed in terms of the random variable

$T_{(n_1,n_2,n_3)}^B = $ "*Time to reach a threshold number*, B, *of bound complexes simultaneously present on the cell surface*, *given the current state of the process* $(n_1, n_2, n_3) \in \mathscr{S}$",

for values $n_2 \leq B \leq n_R^{max}$, with $T_{(n_1,n_2,n_3)}^{n_2} = 0$. In order to study this random variable, we make use of its Laplace–Stieltjes transform [16, Appendix F]

$$\varphi_{(n_1,n_2,n_3)}^B(z) = E\left[e^{-z\,T_{(n_1,n_2,n_3)}^B}\right], \quad \Re(z) \geq 0 ,$$

which uniquely determines the distribution of the random variable and allows us to compute its order moments by successive differentiation, as follows:

$$m^{B,(l)}_{(n_1,n_2,n_3)} = E\left[(T^B_{(n_1,n_2,n_3)})^l\right] = (-1)^l \left.\frac{d^l}{dz^l}\varphi^B_{(n_1,n_2,n_3)}(z)\right|_{z=0}, \quad l \geq 1.$$

The Laplace–Stieltjes transform $\varphi^B_{(n_1,n_2,n_3)}(z)$ can be obtained by a first-step argument

$$\begin{aligned}
(z + \Delta_{(n_1,n_2,n_3)})\, \varphi^B_{(n_1,n_2,n_3)}(z) &= k_{\text{on}}\, n_1\, n_L\, \varphi^B_{(n_1-1,n_2+1,n_3)}(z) + k_{\text{off}}\, n_2\, \varphi^B_{(n_1+1,n_2-1,n_3)}(z) \\
&+ k_s\, n_1\, \varphi^B_{(n_1-1,n_2,n_3)}(z) + \gamma\, n_2\, \varphi^B_{(n_1,n_2-1,n_3+1)}(z) \\
&+ \delta\, n_3\, \varphi^B_{(n_1+1,n_2,n_3-1)}(z) + k_e\, n_3\, \varphi_{(n_1,n_2,n_3-1)}(z) \\
&+ (1 - \delta_{n_1+n_2+n_3,n_R^{max}})\, (\nu_0 + \nu_1\, \sigma(n_2)) \\
&\times \varphi^B_{(n_1+1,n_2,n_3)}(z),
\end{aligned} \tag{2}$$

where $\Delta_{(n_1,n_2,n_3)} = k_{\text{on}}\, n_1\, n_L + k_{\text{off}}\, n_2 + k_s\, n_1 + \gamma\, n_2 + \delta\, n_3 + k_e\, n_3 + (1 - \delta_{n_1+n_2+n_3,n_R^{max}})$ $\times (\nu_0 + \nu_1\sigma(n_2))$, and $\delta_{i,j}$ represents the Kronecker's delta (which is equal to 1 if $i = j$ and 0, otherwise). Equation (2) yields a system of equations involving the Laplace–Stieltjes transforms corresponding to states $(n_1, n_2, n_3) \in \cup_{k=0}^{B-1}\mathscr{S}(k)$, with boundary conditions $\varphi^B_{(n_1,B,n_3)}(z) = 1$ for states $(n_1, B, n_3) \in \mathscr{S}(B)$. This system of equations can be efficiently solved by making use of a matrix formalism, while exploiting the structure of $\mathscr{S}$. We refer the reader to the Appendix where this procedure is shown in some detail.

Once the Laplace–Stieltjes transforms are in hand, the different order moments are obtained by successive differentiation of Eq. (2) with respect to z, and setting $z = 0$, as follows

$$\begin{aligned}
\Delta_{(n_1,n_2,n_3)}\, m^{B,(l)}_{(n_1,n_2,n_3)} &= k_{\text{on}}\, n_1\, n_L\, m^{B,(l)}_{(n_1-1,n_2+1,n_3)} + k_{\text{off}}\, n_2\, m^{B,(l)}_{(n_1+1,n_2-1,n_3)} \\
&+ k_s\, n_1\, m^{B,(l)}_{(n_1-1,n_2,n_3)} + \gamma\, n_2\, m^{B,(l)}_{(n_1,n_2-1,n_3+1)} \\
&+ \delta\, n_3\, m^{B,(l)}_{(n_1+1,n_2,n_3-1)} + k_e\, n_3\, m^{B,(l)}_{(n_1,n_2,n_3-1)} \\
&+ (1 - \delta_{n_1+n_2+n_3,n_R^{max}})\, (\nu_0 + \nu_1\, \sigma(n_2))\, m^{B,(l)}_{(n_1+1,n_2,n_3)} \\
&+ l\, m^{B,(l-1)}_{(n_1,n_2,n_3)},
\end{aligned} \tag{3}$$

so that moments of order l can be obtained, in an algorithmic manner, from previously computed moments of order $l - 1$, starting with $m^{B,(0)}_{(n_1,n_2,n_3)} = \varphi^B_{(n_1,n_2,n_3)}(0)$, computed from Eq. (2). This procedure makes use of a similar matrix formalism to the one for solving Eq. (2), and is also briefly discussed in the Appendix.

3.2 Number of Receptors Synthesised During the Time to Reach a Threshold Number of Bound Complexes on the Cell Surface

In this section our interest is in analysing the random variable

$N^B_{(n_1,n_2,n_3)} =$ "*Number of newly synthesised receptors during the time it takes to reach a threshold number, B, of bound complexes simultaneously present on the cell surface, given the current state of the system* $(n_1, n_2, n_3) \in \mathscr{S}$",

which is defined for values $n_2 \le B \le n_R^{max}$. In order to analyse this random variable, we propose to consider its probability generating function

$$\phi^B_{(n_1,n_2,n_3)}(s) = E\left[s^{N^B_{(n_1,n_2,n_3)}}\right] , \quad |s| \le 1 ,$$

which characterises the random variable, while allowing us at the same time to compute any pth order factorial moment as follows

$$
\begin{aligned}
n^{B,(p)}_{(n_1,n_2,n_3)} &= E\left[N^B_{(n_1,n_2,n_3)}(N^B_{(n_1,n_2,n_3)} - 1)(N^B_{(n_1,n_2,n_3)} - 2)\cdots(N^B_{(n_1,n_2,n_3)} - p + 1)\right] \\
&= \frac{d^p}{ds^p}\,\phi^B_{(n_1,n_2,n_3)}(s)\bigg|_{s=1} , \quad p \ge 0 . \tag{4}
\end{aligned}
$$

A particular advantage of using the probability generating function is that it allows us to compute the probability mass function of the random variable under study. That is, $\mathbb{P}(N^B_{(n_1,n_2,n_3)} = a) = \alpha^B_{(n_1,n_2,n_3)}(a)$ is given by

$$\alpha^B_{(n_1,n_2,n_3)}(a) = \mathbb{P}(N^B_{(n_1,n_2,n_3)} = a) = \frac{1}{a!}\frac{d^a}{ds^a}\,\phi^B_{(n_1,n_2,n_3)}(s)\bigg|_{s=0} , \quad a \ge 0 . \tag{5}$$

Thus, the Laplace–Stieltjes transform $\varphi^B_{(n_1,n_2,n_3)}(z)$ considered in Sect. 3.1 (corresponding to the continuous random variable $T^B_{(n_1,n_2,n_3)}$) can be seen, from a probabilistic perspective, as the continuous analogous of the probability generating function $\phi^B_{(n_1,n_2,n_3)}(s)$, corresponding to the discrete random variable $N^B_{(n_1,n_2,n_3)}$. In particular, both allow the computation of the different factorial (or standard, in the continuous case) order moments of the random variables under study, as well as of the probability mass (or density, by numerical inversion of the Laplace–Stieltjes transform [30]) function of them. We refer the reader to Ref. [31, Appendix B] for an introduction to probability generating functions and Laplace–Stieltjes transforms of discrete and continuous, respectively, random variables. The probability generating function $\phi^B_{(n_1,n_2,n_3)}(s)$ can be obtained by following a first-step argument, in a similar manner to that discussed in the previous subsection. In particular,

$$\Delta_{(n_1,n_2,n_3)} \phi^B_{(n_1,n_2,n_3)}(s) = k_{\text{on}} \, n_1 \, n_L \, \phi^B_{(n_1-1,n_2+1,n_3)}(s) + k_{\text{off}} \, n_2 \, \phi^B_{(n_1+1,n_2-1,n_3)}(s)$$
$$+ k_s \, n_1 \, \phi^B_{(n_1-1,n_2,n_3)}(s) + \gamma \, n_2 \, \phi^B_{(n_1,n_2-1,n_3+1)}(s)$$
$$+ \delta \, n_3 \, \phi^B_{(n_1+1,n_2,n_3-1)}(s) + k_e \, n_3 \, \phi^B_{(n_1,n_2,n_3-1)}(s)$$
$$+ (1 - \delta_{n_1+n_2+n_3,n_R^{max}}) \, (v_0 + v_1 \, \sigma(n_2)) \, s$$
$$\times \phi^B_{(n_1+1,n_2,n_3)}(s) \,, \tag{6}$$

for states $(n_1, n_2, n_3) \in \cup_{k=0}^{B-1} \mathscr{S}(k)$, with boundary conditions $\phi^B_{(n_1,B,n_3)}(s) = 1$ for states $(n_1, B, n_3) \in \mathscr{S}(B)$. Equation (6) yields a system of equations that can be efficiently solved by following the same matrix formalism described in the previous section. This procedure is briefly discussed in the Appendix.

A direct application of Eqs. (4)–(6) leads to a system of equations corresponding to the desired factorial moments and the probability mass function. In fact, we can write

$$\Delta_{(n_1,n_2,n_3)} \, n^{B,(p)}_{(n_1,n_2,n_3)} = k_{\text{on}} \, n_1 \, n_L \, n^{B,(p)}_{(n_1-1,n_2+1,n_3)} + k_{\text{off}} \, n_2 \, n^{B,(p)}_{(n_1+1,n_2-1,n_3)}$$
$$+ k_s \, n_1 \, n^{B,(p)}_{(n_1-1,n_2,n_3)} + \gamma \, n_2 \, n^{B,(p)}_{(n_1,n_2-1,n_3+1)}$$
$$+ \delta \, n_3 \, n^{B,(p)}_{(n_1+1,n_2,n_3-1)} + k_e \, n_3 \, n^{B,(p)}_{(n_1,n_2,n_3-1)}$$
$$+ (1 - \delta_{n_1+n_2+n_3,n_R^{max}}) \, (v_0 + v_1 \, \sigma(n_2))(n^{B,(p)}_{(n_1+1,n_2,n_3)}$$
$$+ p \, n^{B,(p-1)}_{(n_1+1,n_2,n_3)}) \,, \quad p \geq 1 \,,$$

$$\Delta_{(n_1,n_2,n_3)} \, \alpha^B_{(n_1,n_2,n_3)}(a) = k_{\text{on}} \, n_1 \, n_L \alpha^B_{(n_1-1,n_2+1,n_3)}(a) + k_{\text{off}} \, n_2 \, \alpha^B_{(n_1+1,n_2-1,n_3)}(a)$$
$$+ k_s \, n_1 \, \alpha^B_{(n_1-1,n_2,n_3)}(a) + \gamma \, n_2 \, \alpha^B_{(n_1,n_2-1,n_3+1)}(a)$$
$$+ \delta \, n_3 \, \alpha^B_{(n_1+1,n_2,n_3-1)}(a) + k_e \, n_3 \, \alpha^B_{(n_1,n_2,n_3-1)}(a)$$
$$+ (1 - \delta_{n_1+n_2+n_3,n_R^{max}})(1 - \delta_{a,0}) \, (v_0 + v_1 \, \sigma(n_2))$$
$$\times \alpha^B_{(n_1+1,n_2,n_3)}(a - 1) \,, \quad a \geq 0 \,.$$

Boundary conditions for the equations above are $n^{B,(p)}_{(n_1,B,n_3)} = 0$, for all $p \geq 1$ and $(n_1, B, n_3) \in \mathscr{S}(B)$, and $\alpha^B_{(n_1,B,n_3)}(a) = 0$ for all $a \geq 1$ and $\alpha^B_{(n_1,B,n_3)}(0) = 1$. Efficient methods to solve the previous systems of equations can be developed by making use of the matrix formalism introduced above. We do not present the details here.

4 Numerical Results

In this section, we carry out a numerical study of the descriptors previously introduced for the IL-2 stimulation of regulatory T cells. In order to do so, we propose to make use of the physiological parameters and kinetic rates provided in Ref. [1] and reported in Table 1. We are interested in the stimulation dynamics of a regulatory T cell under three different regimes, characterised by the availability of IL-2 (low, medium,

Table 1 Physiological parameters and kinetic rates for the IL-2/IL-2R system from Ref. [1]

Parameter	Value
Regulatory T cell surface area, s_c	$3 \times 10^{-10}\,\mathrm{m}^2$
Distance to a helper T cell secreting IL-2, h	$1 \times 10^{-3}\,\mathrm{m}$
Antigen-induced IL-2R synthesis rate in a regulatory T cell, v_0	10^3 molecules/h
IL-2 induced IL-2R synthesis rate in a regulatory T cell, v_1	8×10^3 molecules/h
IL-2 association rate constant to IL-2R, $\tilde{k}_{\mathrm{on}}$	$111.6\,\mathrm{nM}^{-1}\,\mathrm{h}^{-1}$
IL-2 dissociation rate constant to IL-2R, k_{off}	$0.83\,\mathrm{h}^{-1}$
Internalisation rate constant of IL-2R, k_s	$0.64\,\mathrm{h}^{-1}$
Internalisation rate constant of IL-2/IL-2R complexes, γ	$1.7\,\mathrm{h}^{-1}$
Recycling rate constant of endosomal IL-2R, δ	$9\,\mathrm{h}^{-1}$
Endosomal degradation constant, k_e	$5\,\mathrm{h}^{-1}$

high), given by $n_L \in \{1000, 5000, 10000\}$, respectively. These values, chosen for illustrative purposes, have been selected taking into account that a helper T cell has an antigen-induced IL-2 synthesis rate in the range of $(0 - 2) \times 10^4$ molecules/h [1]. Initial conditions for our process are then given by $R(0) = v_0/k_s, C(0) = E(0) = 0$, which represent the state of the regulatory T cell before stimulation. We have assumed that in the absence of IL-2, the initial number of IL-2R on the surface of a regulatory T cell is given by the balance between receptor synthesis and degradation. We restrict ourselves to the first 60 minutes post-stimulation and for computational convenience, we consider the dynamics occurring on a fraction, $f = 1\%$, of the cell surface. Thus, $n_L \in \{10, 50, 100\}, n_R = 15$ and the kinetic rates have been transformed accordingly (see Table 1). The binding rate, k_{on} (see Fig. 1), is obtained from $\tilde{k}_{\mathrm{on}}$ in Table 1 as follows

$$k_{\mathrm{on}} = \frac{\tilde{k}_{\mathrm{on}}}{f\ h\ s_c\ N_A}\ ,$$

where h is the distance to the source of IL-2 (helper T cells), s_c is the regulatory T cell surface area and N_A is Avogadro's number. Finally, preliminary Gillespie simulations allow us to set $n_R^{max} = 6\,R(0)$. This value is chosen so that the total number of receptors in the system, $R(t) + C(t) + E(t)$, for $t \in [0, 60]$ min, does not exceed the value n_R^{max} with a probability greater than 0.99.

The aim of the numerical experiments carried out in this section is to investigate the main hypothesis of the mathematical model, originally considered in Ref. [1]. Namely, that IL-2R ligand-induced synthesis is driven by a positive feedback from the IL-2/IL-2R complexes on the cell surface. However, a number of other possible alternatives need to be considered: for example, a positive feedback from the IL-2/IL-2R complexes in the endosome, or a synergistic positive feedback from the

IL-2/IL-2R complexes on the surface and those in the endosome. Thus, we propose here three possible alternatives for the synthesis rate considered in reaction ($\mathbb{R}_3$) in Sect. 2. In particular, we consider

$$\sigma(C) = \frac{C^3}{C^3 + K_c^3} \ ,$$

$$\sigma(E) = \frac{E^3}{E^3 + K_c^3} \ ,$$

$$\sigma(C + E) = \frac{(C + E)^3}{(C + E)^3 + K_c^3} \ ,$$

where C and E represent the number of surface complexes and endosomal complexes at a given time, respectively.

In Fig. 2, we plot the average time $E[T_{(15,0,0)}^B]$ to reach a threshold number, B, of bound complexes on the cell surface $\pm$ its standard deviation. These quantities are obtained by following arguments provided in Sect. 3.1, and in particular, by direct implementation of Algorithm 1 in the Appendix. We plot these times as a function of B, for different number of IL-2 molecules, $n_L \in \{10, 50, 100\}$, and for the three synthesis hypotheses, $\sigma(C)$, $\sigma(E)$ and $\sigma(C + E)$. In the first instance (Fig. 2 *top*, $\sigma(C)$), the average time to reach B bound complexes on the cell surface is approximately equal to one hour for values of B equal to $B = 4$, $B = 21$ and $B = 39$, for $n_L = 10$, $n_L = 50$ and $n_L = 100$, respectively. That is, larger numbers of IL-2 molecules lead to a larger number of bound receptors on the surface, that induce synthesis of new IL-2Rs, thus enhancing further IL-2 binding to IL-2R. In the third model (Fig. 2 *bottom*, $\sigma(C + E)$), the corresponding values of B for an average time of one hour are $B = 4$, $B = 23$ and $B = 41$, for $n_L = 10$, $n_L = 50$ and $n_L = 100$, respectively. This illustrates the small but additional positive feedback that endosomal complexes provide to the number of surface complexes, if they are explicitly considered in the synthesis rate. On the other hand, the second hypothesis corresponding to $\sigma(E)$ (Fig. 2 *middle*), which assumes that only endosomal complexes induce positive feedback for the synthesis of new receptors, significantly changes the timescales of the threshold. In particular, values of B corresponding to an average time, $E[T_{(15,0,0)}^B]$, approximately equal to one hour are $B = 4$, $B = 10$ and $B = 13$, for $n_L = 10$, $n_L = 50$ and $n_L = 100$, respectively. That is, if only endosomal complexes were to give positive feedback for the synthesis of new receptors, the stimulation of the regulatory T cell, and in particular the rate at which IL-2/IL-2R bound complexes are formed and maintained on its surface, would significantly decrease.

A similar analysis can be made regarding the second descriptor, the average number $E[N_{(15,0,0)}^B]$ of synthesised receptors during the time it takes B complexes to be displayed on the cell surface. The descriptor is shown in Fig. 3 and plotted as a function of B. Quantities in Fig. 3 are obtained by the arguments provided in Sect. 3.2, that is, by implementing a modified version of Algorithm 1 (discussed at the end of the Appendix). We study the behaviour of this discrete descriptor for different number of IL-2 molecules and considering a number, $E[N_{(15,0,0)}^B]$, to be approximately
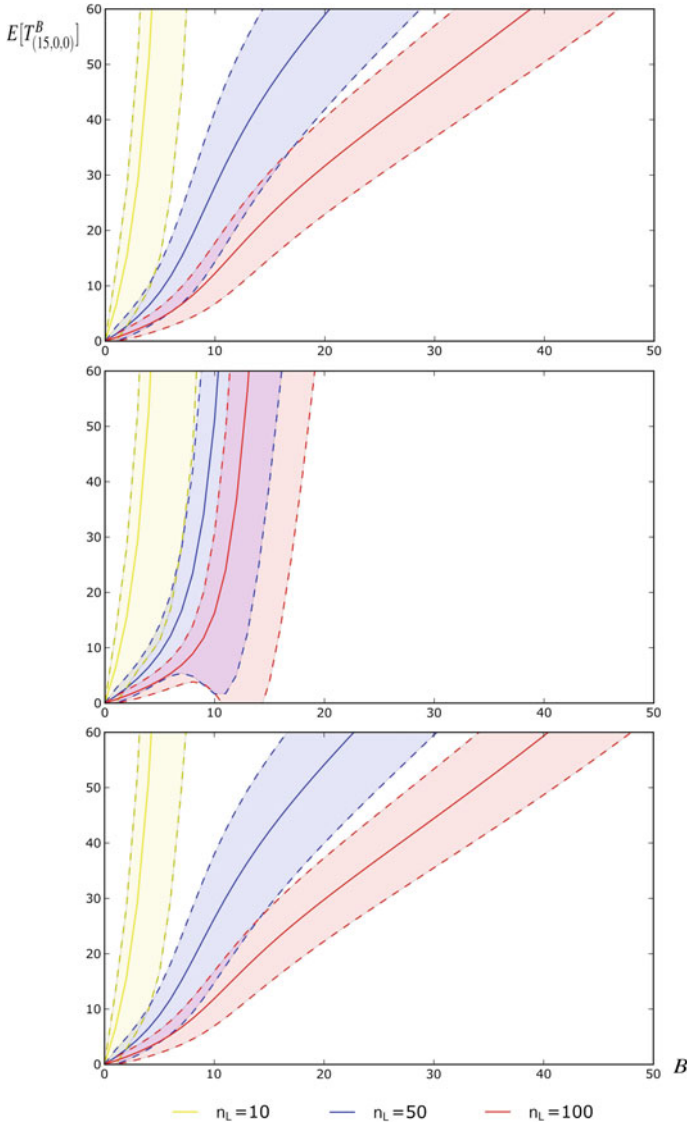
Fig. 2 Mean time $E[T^B_{(15,0,0)}]$ (in minutes) $\pm$ its standard deviation, to reach a threshold number B of bound complexes on the cell surface, as a function of B, for different number of IL-2 molecules, $n_L \in \{10, 50, 100\}$. Three different synthesis rate hypotheses have been considered in the process (from *top* to *bottom*): $\sigma(C)$, $\sigma(E)$ and $\sigma(C + E)$

equal to 40. If we assume the first hypothesis, corresponding to $\sigma(C)$ (Fig. 3 *top*), the threshold value of IL-2/IL-2R corresponds to $B = 7$, $B = 19$ and $B = 26$, for $n_L = 10$, $n_L = 50$ and $n_L = 100$, respectively. If we assume the third hypothesis,
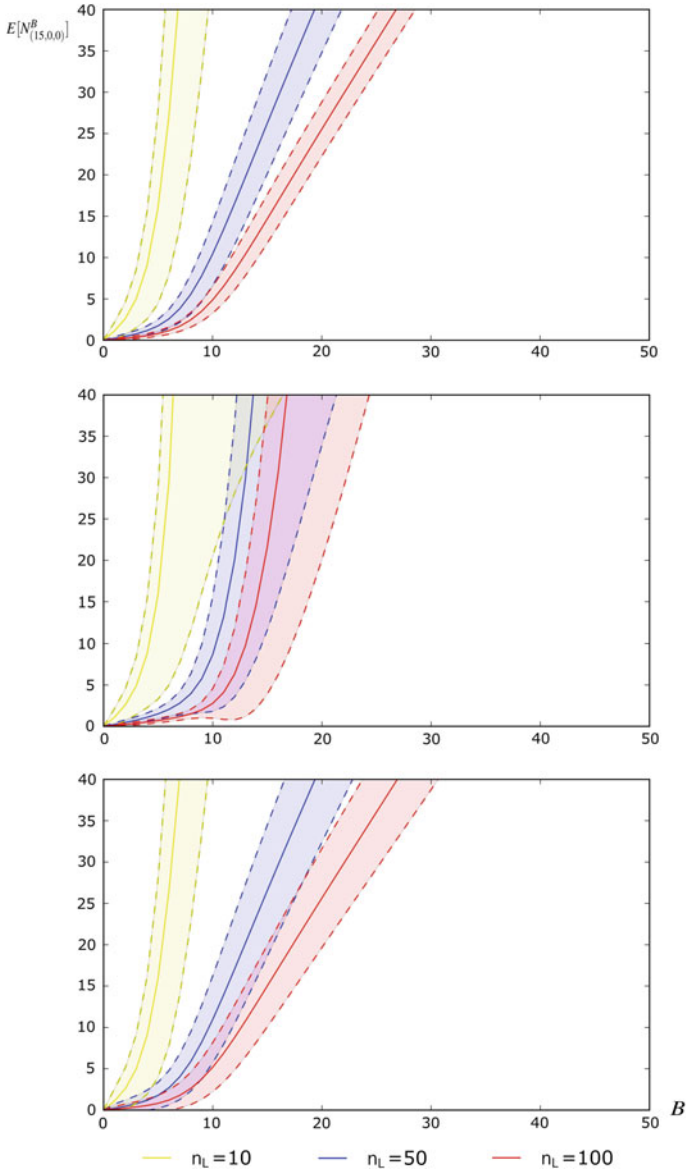
Fig. 3 Mean number $E[N^B_{(15,0,0)}]$ of receptors synthesised $\pm$ its standard deviation, to reach a threshold number B of bound complexes on the cell surface, as a function of B, for different number of IL-2 molecules, $n_L \in \{10, 50, 100\}$. Three different synthesis rate hypotheses have been considered in the process (from *top* to *bottom*): $\sigma(C)$, $\sigma(E)$ and $\sigma(C + E)$

corresponding to $\sigma(C + E)$ (Fig. 3 *bottom*), the threshold values are then equal to $B = 7$, $B = 19$ and $B = 27$, for $n_L = 10$, $n_L = 50$ and $n_L = 100$, respectively. This

means that there is a small contribution of endosomal complexes in $\sigma(C + E)$ when compared with $\sigma(C)$, which allows the regulatory T cell to synthesise receptors slightly faster. On the other hand, the hypothesis corresponding to $\sigma(E)$ (Fig. 3 *middle*) significantly changes the stimulatory dynamics, and the corresponding values of B are approximately equal to $B = 7$, $B = 14$ and $B = 17$, for $n_L = 10$, $n_L = 50$ and $n_L = 100$, respectively. We note that the results in Fig. 3 need to be interpreted together with those of Fig. 2. In particular, since in Fig. 3 we plot the number of synthesised receptors to reach a threshold number of bound complexes on the surface, this number depends on the time it takes to obtain this threshold B, which is plotted in Fig. 2. This explains the behaviour shown in Fig. 3. For example, in Fig. 3 *middle*, and under hypothesis $\sigma(E)$, the number $E[N^B_{(15,0,0)}]$ of receptors synthesised to reach $B = 14$ complexes on the cell surface, for $n_L = 50$, is equal to $E[N^B_{(15,0,0)}] \sim 44$. This large number of receptors synthesised (when compared with the same case in Fig. 3 *top*, and under hypothesis $\sigma(C)$, $E[N^B_{(15,0,0)}] \sim 23$), can be explained as follows: the timescale to reach $B = 14$ complexes, under hypothesis $\sigma(E)$, is significantly larger than one hour (see Fig. 2 *middle*).

From the comments above it is clear that, under the third hypothesis, $\sigma(C + E)$, the contribution of endosomal IL-2/IL-2R complexes to the number of receptors synthesised during an hour is negligible. However, these results do not allow us to separately quantify the contribution from the constitutive synthesis pathway, ν_0, and the ligand-induced pathway, $\nu_1 \sigma(x)$, to the number of receptors synthesised during a given time interval. This can be studied as follows: we note that regardless of the particular hypothesis considered, $\sigma(x)$ (with $x \in \{C, E, C + E\}$), the total number of synthesised receptors to reach a threshold number, B, of surface IL-2/IL-2R complexes, $N^B_{(n_R,0,0)}$, can always be expressed as

$$N^B_{(n_R,0,0)} = N^B_{(n_R,0,0)}(\text{CS}) + N^B_{(n_R,0,0)}(\text{LIS}) \, ,$$

where $N^B_{(n_R,0,0)}(\text{CS})$ is the number of receptors which have been constitutively synthesised and $N^B_{(n_R,0,0)}(\text{LIS})$ is the number of receptors which have been synthesised due to ligand-binding. We can then write

$$E[N^B_{(n_R,0,0)}] = E[N^B_{(n_R,0,0)}(\text{CS})] + E[N^B_{(n_R,0,0)}(\text{LIS})] \, ,$$

where $E[N^B_{(n_R,0,0)}]$ has been plotted in Fig. 3. The values of $E[N^B_{(n_R,0,0)}(\text{CS})]$ can be obtained by a slight modification of the arguments introduced in Sect. 3. In particular, if we define

$$\phi^B_{(n_1,n_2,n_3)}(s; \text{CS}) = E\left[s^{N^B_{(n_1,n_2,n_3)}(\text{CS})} \right] \, , \quad |s| \leq 1 \, ,$$

then Eq. (6) is replaced by

$$\Delta_{(n_1,n_2,n_3)} \, \phi^B_{(n_1,n_2,n_3)}(s; \text{CS}) = k_{\text{on}} \, n_1 \, n_L \, \phi^B_{(n_1-1,n_2+1,n_3)}(s; \text{CS}) + k_{\text{off}} \, n_2 \, \phi^B_{(n_1+1,n_2-1,n_3)}(s; \text{CS})$$

$$+ k_s \, n_1 \, \phi^B_{(n_1-1,n_2,n_3)}(s; \text{CS}) + \gamma \, n_2 \, \phi^B_{(n_1,n_2-1,n_3+1)}(s; \text{CS})$$

$$+ \delta \, n_3 \, \phi^B_{(n_1+1,n_2,n_3-1)}(s; \text{CS}) + k_e \, n_3 \, \phi^B_{(n_1,n_2,n_3-1)}(s; \text{CS})$$

$$+ (1 - \delta_{n_1+n_2+n_3,n_R^{max}}) \left(v_0 \, s + v_1 \, \frac{x^3}{x^3 + K_c^3} \right) \phi^B_{(n_1+1,n_2,n_3)}(s; \text{CS}) \, ,$$

where $x \in \{n_2, n_3, n_2 + n_3\}$ for each synthesis rate hypothesis, that is, $\sigma(C)$, $\sigma(E)$ and $\sigma(C + E)$, respectively. Thus, the moments of $N^B_{(n_R,0,0)}(\text{CS})$ (and, similarly, those of $N^B_{(n_R,0,0)}(\text{LIS})$) can be obtained by reproducing our arguments of Sect. 3 and the Appendix.

We are now able to compute (see Table 2), not only the mean number $E[N^B_{(15,0,0)}]$ of synthesised receptors to reach a threshold number of IL-2/IL-2R complexes, B, under three different hypotheses, but also the percentage contribution to the synthesis of IL-2R from the constitutive and the ligand-induced pathway. Under the first hypothesis, corresponding to a synthesis rate given by $\sigma(C)$, we observe that as the number of IL-2 molecules increases, the ligand-induced pathway becomes more relevant, as expected. However, a saturation behaviour can be seen between $n_L = 50$ and $n_L = 100$, which seems to indicate that a greater number of IL-2 molecules will not lead to a higher contribution from the ligand-induced pathway. This is, of course, due to the Hill function form assumed for $\sigma(x)$, as originally proposed in Ref. [1]. Similar comments can be made for the third hypothesis, which corresponds to the choice $\sigma(C + E)$. As shown in Table 2, differences in the values of $E[N^B_{(15,0,0)}]$ for the cases $\sigma(C)$ and $\sigma(C + E)$, and even for $\sigma(E)$, are small for $B = 5$. This indicates that the ligand-induced synthesis pathway does not play a significant role, in absolute terms, for short timescales. This is not the case for $B = 10$, where a different behaviour can be observed for $\sigma(E)$, when compared to $\sigma(C)$ or $\sigma(C + E)$. Now, the ligand-induced synthesis pathway plays a larger role for long timescales. Finally, we note that the values provided in Table 2 have to be carefully interpreted by looking at both Figs. 2 and 3. For example, the value $E[N^B_{(15,0,0)}] \sim 670$ for $B = 10$, with synthesis rate given by $\sigma(E)$, and $n_L = 10$, can be explained by pointing out that it takes over 66 h to display $B = 10$ IL-2/IL-2R complexes on the cell surface, and during this time 670 IL-2R synthesis events take place. This is indeed, a much longer timescale than the first hour of the experiment (see Fig. 2).

5 Discussion

We have defined and developed a stochastic version of the deterministic model introduced in Ref. [1], for the stimulation of a regulatory T cell by IL-2. Instead of solving the master equation associated with the Markov process, or of carrying out Gillespie simulations, we have introduced two random variables (or stochastic descriptors) to analyse the rate at which IL-2/IL-2R complexes are formed and stay on the cell

Table 2 Values of $E[T^B_{(15,0,0)}]$ (in minutes), $E[N^B_{(15,0,0)}]$, $100\frac{E[N^B_{(15,0,0)}(\text{CS})]}{E[N^B_{(15,0,0)}]}\%$ (that is, the percentage of synthesis events due to the constitutive pathway), and $100\frac{E[N^B_{(15,0,0)}(\text{LIS})]}{E[N^B_{(15,0,0)}]}\%$ (that is, the percentage of synthesis events due to the ligand-induced pathway), for $n_L \in \{10, 50, 100\}$ and $B \in \{5, 10\}$. Three different synthesis rate hypotheses have been considered in the process: $\sigma(C)$, $\sigma(E)$ and $\sigma(C+E)$

B	$\sigma(x)$	n_L	$E[T^B_{(15,0,0)}]$	$E[N^B_{(15,0,0)}]$	$100\frac{E[N^B_{(15,0,0)}(\text{CS})]}{E[N^B_{(15,0,0)}]}\%$	$100\frac{E[N^B_{(15,0,0)}(\text{LIS})]}{E[N^B_{(15,0,0)}]}\%$
5	$\sigma(C)$	10	86.52	15.97	90.33	9.67
		50	8.91	1.73	86.06	13.94
		100	4.10	0.80	85.66	14.34
	$\sigma(E)$	10	95.26	15.92	99.72	0.28
		50	9.00	1.50	99.73	0.27
		100	4.11	0.69	99.84	0.16
	$\sigma(C+E)$	10	84.12	15.98	87.72	12.28
		50	8.88	1.78	83.02	16.98
		100	4.09	0.82	83.46	16.54
10	$\sigma(C)$	10	408.35	107.32	63.43	36.57
		50	27.93	10.41	44.75	55.25
		100	12.23	4.85	42.00	58.00
	$\sigma(E)$	10	3993.32	669.99	99.36	0.64
		50	51.13	8.67	98.33	1.67
		100	16.31	2.76	98.36	1.64
	$\sigma(C+E)$	10	316.02	92.79	56.77	43.23
		50	26.32	10.95	40.05	59.95
		100	11.87	5.18	38.21	61.79

surface, as well as the rate at which IL-2R is synthesised. We have computed the Laplace–Stieltjes transforms and the probability generating functions of these random variables by appropriately arranging the space of states and making use of first-step arguments.

The author in Ref. [1] hypothesises that IL-2R synthesis is induced by the presence of bound IL-2/IL-2R complexes on the cell surface. We have further generalised this hypothesis and have also considered the role of internalised (endosomal) IL-2/IL-2R complexes in the IL-2R synthesis rate. We have made use of numerical experiments to compare three different hypotheses. Our numerical results suggest that if endosomal complexes contribute to the synthesis rate, their effect would be negligible when considering the time to reach a certain signalling threshold (encoded by the number of IL-2/IL-2R complexes on the surface of a regulatory T cell).

We have also been able to quantify the relative contribution to the number of IL-2R molecules synthesised by the constitutive and the ligand-induced pathway, respectively. We have done so by slightly modifying the stochastic descriptors. A particular conclusion from Table 2 is that ligand-induced synthesis is not important

for the short-term dynamics of the system, in which the constitutive receptor synthesis pathway seems to play the central role. On the other hand, for larger number of IL-2 ligand molecules, the ligand-induced synthesis pathway plays a major role, and the three hypotheses for the synthesis rate need to be carefully analysed. In this case, the contribution of endosomal complexes to the synthesis rate (together with that of surface complexes, third hypothesis ($\sigma(C + E)$)) does not seem to change the behaviour of the system, when compared to the first hypothesis ($\sigma(C)$). If the synthesis rate only depends on the number of endosomal IL-2/IL-2R complexes (second hypothesis ($\sigma(E)$)), the results change in a quantitative and qualitative way. Our results also indicate that as the number of ligand molecules is increased, the role of the ligand-induced synthesis pathway is more significant, and a saturation behaviour is observed: above a certain threshold of IL-2 molecules, there are no changes in the relative contribution of the ligand-induced receptor synthesis pathway to that of the constitutive one. We have not done so in this paper, but a parallel study could be carried out for two other stochastic descriptors: the time to reach a threshold number of IL-2/IL-2R complexes in the endosome and the number of IL-2R molecules that are synthesised during this time. This would correspond to the hypothesis that the signalling complexes, that induce IL-2R synthesis, are the IL-2/IL-2R complexes in the endosome of a regulatory T cell.

Finally, we conclude by noting that, although the algorithmic approach followed here allows us to obtain analytical results for the stochastic descriptors considered, it has computational limitations. Thus, the algorithmic procedures developed within the Appendix are essential for efficient numerical computation. It is clear that standard stochastic Gillespie simulations are more efficient, from a computational perspective, than our approach (e.g. the practical implementation of our methods, according to our numerical experiments, seems to be computationally unfeasible for ligand concentrations higher than 15×10^3 IL-2 molecules/cell). On the other hand, our approach not only allows the computation of *exact* results (instead of simulated ones), as described in Figs. 2, 3 and Table 2, but it enables the development of further studies, such as perturbation analysis, which allows us to characterise (by means of the computation of partial derivatives) the impact that each kinetic rate $\theta \in \{k_{\text{on}}, k_{\text{off}}, \nu_0, \nu_1, K_c, \gamma, k_e, \delta, k_s\}$ has on the descriptors here analysed. This, which is not possible by means of Gillespie simulations, is out of the scope of this Chapter. In general, a balance between computational limitations and model complexity needs to be considered, and alternative procedures such as Gillespie simulations will be required when studying, for example, models with a greater number of variables or higher ligand concentrations than the ones presented here.

Appendix

In order to efficiently analyse the first descriptor studied in Sect. 3.1, we express the system of equations given by Eq. (2), in matrix form as

$$\boldsymbol{\varphi}(z) \;=\; \mathbf{A}(z)\,\boldsymbol{\varphi}(z) + \mathbf{b}(z)\;, \tag{7}$$

where the constant B has been omitted to simplify the notation. The vector of *unknowns*, $\boldsymbol{\varphi}(z)$, is structured, due to the organisation of $\mathscr{S}$, in levels and sub-levels, by blocks as follows

$$\boldsymbol{\varphi}(z) = \begin{pmatrix} \boldsymbol{\varphi}_0(z) \\ \boldsymbol{\varphi}_1(z) \\ \vdots \\ \boldsymbol{\varphi}_{B-1}(z) \end{pmatrix}, \quad \boldsymbol{\varphi}_k(z) = \begin{pmatrix} \boldsymbol{\varphi}_0^k(z) \\ \boldsymbol{\varphi}_1^k(z) \\ \vdots \\ \boldsymbol{\varphi}_{n_R^{max}-k}^k(z) \end{pmatrix}, \quad 0 \le k \le B-1,$$

with $\boldsymbol{\varphi}_r^k(z) = (\varphi_{(r,k,0)}(z), \dots, \varphi_{(r,k,n_R^{max}-r-k)}(z))^T$, and where ^{T} represents the transpose operator. In a similar way, the organisation of states within $\mathscr{S}$ by levels and sub-levels, and the consideration of the transition rates given in Eq. (1), lead to

$$\mathbf{A}(z) = \begin{pmatrix} \mathbf{A}_{0,0}(z) & \mathbf{A}_{0,1}(z) & \mathbf{0} & \dots & \mathbf{0} & \mathbf{0} \\ \mathbf{A}_{1,0}(z) & \mathbf{A}_{1,1}(z) & \mathbf{A}_{1,2}(z) & \dots & \mathbf{0} & \mathbf{0} \\ \mathbf{0} & \mathbf{A}_{2,1}(z) & \mathbf{A}_{2,2}(z) & \dots & \mathbf{0} & \mathbf{0} \\ \vdots & \vdots & \vdots & \ddots & \vdots & \vdots \\ \mathbf{0} & \mathbf{0} & \mathbf{0} & \dots & \mathbf{A}_{B-2,B-2}(z) & \mathbf{A}_{B-2,B-1}(z) \\ \mathbf{0} & \mathbf{0} & \mathbf{0} & \dots & \mathbf{A}_{B-1,B-2}(z) & \mathbf{A}_{B-1,B-1}(z) \end{pmatrix},$$

where the sub-matrix $\mathbf{A}_{k,k'}(z)$ contains in an ordered fashion, those coefficients in the system, Eq. (2), related to transitions from states in level $\mathscr{S}(k)$ to states in level $\mathscr{S}(k')$. The specific structure by sub-levels allows us to write the following expressions

$$\mathbf{A}_{k,k}(z) = \begin{pmatrix} \mathbf{B}_{0,0}^{k,k}(z) & \mathbf{B}_{0,1}^{k,k}(z) & \mathbf{0} & \dots & \mathbf{0} & \mathbf{0} \\ \mathbf{B}_{1,0}^{k,k}(z) & \mathbf{B}_{1,1}^{k,k}(z) & \mathbf{B}_{1,2}^{k,k}(z) & \dots & \mathbf{0} & \mathbf{0} \\ \mathbf{0} & \mathbf{B}_{2,1}^{k,k}(z) & \mathbf{B}_{2,2}^{k,k}(z) & \dots & \mathbf{0} & \mathbf{0} \\ \vdots & \vdots & \vdots & \ddots & \vdots & \vdots \\ \mathbf{0} & \mathbf{0} & \mathbf{0} & \dots & \mathbf{B}_{n_R^{max}-k-1,n_R^{max}-k-1}^{k,k}(z) & \mathbf{B}_{n_R^{max}-k-1,n_R^{max}-k}^{k,k}(z) \\ \mathbf{0} & \mathbf{0} & \mathbf{0} & \dots & \mathbf{B}_{n_R^{max}-k,n_R^{max}-k-1}^{k,k}(z) & \mathbf{B}_{n_R^{max}-k,n_R^{max}-k}^{k,k}(z) \end{pmatrix},$$

$$\mathbf{A}_{k,k-1}(z) = \begin{pmatrix} \mathbf{B}_{0,0}^{k,k-1}(z) & \mathbf{B}_{0,1}^{k,k-1}(z) & \mathbf{0} & \dots & \mathbf{0} & \mathbf{0} \\ \mathbf{0} & \mathbf{B}_{1,1}^{k,k-1}(z) & \mathbf{B}_{1,2}^{k,k-1}(z) & \dots & \mathbf{0} & \mathbf{0} \\ \mathbf{0} & \mathbf{0} & \mathbf{B}_{2,2}^{k,k-1}(z) & \dots & \mathbf{0} & \mathbf{0} \\ \vdots & \vdots & \vdots & \ddots & \vdots & \vdots \\ \mathbf{0} & \mathbf{0} & \mathbf{0} & \dots & \mathbf{B}_{n_R^{max}-k-1,n_R^{max}-k}^{k,k-1}(z) & \mathbf{0} \\ \mathbf{0} & \mathbf{0} & \mathbf{0} & \dots & \mathbf{B}_{n_R^{max}-k,n_R^{max}-k}^{k,k-1}(z) & \mathbf{B}_{n_R^{max}-k,n_R^{max}-k+1}^{k,k-1}(z) \end{pmatrix},$$

$$\mathbf{A}_{k,k+1}(z) = \begin{pmatrix} \mathbf{0} & \mathbf{0} & \mathbf{0} \dots & \mathbf{0} & \mathbf{0} \\ \mathbf{B}_{1,0}^{k,k+1}(z) & \mathbf{0} & \mathbf{0} \dots & \mathbf{0} & \mathbf{0} \\ \mathbf{0} & \mathbf{B}_{2,1}^{k,k+1}(z) & \mathbf{0} \dots & \mathbf{0} & \mathbf{0} \\ \vdots & \vdots & \vdots \ddots & \vdots & \vdots \\ \mathbf{0} & \mathbf{0} & \mathbf{0} \dots \mathbf{B}_{n_R^{max}-k-1,n_R^{max}-k-2}^{k,k+1}(z) & \mathbf{0} \\ \mathbf{0} & \mathbf{0} & \mathbf{0} \dots & \mathbf{0} & \mathbf{B}_{n_R^{max}-k,n_R^{max}-k-1}^{k,k+1}(z) \end{pmatrix},$$

where the dimensions of the sub-blocks $\mathbf{0}$ in the previous expressions have been omitted. We note that, in fact, the dimensions of a sub-block $\mathbf{0}$ corresponding to the group of rows $\mathscr{S}(k;r)$ and the group of columns $\mathscr{S}(k';r')$ are $J(k;r) \times J(k';r')$. Expressions for the sub-matrices $\mathbf{B}_{r,r'}^{k,k'}(z)$ can be obtained from Eq. (2) as

$$(\mathbf{B}_{r,r}^{k,k-1}(z))_{ij} = \begin{cases} \gamma \, k \, (z + \Delta_{(r,k,i)})^{-1}, & \text{if } j = i+1, \\ 0, & \text{otherwise}, \end{cases}$$

where $1 \le i \le J(k;r)$, $1 \le j \le J(k-1;r)$, $1 \le k \le B-1$ and $0 \le r \le n_R^{max} - k$;

$$(\mathbf{B}_{r,r+1}^{k,k-1}(z))_{ij} = \begin{cases} k_{\text{off}} \, k \, (z + \Delta_{(r,k,i)})^{-1}, & \text{if } j = i, \\ 0, & \text{otherwise}, \end{cases}$$

where $1 \le i \le J(k;r), 1 \le j \le J(k-1;r+1), 1 \le k \le B-1$ and $0 \le r \le n_R^{max} - k-1$;

$$(\mathbf{B}_{r,r-1}^{k,k}(z))_{ij} = \begin{cases} k_s \, r \, (z + \Delta_{(r,k,i)})^{-1}, & \text{if } j = i, \\ 0, & \text{otherwise}, \end{cases}$$

where $1 \le i \le J(k;r)$, $1 \le j \le J(k;r-1)$, $0 \le k \le B-1$ and $1 \le r \le n_R^{max} - k$;

$$(\mathbf{B}_{r,r}^{k,k}(z))_{ij} = \begin{cases} k_e \, i \, (z + \Delta_{(r,k,i)})^{-1}, & \text{if } j = i-1, \\ 0, & \text{otherwise}, \end{cases}$$

where $1 \le i \le J(k;r), 1 \le j \le J(k;r), 0 \le k \le B-1$ and $0 \le r \le n_R^{max} - k$;

$$(\mathbf{B}_{r,r+1}^{k,k}(z))_{ij} = \begin{cases} (\nu_0 + \nu_1\,\sigma(k))\,(z + \Delta_{(r,k,i)})^{-1}, & \text{if } j = i, \\ \delta\,i\,(z + \Delta_{(r,k,i)})^{-1}, & \text{if } j = i - 1, \\ 0, & \text{otherwise}, \end{cases}$$

where $1 \le i \le J(k;r)$, $1 \le j \le J(k;r+1)$, $0 \le k \le B-1$ and $0 \le r \le n_R^{max} - k - 1$; and

$$(\mathbf{B}_{r,r-1}^{k,k+1}(z))_{ij} = \begin{cases} k_{\mathrm{on}}\,r\,n_L\,(z + \Delta_{(r,k,i)})^{-1}, & \text{if } j = i, \\ 0, & \text{otherwise}, \end{cases}$$

where $1 \le i \le J(k;r)$, $1 \le j \le J(k+1;r-1)$, $0 \le k \le B-2$ and $1 \le r \le n_R^{max} - k$. Finally, the expression for the vector $\mathbf{b}(z)$ in Eq. (7) is given by

$$\mathbf{b}(z) = \begin{pmatrix} \mathbf{0} \\ \mathbf{0} \\ \vdots \\ \mathbf{0} \\ \mathbf{A}_{B-1,B}(z)\,\mathbf{e}_{J(B)} \end{pmatrix},$$

where $\mathbf{e}_j$ represents a column vector of ones with dimension j. Then, following a forward-elimination backward-substitution method suggested by Ciarlet [32, p. 144], Algorithm 1 is obtained. This Algorithm allows us to compute all the Laplace–Stieltjes transforms in Eq. (2) in an efficient and recursive manner.

Algorithm 1 [to obtain the Laplace–Stieltjes transforms $\varphi_{(n_1,n_2,n_3)}^B(z)$]

$\mathbf{H}_0(z) = \mathbf{I}_{J(0)} - \mathbf{A}_{0,0}(z);$
For $k = 1, \dots, B-1$:
$\quad \mathbf{H}_k(z) = \mathbf{I}_{J(k)} - \mathbf{A}_{k,k}(z) - \mathbf{A}_{k,k-1}(z)\mathbf{H}_{k-1}^{-1}(z)\mathbf{A}_{k-1,k}(z);$
$\boldsymbol{\varphi}_{B-1}(z) = \mathbf{H}_{B-1}^{-1}(z)\mathbf{A}_{B-1,B}(z)\mathbf{e}_{J(B)};$
For $k = B-2, \dots, 0$:
$\quad \boldsymbol{\varphi}_k(z) = \mathbf{H}_k^{-1}(z)\mathbf{A}_{k,k+1}(z)\boldsymbol{\varphi}_{k+1}(z);$

Finally, the order moments, $m_{(n_1,n_2,n_3)}^{B,(l)}$, of the random variable $T_{(n_1,n_2,n_3)}^B$ can be obtained by means of a matrix formalism similar to that described for Eq. (3). In particular, the system given by Eq. (3) can be expressed in matrix form as

$$\mathbf{m}^{(l)} = \mathbf{A}(0)\,\mathbf{m}^{(l)} + \tilde{\mathbf{b}}^l,$$

with

$$(\tilde{\mathbf{b}}^l)_i = l\,\frac{1}{\Delta_i}\,(\mathbf{m}^{(l-1)})_i, \quad 0 \le i \le \sum_{k=0}^{B-1} \#\mathscr{S}(k),$$

where Δ_i represents the value $\Delta_{(n_1,n_2,n_3)}$ for the state (n_1, n_2, n_3) corresponding to row i. The vector $\tilde{\mathbf{b}}^l$ can be structured by blocks as follows

$$
\tilde{\mathbf{b}}^l = \begin{pmatrix} \tilde{\mathbf{b}}_0^l \\ \tilde{\mathbf{b}}_1^l \\ \vdots \\ \tilde{\mathbf{b}}_{B-2}^l \\ \tilde{\mathbf{b}}_{B-1}^l \end{pmatrix}.
$$

Similar arguments to those used to derive Algorithm 1 lead to Algorithm 1 (continuation), which allows us to compute the moments in vector $\mathbf{m}^{(p)}$ from those previously computed in vector $\mathbf{m}^{(p-1)}$, starting at $\mathbf{m}^{(0)} = \boldsymbol{\varphi}(0)$ and until the desired order, $p = l$, is reached.

Algorithm 1 (Continuation) [to obtain the l-th order moments $m_{(n_1,n_2,n_3)}^{B,(l)}$]

> *For $k = 0, 1, \ldots, B - 1$:*
> $\quad \mathbf{m}_k^{(0)} = \boldsymbol{\varphi}_k(0)$;
> *For $p = 1, \ldots, l$:*
> $\quad \mathbf{J}_0^{(p)} = \tilde{\mathbf{b}}_0^p$;
> $\quad$ *For $j = 1, \ldots, B - 1$:*
> $\quad\quad \mathbf{J}_j^{(p)} = \mathbf{A}_{j,j-1}(0)\mathbf{H}_{j-1}^{-1}(0)\mathbf{J}_{j-1}^{(p)} + \tilde{\mathbf{b}}_j^p$;
> $\quad \mathbf{m}_{B-1}^{(p)} = \mathbf{H}_{B-1}^{-1}(0)\mathbf{J}_{B-1}^{(p)}$;
> $\quad$ *For $j = B - 2, \ldots, 1, 0$:*
> $\quad\quad \mathbf{m}_j^{(p)} = \mathbf{H}_j^{-1}(0)\left(\mathbf{J}_j^{(p)} + \mathbf{A}_{j,j+1}(0)\mathbf{m}_{j+1}^{(p)}\right)$;

We now turn to the second descriptor analysed in Sect. 3.2. Equation (6) can be expressed in matrix form as

$$
\boldsymbol{\phi}(s) = \overline{\mathbf{A}}(s)\,\boldsymbol{\phi}(s) + \overline{\mathbf{b}}, \tag{8}
$$

where we are omitting again B in the notation, and where the probability generating functions $\phi_{(n_1,n_2,n_3)}^B(s)$ for $(n_1, n_2, n_3) \in \cup_{k=0}^{B-1} \mathscr{S}(k)$ are stored in a column vector $\boldsymbol{\phi}(s)$, which is organised in sub-vectors following the structure of levels and sub-levels of $\mathscr{S}$. This follows similar arguments to those used for the vector $\boldsymbol{\varphi}(z)$. A direct comparison between Eqs. (2) and (6) allows us to write $\overline{\mathbf{A}}(s) = \mathbf{A}(z = 0)$, except for sub-blocks $\mathbf{B}_{r,r+1}^{k,k}(z)$, which should be replaced by $\overline{\mathbf{B}}_{r,r+1}^{k,k}(s)$ given by

$$
(\overline{\mathbf{B}}_{r,r+1}^{k,k}(s))_{ij} = \begin{cases} (v_0 + v_1\,\sigma(k))\,s\,\Delta_{(r,k,i)}^{-1}, & \text{if } j = i, \\ \delta\,i\,\Delta_{(r,k,i)}^{-1}, & \text{if } j = i - 1, \\ 0, & \text{otherwise,} \end{cases}
$$

for $1 \leq i \leq J(k; r)$, $1 \leq j \leq J(k; r + 1)$, $0 \leq k \leq B - 1$ and $0 \leq r \leq n_R^{max} - k - 1$. Finally, the vector $\bar{\bar{\mathbf{b}}} = \mathbf{b}(z = 0)$ and Algorithm 1 leads to the computation of the vector $\boldsymbol{\phi}(s)$ from Eq. (8).

The factorial moments $n_{(n_1, n_2, n_3)}^{B, (p)}$ and the probabilities $\alpha_{(n_1, n_2, n_3)}^{B}(a)$ of the random variable $N_{(n_1, n_2, n_3)}^{B}$ can be computed following similar arguments to those provided above, and are not included here.

References

1. D Busse. *Dynamics of the IL-2 cytokine network and T-cell proliferation*. Logos Verlag Berlin GmbH, 2010.
2. L Klein, B Kyewski, PM Allen, and KA Hogquist. Positive and negative selection of the T cell repertoire: what thymocytes see (and don't see). *Nature Reviews Immunology*, 14(6):377–391, 2014.
3. E Palmer. Negative selection? clearing out the bad apples from the T-cell repertoire. *Nature Reviews Immunology*, 3(5):383–391, 2003.
4. K Shortman, D Vremec, and M Egerton. The kinetics of T cell antigen receptor expression by subgroups of CD4+ 8+ thymocytes: delineation of CD4+ 8+ 3 (2+) thymocytes as post-selection intermediates leading to mature T cells. *The Journal of Experimental Medicine*, 173(2):323–332, 1991.
5. Y Xing and KA Hogquist. T-cell tolerance: central and peripheral. *Cold Spring Harbor Perspectives in Biology*, 4(6):a006957, 2012.
6. EM Janssen, EE Lemmens, T Wolfe, U Christen, MG von Herrath, and SP Schoenberger. CD4+; T cells are required for secondary expansion and memory in CD8+; T lymphocytes. *Nature*, 421(6925):852–856, 2003.
7. O Boyman and J Sprent. The role of interleukin-2 during homeostasis and activation of the immune system. *Nature Reviews Immunology*, 12(3):180–190, 2012.
8. LM Sompayrac. *How the immune system works*. John Wiley & Sons, 2011.
9. TR Malek, BO Porter, EK Codias, P Scibelli, and A Yu. Normal lymphoid homeostasis and lack of lethal autoimmunity in mice containing mature T cells with severely impaired IL-2 receptors. *The Journal of Immunology*, 164(6):2905–2914, 2000.
10. TR Malek, A Yu, V Vincek, P Scibelli, and L Kong. CD4 regulatory T cells prevent lethal autoimmunity in IL-2Rβ-deficient mice: implications for the nonredundant function of IL-2. *Immunity*, 17(2):167–178, 2002.
11. ARM Almeida, N Legrand, M Papiernik, and AA Freitas. Homeostasis of peripheral CD4+ T cells: IL-2Rα and IL-2 shape a population of regulatory cells that controls CD4+ T cell numbers. *The Journal of Immunology*, 169(9):4850–4860, 2002.
12. ARM Almeida, B Zaragoza, and AA Freitas. Indexation as a novel mechanism of lymphocyte homeostasis: the number of CD4+ CD25+ regulatory T cells is indexed to the number of IL-2-producing cells. *The Journal of Immunology*, 177(1):192–200, 2006.
13. TR Malek, A Yu, L Zhu, T Matsutani, D Adeegbe, and AL Bayer. IL-2 family of cytokines in T regulatory cell development and homeostasis. *Journal of Clinical Immunology*, 28(6):635–639, 2008.
14. TR Malek and I Castro. Interleukin-2 receptor signaling: at the interface between tolerance and immunity. *Immunity*, 33(2):153–165, 2010.
15. SK Dower, SR Kronheim, CJ March, PJ Conlon, TP Hopp, S Gillis, and DL Urdal. Detection and characterization of high affinity plasma membrane receptors for human interleukin 1. *The Journal of Experimental Medicine*, 162(2):501–515, 1985.
16. VG Kulkarni. *Modeling and analysis of stochastic systems*. CRC Press, 2009.

17. DT Gillespie. Exact stochastic simulation of coupled chemical reactions. *The Journal of Physical Chemistry*, 81(25):2340–2361, 1977.
18. NG Van Kampen. *Stochastic processes in physics and chemistry*, volume 1. Elsevier, 1992.
19. MF Neuts. Matrix-analytic methods in queuing theory. *European Journal of Operational Research*, 15(1):2–12, 1984.
20. A Gómez-Corral and M López-García. Extinction times and size of the surviving species in a two-species competition process. *Journal of Mathematical Biology*, 64(1–2):255–289, 2012.
21. A Economou, A Gómez-Corral, and M López-García. A stochastic SIS epidemic model with heterogeneous contacts. *Physica A: Statistical Mechanics and its Applications*, 421:78–97, 2015.
22. M López-García. Stochastic descriptors in an SIR epidemic model for heterogeneous individuals in small networks. *Mathematical Biosciences*, 271:42–61, 2015.
23. JR Artalejo, A Gómez-Corral, M López-García, and C Molina-París. Stochastic descriptors to study the fate and potential of naive T cell clonotypes in the periphery. *Journal of Mathematical Biology*. doi:10.1007/s00285-016-1020-6, 2016.
24. KG Gurevich, PS Agutter, and DN Wheatley. Stochastic description of the ligand-receptor interaction of biologically active substances at extremely low doses. *Cellular Signalling*, 15(4):447–453, 2003.
25. QM He. *Fundamentals of matrix-analytic methods*. Springer, 2014.
26. C Starbuck and DA Lauffenburger. Mathematical model for the effects of epidermal growth factor receptor trafficking dynamics on fibroblast proliferation responses. *Biotechnology Progress*, 8(2):132–143, 1992.
27. B Goldstein, JR Faeder, and WS Hlavacek. Mathematical and computational models of immune-receptor signalling. *Nature Reviews Immunology*, 4(6):445–456, 2004.
28. PW Zandstra, DA Lauffenburger, and CJ Eaves. A ligand-receptor signaling threshold model of stem cell differentiation control: a biologically conserved mechanism applicable to hematopoiesis. *Blood*, 96(4):1215–1222, 2000.
29. J Currie, M Castro, G Lythe, E Palmer, and C Molina-París. A stochastic T cell response criterion. *Journal of The Royal Society Interface*, 9(76):2856–2870, 2012.
30. J Abate and W Whitt. Numerical inversion of Laplace transforms of probability distributions. *ORSA Journal on Computing*, 7(1):36–43, 1995.
31. D Insua, F Ruggeri, and M Wiper. *Bayesian analysis of stochastic process models*, volume 978. John Wiley & Sons, 2012.
32. PG Ciarlet, B Miara, and JM Thomas. *Introduction to numerical linear algebra and optimisation*. Cambridge University Press, 1989.

Understanding the Role of Mitochondria Distribution in Calcium Dynamics and Secretion in Bovine Chromaffin Cells

Amparo Gil, Virginia González-Vélez, José Villanueva and Luis M. Gutiérrez

Abstract Adrenomedullary chromaffin cells are widely used as a valuable model to study calcium-induced exocytosis of dense vesicles. Functional studies demonstrated the important role of organelles in shaping calcium signals in this cell type. Therefore, the study of mitochondria distribution in relation with exocytotic sites is relevant to understand the nature of such modulation. In this paper, we discuss the spatial distribution of mitochondria in bovine chromaffin cells in culture inferred from experimental observations and use a theoretical model for understanding the role played by these organelles in the fine tuning of calcium signals and the modulation of secretion.

1 Introduction

It is well known the key role that calcium plays as messenger in a large number of vital processes, such as secretion of hormones and neurotransmitters, muscle contraction and genetic transcription, among others [1, 20]. Regarding the release of neurotransmitters, the vast majority of synapses in the central nervous system are chemical, as are all synapses between nerves and muscles. When an action

A. Gil (✉)
Depto. de Matemática Aplicada Y CC de la Comput, Universidad de Cantabria, 39005 Santander, Spain
e-mail: amparo.gil@unican.es

V. González-Vélez
Area de Química Aplicada, Universidad Autónoma Metropolitana-Azcapotzalco, 02200 Mexico city, Mexico
e-mail: vgv@correo.azc.uam.mx

J. Villanueva · L.M. Gutiérrez
Instituto de Neurociencias, Centro Mixto Universidad Miguel Hernández-CSIC, Sant Joan d'Alacant, Alicante, Spain
e-mail: jvillanueva@umh.es

L.M. Gutiérrez
e-mail: luisguti@umh.es

potential invades the terminal, the depolarization opens voltage-sensitive calcium channels, allowing calcium ions to enter the nerve terminal and trigger the transmitter release process. This model, established by Katz and Miledi [10, 11] for the release of neurotransmitter in the frog neuromuscular junction, has been extended to release processes in neurons, neuroendocrine and endocrine cells and many other cell types.

In the particular case of chromaffin cells (a type of neuroendocrine cells located in the adrenal glands), the release of catecholamines takes place in response to the elevation of cytosolic calcium in a process involving the transport of granules, translocation to the plasma membrane, docking at the secretory sites, and finally the fusion of membranes with extrusion of soluble contents [2]. Chromaffin cells have been widely used to study neurosecretion since they exhibit similar calcium dependence of several exocytotic steps as synaptic terminals do, but having the great advantage of being larger than neurons that facilitates the experimental study of exocytosis and calcium dynamics. In chromaffin cells, major cellular structures such as the cortical cytoskeleton seem to play fundamental roles in different stages of the secretory cascade [9], whereas organelles such as mitochondria and the endoplasmic reticulum appear to control and shape calcium elevations at the subplasmalemmal region [5]. In connection to this second aspect, a characterization of the populations of mitochondria and ER elements in cultured bovine chromaffin cells in relation with its distance to the secretory apparatus or exocytotic sites, was presented in [18].

In this paper, we discuss experimental findings on the mitochondria distribution in bovine chromaffin cells in culture obtained using confocal fluorescence microscopy and use a theoretical stochastic model for understanding the role played by these organelles in the fine tuning of calcium signals and the modulation of secretion. The modeling approach, which describes the entry through L and P/Q voltage-dependent calcium channels (VDCC), the 3-D diffusion of calcium ions and the kinetic reactions of calcium and buffers, is particularly appropriated for the study of media with an inhomogeneous spatial distribution of obstacles [15], as seems to be the case of mitochondria in chromaffin cells. It should be mentioned that the specific model for mitochondria organelles is not yet perfect and should be further validated using more experimental data and more extensive simulations.

2 Experimental Results

The experimental protocol for characterizing the populations of mitochondria and ER elements in cultured bovine chromaffin cells, was described in detail in [18]. We briefly discuss here the experimental protocol and present two new figures summarizing the experimental findings.

2.1 Experimental Materials and Methods

Bovine chromaffin cell isolation and culture chromaffin cells were prepared from bovine adrenal glands by collagenase digestion and separated from the debris and erythrocytes using centrifugation on Percoll gradients as described before [7, 8]. After extensive washing, cells were maintained as monolayer cultures in Dulbeccos modified Eagles medium (DMEM) supplemented with 10% fetal calf serum, $10 \mu m$ cytosine arabinoside, $10 \mu m$ 5-fluoro-$2'$-deoxyuridine, 50 IU/ml penicillin, and 50 g/ml streptomycin. Finally, cells were harvested at a density of 150,000 cells/cm^2 in 22 mm diameter coverslips coated with polylysine. Experiments were done in Krebs/HEPES (K/H) basal solution containing 134 mm NaCl, 4.7 mm KCl, 1.2 mm KH_2PO_4, 1.2 mm $MgCl_2$, 2.5 mm $CaCl_2$, 11 mm glucose, 0.56 mm ascorbic acid and 15 mm HEPES/Na, pH 7.4. Cells were stimulated for 1 min using a depolarizing solution with 59 mm high potassium (obtained by replacing isosmotically NaCl by KCl) in K/H basal solution. Cells were used between the third and sixth day after plating.

2.1.1 Visualization of F-Actin Cytoskeleton and Mitochondria by Confocal Fluorescence Microscopy

Chromaffin cells were transfected with GFP-lifeact, a 17 amino acid peptide binding to F-actin without altering its dynamics in vivo or in vitro studies using the Amaxa basic nucleofector kit for primary mammalian neuronal cells (Amaxa GmbH. Koehl, Germany) as described in [17]. 48 h later, cells were incubated either with 1 μm mito-tracker green (Invitrogen, Eugene, Or, USA) for a 15 min period at room temperature.

Cell fluorescence was studied in an Olympus Fluoview FV300 confocal laser system mounted on a IX-71 inverted microscope incorporating a 100X PLAN-Apo oil-immersion objective with 1.45 n.a. Excitation was achieved using Ar and HeNe visible light lasers. After acquisition, images were processed using the ImageJ program. For the statistical analysis, the nonparametric Mann Whitney test for paired samples or the 1 way ANOVA Kruskal–Wallis test were used. Differences were considered significant when $p < 0.05$. Data are expressed as mean + SEM obtained from experiments performed in a number (n) of individual cells from at least three different cultures.

2.2 Mitochondria Distribution in Bovine Chromaffin Cells in Culture

The confocal fluorescence images shown in Fig. 1 evidence two different populations of mitochondria in bovine chromaffin cells in the culture. These populations are represented in distinct green (perinuclear mitochondria) and yellow (cortical mitochondria) in the 3-D reconstruction shown in Fig. 1b. The existence of these two different populations was further supported with the measurements of the green
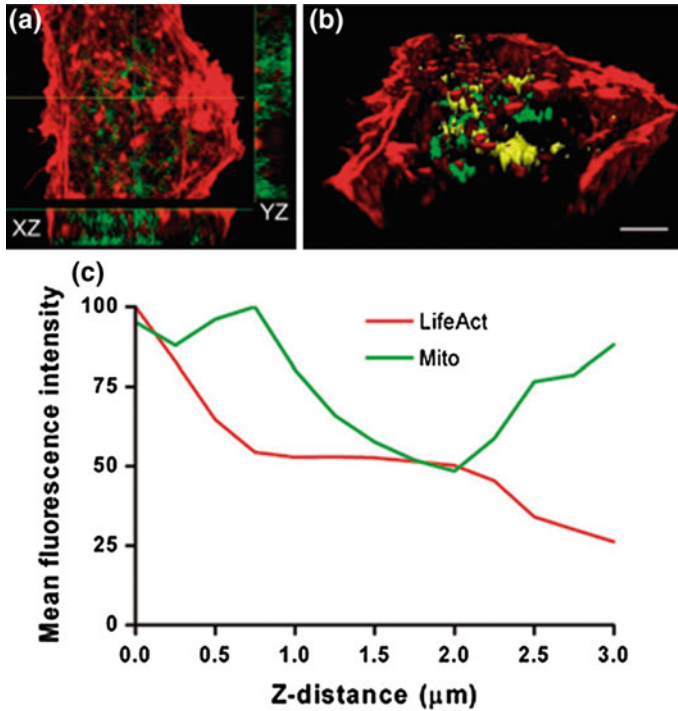
Fig. 1 Confocal microscopy images show two populations of mitochondria in chromaffin cells. Confocal images from representative experiments performed in cultured bovine chromaffin cells expressing RFP- Life Act (*red channel*) and labeled with mitotracker *green*. **a** Confocal planes separated by $0.2\,\mu m$ from the basal cortical region to the equatorial plane were used to reconstruct cell fluorescence (XY, YZ and XZ planes). The YZ and XZ planes evidenced the low fluorescence layer separating two populations of mitochondria. **b** 3-D image obtained with Imaris showing the perinuclear mitochondria in *green* as well as the cortical mitochondria in *yellow*. **c** Normalized fluorescence for the different confocal planes determined for Life Act fluorescence (*red line*), and mitotracker (*green line*) represented in function of the distance measured from cortical basal to the equatorial plane ($3\,\mu m$ in total). Bar in **b** represents $3\,\mu m$

fluorescence intensity in the different confocal planes (Fig. 1c, green line). From these measurements, it is clear the presence of an external population of mitochondria associated with the cortical region ($0–1\,\mu m$ of the cell limit) and an internal population around $2–3\,\mu m$ of the cell limits.

The experiments also reveal that two subpopulations of cortical mitochondria exist in the vicinity of exocytotic sites: the images shown in Fig. 2a, b were used to measure distances of secretory sites (punctate green dots) to the nearest mitochondria (red elongate forms) and represented in form of distributions. The distance distribution analysis shown in Fig. 2c shows that ∼30% of secretory sites colocalized with mitochondria. As can be seen, there is also a significant population of mitochondria around the 300–500 nm distance.
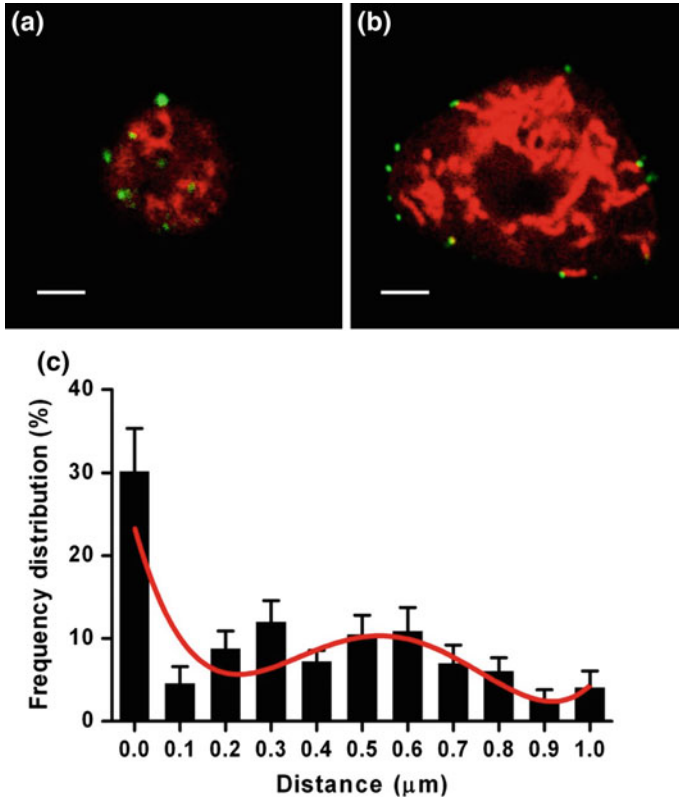
Fig. 2 Cortical mitochondria locate close to the secretory sites. Cultured chromaffin cells incubated with mitotracker red were stimulated during 1 min with a 59 mm KCl solution at room temperature (21–22 C). Secretion was stopped by lowering the temperature using ice-cooled buffer. Secretory sites were labeled using an anti-DβH antibody followed by a secondary antibody coupled to Cy-2 (*green fluorescence*) in ice-cold buffer to prevent endocytosis. The distribution of cortical mitochondria and secretory sites was studied acquiring confocal images of the cortical area in polar sections (**a**) or equatorial sections (**b**) to calculate distances between secretory sites and the nearest mitochondria (N = 347 distances from 10 cells). These distances were used to build a distribution using 0.1 nm bin size (**c**). *Red line* is the best fit to a polynomial function. Bars in **a** and **b** represent 3 μm

3 Theoretical Model

The simulation scheme used in this work is an extension of the algorithms developed by the authors [6, 14]. The Monte Carlo algorithm has proved to be successful in the study of the influence of the geometry in the exocytotic response of neuroendocrine cells and presynaptic terminals. For the spatial resolutions that are relevant (of the order of 100 nm in neuroendocrine cells or 10 nm in presynaptic terminals) and the typical concentrations of calcium in chromaffin cells, we can expect few calcium

ions inside each cube of 100 nm of side (~7 ions for 10 μm) and also a moderate number of calcium binding sites. Then, it seems more appropriate a particle-based approach instead of using a continuous modeling in terms of concentrations.

Our algorithm implements a microscopic simulation in which the fundamental variables are the number of ions and buffers. The average values of the output of our simulation converge to macroscopic simulations when considering symmetrical configurations.

A conical domain is appropriate to describe buffered diffusion in the submembrane domain of spherical cells (which is the case of chromaffin cells in good approximation). The base of the cone represents the membrane of the cell in which voltage-dependent calcium channels are distributed. An orthogonal 3-D regular grid maps the domain of simulation with a distance between grid points Δl. Each point of the grid is associated with a cubic compartment of volume $(\Delta l)^3$. The 3-D diffusion of calcium ions and possible mobile buffers is modeled as a random walk process. The first-order kinetic reactions of calcium ions and buffers are interpreted (and solve) probabilistically.

Some of the parameter values used in the model can be found in the Table 1.

To simulate currents through calcium channels, we use a simple stochastic scheme where every channel of the total population may transit from its present state to an open, closed or inactive state in response to voltage and calcium concentrations (the transition parameters between states depend on voltage and local calcium concentrations). Then, the total current is the sum of unitary currents due to open channels; the unitary currents are specific to each channel type and depend on its unitary conductance. In our simulations, we consider that each channel cluster is formed by

Table 1 Parameters used in the simulations

Geometrical parameters	
Radius	$r = 1\,\mu m$
Height	$h = 5\,\mu m$
Spatial resolution	$\Delta x = 100\,nm$
Kinetic parameters	
Calcium	
Basal concentration	$[Ca^{2+}]_0 = 0.1\,\mu m$
Diffusion coefficient	$D_{Ca} = 220\,\mu m^2/s$
Endogenous Buffer	
Total concentration	$[B] = 500\,\mu m$
Forward binding rate	$k_{on} = 5.10^8\,m^{-1}s^{-1}$
Dissociation constant	$K_D = 10\,\mu m$
Secretory vesicles	
Number of binding sites	3
Forward binding rate	$k_{on} = 8.10^6\,m^{-1}s^{-1}$
Dissociation constant	$K_D = 13\,\mu m$

Fig. 3 Simulation of calcium entry through P/Q and L-type Ca^{2+} channels in our algorithm: current to voltage relationships considered in the channel gating kinetic schemes
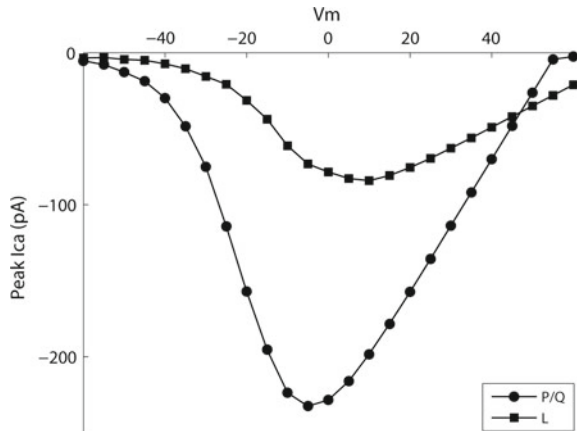
two P/Q- and one L-type calcium channels, according to experimental estimations of channel populations involved in secretion in chromaffin cells [13]. In Fig. 3, the simulated currents to voltage relationships for the L and P/Q calcium channels are shown.

3.1 Modeling Mitochondria as Obstacles for Diffusion of Calcium Ions

In our simulation scheme, mitochondria are modeled as permeable obstacles for diffusion. The distribution of mitochondria inside the simulation domain is made (randomly) according to the experimental findings: (a) 38% of cortical mitochondria (located from 0 to 1 µm to the cellular membrane); (b) 15% of cytoplasmic mitochondria (located from 1 to 2 µm to the cellular membrane); and (c) 47% of internal mitochondria (located from 2 to 3 µm to the cellular membrane). From the cortical mitochondria 1/3 (12.6% of total) are colocalized with calcium channels and 2/3 (25.4% of total) are at 300 nm mean distance. In Fig. 4, we show a representation of the base of the cone used as 3-D simulation domain and its first three slices. Three clusters of voltage-dependent calcium channels (VDCC) and two cortical mitochondria are also shown in the figure. The calcium ions enter through the calcium channels and diffuse inside the cytosol. When in the diffusion process calcium ions are trapped by a compartment corresponding to a mitochondria, the obstructed diffusion inside the mitochondrial matrix is simulated by moving them in exactly the same way that calcium ions are moved in the cytosol, but only after a number N of simulation steps. Although the treatment of diffusion inside mitochondria is simplistic, it has the advantage of using just a single parameter that can be constrained by the available experimental observations.
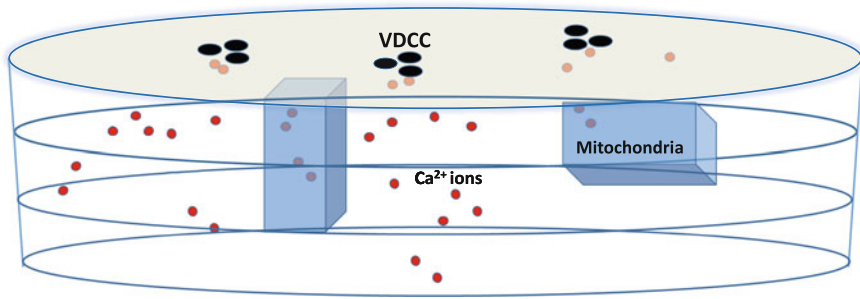
Fig. 4 Schematic representation of the three upper slices of the 3-D simulation domain including three VDCC and two cortical mitochondria

In order to estimate a reasonable value of N in our approach, we have taken into account experimental evidence in chromaffin cells suggesting that: (a) the amount of calcium taken up by the subpopulation of mitochondria in the immediate vicinity of the VDCC could be very large, even as high as 300–400 μm during maximal stimulation of Ca^{2+} entry through calcium channels [16] and (b) during stimulation, calcium entering through the plasma membrane is taken up preferentially by mitochondria and that there is very little calcium uptake by the endoplasmic reticulum (ER). Therefore, in a first approximation to the problem it seems reasonable to exclude the effect of the ER on the calcium profiles and limit to the study of mitochondria organelles.

Figure 5 (lower figure) shows the average calcium concentration for two different values of N ($N = 50, 100$) inside the compartments corresponding to the cortical mitochondria closest to the VDCC during the simulated stimulus. As can be seen, the calcium fluctuations inside the mitochondria peak at ∼200, ∼400 μm for $N = 50$, $N = 100$, respectively. Therefore, a value of $N = 100$ for simulating the obstructed diffusion inside the mitochondrial matrix, seems to generate mitochondrial calcium concentrations closer to the experimental observations during the simulated stimulus.

As a comparison, Fig. 5 (upper figure) also shows the average cytoplasmic calcium concentration from 0 to 100 nm to the cellular membrane. In the computation of the cytoplasmic calcium concentration we have excluded those compartments corresponding to a mitochondria. As can be seen, this average calcium concentration peaks at few micromolar, in contrast to the high calcium levels reached inside the mitochondria matrix. These findings are in agreement with the idea that mitochondria may act as a spatial buffer in many cells, regulating the local Ca^{2+} concentration in cellular microdomains [3] and stopping the progression of the calcium ions toward the cell core [5].

In our study, we have also computed the possible impact of the mitochondria calcium uptake on the secretory response of chromaffin cells using a standard kinetic model for the secretory sensor of vesicles in this cell type [12]. The kinetic model is a noncooperative kinetic scheme in which three calcium ions have to bind to a protein to achieve vesicle fusion. In the simulation scheme, secretory vesicles are considered

Fig. 5 Calcium concentrations in the submembrane domain. *Upper figure* average cytoplasmic calcium concentration from 0 to 100 nm to the cellular membrane. *Lower figure* average calcium concentrations inside the compartments corresponding to the cortical mitochondria closest to the VDCC. Two different values of the retarded diffusion steps ($N = 50, 100$) are considered in the calculations for comparison
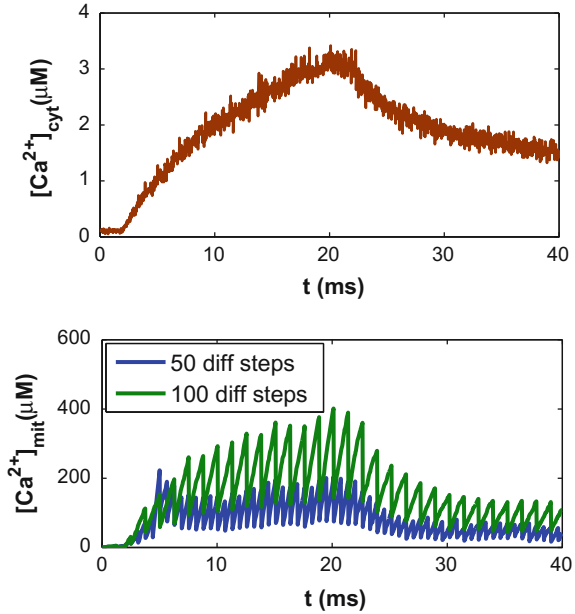

as additional buffers in the medium. These vesicles are assumed to represent the readily releasable pool of vesicles (RRP) [19]. Different distances of vesicles in this pool from the VDCC were simulated by considering few hundreds of random configurations in the first slice of the simulation domain.

In Fig. 6, we show the comparison of the percentage of the accumulated number of vesicles that have fused to the membrane when mitochondria are considered or not in the medium. It is important to note, that the accumulated secretion time course shown is the average of the results obtained with the hundreds of random distances of vesicles from the VDCC mentioned before, not a particular simulation result. As can be seen, the presence of mitochondria moderates the secretory response of the RRP after the calcium peak of the simulated stimulus, in agreement with the idea that mitochondria could play a significant role in the modulation of secretion in chromaffin cells [4].

Future work will involve the refinement of the model for mitochondria organelles in chromaffin cells and other cell types: the model should be further validated using more experimental data and more extensive simulations. Also, the predictive power of the model should be studied. It will be also interesting to include the effect of the Ca^{2+}-induced Ca^{2+} release (CICR) mechanism from the endoplasmic reticulum (excluded in the present study). Modeling this process, along with the entry of calcium through calcium channels and the mitochondria calcium uptake, will allow us to obtain a more clear perspective of the functional triad controlling exocytosis in chromaffin cells.

Fig. 6 Percentage of the accumulated number of vesicles that have fused to the membrane when mitochondria are considered or not in the medium. The accumulated secretion time course shown is the average of the results obtained with few hundreds of random distances of vesicles from the VDCC
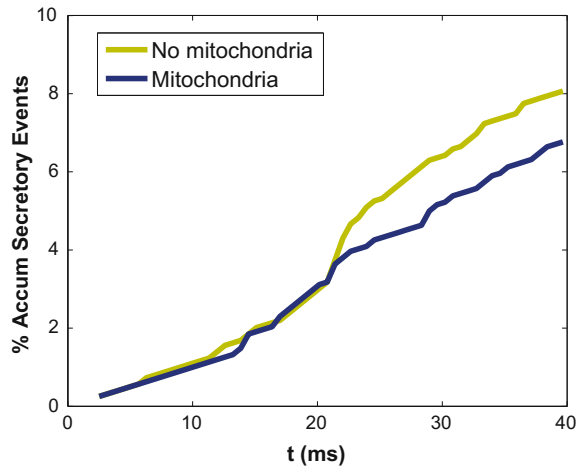
References

1. Augustine, G.J. How does calcium trigger neurotransmitter release?. Curr Opinion Neurobiol, 11:320–326 (2001)
2. Burgoyne, R.D., Morgan, A., Robinson, I., Pender, N., Cheek, T.R. Exocytosis in adrenal chromaffin cells. J. Anat. 183 (Pt 2):309–314 (1993)
3. Duchen, M.R. Mitochondria and calcium: from cell signalling to cell death. J. Physiol. 529.1: 5768 (2000)
4. García, A.G., García-De-Diego, A.M., Gandía, L., Borges, R., García-Sancho, J. Calcium signaling and exocytosis in adrenal chromaffin cells. Physiol Rev. 86(4):1093–131 (2006)
5. Garcia-Sancho, J., de Diego, A.M., Garcia, A.G. Mitochondria and chromaffin cell function. Pflugers Arch. 464:33–41 (2012)
6. Gil, A., Segura, J., Pertusa, J.A.G., Soria, B. Monte Carlo Simulation of 3-D Buffered Ca2+ Diffusions in Neuroendocrine Cells. Biophys. J. 78(1): 13–33 (2000)
7. Gil, A., Gutierrez, L. M., Carrasco-Serrano, C., Alonso, M. T., Viniegra, S. and Criado, M. Modifications in the C terminus of the synaptosome associated protein of 25 kDa (SNAP-25) and in the complementary region of synaptobrevin affect the final steps of exocytosis. J. Biol. Chem. 277: 9904–9910 (2002)
8. Gutierrez, L. M., Ballesta, J. J., Hidalgo, M. J., Gandia, L., Garcia, A. G. and Reig, J. A. A two-dimensional electrophoresis study of phosphorylation and dephosphorylation of chromaffin cell proteins in response to a secretory stimulus. J. Neurochem. 51: 1023–1030 (1988)
9. Gutierrez, L.M. New insights into the role of the cortical cytoskeleton in exocytosis from neuroendocrine cells. Int. Rev. Cell Mol. Biol. 295:109–137 (2012)
10. Katz, B., Miledi, R. The effect of calcium on acetylcholine release from motor nerve terminals. Proc. R. Soc. London B 161: 496503 (1965)
11. Katz, B., Miledi, R. The timing of calcium action during neuromuscular transmission J. Physiol. (London) 189: 535544 (1967)

12. Klingauf, J., E. Neher. Modeling buffered Ca^{2+} diffusion near the membrane: implications for secretion in neuroendocrine cells. Biophys. J. 72:674–690 (1997)
13. Lukyanetz, E.A., Neher, E. Different types of calcium channels and secretion from bovine chromaffin cells. Eur. J. Neurosci. 11: 2865–2873 (1999)
14. Segura, J., Gil, A., Soria, B. Biophys. J. Modeling study of exocytosis in neuroendocrine cells: influence of the geometrical parameters. 79(4): 1771-1786 (2000)
15. Vilaseca, E., Pastor, I., Isvoran, A., Madurga, S., Garcés, J.L., Mas, F. Diffusion in macromolecular crowded media: Monte Carlo simulation of obstructed diffusion vs. FRAP experiments. Theor. Chem. Acc. 128, Issue 4–6: 795–805 (2011)
16. Villalobos, C., Nunez, L., Montero, M., García, A.G., Alonso, M.T., Chamero, P., Alvarez, J., García-Sancho, J. Redistribution of Ca^{2+} among cytosol and organella during stimulation of bovine chromaffin cells. FASEB J 16:343–353 (2002)
17. Villanueva, J., Torres, V., Torregrosa-Hetland, C. J., Garcia-Martinez, V., Lopez- Font, I., Viniegra, S. and Gutierrez, L. M. F-Actin-Myosin II Inhibitors Affect Chromaffin Granule Plasma Membrane Distance and Fusion Kinetics by Retraction of the Cytoskeletal Cortex. J. Mol. Neurosci. 48: 328–338 (2012)
18. Villanueva, J., Viniegra, S., Giménez-Molina, Y., García-Martínez, V., Expósito-Romero, G., del Mar Frances, M., García-Sancho, J., Gutiérrez, L.M. The position of mitochondria and ER in relation to that of the secretory sites in chromaffin cells. J Cell Sci. 127(23), 5105–14 (2014)
19. Voets, T., Neher, E., Moser, T. Mechanisms underlying phasic and sustained secretion in chromaffin cells from mouse adrenal slices Neuron (23): 607–615 (1999)
20. Whitfield, J.F., Chakravarthy, B.: Calcium: The Grand-Master Cell Signaler. NRC Research, Otawa (2001)

Dynamical Features of the MAP Kinase Cascade

Juliette Hell and Alan D. Rendall

Abstract The MAP kinase cascade is an important signal transduction system in molecular biology for which a lot of mathematical modelling has been done. This paper surveys what has been proved mathematically about the qualitative properties of solutions of the ordinary differential equations arising as models for this biological system. It focuses, in particular, on the issues of multistability and the existence of sustained oscillations. It also gives a concise introduction to the mathematical techniques used in this context, bifurcation theory and geometric singular perturbation theory, as they relate to these specific examples. In addition further directions are presented in which the applications of these techniques could be extended in the future.

1 Introduction

An important process in cell biology is the transmission of information by signalling networks from the cell membrane to the nucleus, where it can influence transcription. This provides the cell with a possibility of reacting to its environment. A common module in many signalling networks is the mitogen activated protein kinase cascade (MAPK cascade). It is the subject of what follows. The MAPK cascade is a pattern of chemical reactions which is widespread in eukaryotes [45]. The individual proteins which make up the cascade differ between different organisms and between different examples within a given organism but what is common is a certain architecture. The cascade consists of three parts which we will call layers. Each layer is a phosphorylation cycle or, as it is sometimes called, a multiple futile cycle [43].

J. Hell (✉)
Institut Für Mathematik, Freie Universität Berlin, Arnimallee 7, 14195 Berlin, Germany
e-mail: jhell@zedat.fu-berlin.de

A.D. Rendall (✉)
Institut Für Mathematik, Johannes Gutenberg-Universität Mainz, Staudingerweg 9, 55099 Mainz, Germany
e-mail: rendall@uni-mainz.de

A multiple futile cycle consists of a protein X which can be phosphorylated by a kinase E at n sites. The resulting phosphoproteins can be dephosphorylated by a phosphatase F. The cases of interest for the MAPK cascade are $n = 1$ and $n = 2$. The following sketch shows the MAPK cascade with three layers. Each plain arrow marked with an enzyme represents an enzymatic reaction, i.e. $Y \xrightarrow{G} Z$ stands for the chemical reactions $Y + G \rightleftarrows YG \to Z + G$. The dotted arrows between a phosphorylated protein and an enzyme in the next layer stand for equality, i.e. $Z \dashrightarrow G$ means $Z = G$. The first layer of the cascade is a simple phosphorylation, i.e. $n = 1$. The next layers are double phosphorylations, i.e. $n = 2$. The species X_i are the proteins in the cascade, or in more detail $X_1 = MAPKKK$ (MAP kinase kinase kinase), $X_2 = MAPKK$ (MAP kinase kinase), $X_3 = MAPK$ (MAP kinase).

(1)
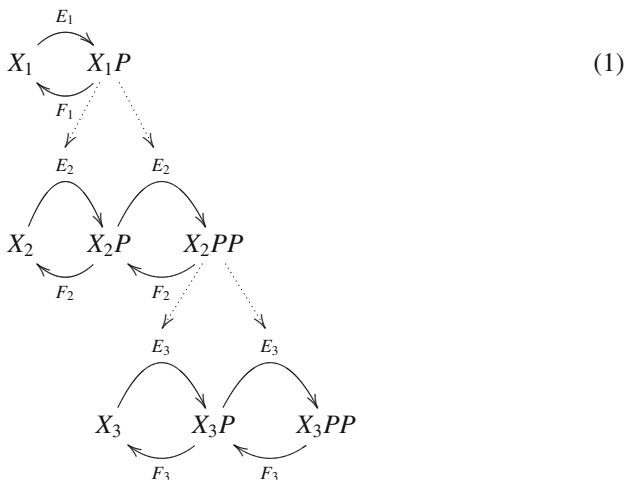
It is important that even when there is more than one site where the protein can be phosphorylated there is only one kinase and one phosphatase. Thus different phospho-forms of the protein may compete for binding to one of the enzymes. A MAPK cascade consists of three layers, each of which is a multiple futile cycle with a different protein. The connection between the layers is that the maximally phosphorylated forms of the protein in the first and second layers are the kinases which catalyze the phosphorylations in the second and third layers, respectively. The most extensively studied example in mammals is that where the proteins in the three layers are Raf, MEK and ERK.

The subject of what follows is mathematical modelling of the MAPK cascade. It turns out that this system has a rich dynamics which needs mathematical modelling for its understanding. Pioneering work in studying this question was done by Huang and Ferrell [21]. In that paper the authors presented both theoretical and experimental results and compared them. Their experiments where done in cell extracts from *Xenopus* oocytes. On the theoretical side they wrote down a system of ordinary differential equations describing the time evolution of the concentrations of the

substances involved in the MAPK cascade and simulated these equations numerically. The results of the simulations reproduced important qualitative features of the experimental data.

In order to model the reactions taking place it is necessary to make assumptions about the kinetics. In many enzymatic reactions the concentrations of the enzymes are much less than those of the corresponding substrates. This cannot necessarily be assumed in the case of the MAPK cascade. In particular there are substances, for example the doubly phosphorylated form of MEK, which are the substrate for one reaction and the enzyme for others. For this reason the model in [21] uses a Michaelis–Menten scheme for each reaction with a substrate, an enzyme and a substrate-enzyme complex without making an assumption of small enzyme concentration. The elementary reactions involved are assumed to obey mass action kinetics. There are seven conservation laws for the total amounts of the three substrates and the four enzymes which are not also substrates (one kinase, E_1 and three phosphatases, F_i, $i = 1, 2, 3$). It is assumed that the phosphorylation and dephosphorylation are distributive and sequential. In other words in any one encounter of a substrate with an enzyme only one (de-)phosphorylation takes place, after which the enzyme is released. To add or remove more than one phosphate group more than one encounter is necessary. The phosphorylations take place in a particular order and the dephosphorylations in the reverse order. These assumptions are implemented in the model of [21]. They have also frequently been adopted in other literature concerned with the modelling of this system and we will call them the standard assumptions. The authors of [21] mention that they also did simulations for cases where one or more of the reactions is processive (i.e. more than one phosphate group is added or removed during one encounter). The standard assumptions may not be correct in all biological examples but they are a convenient starting point for modelling which can later be modified if necessary.

In real biological systems the MAPK cascade is part of a larger signalling network and cannot be seen in isolation. Nevertheless, one can hope to obtain insights by first understanding the isolated cascade and later combining it with other reactions. Similarly it can be helpful to approach an understanding of the cascade itself by studying its component parts, the multiple futile cycles.

The most frequent approaches to these modelling questions in the literature use simulations and heuristic considerations. An alternative possibility, which is the central theme of this paper, is to prove mathematical theorems about certain aspects of the dynamics with the aim of obtaining insights complementary to those coming from the numerical procedures. The number of mathematically rigorous results on this subject known up to now is rather limited. The aim of this paper is to survey the results of this type which are available and to outline perspectives of how they might be extended. At the same time it gives an introduction to some of the techniques which are useful in this kind of approach. The description starts from the simplest models and proceeds to more complicated ones. We discuss successively the simple futile cycle, the dual futile cycle and the full cascade. The description also proceeds from simpler dynamical features to more complicated ones, from multistationarity to multistability and then to sustained oscillations. After this core material has been

treated further directions are explored. What happens when the basic cascade is embedded in feedback loops? What happens in systems with other phosphorylation schemes?

2   The Simple Futile Cycle

In this section we look at the case $n = 1$ of the multiple futile cycle, in other words we isolate the first layer of the cascade Eq. (1). We omit the index 1 of the chemical species for clarity in this section, since the other layers will play no role here. Modelling this system in a way strictly analogous to that applied to the MAPK cascade in [21] leads to a system of six equations for the substrates X and XP, the enzymes E, F and the substrate-enzyme complexes $X \cdot E$ and $XP \cdot F$. There are three conserved quantities, which are the total amounts of the enzymes and the substrate, $E_{tot} = [E] + [X \cdot E]$, $F_{tot} = [F] + [XP \cdot F]$ and $X_{tot} = [X] + [XP] + [X \cdot E] + [XP \cdot F]$. where here and in the following $[Z]$ denotes the concentration of the species Z. These can be used to eliminate three of the equations if desired. When the evolution is modelled by mass-action kinetics, these manipulations can be done explicitly:

$$\frac{d[X]}{dt} = -k_1[X](E_{tot} - [X \cdot E]) + k_2[X \cdot E] + k_6[XP \cdot F],$$

$$\frac{d[X \cdot E]}{dt} = k_1[X](E_{tot} - [X \cdot E]) - (k_2 + k_3)[X \cdot E], \qquad (2)$$

$$\frac{d[XP \cdot F]}{dt} = k_4[XP](F_{tot} - [XP \cdot F]) - (k_5 + k_6)[XP \cdot F],$$

where k_i, $i = 1, \ldots, 6$, are the reaction constants of the six reactions involved. The remaining concentrations are given by the relations $[E] = E_{tot} - [X \cdot E]$, $[F] = F_{tot} - [XP \cdot F]$, $[XP] = X_{tot} - [X] - [X \cdot E] - [XP \cdot F]$.

Suppose we have a system $\dot{x}_i = f_i(x)$, $x = (x_1, \ldots, x_n) \in \mathbb{R}^n$ representing the dynamics of a chemical reaction network. The $x_i(t)$ are the concentrations of the substances involved as functions of time and the dot denotes the time rate of change. A stationary solution (or steady state) is one which satisfies for all $i \in \{1, \ldots, n\}$, $x_i(t) \equiv x_{i,0}$ for some fixed concentrations $x_0 = (x_{1,0}, \ldots, x_{n,0})$. Thus it satisfies $\dot{x} = 0$ or equivalently $f(x_0) = 0$. A solution $x(t)$ is said to converge to the steady state x_0 if $\lim_{t \to \infty} x(t) = x_0$. This is an idealization of the situation where an experimental system settles down to a steady state on a sufficiently long time scale. For instance in the experiments of [21] the system was found to approach a steady state after 100 minutes. Corresponding behaviour was found in the simulations. There is no reason why a chemical system should behave in this simple way for all initial data. The results of [21] indicate that it does so for the data considered there. Even if for a particular system all solutions converge to a steady state, it may be that there exist more than one steady state for fixed values of the total amounts of the substances involved.

In the language of chemical reaction network theory [11], there may be more than one steady state in one stoichiometric compatibility class. This is the phenomenon of multistability. It is important for biological processes such as cell differentiation.

In the case of the simple futile cycle it was proved in [5] that there is always exactly one steady state for fixed values of the total amounts E_{tot}, F_{tot} and X_{tot} and that all other solutions converge to that steady state. The steady state is globally asymptotically stable and bistability is ruled out in this case. We cannot enter into the details of the proof of this result here but it is appropriate to mention some of the key ideas involved. Suppose that the system $\dot{x}_i = f_i(x)$ has the property that $\partial f_j/\partial x_i > 0$ for all $i \neq j$ and all x. Then the system is called monotone. If a system does not satisfy this property we may try to make it do so by reversing the signs of some of the variables. In other words we replace the variables x_i by $y_i = \varepsilon_i x_i$, where each ε_i is plus or minus one. In general a system is called monotone if there is a mathematical transformation of this kind which makes all partial derivatives of the right hand sides of the equations with $i \neq j$ positive. There is a graphical criterion to decide whether this is possible. Define a graph which has a vertex for each variable x_i and which has an oriented edge connecting node i to node j if $\partial f_j/\partial x_i \neq 0$. Label each edge with the sign of the corresponding derivative. Alternatively we can use the convention that a positive sign is represented by a normal arrow while a negative sign is represented by a blunt-headed arrow. This object is called the species graph. For example the species graph of the simple futile cycle is the following.

$$\tag{3}$$
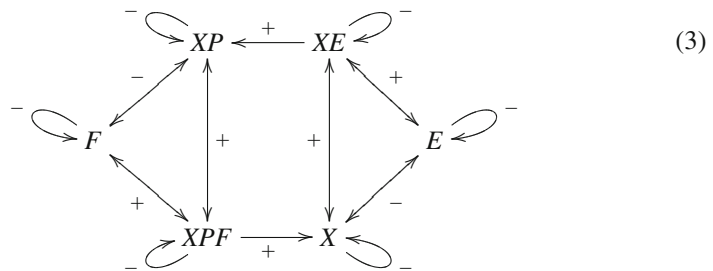
Since the use of terms concerning feedback loops is not always consistent between different sources in the literature we specify the terminology which we will use. A feedback loop is a sequence of arrows which starts at one node and ends at the same node, i.e. a cycle. It is called a positive or negative feedback loop according to whether the number of edges with a negative sign it contains is even or odd. More precisely this object may be called a directed feedback loop, while the corresponding definition where the orientation of the edges is ignored is called an undirected feedback loop. Suppose we have a system of ordinary differential equations for which the sign of the derivative $\partial f_j/\partial x_i$ is independent of x for each fixed i and j. Then it can be proved that the system is monotone if and only if the species graph contains no negative undirected feedback loops of length greater than one. In the case of the simple futile cycle the species graph contains at least one negative feedback loop. This is true both for the full six-dimensional system and for the three-dimensional system obtained by

eliminating the concentrations of E, F and XP using the conservation laws. However, it was shown in [5] that there is a different type of transformation which makes this system monotone. In this transformation the concentrations are replaced as variables by the extents of the reactions. The resulting monotone system has additional good properties and this allows the property of convergence to a unique steady state to be concluded for the original system.

Many chemical systems have interesting limiting cases obtained by letting certain combinations of reaction constants tend to zero. This can lead to a significant reduction in the number of variables in the system and make analytical investigations simpler. Under suitable circumstances solutions of the limiting system approximate solutions of the original system in a certain parameter regime. This can be illustrated by the case of the simple futile cycle. For the species $E, F, X \cdot E, XP \cdot F$ involving the enzymes E, F, alone or in a complex, scale the concentrations with a parameter $\varepsilon > 0$ while the remaining concentrations $[X]$ and $[XP]$ are not rescaled. In other words, if $y = ([E], [F], [X \cdot E], [XP \cdot F])$ is the vector of their concentrations, define $\tilde{y} = \varepsilon y$, where ε is a positive constant. If $x = ([X], [XP])$ is the vector of the remaining concentrations, the original system with mass-action kinetics is of the form

$$\begin{cases} \dot{x} = f(x, y), \\ \dot{y} = g(x, y), \end{cases} \tag{4}$$

where f, g are linear in each of the concentrations, i.e. entries of the vectors x, y. The smallness of ε corresponds to the fact that the amount of enzymes is small compared to the amount of the other species. Define a new time coordinate by $\tau = \varepsilon t$ and let a prime denote the derivative with respect to time τ. The time τ is called the slow time scale because its velocity $\frac{d\tau}{dt} = \varepsilon$ is small. This gives rise to a system of the general form
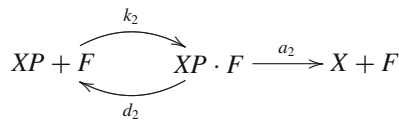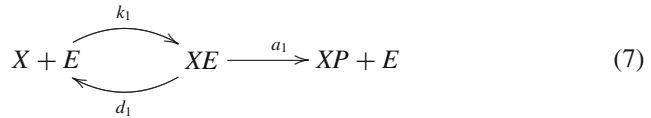
$$\begin{cases} x' = f(x, \tilde{y}), \\ \varepsilon \tilde{y}' = g(x, \tilde{y}). \end{cases} \tag{5}$$

In the limit $\varepsilon \to 0$, and dropping the tildes, the second equation $\varepsilon y' = g(x, y)$ changes from being an ordinary differential equation to being an algebraic equation $0 = g(x, y)$. Under favourable conditions this equation can be solved for y in terms of x and the result $y = h(x)$ substituted into the first equation to give an equation for x alone,

$$x' = f(x, h(x)). \tag{6}$$

The result is a system with fewer unknowns. The degeneration to an algebraic equation means that the limit is singular. It may be asked whether the solutions themselves nevertheless behave in a regular way in the limit and indeed this is the case under certain conditions. The appropriate mathematical techniques for studying this are known as geometric singular perturbation theory (GSPT) as introduced by Fenichel, see [12]. This theory will be discussed in more detail below. The particular type of limit just exhibited for the simple futile cycle is sometimes called a

Michaelis–Menten limit. In this case it leads to a two-dimensional system. The conservation law for the total amount of substrate survives in the limit in a simplified form and can be used to reduce the system further to a single equation. Let the reaction constants for complex formation, complex dissociation and product formation be denoted by k_i, d_i and a_i respectively, with $i = 1$ corresponding to phosphorylation and $i = 2$ to dephosphorylation.

$$X + E \underset{d_1}{\overset{k_1}{\rightleftharpoons}} XE \xrightarrow{a_1} XP + E \tag{7}$$

$$XP + F \underset{d_2}{\overset{k_2}{\rightleftharpoons}} XP \cdot F \xrightarrow{a_2} X + F$$

The Michaelis constants are defined as usual by $K_{m,i} = \frac{d_i + a_i}{k_i}$. Then the equation can be written as

$$\frac{d}{dt}[XP] = -\frac{k_2 F_{\text{tot}}(X_{\text{tot}} - [XP])}{K_{m,2} + X_{\text{tot}} - [XP]} + \frac{k_1 E_{\text{tot}}[XP]}{K_{m,1} + [XP]}, \tag{8}$$

After this reduction it is possible to get an explicit formula for the unique steady state by solving a quadratic equation in the variable $[XP]$ [16]. For ε small the total amounts of the enzymes are small compared to the total amount of substrate and this is sometimes described by saying that the enzymes are close to saturation. Varying one of the parameters in the system and monitoring the concentration of phosphorylated protein gives a response function. The main concern of [16] is the form of this function, which corresponds to the property of ultrasensitivity: A small change in the parameter leads to a large change in the value of the response function. This property is quantitative rather than qualitative and not obviously amenable to the application of the analytical techniques to be discussed in this paper. It is an interesting question, whether these techniques can be extended so as to give more information about quantitative properties. This will not be discussed further here except to mention that ultrasensitivity was also the central feature of interest in [21], where the response of the concentration of maximally phosphorylated ERK as a function of that of the first kinase in the cascade was investigated.

3   The Dual Futile Cycle

This section is concerned with the case $n = 2$ of the multiple futile cycle. The second layer of the MAPK cascade Eq. (1) is an example of a dual futile cycle. We omit the

index indicating the layer in this section, since we consider a single layer of the cascade. The basic system with mass action kinetics can be found, for instance, in [43]. It is possible to do a Michaelis–Menten reduction in a similar way to that done in the last section. We recall that this consists in scaling the concentration Z of the species containing one of the two enzymes E, F, alone or in a complex, via the transformation $\tilde{y} = \varepsilon y$ of their concentration vector y, as well as the time by $\tau = \varepsilon t$. The limit $\varepsilon \to 0$ can be reduced to a lower dimensional ODE by solving an algebraic equation. This leads, after using all conservation laws to eliminate as many variables as possible, to a two-dimensional system, which will be called the MM system (for Michaelis–Menten). More details on this can be found in [19]. The system can be written in the form

$$\frac{d}{dt}[X] = -\frac{k_1 K_{m,1}^{-1} E_{\text{tot}}[X]}{1 + K_{m,1}^{-1}[XP] + K_{m,3}^{-1}[XPP]} + \frac{k_2 K_{m,1}^{-2} F_{\text{tot}}[XP]}{1 + K_{m,2}^{-1}[XP] + K_{m,4}^{-1}[XPP]}. \quad (9)$$

$$\frac{d}{dt}[XPP] = \frac{k_3 K_{m,3}^{-1} E_{\text{tot}}[XP]}{1 + K_{m,1}^{-1}[XP] + K_{m,3}^{-1}[XPP]} - \frac{k_4 K_{m,4}^{-1} F_{\text{tot}}[XP]}{1 + K_{m,2}^{-1}[XP] + K_{m,4}^{-1}[XPP]}. \quad (10)$$

When using the conservation law for X_{tot} we have the choice, which of the three concentrations $[X]$, $[XP]$ or $[XPP]$ to eliminate. Here the equation for $[XP]$ has been discarded and on the right hand side of the equations $[XP]$ should be regarded as an abbreviation for $X_{\text{tot}} - [X] - [XPP]$. In this case the MM system is monotone, as defined in the previous section. Since it is two-dimensional this implies that all solutions converge to steady states. Moreover it can be shown using GSPT that for ε small but non-zero almost all initial data give rise to solutions which converge to steady states [44]. For general ε it was not known until very recently whether the corresponding statement was true. In [10] the authors used computer-assisted methods to find periodic solutions of this system, indicating that the statement is false for general ε. They do not only use dynamical simulations but also use computer algebra to help implement a theoretical approach to finding Hopf bifurcations. They do not obtain evidence for the existence of stable periodic solutions, so that it would be consistent with their findings if periodic solutions, while present, were only relevant for exceptional initial conditions. Despite the results of [10] the global behaviour of solutions of the dual futile cycle is much less well understood than that in the case of the simple futile cycle.

What has been proved is that multistationarity (existence of more than one steady state) occurs in the dual futile cycle for certain values of the parameters [43]. In fact it is known that there exist up to three steady states for given values of the total amounts and that there are never more than three. The proof of the existence result can be split into two steps. In the first step the equations for steady states are partly solved explicitly. This leaves a system of two equations for two unknowns. The second step involves taking a limit of these equations as a parameter ε tends to zero. This limit is essentially the Michaelis–Menten limit discussed above. Since we are dealing with steady states the factor ε in the equation for y plays no role and the limit is regular. In the limit a single equation for one variable is obtained and this is relatively easy

to analyze. It is possible to find cases where there are three solutions of the equation $F(x) = 0$ for steady states of the equation with $\varepsilon = 0$, all of which satisfy $dF/dx \neq 0$. This implies, using the implicit function theorem, that corresponding solutions exist for ε small but positive. This argument gives no information on the important issue of stability of these solutions. A steady state x_0 will only be observed in practice if it is stable. This means that if a solution starts close enough to x_0 it will stay close to x_0 for all future times. For example if the linearization at the equilibrium x_0 has only eigenvalues with strictly negative real parts, then the equilibrium x_0 is stable.

On the level of simulations multistationarity was already observed for the system with mass action kinetics in [29] and it was found that two of the three steady states are stable. Simulations in [31] indicated that these features are already present in the MM system. On the other hand until recently there was no mathematical proof of bistability for the dual futile cycle. A strategy suggested by what has been said up to now for obtaining such a proof is to first prove bistability for the MM system and then use GSPT to conclude the corresponding result for the mass action system. This strategy was carried out in [19] and in that paper we proved bistability. We now sketch the main lines of the proof.

In the previous section, we saw that the MM reduction is the singular limit as $\varepsilon \to 0$ of the system on the slow time scale Eq. (5), where $g(x, \tilde{y}) = 0 \Leftrightarrow \tilde{y} = h(x)$. Now consider the fast time scale, i.e. the same equations expressed in the original time t, augmented by the trivial evolution of the parameter ε. This system is called the extended system.

$$\begin{cases} \dot{x} = \varepsilon f(x, \tilde{y},) \\ \dot{\tilde{y}} = g(x, \tilde{y},) \\ \dot{\varepsilon} = 0 \end{cases} \tag{11}$$

The curve $\{(x, \tilde{y} = h(x), \varepsilon = 0)\}$ is a curve of equilibria in the extended system. The linearization of the extended system Eq. (11) at such an equilibrium admits two zero eigenvalues with the corresponding eigenvector being $(0, 0, 1)$ pointing in direction of ε orthogonally to the (x, y)-plane, and a second vector in the (x, y)-plane tangent to the curve $\{(x, h(x))\}$. If the linearization $D_y g(x, h(x), 0)$ admits only eigenvalues with strictly negative real parts, then the centre eigenspace (i.e. the eigenspace spanned by the eigenvectors associated to purely imaginary eigenvalues) is exactly two dimensional. The eigenspace is tangential to a manifold called the centre manifold: see [40] for details about center manifold theory. The (local) centre manifold $M^c(x, h(x), 0)$ of such an equilibrium is an invariant manifold containing all bounded solutions sufficiently near the equilibrium. The centre manifold M^c can be written as a graph of a function Ψ over the centre eigenspace:

$$M^c(x, h(x), 0) = \{(x, \Psi(x, \varepsilon), \epsilon), \varepsilon \text{ small}\}, \tag{12}$$

with $\Psi(x, 0) = h(x)$. The manifold M^c is tangent to the centre eigenspace of the extended system at each equilibrium $(x, h(x), 0)$. Because of the equation $\dot{\varepsilon} = 0$, the invariant two-dimensional centre manifold M^c is foliated by invariant 1-dimensional

Fig. 1 Sketch of the phase portrait of the extended system with a curve of equilibria $\{y = h(x) \equiv 0\}$. The one dimensional dynamics of the MM-reduced system consists of one unstable equilibrium connected via heteroclinic orbits to two stable equilibria. This dynamics persists on the invariant ε-leaves for small ε
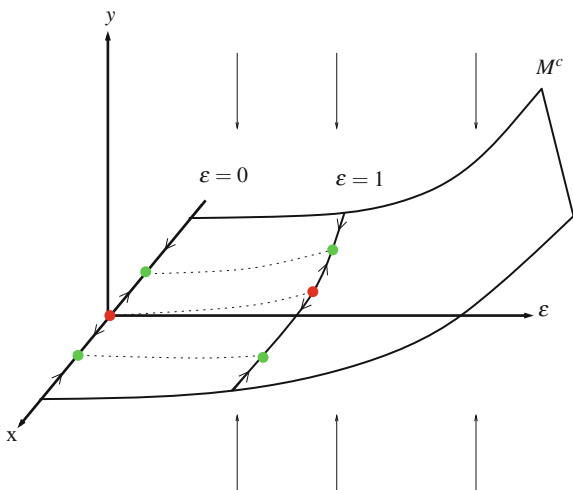
leaves $\varepsilon = constant$. If the leaf at $\varepsilon = 0$ consists of hyperbolic equilibria (i.e. the linearization there admits no purely imaginary eigenvalues) connected by heteroclinic orbits as depicted in Fig. 1, then this dynamics is preserved in the leaves at ε small. Furthermore, the linearization theorem of Shoshitaishvili (see [26], Theorem 5.4) tells us that, if $D_y g(x, h(x))$ has only stable eigenvalues, the center manifold M^c is attracting. Hence hyperbolic equilibria that are stable in the MM-reduced system Eq. (6) give rise to stable equilibria in the extended system. Undoing the scaling $\tilde{y} = \varepsilon y$ provides us with stable equilibria for the original mass-action system Eq. (4).

In order to apply GSPT in this context the main property to be checked concerns the eigenvalues of the matrix $A = D_y g(x, h(x))$. By this we mean the matrix of partial derivatives of the function g with respect to the variables y at a point $(x, h(x))$. The condition to be checked for the center manifold M^c to be attracting is that the real parts of these eigenvalues are negative. Fortunately in this case the calculation can be reduced to one for the eigenvalues of two by two matrices, which is relatively simple.

The remaining part of the argument is to prove bistability for the MM system. When this has been done and if the stable steady states are hyperbolic (i.e. the linearization of the system at those points has no eigenvalues with zero real parts) then GSPT tells us that these steady states continue to exist and be stable for ε small but non-zero. For more details we refer to [19]. Bistability for the MM system is proved using bifurcation theory and now some more information will be given concerning that technique. Consider a system of ordinary differential equations $\dot{x} = f(x, \alpha)$ and a steady state (x_0, α_0), i.e. $f(x_0, \alpha_0) = 0$. Here α denotes one or more parameters. The linearization of the system at (x_0, α_0) is the matrix of partial derivatives $A = D_x f(x_0, \alpha_0)$. If no eigenvalue of A has zero real part the equilibrium x_0 is said to be hyperbolic. Then for α close to α_0 there is a unique solution of $f(x_*(\alpha), \alpha) = 0$ with x_* close to x_0 by the implicit function theorem. The stability properties of the

solution are preserved, the dynamics nearby is the same as the dynamics of the linearized system by the Hartman–Grobman Theorem (see [17], Theorem 1.3.1). For instance if x_0 is stable then $x_*(\alpha)$ is stable. If, on the other hand, A has an eigenvalue whose real part is zero then (x_0, α_0) is said to be a bifurcation point and the qualitative dynamics of the system may change at that parameter value. For instance as the parameter is varied one steady state may split into several. In other words, new branches of equilibria may come into being at the critical parameter value α_0. Identifying a suitable bifurcation is a way of proving that several steady states exist for certain parameter values.

For example, consider a system $\dot{x} = f(x, \alpha)$ with one unknown x depending on two parameters, $\alpha = (\alpha_1, \alpha_2)$. Denote by a prime the partial derivative of a function of x and α with respect to x. Suppose that $f(0, 0) = 0, f'(0, 0) = 0, f''(0, 0) = 0$ and $f'''(0, 0) \neq 0$ and that an additional quantity depending on derivatives with respect to the parameters is non-zero. The eigenvalue of the linearization A that crosses zero depends on the two parameters. In this example there is only one eigenvalue of the Jacobian, which is $f'(0, 0) = 0$. When the above mentioned quantity is non-zero, it guarantees that the crossing happens at a non-zero velocity with respect to the parameters and transversally to the imaginary axis. This is called a transversality condition. See [26] for details. These are the defining properties of what is called a generic cusp bifurcation. There is a surface of equilibria over the two dimensional parameter space which develops a fold at $(0, 0)$. In a cusp region of the parameter space, three equilibria coexist - two stable ones and an unstable one. See Fig. 2. Then there are parameter values near zero for which the system has three steady states close to zero. The case of relevance for the examples considered in this paper is that where $f'''(0, 0) < 0$ and from now on we will only discuss that case. There two of the steady states close to zero are stable and one unstable. Now suppose there are several variables x_i and that at the point $(0, 0)$ the derivative $A = D_x f$ has a zero eigenvalue of multiplicity one. The kernel of A is of dimension one. The qualitative behaviour of solutions near the steady state is determined by the restriction of the dynamics to a curve, the one dimensional centre manifold, which is tangent to the kernel of A and invariant under the flow. While the local stable and unstable manifolds contain all initial conditions for solutions that converge exponentially to the equilibrium in

Fig. 2 Bifurcation diagram for a generic cusp bifurcation: the unstable branch of the surface of equilibria is *shaded*, as well as the region in the parameter plane where two stable and one unstable equilibria coexist
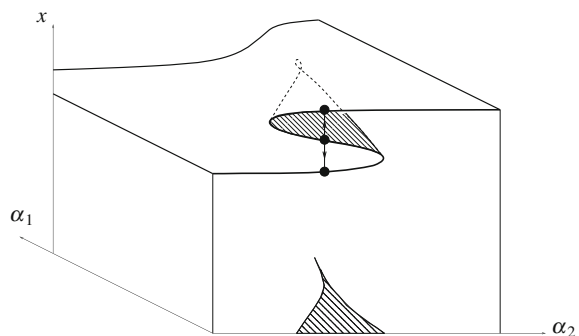
forward or backward time direction respectively, the center manifold contains local bounded dynamics that depends heavily on the nonlinear terms. In this way the general case may be reduced to the one-dimensional case already discussed when the kernel of A is of dimension one. In fact the dynamics in the stable and unstable directions corresponding to eigenvalues with nonzero real parts do not change. These are the main techniques used in the proof of bistability in [19].

It is clear that in order to linearize about a steady state we first have to have that steady state. It is not too difficult to find steady states since there are many parameters in the problem which can be varied. In [19] steady states were considered for which the concentrations of X and XPP are equal, since this simplifies the algebra. Moreover it was assumed that all Michaelis constants have a common value K. In this case the relation

$$\left(\frac{E_{\text{tot}}}{F_{\text{tot}}}\right)^2 = \frac{k_2 k_4}{k_1 k_3} \tag{13}$$

holds. A bifurcation point was found under the restriction that $q^2 = (k_1 k_4)/(k_2 k_3) < 1$. The bifurcation occurs when $K X_{\text{tot}} = \frac{2+q}{1-q}$.

It is important to note that here Michaelis–Menten reduction was carried out for the whole system and not for the two phosphorylation steps separately. The latter alternative leads to a different set of equations. It was used in [24], where the effect of embedding a MAPK cascade in a negative feedback loop was investigated. Consider, for instance, the dual futile cycle which is the third layer of the cascade in [24] and the equation for the unphosphorylated protein. It is of the form

$$\frac{d}{dt}[X] = -\frac{k_7 E_{\text{tot}}[X]}{K_7 + [X]} + \frac{k_7 F_{\text{tot}}[XP]}{K_{10} + [XP]} \tag{14}$$

which is clearly different from the corresponding equation in the MM system introduced above, even when all Michaelis constants are taken to be equal (which is done in the simulations of [24]).

The results just discussed only give limited information on the region of parameter space in which bistability occurs. In contrast, in [7] rigorous quantitative results on multistationarity were proved. Rather general conditions on the reaction constants were exhibited for which there are one or three steady states.

Bistability is important for the property of being a 'good switch': consider our system as an input–output relation where the input consists of the values of the conserved quantities and the output consists of the equilibrium reached by the system after a certain amount of time. For certain values of the input, the stable equilibrium reached by the system is unique and, say, on the lower part of the folded surface of equilibria. When the input enters the cusp region, the output remains on the lower part of the fold until the cusp region is left: at this point, the output switches to the upper part of the folded surface. In fact, the same phenomenon of switching is present when the parameter (input) is one dimensional and there exists a S-shaped curve of equilibria. See Fig. 3.

Fig. 3 The *input–output relation* follows the lower stable equilibria until it becomes unstable through a fold (also called saddle-node) bifurcation, then jumps to the upper stable branch. Hence such an input–output relation is a good switch
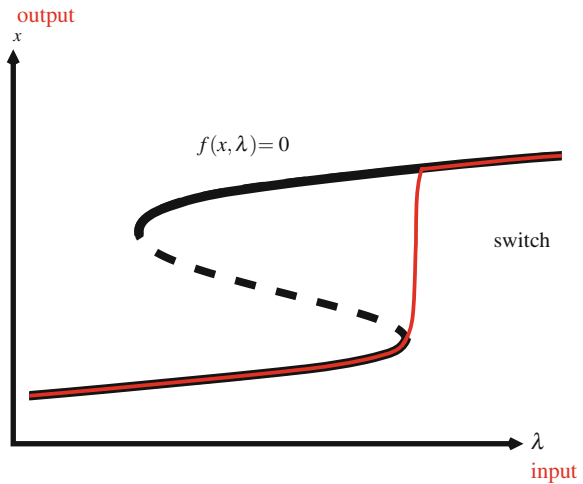
Sometimes when modelling phosphorylation systems the enzyme concentrations are not included explicitly and instead mass action kinetics is used for the substrates alone. If this is done for the cycle with two phosphorylations, or indeed for a cycle with any number of phosphorylations, a dynamical system is obtained which has a unique stationary solution to which all other solutions converge. This is because it can be shown that the system is a weakly reversible system of deficiency zero and the Deficiency Zero Theorem of chemical reaction network theory (see [11]) can be applied. This type of argument was used to prove corresponding results for the kinetic proofreading model of T cell activation in [38] and for the multiple phosphorylation of the transcription factor NFAT in [34]. These systems only describe small parts of the network involved in T cell activation, which also contains a MAPK cascade. A comprehensive model of this phenomenon presented in [1] is too large to be accessible by direct analytical investigation. Interestingly a very much simplified version of this model introduced in [13] reproduces some of the key features of T cell activation such as specificity, speed and sensitivity. In the simplified model the MAPK cascade is represented by a simple response function.

4 The MAPK Cascade

The starting point of this section is the model of the MAPK cascade introduced in [21]. Simulations in [33] revealed the presence of bistability and sustained oscillations in this model. Mathematically the latter correspond to periodic solutions, i.e. solutions which satisfy $x(t + T) = x(t)$ for some time interval T but are not steady states. In [33] similar results were obtained for the truncated cascade consisting of just the first two layers. Michaelis–Menten reduction for the MAPK cascade is made difficult

by the fact that there is not a clear division between substrates and enzymes. This issue was studied in [41]. A further development of these ideas in [42] indicated that periodic solutions already occur in the Michaelis–Menten limit. It was shown in [19] that a small modification of these ideas allows a Michaelis–Menten limit of the equations for the truncated cascade to be defined which is well-behaved in the sense of GSPT. Since the truncated system contains a species, X_1P, which is a product in the first layer and an enzyme in the second layer, the ε-scaling of the MM-reduction has to be carried out using two different powers of ε. We first define a new variable $\overline{X_1}$ replacing $[X_1P]$ as follows.

$$\overline{X_1} := [X_1P] + [X_2 \cdot X_1P] + [X_2P \cdot X_1P],$$

The concentration vector is split into three vectors v_0, v_1, v_2. The vector v_2 is the vector of concentrations of species containing the enzymes of the first layer of the cascade, alone or in a complex, i.e. $v_2 = ([E_1], [F_1], [X_1 \cdot E_1], [X_1P \cdot F_1])$. This vector is rescaled by $\tilde{v}_2 = \varepsilon^2 v_2$. The vector v_1 is the vector of concentrations of species containing X_1 or the enzymes $X_1P = E_2$ and F_2 of the second layer of the cascade, alone or in a complex, i.e. $v_1 = (\overline{X_1}, [X_1], [X_1P], [E_2], [X_2 \cdot X_1P], [X_2P \cdot X_1P], [X_2P \cdot F_2], [X_2PP \cdot F_2])$. This vector is rescaled by $\tilde{v}_1 = \varepsilon v_1$. Finally, the vector v_0 contains the concentrations of the remaining species, i.e. $x = ([X_2], [X_2P], [X_2PP])$ and is not rescaled. Furthermore the reaction constants of the first layer are also rescaled by ε. A slow time variable $\tau = \varepsilon t$ is introduced: the time derivative w.r.t. t is denoted by an upper dot while the time derivative w.r.t. τ is denoted by $'$. Using conserved quantities to reduce the dimension of the concentration vectors and the new variable $\overline{X_1}$, we get a system of the form

$$\begin{cases} x' = f(x, y, z), \\ \varepsilon y' = g(x, y, z), \end{cases} \tag{15}$$

where $x = (\overline{X_1}, [X_2], [X_2PP])$ and $y=([X_1 \cdot E_1], [X_1P \cdot F_1], [X_2 \cdot X_1P], [X_2P \cdot X_1P], [X_2P \cdot F_2], [X_2PP \cdot F_2])$. The limit $\varepsilon \to 0$ of this system allows a MM-reduction that is well-behaved in terms of GSPT. For more details see [19, 20]. This result was extended to the full cascade in [20].

The facts just listed indicate that the strategy used to prove bistability in the dual futile cycle might also be used to prove the existence of sustained oscillations in the truncated MAPK cascade, i.e. layers 1 and 2 of cascade Eq. (1). Here the relevant type of bifurcation is a Hopf bifurcation where the linearization at an equilibrium admits a pair of imaginary eigenvalues for a critical parameter. By a classical theorem of Hopf, if under variation of a parameter a pair of complex conjugate eigenvalues of the linearization passes through the imaginary axis (away from zero) with non-zero velocity then there exist periodic solutions for at least some parameter values. See [17, 26] for details. In [20] it was proved that Hopf bifurcations occur in the MM system for the MAPK cascade. As a consequence periodic solutions occur. If an additional genericity condition (hyperbolicity of the periodic orbit) were satisfied

then it could further be concluded using GSPT that periodic solutions also occur in the mass action system for the truncated MAPK cascade. In fact it has not yet been possible to prove hyperbolicity. Instead it was proved that the Hopf bifurcation itself can be lifted to the mass action system and this then gives the existence of periodic solutions of that system. Unfortunately these arguments give no information on the stability of the periodic solutions involved. It is interesting to look at this situation in the light of results on feedback loops. It has been proved that a system can only admit a stable periodic solution if it includes a directed negative feedback loop [4, 35]. It can easily be checked directly that this condition holds in the case of the MM system for the truncated MAPK cascade.

The results for the truncated cascade imply analogous results for the full cascade by another application of GSPT. What must be shown is that the truncated cascade can be represented as a limit of the full cascade which is well-behaved in the sense of GSPT. Consider the MM system for the full cascade. Let Z be the concentration of a protein in the first or second layer and define a new variable by $\tilde{Z} = \varepsilon^{-1}Z$. Let c_i be any of the rate constants in the third layer and define $\tilde{c}_i = \varepsilon c_i$. The transformed system has a limit for $\varepsilon \to 0$ which is well-behaved in the sense of GSPT and the limiting system is the MM system for the truncated cascade. Thus in the context of the MM system the Hopf bifurcation can be lifted from the truncated to the full cascade. It can then be further lifted from the MM system for the full cascade to the mass action system.

In [32] an *in vitro* model of the MAPK cascade was introduced. The substances involved are modified in such a way that certain features of the reaction network are modified. In the first layer Raf is constitutively active which means that for modelling this layer can be ignored. In the third layer ERK can only be phosphorylated once, on tyrosine and not on threonine. (In the wild type system MEK has the unusual property of being a dual specificity kinase which can phosphorylate both threonine and tyrosine.) This leads to a cascade with two layers where the first has two phosphorylation steps and the second only one:


(16)
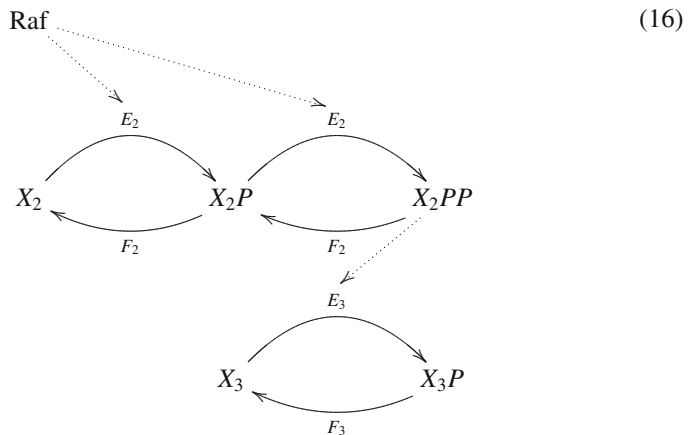
Here $X_3 = ERK$. This was modelled mathematically in a certain way in [32] and it was proved that for that system of equations there is a unique steady state and all other solutions converge to it. If, on the other hand, the system is modelled in direct analogy to what was done in [21] a system is obtained which might potentially admit Hopf bifurcations and hence periodic solutions. It was written down in [20] but attempts to prove the existence of Hopf bifurcations using the methods applied to the truncated MAPK cascade have not succeeded. Simulations done in [46] indicate that there may be chaotic behaviour in the MAPK cascade. The approach of the authors was via (numerical) bifurcation theory. They discovered the presence of fold-Hopf bifurcations (where the linearization of the system at the bifurcation point has one zero and a pair of non-zero imaginary eigenvalues) and Hopf-Hopf bifurcations (where the linearization of the system at the bifurcation point has two pairs of non-zero imaginary eigenvalues). See [26] for more details on these types of bifurcations. Bifurcations of these types are often associated with chaos. Simulations for initial data close to the bifurcation points gave pictures consistent with the presence of chaotic behaviour.

In [33] a heuristic explanation for the existence of oscillations in the MAPK cascade was given, involving the embedding of a bistable system in a negative feedback loop. This point of view played no role in the proof of the existence of periodic solutions using bifurcation theory which has just been discussed. It could, however, in principle lead to an alternative proof of that result which could also provide information on the stability of the periodic solution. A corresponding strategy, which makes use of the Conley index (see [6]), has been developed and applied to a system related to that considered in [24]. More details can be found in [3, 14, 15].

5   Embedding the Cascade in Feedback Loops

Given that modelling predicts oscillatory behaviour in the MAPK cascade it is of great interest to try to observe it experimentally. This has been done in [36]. Oscillations were found in the concentration of activated (i.e. doubly phosphorylated) ERK which had a period of about fifteen minutes and lasted up to ten hours. This effect was monitored by observing the translocation of ERK tagged with GFP between the cytosol and the nucleus. This is relevant because activated ERK is imported into the nucleus and inactive ERK is exported into the cytosol. Mathematical models presented in [36] are more complicated than the basic model of [21] in several ways.

One is that a two-compartment model is used so that transport between cytosol and nucleus is included. This network is sketched in Fig. 4 below, where Raf $= X_1$, MEK $= X_2$, ERK $= X_3$. A second is that the fact is included that ERK and MEK which are not fully phosphorylated can bind to each other ($\sim\sim$/ /$\sim\sim$ in Fig. 4). This protects ERK from phosphorylation by MEK and thus represents a kind of negative feedback. Note that the tendency of this type of feedback to encourage bistability was already pointed out in [27]. A third way is that a negative feedback due the repression of SOS by ERK is included (———/   in Fig. 4). This is important since
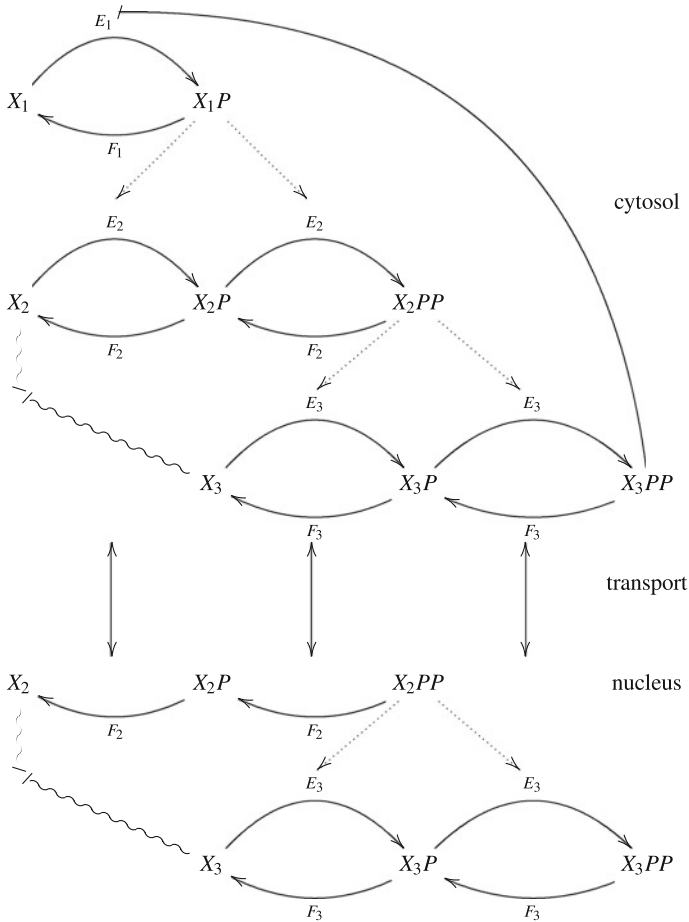
Fig. 4 Two-compartment model with a full MAPK cascade in the cytosol, a lower half of the MAPK cascade in the nucleus, transport of X_3PP from the cytosol to the nucleus and transport of X_3 from the nucleus to the cytosol

SOS influences the rate of phosphorylation of Raf. This last effect is modelled in a simple phenomenological manner. It was discovered that certain aspects of the experimental data do not fit the mathematical model with an isolated cascade. In particular this concerns the facts that the oscillations are found for a large range of total amounts of ERK and that the period of the oscillations is found to depend only weakly on the total amount of EGF, the substance being used to stimulate the cascade. It is assumed that the phosphorylation of Raf is proportional to the amount of EGF. Incorporating the negative feedback loop via SOS in the model allows the experimental results to be reproduced.

Yet another type of negative feedback which may lead to oscillations arises via the competition of a substrate of ERK with a phosphatase being reduced by increasing degradation of the activated substrate [28]. In this paper the authors present both mass action and reduced models and find periodic solutions in simulations.

6 Alternative Phosphorylation Mechanisms

In this paper we have concentrated on distributive phosphorylation. If this is partly replaced by processive (but still sequential) phosphorylation then this often results in simpler dynamics. For instance it was proved in [8] that when phosphorylation, dephosphorylation or both are replaced in the dual futile cycle by their processive versions, then there is a unique steady state for fixed values of the total amounts. This follows from the deficiency one algorithm of chemical reaction network theory. The result was generalized to the analogue of the multiple futile cycle with strictly processive and sequential phosphorylation in [9]. In addition it was proved that all other solutions converge to the steady state. Note that other types of (partially) processive phosphorylation may also be considered [18].

One of the most important roles of oscillations in biology is that they can act as clocks, for instance those defining circadian rhythms. Many of these clocks are dependent on translation but a clock has been found in cyanobacteria which is not. It uses only phosphorylation states of the proteins KaiA, KaiB and KaiC. This has been demonstrated by reconstructing the clock *in vitro* [30]. In KaiC the phosphorylation is cyclic rather than sequential. In other words the first of two sites to be phosphorylated is also the first to be dephosphorylated. This motivated the study of oscillations in dual phosphorylation models more general than the usual dual futile cycle [23]. In that paper the case of unordered phosphorylation was considered, i.e. that where the two (de-)phosphorylations may take place in any order. Simulations indicate that this is sufficient to produce sustained oscillations.

While the MAPK cascade is a type of phosphorylation system of central importance in eukaryotic signalling pathways, signalling pathways in prokaryotes more often use a different type of phosphorylation system known as a two-component system [39]. These are uncommon in eukaryotes and unknown in mammals. The central mechanism is as follows. The two components are proteins generically called HK and RR. The protein HK is a histidine kinase which, under appropriate conditions, phosphorylates itself on a histidine. RR, the response regulator, catalyzes the transfer of the phosphate group from the histidine of HK to an aspartate in RR. In this way the RR is activated. HK can also dephosphorylate RR.

What is the advantage of the process of phosphorylation of RR taking place in two steps rather than directly? It has been suggested that the motivation is that the two-step process leads to absolute concentration robustness [37]. This means that the output signal is independent of the total concentrations of the enzymes, so that the system achieves independence from the stochastic variation in protein levels between different cells.

Bistability has been observed in two-component systems. The conditions for bistability in these systems have been discussed in [22]. This dynamical property has also been studied in [2]. The case treated there is that of a split kinase. This means that instead of one kinase HK phosphorylating itself one kinase binds to a second which then phosphorylates the first. These authors investigated bistability in different models using both dynamical simulations and the Chemical Reaction Network Toolbox. The latter is a computer programme which provides positive or negative results on bistability on the basis of chemical reaction network theory.

Some signalling pathways include phosphorelays in which the phosphate group is transferred from one species to the next. They also have a cascade structure, in many cases with four layers. In some layers, a phosphate group can easily be lost by hydrolysis. Furthermore some species can be bifunctional, i.e. able to give as well as take a phosphate group to/from the species on the next layer. As for the MAPK cascade, such phosphorelays can be embedded in transcriptional feedback loops. See for example [25] where mathematical results have been obtained on the form of response functions and bistability in certain cases. There are many possible topologies for these systems and questions arise which are similar to those which could be posed for the MAPK cascade: how complicated should the architecture of the network be in order to achieve a 'good switch' property of the input–output relation? We saw that bistability could give an answer. Furthermore the methods explained in the previous sections could give insight on the dynamics beyond the steady states (heteroclinic structure, oscillations).

7 Summary and Outlook

The MAPK cascade is a system of chemical reactions occurring as a part of many signal transduction networks. This cascade on its own has the potential to give rise to complicated dynamical behaviour such as multistability, sustained oscillations and even chaos. The positive and negative feedback loops in which the cascade is embedded in real biological systems present even more possibilities for generating this type of phenomena. One way of trying to obtain deeper insights into the conditions leading to different types of dynamical behaviour is to carry out mathematically rigorous investigations of systems of ordinary differential equations modelling the cascade. In this context it is natural to start by studying small building blocks in detail and build up from there. In particular we can pass from single layers of the cascade to the full cascade without feedback and then the full cascade with feedback.

In the first four sections of this paper the results on the MAPK cascade or parts of it which have been proved rigorously are summarized. In the case of a single phosphorylation loop it could be shown that the dynamics are simple: there is only one steady state and it is globally stable. For a series of several phosphorylation loops it has been known for some time that multiple stationary solutions are possible and information is available on their number. More recently it could be proved that for a system with two loops there are parameter values which give bistability, thus confirming previous

conclusions based on numerical simulations and heuristic considerations. It could also be proved that for the MAPK cascade (or even for the first two layers of it) there exist periodic solutions. An introduction is given to some of the mathematical techniques used to obtain these results, geometric singular perturbation theory and bifurcation theory.

Cases are pointed out where further progress would be desirable. It could not yet be proved that the oscillations in the MAPK cascade are stable although simulations indicate that this is the case. In fact if they were not stable then it would be hard to find them by simulations. There are also no analytical results available on the presence of chaos. Obtaining results of this kind would require analyzing bifurcations much more complicated than those treated up to now. It would also be valuable to obtain more results which in addition to showing that certain types of behaviour can occur in a given system also give useful information on the range of parameters for which it occurs.

The fifth section contains some remarks of the influence of feedback loops on the dynamics of the cascade. This should be a fruitful field of application for the techniques already developed for the cascade on its own. Interestingly it seems based on simulations that the range of parameters for which bistability or sustained oscillations occur is increased by the presence of feedback loops and this may be important for the question of whether these features are present for biologically reasonable parameters and if so, whether the ranges of these parameters are large enough to allow the oscillations to be observed experimentally.

The sixth section discusses some generalizations to other types of phosphorylation systems. The focus in this paper is on distributive and sequential phosphorylation and this mirrors a more general tendency in the theoretical literature on this subject. Replacing distributive by processive phosphorylation in some reactions appears to lead to a simplification of the dynamics. On the other hand distributive unordered phosphorylation can lead to oscillations not present in the corresponding sequential case. Here again there is a lot of potential for further analytical investigations. Remarks are also made on the relations to signal transduction networks based on two-component systems.

Phosphorylation systems involved in signal transduction give rise to many challenges for mathematical analysis which have only started to be addressed. It is to be hoped that further progress in this direction will be rewarded by a deeper understanding of the mechanisms of the biological processes involved.

References

1. Altan-Bonnet, G. and Germain, R.N. 2005 Modelling T cell antigen discrimination based on feedback control of digital ERK responses. PloS Biol. 3 (11): e356.
2. Amin, M., Porter, S. L. and Soyer, O. S. 2013 Split histidine kinases enable ultrasensitivity and bistability in two-component signalling networks. PloS Comp. Biol. 9 (3): e1002949.

3. Angeli, D., Ferrell, J. E. Jr. and Sontag, E. D. 2004 Detection of multistability, bifurcation and hysteresis in a large class of biological positive-feedback systems. Proc. Natl. Acad. Sci. USA 101, 1822–1827.

4. Angeli, D., Hirsch, M. and Sontag, E. 2009 Attractors in coherent systems of differential equations. J. Diff. Eq. 246, 3058–3076.

5. Angeli, D. and Sontag, E. D. 2006 Translation-invariant monotone systems and a global convergence result for enzymatic futile cycles. Nonlin. Anal. RWA 9, 128–140.

6. Conley, C. 1978 Isolated invariant sets and the Morse index. CBMS Regional Conference Series in Mathematics 38.

7. Conradi, C. and Mincheva, M. 2014 Catalytic constants enable the emergence of bistability in dual phosphorylation. Royal Society Interface 11, 20140158.

8. Conradi, C., Saez-Rodriguez, J., Gilles, E.-D. and Raisch, J. 2005 Using chemical reaction network theory to discard a kinetic mechanism hypothesis. IEEE Syst. Biol. 152, 243–248.

9. Conradi, C. and Shiu, A. 2015 A global convergence result for processive multisite phosphorylation systems. Bull. Math. Biol. 77, 126–155.

10. Errami, H., Eiswith, M., Grigoriev, D., Seiler, W. M. and Weber, A. 2015 Detection of Hopf bifurcations in chemical reaction networks using convex coordinates. J. Comp. Phys. 291, 279–302.

11. Feinberg, M. 1980 Lectures on chemical reactions networks. Available at https://crnt.osu.edu/lectures-chemical-reaction-networks.

12. Fenichel, N. 1979 Geometric perturbation theory for ordinary differential equations. J. Diff. Eq. 31, 53–98.

13. François, P., Voisinne, G., Siggia, E. D., Altan-Bonnet, G. and Vergassola, M. 2013 Phenotypic model for early T cell activation displaying sensitivity, specificity and antagonism. Proc. Natl. Acad. Sci. USA. 110 E888–E897.

14. Gedeon, T. 2010 Oscillations in monotone systems with a negative feedback. SIAM J. Dyn. Sys. 9, 84–112.

15. Gedeon, T. and Sontag, E. D. 2007 Oscillations in multi-stable monotone systems with slowly varying feedback. J. Diff. Eq. 239, 273–295.

16. Goldbeter, A. and Koshland, D. E., Jr. 1981 An amplified sensitivity arising from covalent modification in biological systems. Proc. Natl. Acad. Sci. USA 78, 6840–6844.

17. Guckenheimer, J. and Holmes, P. 1983 Nonlinear oscillations, dynamical systems, and bifurcations of vector fields. Springer.

18. Gunawardena, J. 2007 Distributivity and processivity in multisite phosphorylation can be distinguished through steady-state invariants. Biophys. J. 93, 3828–3834.

19. Hell, J. and Rendall, A. D. 2015 A proof of bistability for the dual futile cycle. Nonlin. Anal. RWA. 24, 175–189.

20. Hell, J. and Rendall, A. D. 2016 Sustained oscillations in the MAP kinase cascade. Math. Biosci. 282, 162–173.

21. Huang, C.-Y. F. and Ferrell, J. E., Jr. 1996 Ultrasensitivity in the mitogen-activated protein kinase cascade. Proc. Natl. Acad. Sci. USA 93, 10078–10083.

22. Igoshin, O. A., Alves, R. and Savageau, M. A. 2008 Hysteretic and graded responses in bacterial two-component signal transduction. Mol. Microbiol. 68, 1196–1215.

23. Jolley, C. C., Ode, K. L. and Ueda, H. R. 2012 A design principle for a posttranslational biochemical oscillator. Cell Reports 2, 938–950.

24. Kholodenko, B. N. 2000 Negative feedback and ultrasensitivity can bring about oscillations in the mitogen activated protein kinase cascades. Eur. J. Biochem. 267, 1583–1588.

25. Kothamachu, V.B., Feliu, E., Wiuf, C., Cardelli, L., Soyer, O.S. 2013 Phosphorelays provide tunable signal processing capabilities for the cell. PLoS Comp. Biol. 9(11):e1003322.

26. Kuznetsov, Y. 1995 Elements of Bifurcation Theory. Springer, Berlin.

27. Legewie, S., Schoeberl, B., Blüthgen, N, and Herzel, H. 2007 Competing docking interactions can bring about bistability in the MAPK cascade. Biophys. J. 93, 2279–2288.

28. Liu, P., Kevrekidis, I. G. and Shvartsman, S. V. 2011 Substrate-dependent control of ERK phosphorylation can lead to oscillations. Biophys. J. 101, 2572–2581.

29. Markevich, N. I., Hoek, J. B. and Kholodenko, B. N. 2004 Signaling switches and bistability arising from multisite phosphorylation in protein kinase cascades. J. Cell Biol. 164, 353–359.
30. Nakajima, T., Satomi, Y., Kitayama, Y., Terauchi, K., Kiyohara, R., Takao, T. and Kondo, T. 2005 Reconstitution of circadian oscillation of cyanobacterial KaiC phosphorylation in vitro. Science 308, 414–415.
31. Ortega, F., Garcés, J. L., Mas, F., Kholodenko, B. N. and Cascante, M. 2006 Bistability from double phosphorylation in signal transduction. FEBS J. 273, 3915–3926.
32. Prabakaran, S., Gunawardena, J. and Sontag, E. D. 2014 Paradoxical results in perturbation-based network reconstruction. Biophys. J. 106, 2720–2728.
33. Qiao, L., Nachbar, R. B., Kevrekidis, I. G. and Shvartsman, S. Y. 2007 Bistability and oscillations in the Huang-Ferrell model of MAPK signaling. PloS Comp. Biol. 3, 1819–1826.
34. Rendall, A. D. 2012 Mathematics of the NFAT signalling pathway. SIAM J. Appl. Dyn. Sys. 11, 988–1006.
35. Richard, A. and Comet, J. P. 2010 Stable periodicity and negative circuits in differential systems. J. Math. Biol. 63, 593–600.
36. Shankaran, H., Ippolito, D. L., Chrisler, W. B., Resat, H., Bollinger, N., Opresko, L. K. and Wiley, H. S. 2009 Rapid and sustained nuclear-cytoplasmic ERK oscillations induced by epidermal growth factor. Mol. Sys. Biol. 5, 332.
37. Shinar, G. and Feinberg, M. 2010 Structural sources of robustness in biochemical reaction networks. Science 327, 1389–1391.
38. Sontag E. D. 2001 Structure and stability of certain chemical networks and applications to the kinetic proofreading model of T-cell receptor signal transduction. IEEE Trans. Automat. Contr. 46, 1028–1047.
39. Stock, A. M., Robinson, V. L. and Goudreau, P. N. 2000 Two-component signal transduction. Ann. Rev. Biochem. 69, 183–215.
40. Vanderbauwhede, A. 1989 Centre Manifolds, Normal Forms and Elementary Bifurcations. Dynamics Reported 2, 89–169.
41. Ventura, A. C., Sepulchre, J.-A. Merajver, S. D. 2008 A hidden feedback in signalling cascades is revealed. PLoS Comp. Biol. 4(3):e1000041.
42. Ventura, A. C. and Sepulchre, J.-A. 2013 Intrinsic feedbacks in MAPK signalling cascades lead to bistability and oscillations. Acta Biotheor. 61, 59–78.
43. Wang, L. and Sontag, E. D. 2008 On the number of steady states in a multiple futile cycle. J. Math. Biol. 57, 29–52.
44. Wang, L. and Sontag, E. D. 2008 Singularly perturbed monotone systems and an application to double phosphorylation cycles. J. Nonlin. Sci. 18, 527–550.
45. Widmann, C., Gibson, G., Jarpe, M. B. and Johnson, G. L. 1999 Mitogen-activated protein kinase: conservation of a three-kinase module from yeast to human. Physiol. Rev. 79, 143–180.
46. Zumsande, M. and Gross, T. 2010 Bifurcations and chaos in the MAPK signalling cascade. J. Theor. Biol. 265, 481–491.

Numerical Treatment of the Filament-Based Lamellipodium Model (FBLM)

Angelika Manhart, Dietmar Oelz, Christian Schmeiser and Nikolaos Sfakianakis

Abstract We describe in this work the numerical treatment of the Filament-Based Lamellipodium Model (FBLM). This model is a two-phase two-dimensional continuum model, describing the dynamics of two interacting families of locally parallel F-actin filaments. It includes, among others, the bending stiffness of the filaments, adhesion to the substrate, and the cross-links connecting the two families. The numerical method proposed is a Finite Element Method (FEM) developed specifically for the needs of this problem. It is comprised of composite Lagrange–Hermite two-dimensional elements defined over a two-dimensional space. We present some elements of the FEM and emphasize in the numerical treatment of the more complex terms. We also present novel numerical simulations and compare to in-vitro experiments of moving cells.

1 Introduction

The lamellipodium is a flat cell protrusion functioning as a motility organelle in protrusive cell migration [28]. It is a very dynamic structure mainly consisting of a network of branched actin filaments. These are semi-elastic rods that represent the polymer form of the protein actin. They are continuously remodeled by polymeriza-

A. Manhart · C. Schmeiser
Faculty of Mathematics, University of Vienna, Oskar-Morgenstern Platz 1,
1090 Vienna, Austria
e-mail: angelika.manhart@univie.ac.at

C. Schmeiser
e-mail: christian.schmeiser@univie.ac.at

D. Oelz
Courant Institute of Mathematical Sciences, New York University,
251 Mercer Street, New York, NY 10012-1185, USA
e-mail: dietmar@cims.nyu.edu

N. Sfakianakis (✉)
Johannes-Gutenberg University, Staudungerweg 9, 55099 Mainz, Germany
e-mail: sfakiana@uni-mainz.de

tion and depolymerization and therefore undergo treadmilling [2]. Actin associated cross-linker proteins and myosin motor proteins integrate them into the lamellipodial meshwork which plays a key role in cell shape stabilization and in cell migration. Different modes of cell migration result from the interplay of protrusive forces due to polymerization, actomyosin dependent contractile forces and regulation of cell adhesion [9].

The first modeling attempts have resolved the interplay of protrusion at the front and retraction at the rear in a one-dimensional spatial setting [1, 6]. Two-dimensional continuum models were developed in order to include the lateral flow of F-actin along the leading edge of the cell into the quantitative picture. Those models can explain characteristic shapes of amoeboid cell migration [21, 22] on two-dimensional surfaces as well as the transition to mesenchymal migration [23].

One of the still unresolved scientific questions concerns the interplay between macroscopic observables of cell migration and the microstructure of the lamellipodium meshwork. Specialized models have been developed separately from the continuum approach to track microscopic information on filament directions and branching structure [8, 11, 24]. However, solving fluid-type models that describe the whole cytoplasm while retaining some information on the microstructure of the meshwork has turned out to be challenging. One approach is to formulate hybrid models [14], another one to directly formulate models on the computational, discrete level [13]. Recently the approach to directly formulate a computational model has been even extended into the three-dimensional setting making use of a finite element discretization [15].

In an attempt to create a simulation framework that addresses the interplay of macroscopic features of cell migration and the meshwork structure the Filament-Based Lamellipodium Model (FBLM) has been developed. It is a two-dimensional, two-phase, anisotropic continuum model for the dynamics of the lamellipodium network which retains key directional information on the filamentous substructure of this meshwork [20].

The model has been derived from a microscopic description based on the dynamics and interaction of individual filaments [18], and it has by recent extensions [12] reached a certain state of maturity. Since the model can be written in the form of a generalized gradient flow, numerical methods based on optimization techniques have been developed [19, 20]. Numerical efficiency had been a shortcoming of this approach. This has led to the development of a Finite Element numerical method which is presented in this article alongside simulations of a series of migration assays (Figs. 1 and 2).

2 Mathematical Modeling

In this section the FBLM will be sketched (see [12] for more detail). The main unknowns of the model are the positions of the actin filaments in two locally parallel families (denoted by the superscripts $+$ and $-$). Each of these families covers a
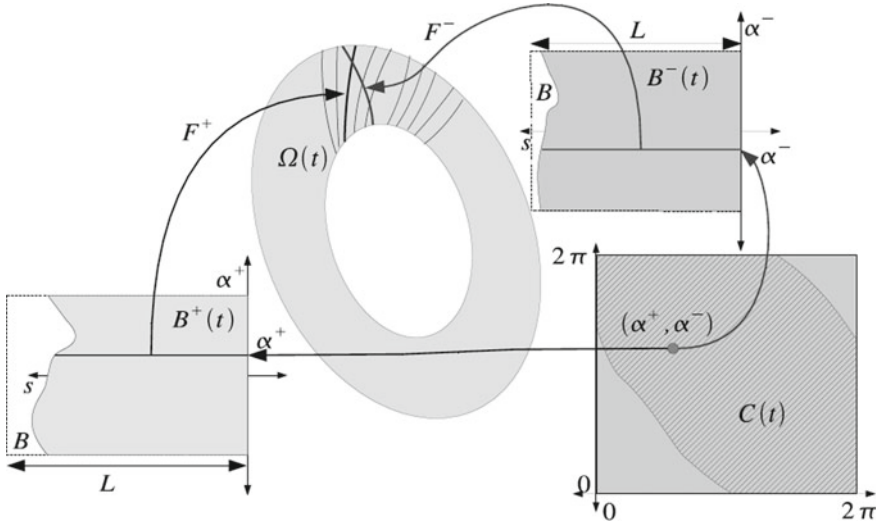
Fig. 1 Graphical representation of (3); showing here the lamellipodium $\Omega(t)$ "produced" by the mappings $\mathbf{F}^\pm$ and the crossing–filament domain $\mathscr{C}$
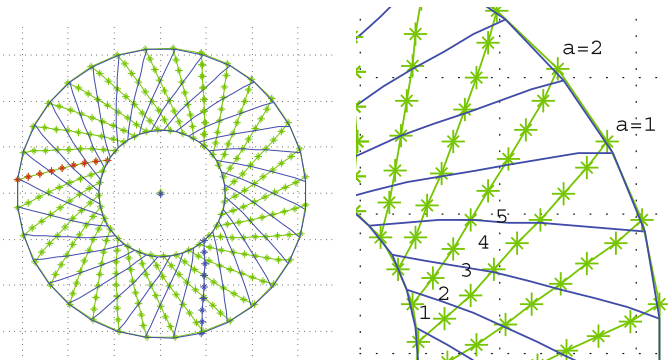

Fig. 2 Discretized lamellipodium (*left*) and lamellipodium fragment (*right*)

topological ring with all individual filaments connecting the inner boundary with the outer boundary. The outer boundaries are the physical leading edge and therefore identical, whereas the inner boundaries of the two families are artificial and may be different. Filaments are labeled by $\alpha \in [0, 2\pi)$, where the interval represents a one-dimensional torus, which means that in the following all functions of α are assumed periodic with period 2π. The maximal arclength of the filaments in an infinitesimal element $d\alpha$ of the $\pm$-family at time t is denoted by $L^\pm(\alpha, t)$, and an arclength parametrization of the filaments is denoted by $\{\mathbf{F}^\pm(\alpha, s, t) : -L^\pm(\alpha, t) \leq s \leq 0\} \subset \mathbb{R}^2$, where the leading edge corresponds to $s = 0$, i.e.

$$\left\{\mathbf{F}^+(\alpha, 0, t) : 0 \le \alpha < 2\pi\right\} = \left\{\mathbf{F}^-(\alpha, 0, t) : 0 \le \alpha < 2\pi\right\} \qquad \forall\, t \,, \qquad (1)$$

which together with

$$\left|\partial_s \mathbf{F}^\pm(\alpha, s, t)\right| = 1 \qquad \forall\, (\alpha, s, t) \,, \qquad (2)$$

constitutes constraints for the unknowns $\mathbf{F}^\pm$. The second constraint is connected to an *inextensibility* assumption on the filaments, which implies that s can also be interpreted as a monomer counter along filaments.

We expect that different filaments of the same family do not intersect each other, and each plus-filament crosses each minus-filament at most once. The first condition is guaranteed by $\det(\partial_\alpha \mathbf{F}^\pm, \partial_s \mathbf{F}^\pm) > 0$, where the sign indicates that the labeling with increasing α is in the clockwise direction. The second condition uniquely defines $s^\pm = s^\pm(\alpha^+, \alpha^-, t)$ such that $\mathbf{F}^+(\alpha^+, s^+, t) = \mathbf{F}^-(\alpha^-, s^-, t)$, for all $(\alpha^+, \alpha^-) \in \mathscr{C}(t)$, the set of all pairs of crossing filaments. It has to be noted that the validity of these properties is not guaranteed. For this and other reasons finite-time breakdown of the model cannot be excluded, although elements of the model like filament repulsion (see below) provides a regularization. As a consequence of the above assumptions, there are coordinate transformations $\psi^\pm : (\alpha^\mp, s^\mp) \mapsto (\alpha^\pm, s^\pm)$ such that

$$\mathbf{F}^\mp = \mathbf{F}^\pm \circ \psi^\pm \,.$$

In the following, we shall concentrate on one of the two families and skip the superscripts except that the other family is indicated by the superscript $*$. The heart of the FBLM is the force balance

$$0 = \underbrace{\mu^B \partial_s^2 \left(\eta \partial_s^2 \mathbf{F}\right)}_{\text{bending}} - \underbrace{\partial_s \left(\eta \lambda_{\text{inext}} \partial_s \mathbf{F}\right)}_{\text{inextensibility}} + \underbrace{\mu^A \eta D_t \mathbf{F}}_{\text{adhesion}} \qquad (3)$$
$$+ \underbrace{\partial_s \left(p(\rho) \partial_\alpha \mathbf{F}^\perp\right) - \partial_\alpha \left(p(\rho) \partial_s \mathbf{F}^\perp\right)}_{\text{pressure}}$$
$$\pm \underbrace{\partial_s \left(\eta \eta^* \widehat{\mu^T} (\phi - \phi_0) \partial_s \mathbf{F}^\perp\right)}_{\text{twisting}} + \underbrace{\eta \eta^* \widehat{\mu^S} \left(D_t \mathbf{F} - D_t^* \mathbf{F}^*\right)}_{\text{stretching}} \,,$$

where the notation $\mathbf{F}^\perp = (F_1, F_2)^\perp = (-F_2, F_1)$ has been used. For fixed s and t, the function $\eta(\alpha, s, t)$, is the number density of filaments of length at least $-s$ at time t with respect to α. Its dynamics and that of the maximal length $L(\alpha, t)$ will not be discussed here. It can be modeled by incorporating the effects of polymerization, depolymerization, branching, and capping (see [12]). We only note that faster polymerization (even locally) leads to wider lamellipodia.

The first term on the right hand side of (3) describes the filaments' resistance against bending with the stiffness parameter $\mu^B > 0$. The second term is a tangential tension force, which arises from incorporating the inextensibility constraint (2) with the Lagrange multiplier $\lambda_{\text{inext}}(\alpha, s, t)$. The third term describes friction of

the filament network with the nonmoving substrate (see [18] for its derivation as a macroscopic limit of the dynamics of transient elastic adhesion linkages). Since filaments polymerize at the leading edge with the polymerization speed $v(\alpha, t) \geq 0$, they are continuously pushed into the cell with that speed, and the material derivative

$$D_t \mathbf{F} := \partial_t \mathbf{F} - v \partial_s \mathbf{F}$$

is the velocity of the actin material relative to the substrate. For the modeling of v see [12].

The second line of (3) models a pressure effect caused by Coulomb repulsion between neighboring filaments of the same family with pressure $p(\rho)$, where the actin density in physical space is given by

$$\rho = \frac{\eta}{|\det(\partial_\alpha \mathbf{F}, \partial_s \mathbf{F})|} . \tag{4}$$

Finally, the third line of (3) models the interaction between the two families caused by transient elastic cross-links and/or branch junctions. The first term describes elastic resistance against changing the angle $\phi = \arccos(\partial_s \mathbf{F} \cdot \partial_s \mathbf{F}^*)$ between filaments away from the angle ϕ_0 of the equilibrium conformation of the cross-linking molecule. The last term describes friction between the two families analogously to friction with the substrate. The friction coefficients have the form

$$\widehat{\mu^{T,S}} = \mu^{T,S} \left| \frac{\partial \alpha^*}{\partial s} \right| ,$$

with $\mu^{T,S} > 0$, and the partial derivative refers to the coordinate transformation ψ^*, which is also used when evaluating partial derivatives of $\mathbf{F}^*$.

The system (3) is considered subject to the boundary conditions

$$- \mu^B \partial_s \left(\eta \partial_s^2 \mathbf{F} \right) - p(\rho) \partial_\alpha \mathbf{F}^\perp + \eta \lambda_{\text{inext}} \partial_s \mathbf{F} \mp \eta \eta^* \widehat{\mu^T} (\phi - \phi_0) \partial_s \mathbf{F}^\perp \tag{5}$$
$$= \begin{cases} \eta \left(f_{\text{tan}}(\alpha) \partial_s \mathbf{F} + f_{\text{inn}}(\alpha) \mathbf{V}(\alpha) \right), & \text{for } s = -L , \\ \pm \lambda_{\text{tether}} \nu, & \text{for } s = 0 , \end{cases}$$
$$\eta \partial_s^2 \mathbf{F} = 0, \quad \text{for } s = -L, 0 .$$

The terms in the second line are forces applied to the filament ends. The force in the direction ν orthogonal to the leading edge at $s = 0$ arises from the constraint (1) with the Lagrange parameter λ_{tether}. Its biological interpretation is due to tethering of the filament ends to the leading edge. The forces at the inner boundary $s = -L$ are models of the contraction effect of actin-myosin interaction in the interior region (see [12] for details).

3   Numerical Method

Before discretization, the problem for each filament family is transformed to a rectangular domain. For this formulation, a new anisotropic Finite Element (FE) method is presented, and several implementational issues are discussed.

3.1   Reparametrization

The fact that the maximal filament length varies along the lamellipodium and potentially with time has the consequence that the computational domain $B(t) = \{(\alpha, s) : 0 \le \alpha < 2\pi, \ -L(\alpha, t) \le s < 0\}$ is non-rectangular. In order to be able to use tensor product grids, we introduce the coordinate change

$$(\alpha, s, t) \rightarrow (\alpha, L(\alpha, t)s, t) ,$$

with the new domain $(\alpha, s) \in B_0 := [0, 2\pi) \times [-1, 0)$. Accordingly, a weak formulation of the transformed version of (3), (5) is given by

$$
\begin{aligned}
0 = & \int_{B_0} \eta \left(\mu^B \partial_s^2 \mathbf{F} \cdot \partial_s^2 \mathbf{G} + L^4 \mu^A \widetilde{D_t} \mathbf{F} \cdot \mathbf{G} + L^2 \lambda_{\text{inext}} \partial_s \mathbf{F} \cdot \partial_s \mathbf{G} \right) d(\alpha, s) \\
& + \int_{B_0} \eta \eta^* \left(L^4 \widehat{\mu^S} \left(\widetilde{D_t} \mathbf{F} - \widetilde{D_t^*} \mathbf{F}^* \right) \cdot \mathbf{G} \mp L^2 \widehat{\mu^T} (\phi - \phi_0) \partial_s \mathbf{F}^\perp \cdot \partial_s \mathbf{G} \right) d(\alpha, s) \\
& - \int_{B_0} p(\rho) \left(L^3 \partial_\alpha \mathbf{F}^\perp \cdot \partial_s \mathbf{G} - \frac{1}{L} \partial_s \mathbf{F}^\perp \cdot \partial_\alpha (L^4 \mathbf{G}) \right) d(\alpha, s) \\
& + \int_0^{2\pi} \eta \left(L^2 f_{\tan} \partial_s \mathbf{F} + L^3 f_{\text{inn}} \mathbf{V} \right) \cdot \mathbf{G} \Big|_{s=-1} d\alpha \mp \int_0^{2\pi} L^3 \lambda_{\text{tether}} \nu \cdot \mathbf{G} \Big|_{s=0} d\alpha , \quad (6)
\end{aligned}
$$

with $\mathbf{F}, \mathbf{G} \in H_\alpha^1((0, 2\pi); H_s^2(-1, 0))$, with the modified material derivative

$$\widetilde{D_t} = \partial_t - \left(\frac{\nu}{L} + \frac{s \partial_t L}{L} \right) \partial_s$$

and with the inextensibility constraint

$$|\partial_s \mathbf{F}(\alpha, s, t)| = L(\alpha, t) .$$

3.2   The Finite Element Formulation

As previously, we skip the superscripts ($\pm$) except for those of the other family that we indicate by $*$. For $N_\alpha, N_s \in \mathbb{N}$ we define the rectangular grid

$$\alpha_i = (i-1)\Delta\alpha, \quad i = 1, \ldots, N_\alpha + 1, \qquad \Delta\alpha = \frac{2\pi}{N_\alpha},$$

$$s_j = -1 + (j-1)\Delta s, \quad j = 1, \ldots, N_s, \qquad \Delta s = \frac{1}{N_s - 1},$$

where $\alpha_{N_\alpha+1} = 2\pi$ is identified with $\alpha_1 = 0$. Then the domain $B_0 = [0, 2\pi) \times [-1, 0)$ can be decomposed into rectangular computational cells:

$$B_0 = \bigcup_{i=1}^{N_\alpha} \bigcup_{j=1}^{N_s-1} C_{i,j}, \quad \text{with } C_{i,j} = [\alpha_i, \alpha_{i+1}) \times [s_j, s_{j+1}). \tag{7}$$

We introduce the conforming Finite Element space

$$\mathscr{V} := \Big\{ \mathbf{F} \in C_\alpha([0, 2\pi]; \, C_s^1([-1, 0]))^2 : \mathbf{F}\big|_{C_{i,j}} (\cdot, s) \in \mathbb{P}_\alpha^1,$$

$$\mathbf{F}\big|_{C_{i,j}} (\alpha, \cdot) \in \mathbb{P}_s^3 \quad \text{for } i = 1, \ldots, N_\alpha; \, j = 1, \ldots, N_s - 1 \Big\},$$

of continuous functions, continuously differentiable with respect to s, and on each computational cell coinciding with a first order polynomial in α for fixed s, and a third order polynomial in s for fixed α.

For representing the elements of $\mathscr{V}$, we introduce, for $(a, s) \in C_{i,j}$, the *shape functions*

$$
\begin{aligned}
L_1^{i,j}(\alpha) &= \frac{\alpha_{i+1} - \alpha}{\Delta\alpha}, & G_1^{i,j}(s) &= 1 - \frac{3(s-s_j)^2}{\Delta s^2} + \frac{2(s-s_j)^3}{\Delta s^3}, \\
L_2^{i,j}(\alpha) &= 1 - L_1^{i,j}(\alpha), & G_2^{i,j}(s) &= s - s_j - \frac{2(s-s_j)^2}{\Delta s} + \frac{(s-s_j)^3}{\Delta s^2}, \\
& & G_3^{i,j}(s) &= 1 - G_1^{i,j}(s), \\
& & G_4^{i,j}(s) &= -G_2^{i,j}(s_j + s_{j+1} - s),
\end{aligned}
\tag{8}
$$

which satisfy

$$
\begin{array}{llll}
L_1^{i,j}(\alpha_i) = 1, & L_1^{i,j}(\alpha_{i+1}) = 0, & & \\
L_2^{i,j}(\alpha_i) = 0, & L_2^{i,j}(\alpha_{i+1}) = 1, & & \\
G_1^{i,j}(s_j) = 1, & G_1^{i,j}(s_{j+1}) = 0, & (G_1^{i,j})'(s_j) = 0, & (G_1^{i,j})'(s_{j+1}) = 0, \\
G_2^{i,j}(s_j) = 0, & G_2^{i,j}(s_{j+1}) = 0, & (G_2^{i,j})'(s_j) = 1, & (G_2^{i,j})'(s_{j+1}) = 0, \\
G_3^{i,j}(s_j) = 0, & G_3^{i,j}(s_{j+1}) = 1, & (G_3^{i,j})'(s_j) = 0, & (G_{i,j})'(s_{j+1}) = 0, \\
G_4^{i,j}(s_j) = 0, & G_4^{i,j}(s_{j+1}) = 0, & (G_4^{i,j})'(s_j) = 0, & (G_4^{i,j})'(s_{j+1}) = 1,
\end{array}
\tag{9}
$$

and that they span $\mathbb{P}_\alpha^1$ and, respectively, $\mathbb{P}_s^3$. Consequentially, we define the composite *Lagrange–Hermite shape functions* (see also [3]), for $(\alpha, s) \in C_{i,j}$, by

(a) H_1^C (b) H_2^C (c) H_3^C (d) H_4^C
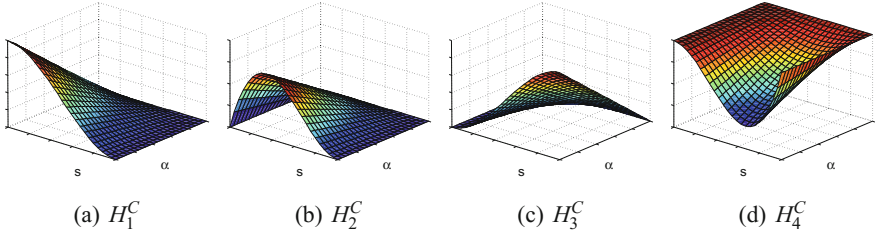
Fig. 3 Graphical representation of the Lagrange–Hermite shape functions (10). Each one of the shape functions attains the value 1 in one degree of freedom, and 0 on all the rest

$$
\begin{aligned}
H_1^{i,j}(\alpha, s) &= L_1^{i,j}(\alpha)G_1^{i,j}(s), & H_5^{i,j}(\alpha, s) &= L_2^{i,j}(\alpha)G_1^{i,j}(s), \\
H_2^{i,j}(\alpha, s) &= L_1^{i,j}(\alpha)G_2^{i,j}(s), & H_6^{i,j}(\alpha, s) &= L_2^{i,j}(\alpha)G_2^{i,j}(s), \\
H_3^{i,j}(\alpha, s) &= L_1^{i,j}(\alpha)G_3^{i,j}(s), & H_7^{i,j}(\alpha, s) &= L_2^{i,j}(\alpha)G_3^{i,j}(s), \\
H_4^{i,j}(\alpha, s) &= L_1^{i,j}(\alpha)G_4^{i,j}(s), & H_8^{i,j}(\alpha, s) &= L_2^{i,j}(\alpha)G_4^{i,j}(s),
\end{aligned}
\tag{10}
$$

and by $H_k^{i,j}(\alpha, s) = 0$, $k = 1, \ldots, 8$, for $(\alpha, s) \notin C_{i,j}$. Refer to Fig. 3 for a graphical representation presentation of (10). For a scalar function, there are eight degrees of freedom on each computational cell, which can be chosen as the function values and the derivatives with respect to s at the vertices. These degrees of freedom are the coefficients in a representation in terms of the basis $\{H_1^{i,j}, \ldots, H_8^{i,j}\}$.

Consequentially, every element $\mathbf{F}$ of the Finite Element space $\mathcal{V}$ can be represented in terms of the function values $\mathbf{F}_{i,j}$ and the s-derivatives $\partial_s \mathbf{F}_{i,j}$ at all grid points:

$$
\mathbf{F}(\alpha, s) = \sum_{i=1}^{N_\alpha} \sum_{j=1}^{N_s} \left(\mathbf{F}_{i,j} \Phi_{i,j}(\alpha, s) + \partial_s \mathbf{F}_{i,j} \Psi_{i,j}(\alpha, s) \right),
\tag{11}
$$

with the basis functions

$$
\begin{aligned}
\Phi_{i,j} &:= H_7^{i-1,j-1} + H_5^{i-1,j} + H_3^{i,j-1} + H_1^{i,j}, \\
\Psi_{i,j} &:= H_8^{i-1,j-1} + H_6^{i-1,j} + H_4^{i,j-1} + H_2^{i,j}, \\
& i = 1, \ldots, N_\alpha, \ j = 1, \ldots, N_s.
\end{aligned}
\tag{12}
$$

The Finite Element formulation of the lamellipodium problem on the time interval $[0, T]$ is to find $\mathbf{F} \in C^1([0, T]; \mathcal{V})$, such that the weak formulation (6) holds for all $\mathbf{G} \in C([0, T]; \mathcal{V})$.

3.3   Time Discretization – Implementation Issues

In this section we go through all the terms in (6) and discuss their time discretization and some implementation details. This will lead to a semi-implicit time discretization of the problem, where at each time step a linear system has to be solved. We shall use the superscripts n and $n + 1$ for the numerical approximations at the old time t_n and, respectively, the new time $t_{n+1} = t_n + \Delta t$, i.e.

$$\mathbf{F}^n(\alpha, s) = \sum_{i=1}^{N_\alpha} \sum_{j=1}^{N_s} \left(\mathbf{F}^n_{i,j} \Phi_{i,j}(\alpha, s) + \partial_s \mathbf{F}^n_{i,j} \Psi_{i,j}(\alpha, s) \right). \tag{13}$$

Finally, we shall also describe a regridding procedure in the α-direction, which has the goal to equidistribute the computational filaments.

Resistance Against Filament Bending

The bending term is evaluated at the new time step and therefore becomes

$$\int_{B_0} \eta \mu^B \partial_s^2 \mathbf{F}^{n+1} \cdot \partial_s^2 \mathbf{G} \, d(\alpha, s) \, ,$$

where for $\mathbf{G}$ the basis functions (12) are inserted. For the computation of the integral, a piecewise constant approximation for η is used.

Adhesion with the Substrate

For the transport operator $\widetilde{D_t} \mathbf{F}$ in

$$\int_{B_0} \eta L^4 \mu^A \widetilde{D_t} \mathbf{F} \cdot \mathbf{G} \, d(\alpha, s) \, ,$$

an explicit time discretization is used, i.e., it is replaced by

$$\frac{\mathbf{F}^{n+1} - \mathbf{F}^n}{\Delta t} - \left(\frac{v}{L} + \frac{s \partial_t L}{L} \right) \partial_s \mathbf{F}^n \, .$$

For the computation of the integral, piecewise constant approximations for η and $1/L$ were used. For the factor L^4, L was approximated by piecewise linear functions.

Stretching of Cross-Links

The friction term caused by the stretching of cross-links requires the computation of the relative velocity $D_t \mathbf{F} - D_t^* \mathbf{F}^*$, which is a subtle issue since the material derivative of $\mathbf{F}^*$ has to be evaluated at (α^*, s^*), defined by

$$\mathbf{F}(\alpha, s, t) = \mathbf{F}^*(\alpha^*, s^*, t) \, . \tag{14}$$

The computation

$$
\begin{aligned}
&\Delta t \left(D_t \mathbf{F}(\alpha, s) - D_t \mathbf{F}^*(\alpha^*, s^*) \right) \\
&\approx \mathbf{F}^{n+1}(\alpha, s) - \mathbf{F}^n(\alpha, s) - v \Delta t \partial_s \mathbf{F}^n(\alpha, s) \\
&\quad - \mathbf{F}^{n+1,*}(\alpha^*, s^*) + \mathbf{F}^{n,*}(\alpha^*, s^*) + v^* \Delta t \partial_s \mathbf{F}^{n,*}(\alpha^*, s^*) \\
&\approx \mathbf{F}^{n+1}(\alpha, s) - \mathbf{F}^n(\alpha, s + v \Delta t) - \mathbf{F}^{n+1,*}(\alpha^*, s^*) + \mathbf{F}^{n,*}(\alpha^*, s^* + v^* \Delta t)
\end{aligned}
$$

shows that it is convenient to introduce an additional $O(\Delta t)$-discretization error, replacing (14) by

$$
\mathbf{F}^n(\alpha, s + v \Delta t) = \mathbf{F}^{*,n}(\alpha^*, s^* + v^* \Delta t) . \tag{15}
$$

Another difficulty originates from the fact that the s^*-direction in the (α^*, s^*)-plane does not correspond to the s-direction in the (α, s)-plane, and therefore it is difficult to express the information encoded in the values of $\partial_{s^*} \mathbf{F}^*$ in terms of (α, s). We therefore decided for approximations of the cross-link terms only in terms of the filament positions:

$$
\mathbf{F}^n(\alpha, s) = \sum_{i=1}^{N_\alpha} \sum_{j=1}^{N_s} \mathbf{F}_{i,j}^n \widehat{\Phi_{i,j}}(\alpha, s) , \qquad \mathbf{F}^{*,n}(\alpha^*, s^*) = \sum_{i=1}^{N_\alpha} \sum_{j=1}^{N_s} \mathbf{F}_{i,j}^{*,n} \widehat{\Phi_{i,j}}(\alpha^*, s^*) ,
$$

where the hat-functions $\widehat{\Phi_{i,j}}$ are piecewise bilinear. The Eq. (15) is solved for $(\alpha, s) = (\alpha_i, s_j)$, $i = 1, \ldots, N_\alpha$, $j = 1, \ldots, N_s$, using these representations, which involves a search for the quadrilateral of $\mathbf{F}^{*,n}$-positions containing $\mathbf{F}^n(\alpha_i, s_j + v \Delta t)$. The nonlinear system is then solved by using a bilinear representation of $\mathbf{F}$, which allows to solve the system exactly. The resulting values for (α^*, s^*) are denoted by $(\alpha_{i,j}^*, s_{i,j}^*)$. Finally, the relative velocity is approximated by

$$
(D_t \mathbf{F} - D_t^* \mathbf{F}^*)(\alpha, s) \approx \sum_{i=1}^{N_\alpha} \sum_{j=1}^{N_s} \frac{\mathbf{F}_{i,j}^{n+1} - \mathbf{F}^{*,n+1}(\alpha_{i,j}^*, s_{i,j}^*)}{\Delta t} \widehat{\Phi_{i,j}}(\alpha, s)
$$

in the cross-link stretching term

$$
\int_{B_0} \eta \eta^* L^4 \widehat{\mu^S} \left(D_t \mathbf{F} - D_t^* \mathbf{F}^* \right) \cdot \mathbf{G} \, d(\alpha, s) , \tag{16}
$$

where, again η and η^* are approximated as piecewise constant and L as piecewise linear.

Twisting of Cross-Links

For the cross-link twisting term, a semi-implicit time discretization is used. The angle between filaments is evaluated at each grid point and at the old time step:

$$\phi_{i,j}^n = \arccos\left(\partial_s \mathbf{F}_{i,j}^n \cdot \partial_s \mathbf{F}^{*,n}(\alpha_{i,j}^*, s_{i,j}^*)\right),$$

with $(\alpha_{i,j}^*, s_{i,j}^*)$ computed as above. A piecewise constant approximation ϕ^n is then obtained from averaging over grid cells. This is used in the evaluation of

$$\int_{B_0} \eta\eta^* L^2 \widehat{\mu^T}(\phi^n - \phi_0)\partial_s\mathbf{F}^{n+1,\perp} \cdot \partial_s\mathbf{G}\, d(\alpha, s),$$

where also η and η^* are approximated by piecewise constant functions and L by piecewise linear functions.

Filament Repulsion

For the pressure $p(\rho)$ with $\rho = \eta/|\partial_s\mathbf{F} \cdot \partial_\alpha\mathbf{F}^\perp|$ a piecewise constant approximation ρ^n evaluated at the old time step is used. It is calculated using the representation of F given in (13) to compute cell averages of $\partial_s F$ and $\partial_\alpha F$. The function η is approximated by a piecewise constant function. The pressure term is discretized semi-implicitly as

$$\int_{B_0} p(\rho^n)\left(L^3\partial_\alpha\mathbf{F}^{n+1,\perp} \cdot \partial_s\mathbf{G} - \frac{1}{L}\partial_s\mathbf{F}^{n+1,\perp} \cdot \partial_\alpha(L^4\mathbf{G})\right) d(\alpha, s).$$

As above L is approximated by a piecewise linear function, with the exception of the coefficient $1/L$, which is approximated by a piecewise constant function.

Inextensibility Constraint

With a penalization approach, the inextensibility term

$$\int_{B_0} \eta L^2 \lambda_{\text{inext}} \partial_s\mathbf{F} \cdot \partial_s\mathbf{G}\, d(\alpha, s)$$

in (6) is replaced by

$$\int_{B_0} \eta L^2 \frac{|\partial_s\mathbf{F}|^2 - L^2}{\varepsilon}\partial_s\mathbf{F} \cdot \partial_s\mathbf{G}\, d(\alpha, s),$$

with a small positive parameter ε. We use the semi-implicit linearization

$$\left(|\partial_s\mathbf{F}|^2 - L^2\right)\partial_s\mathbf{F} \approx \left(|\partial_s\mathbf{F}^n|^2 - L^2\right)\partial_s\mathbf{F}^{n+1} + 2\left(\partial_s\mathbf{F}^n \cdot \partial_s\mathbf{F}^{n+1} - |\partial_s\mathbf{F}^n|^2\right)\partial_s\mathbf{F}^n$$

and employ the augmented Lagrangian method, whence the inextensibility term becomes

$$\int_{B_0} \eta L^2 \left(\left(\lambda^n + \frac{|\partial_s\mathbf{F}^n|^2 - L^2}{\varepsilon}\right)\partial_s\mathbf{F}^{n+1} + \frac{2}{\varepsilon}\left(\partial_s\mathbf{F}^n \cdot \partial_s\mathbf{F}^{n+1} - |\partial_s\mathbf{F}^n|^2\right)\partial_s\mathbf{F}^n\right)$$
$$\cdot\partial_s\mathbf{G}\, d(\alpha, s).$$

After the time step is carried out, the Lagrange multiplier is updated by

$$\lambda^{n+1} = \lambda^n + \frac{|\partial_s \mathbf{F}^n|^2 - L^2}{\varepsilon} + \frac{2}{\varepsilon} \left(\partial_s \mathbf{F}^n \cdot \partial_s \mathbf{F}^{n+1} - |\partial_s \mathbf{F}^n|^2 \right) .$$

Again, L is approximated as piecewise linear.

Spatial Equidistribution of Computational Filaments

In some simulations, the computational filaments tend to be distributed unevenly. This is avoided by a regridding procedure, where the computational barbed ends are evenly distributed along the leading edge, which can be achieved by a coordinate change $\alpha \to \beta$, defined by

$$\beta = 2\pi \int_0^\alpha |\partial_\alpha \mathbf{F}(\hat{\alpha}, 0, t)| d\hat{\alpha} \left(\int_0^{2\pi} |\partial_\alpha \mathbf{F}(\hat{\alpha}, 0, t)| d\hat{\alpha} \right)^{-1} .$$

Numerically this is realized after carrying out a time step $t_{n-1} \to t_n$, by defining a piecewise linear function $g(\alpha)$ through its values at the grid:

$$g(\alpha_i) := 2\pi \sum_{j=1}^{i-1} |\mathbf{F}^n_{j+1,N_s} - \mathbf{F}^n_{j,N_s}| \left(\sum_{j=1}^{N_\alpha} |\mathbf{F}^n_{j+1,N_s} - \mathbf{F}^n_{j,N_s}| \right)^{-1} , \quad i = 1, \ldots, N_\alpha + 1 .$$

Then $\widetilde{\alpha}_1, \ldots, \widetilde{\alpha}_{N_\alpha+1}$ are determined as the solutions of

$$g(\widetilde{\alpha}_i) = (i-1)\Delta\alpha , \quad i = 1, \ldots, N_\alpha + 1 .$$

Now the computational filaments, corresponding to $\alpha = \alpha_1, \ldots, \alpha_{N_\alpha+1}$, are replaced by those located at $\alpha = \widetilde{\alpha}_1, \ldots, \widetilde{\alpha}_{N_\alpha+1}$:

$$\widetilde{\mathbf{F}}^n_{i,j} := \mathbf{F}^n(\widetilde{\alpha}_i, s_j) , \qquad \widetilde{\partial_s \mathbf{F}}^n_{i,j} := \partial_s \mathbf{F}^n(\widetilde{\alpha}_i, s_j) ,$$

and the density also needs to be redefined:

$$\widetilde{\eta}^n_{i,j} := \frac{\eta^n(\widetilde{\alpha}_i, s_j)}{g'(\widetilde{\alpha}_i)} .$$

This procedure can be carried out whenever needed. In the simulations of the following section, it was done after every time step.

4 Numerical Simulations

The purpose of this section is to demonstrate that the model is capable of predicting the outcome of migration experiments on inhomogeneous adhesive patterns. In [12] the effect of varying different model parameters has been demonstrated. Additionally the model has been used to simulate chemotactic migration and to study the

effect of changes in the signaling cascade on cell shape and filament density. Here we go a step further and simulate how the shape of a migrating cell is influenced by inhomogeneous adhesive patterns. Such studies are used to better understand the interplay between adhesion, contraction, actin polymerization and other actin associated proteins.

4.1 Experiment 1: Strongly Versus Weakly Adhesive Stripes

We show that model predictions are consistent with experimental data on migration experiments published in [4]. In these experiments migrating fish keratocytes were placed on substrates coated with distinct patterns of the extra-cellular-matrix (ECM) protein fibronectin which binds to integrin transmembrane receptors mediating adhesion. In [4] striped patterns were used featuring adhesive (fibronectin containing) strips of 5 µm width and nonadhesive strips (without fibronectin) varying between 5 and 30 µm in width. In [4] it was reported that this affects cell shape in a very distinct way. Protruding bumps on the adhesive strips and lagging bumps on the nonadhesive stripes were observed and their width was correlated to the stripe width. Also it was observed that cells tend to assume a symmetric shape such that they had an equal
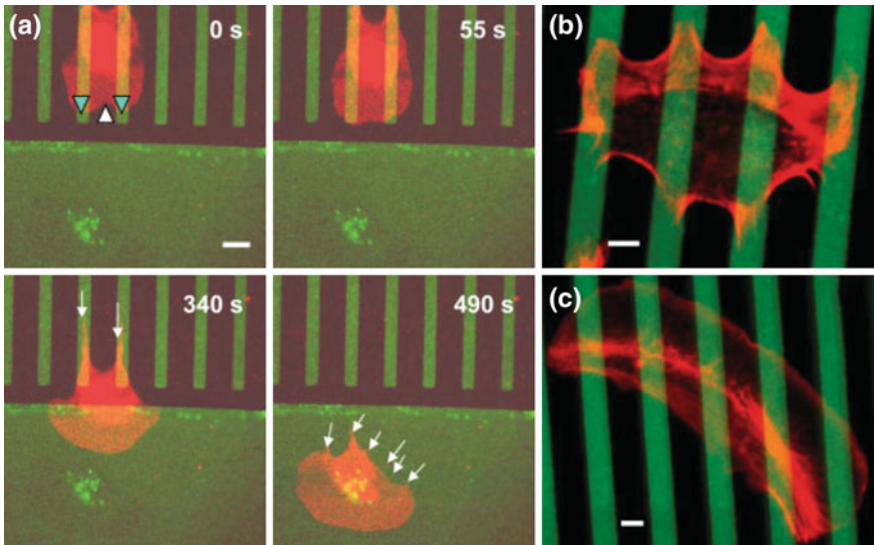
Fig. 4 Figure reproduced from [4]: "Reversible deformation of the leading edge on line patterns. **a**: ... keratocyte crawling from a 5–9 pattern ... onto an unpatterned region ... **b**: Deformation of the leading edge on a 5–7 pattern with protruding bumps on adhesive stripes and lagging bumps on non-adhesive stripes... **c**: Control experiment on a 5–7 line pattern where unprinted regions (black) are not backfilled ... rendering the substrate homogeneously adhesive. Cells restore their characteristic crescent-shaped outline ... Scale bars: 5 µm"
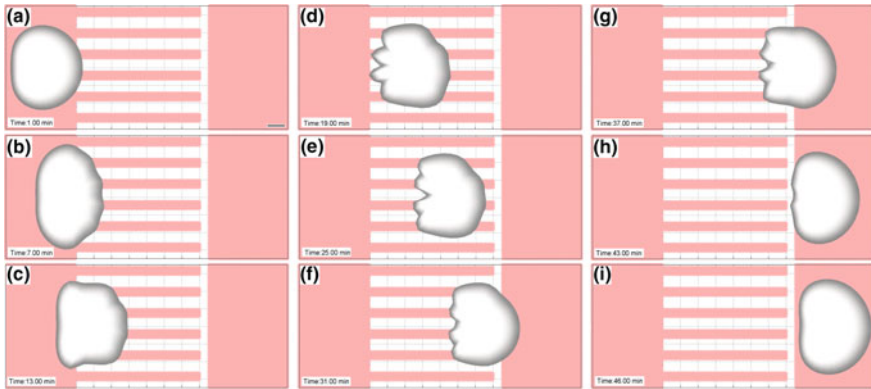
Fig. 5 a–i Times series of the simulation of a cell moving over a striped adhesive pattern (*red*) with a 80% drop in adhesiveness (*white*) between adhesive strips. *Shading* represents actin network density. Parameter values as in Table 1. The *bar* represents 10 μm

number of adhesive strips to the right and to the left of their cell center (Fig. 4 shows some of the data published in [4]).

In the numerical experiment we used the same geometrical pattern with adhesive strips of 5 μm width interspaced with 7 μm wide strips of reduced adhesiveness. In the mathematical model adhesion forces result in friction between the cell and the substrate and, speaking in numerical terms, they link one time step to the next. We simulated the inhomogeneous adhesive pattern by decreasing the friction coefficient by 80–90% in those regions of low fibronectin concentration as compared to adhesive regions. Whilst the keratocytes in the original experiments move spontaneously without an external signal, we simulate chemotactic cells under an external cue, since at this point the model cannot describe the dynamics of contractile rear bundles which stabilize autonomously migrating keratocytes. However the numerical results show that there are many similarities as far as general behavior and morphology are concerned, suggesting that the underlying phenomena are very similar. In Fig. 5a–i a time series resulting from the simulation of a cell on a striped adhesive pattern with a drop in adhesiveness of 80% is depicted. The following agreements between the simulation and the experiments (Fig. 4) were found:

- On the striped adhesion pattern the cell shape becomes more rectangular as compared to the crescent shape in the homogeneously adhesive region.
- Cells show protruding bumps on the adhesive stripes and lagging bumps on non-adhesive stripes.
- The width of the bumps is correlated with the widths of the stripes.
- Spikes appear at the rear of the cell.
- After leaving the striped region the cell resumes its crescent shape and continues to migrate as before.
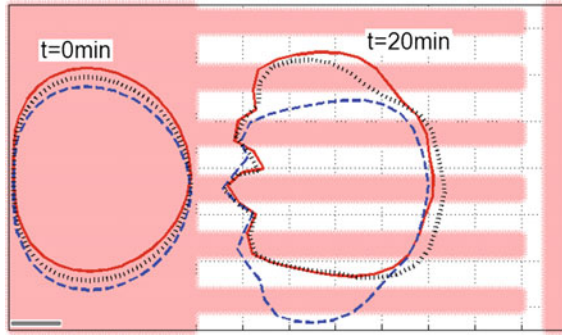
Fig. 6 Comparison of the cell shape for three different starting positions. Parameter values as in Table 1. The bar represents 10 μm
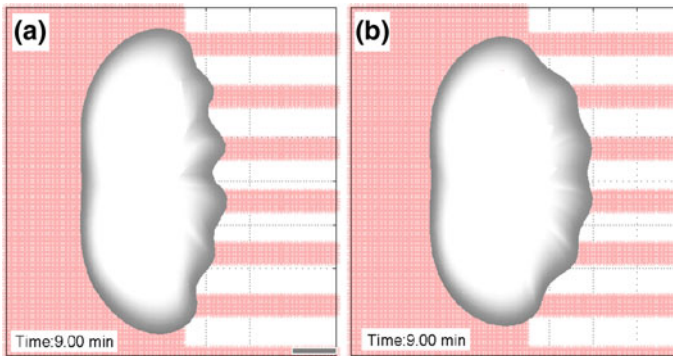

Fig. 7 Movement of a cell on an adhesive substrate (*red*) with less-adhesive stripes (*white*). *Shading* represents actin network density. **a** 90% drop in adhesiveness, **b** 80% drop in adhesiveness. Parameter values as in Table 1. The *bar* represents 10 μm

To compare the influence of the starting position on the shape of the cell, the simulation was performed with three different initial conditions differing by 2 μm shifts in the y-direction. The outcome is depicted in Fig. 6. It can be observed that the shape of the cell starting at the lowest position (blue, dashed) differs significantly from the other two. This is due to the fact that it interacts with the lowest adhesive stripe causing it to shift further down as compared to the other cells.

In Fig. 7a, b a comparison between the bumps on stripes with a 90% (a) and a 80% (b) drop in adhesiveness is shown. Here the α-discretization used was twice as fine to resolve more details. As expected bumps when adhesiveness drops by 90% are more pronounced. Over a time interval of several minutes the amplitude of the bumps fluctuated, an observation also made in the experiment of [4].
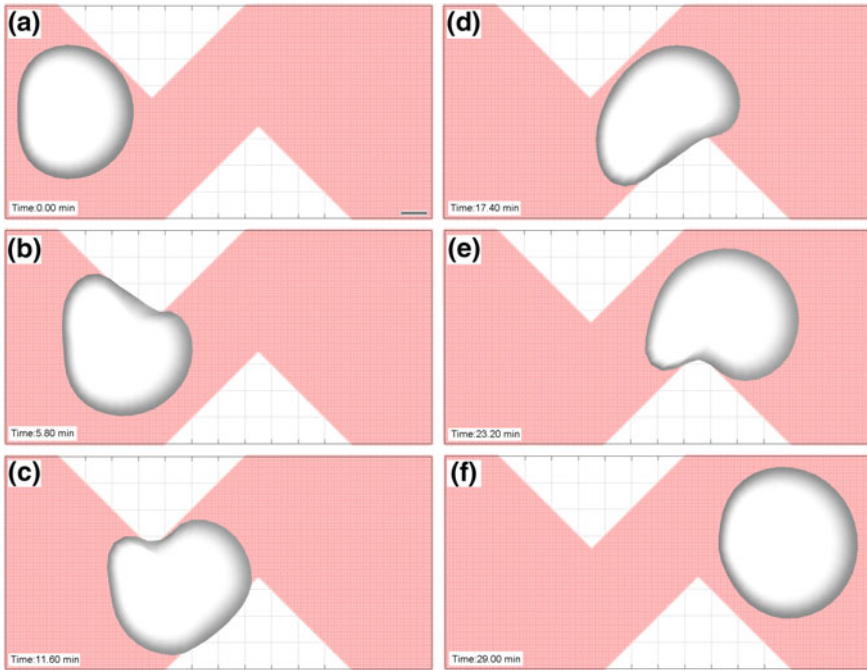
Fig. 8 Movement of a cell on an adhesive substrate (*red*) with less-adhesive spikes (*white*). *Shading* represents actin network density. Parameter values as in Table 1. The *bar* represents 10 μm

4.2 Experiment 2: Less-Adhesive Spikes on Strongly Adhesive Ground

Next we demonstrate the predictive capacity of the model simulating cell migration along an adhesive path lined by irregular regions of low adhesion. The low-adhesion pattern consists of two shifted spikes lining the trajectory of the cell from both sides. The drop in adhesiveness was chosen to be 80%. As opposed to the situation above, the cell is now able to almost fully avoid the less-adhesive regions. The behavior observed over a time period of 30 min is depicted in the time series shown in Fig. 8. The outcome of the simulation is counterintuitive in the cell does not simply slide of the nonadhesive areas. Instead it behaves as if the less-adhesive spikes were obstacles and only a very small portion of the lamellipodium enters the less-adhesive areas.

4.3 Parameters Values

For the discretization we used a time step of 0.12 s and nine nodes per filament. For the first experiment we used 36 and 72 discrete filaments, for the second one 36.

Table 1 Parameter values

Var.	Meaning	Value	Comment
μ^B	Bending elasticity	$0.07\,\mathrm{pN}\,\mu\mathrm{m}^2$	[5]
μ^A	Macroscopic friction caused by adhesions	$0.041, 0.082,$ $0.41\,\mathrm{pN}\,\mathrm{min}\,\mu\mathrm{m}^{-2}$	Lower values for less-adhesive regions, highest value for adhesive regions, order of magnitude from measurements in [10, 16], estimation and calculations in [17, 18, 20]
κ_{br}	Branching rate	$10\,\mathrm{min}^{-1}$	Order of magnitude from [7], chosen to fit $2\overline{\rho}_{\mathrm{ref}} = 90\,\mu\mathrm{m}^{-1}$ [26]
κ_{cap}	Capping rate	$5\,\mathrm{min}^{-1}$	Order of magnitude from [7], chosen to fit $2\overline{\rho}_{\mathrm{ref}} = 90\,\mu\mathrm{m}^{-1}$ [26]
c_{rec}	Arp2/3 recruitment	$900\,\mu\mathrm{m}^{-1}\,\mathrm{min}^{-1}$	Chosen to fit $2\overline{\rho}_{\mathrm{ref}} = 90\,\mu\mathrm{m}^{-1}$ [26]
κ_{sev}	Severing rate	$0.38\,\mathrm{min}^{-1}\,\mu\mathrm{m}^{-1}$	Chosen to give lamellipodium widths similar as described in [26]
μ^{IP}	Actin–myosin interaction strength	$0.1\,\mathrm{pN}\,\mu\mathrm{m}^{-2}$	
A_0	Equilibrium inner area	$450\,\mu\mathrm{m}^2$	Order of magnitude as in [25, 27]
$v_{\min}$	Minimal polymerization speed	$1.5\,\mu\mathrm{m}\,\mathrm{min}^{-1}$	In biological range
$v_{\max}$	Maximal polymerization speed	$8\,\mu\mathrm{m}\,\mathrm{min}^{-1}$	In biological range
μ^P	Pressure constant	$0.05\,\mathrm{pN}\,\mu\mathrm{m}$	
μ^S	Cross-link stretching constant	$7.1\times10^{-3}\,\mathrm{pN}\,\mathrm{min}\,\mu\mathrm{m}^{-1}$	
μ^T	Cross-link twisting constant	$7.1\times10^{-3}\,\mu\mathrm{m}$	
κ_{ref}	Reference leading edge curvature for polymerization speed reduction	$(5\,\mu\mathrm{m})^{-1}$	

For the biological parameters, we used the same as those in [12], apart from the adhesion coefficient which was increased for the adhesive regions and decreased for the less-adhesive regions. They are summarized in Table 1.

References

1. W. Alt and M. Dembo. Cytoplasm dynamics and cell motion: Two-phase flow models. *Math. Biosci.*, 156(1–2):207–228, 1999.
2. L. Blanchoin, R. Boujemaa-Paterski, C. Sykes, and J. Plastino. Actin dynamics, architecture, and mechanics in cell motility. *Physiological Reviews*.
3. D. Braess. *Finite Elements. Theory, fast solvers, and applications to solid mechanics.* Cambridge University Press, 2001.
4. G. Csucs, K. Quirin, and G. Danuser. Locomotion of fish epidermal keratocytes on spatially selective adhesion patterns. *Cell Motility and the Cytoskeleton*, 64(11):856–867, 2007.
5. F. Gittes, B. Mickey, J. Nettleton, and J. Howard. Flexural rigidity of microtubules and actin filaments measured from thermal fluctuations in shape. *The Journal of Cell Biology*, 120(4):923–34, 1993.
6. M.E. Gracheva and H.G. Othmer. A continuum model of motility in ameboid cells. *Bull. Math. Biol.*, 66(1):167–193, 2004.
7. H.P. Grimm, A.B. Verkhovsky, A. Mogilner, and J.-J. Meister. Analysis of actin dynamics at the leading edge of crawling cells: implications for the shape of keratocytes. *European Biophysics Journal*, 32:563–577, 2003.
8. C.I. Lacayo, Z. Pincus, M.M. VanDuijn, C.A. Wilson, D.A. Fletcher, F.B. Gertler, A. Mogilner, and J.A. Theriot. Emergence of large-scale cell morphology and movement from local actin filament growth dynamics. 2007.
9. T. Lämmermann, M. Sixt, Mechanical modes of amoeboid cell migration. *Current Opinion in Cell Biology* **21**(5), 636–644 (2009)
10. F. Li, S.D. Redick, H.P. Erickson, and V.T. Moy. Force measurements of the $\alpha 5 \beta 1$ integrin-fibronectin interaction. *Biophysical Journal*, 84(2):1252–1262, 2003.
11. I.V. Maly and G.G. Borisy. Self-organization of a propulsive actin network as an evolutionary process. *Proc. Natl. Acad. Sci.*, 98:11324–11329, 2001.
12. A. Manhart, D. Oelz, C. Schmeiser, and N. Sfakianakis. An extended Filament Based Lamellipodium Model produces various moving cell shapes in the presence of chemotactic signals. *J. Theor. Biol.*, 382:244–258, 2015.
13. A. F. M. Marée, A. Jilkine, A. Dawes, V. A. Grieneisen, and L. Edelstein-Keshet. Polarization and movement of keratocytes: a multiscale modelling approach. *Bull. Math. Biol.*, 68(5):1169–1211, 2006.
14. R.W. Metzke, M.R.K. Mofrad, and W.A. Wall. Coupling atomistic simulation to a continuum based model to compute the mechanical properties of focal adhesions. *Biophysical Journal*, 96(3, Supplement 1):673a –, 2009.
15. S.J. Mousavi and M.H. Doweidar. Three-dimensional numerical model of cell morphology during migration in multi-signaling substrates. *PLoS ONE*, 10(3), 2015.
16. A.F. Oberhauser, C. Badilla-Fernandez, M. Carrion-Vazquez, and J.M. Fernandez. The mechanical hierarchies of fibronectin observed with single-molecule AFM. *Journal of Molecular Biology*, 319(2):433–47, 2002.
17. D. Oelz and C. Schmeiser. *Cell mechanics: from single scale-based models to multiscale modeling.*, chapter How do cells move? Mathematical modeling of cytoskeleton dynamics and cell migration. Chapman and Hall, 2010.
18. D. Oelz and C. Schmeiser. Derivation of a model for symmetric lamellipodia with instantaneous cross-link turnover. *Archive for Rational Mechanics and Analysis*, 198:963–980, 2010.
19. D. Oelz and C. Schmeiser. Simulation of lamellipodial fragments. *Journal of Mathematical Biology*, 64:513–528, 2012.
20. D. Oelz, C. Schmeiser, and J.V. Small. Modeling of the actin-cytoskeleton in symmetric lamellipodial fragments. *Cell Adhesion and Migration*, 2:117–126, 2008.
21. B. Rubinstein, K. Jacobson, and A. Mogilner. Multiscale two-dimensional modeling of a motile simple-shaped cell. *Multiscale Model. Simul.*, 3(2):413–439, 2005.
22. B. Rubinstein, M.F. Fournier, K. Jacobson, A.B Verkhovsky, and A. Mogilner. Actin-myosin viscoelastic flow in the keratocyte lamellipod. *Biophysical Journal*, 97(7):1853–1863, 2009.

23. Y. Sakamoto, S. Prudhomme, and M.H. Zaman. Modeling of adhesion, protrusion, and contraction coordination for cell migration simulations. *Journal of Mathematical Biology*, 68(1–2):267–302, 2014.
24. T.E. Schaus, E. W. Taylor, and G. G. Borisy. Self-organization of actin filament orientation in the dendritic-nucleation/array-treadmilling model. *Proc Natl Acad Sci USA*, 104(17):7086–91, 2007.
25. J.V. Small, G. Isenberg, and J.E. Celis. Polarity of actin at the leading edge of cultured cells. *Nature*, bf 272:638–639, 1978.
26. J.V. Small, T. Stradal, E. Vignal, and K. Rottner. The lamellipodium: where motility begins. *Trends in Cell Biology*, 12(3):112–20, 2002.
27. A.B. Verkhovsky, T.M. Svitkina, and G.G. Borisy. Self-polarisation and directional motility of cytoplasm. *Current Biology*, 9(1):11–20, 1999.
28. M. Vinzenz, M. Nemethova, F. Schur, J. Mueller, A. Narita, E. Urban, C. Winkler, C. Schmeiser, S.A. Koestler, K. Rottner, G.P. Resch, Y. Maeda, and J.V. Small. Actin branching in the initiation and maintenance of lamellipodia. *Journal of Cell Science*, 125(11):2775–2785, 2012.

Author Index